

TECHNOLOGY DRIVEN. WARFIGHTER FOCUSED.

FY15

PROCEEDINGS OF THE
EDGEWOOD CHEMICAL BIOLOGICAL CENTER

IN-HOUSE LABORATORY INDEPENDENT RESEARCH AND SURFACE SCIENCE INITIATIVE PROGRAMS



U.S. ARMY
RDECOM



MESSAGE from the IN-HOUSE LABORATORY INDEPENDENT RESEARCH PROGRAM MANAGER

It is my pleasure to present the 2015 edition of the Proceedings of the Edgewood Chemical Biological Center's (ECBC) In-House Laboratory Independent Research (ILIR) and Surface Science Initiative (SSI) Programs. The ECBC ILIR program funds innovative basic research projects that are high-risk with high potential for fulfilling future Army capability needs. Specifically designed to foster increased innovation, the ILIR program also aims to mentor junior investigators in the art and practice of initiating technological innovations and pursuing phenomenology at the boundaries of chemistry, biology, mathematics, or physics to gain insight and advances in support of CBRNE defense missions.

This report includes a description of the ILIR program's rigorous project selection and evaluation process by external senior scientists across the government. These reviews ensure that we not only fund projects with the greatest potential for fulfilling future Army capability needs, but that we receive an honest and unbiased assessment of our research efforts to hone the Basic Research program year after year.

This report also highlights how we are ensuring ECBC's basic research portfolio aligns to the future science and technology capability needs of the Department of Defense (DoD). Starting this year with the Innovative Development of Employee Advanced Solutions (IDEAS) program (formerly the Section 219 program) and beginning in fiscal year (FY) 2017 for the ILIR program, we are instituting progressive changes to ensure the Center not only responds to technology pulls, but pushes innovative technology forward to meet current capability gaps of the Warfighter.

Finally, the report concludes with the technical manuscripts from each of the six ILIR, five SSI, and seven internally-funded Seedling projects in FY15. Together, these projects covered areas of interest across the chemical, biological, and physical sciences, including: *Rational Molecular Synthesis and Nano-system Design*, *Synthetic Biology*, *Nano Chemical and Biological Sensing*, *Panomics and Molecular Toxicology*, *Aerosol Sciences*, *Algorithm Design and Development*, and *Surface Science*.

If you have questions about the ILIR Program or this report, please do not hesitate to contact me or the ILIR Administrative Coordinator directly. I can be reached by telephone at (410) 436-0683, DSN 584-0683, or by email at augustus.w.fountain.civ@mail.mil. The ILIR Administrative Coordinator, Ms. Rebecca Braun, can be reached at (410) 297-5979 or by email at rebecca.m.braun.ctr@mail.mil.

Sincerely,

Augustus W. Fountain III, Ph.D.
Senior Research Scientist (ST), Chemistry



Strategic Mission and Vision

The US Army Edgewood Chemical Biological Center (ECBC) is the nation's principal research, development, and engineering resource for non-medical chemical and biological (CB) defense applications. ECBC's mission to be the Nation's provider of innovative chemical and biological solutions supports the Center's vision of being a Provider of World Class Solutions. ECBC understands the comprehensive threat to the world, and provides the scientific knowledge, technology, and materiel required to protect and enable the Warfighter to effectively operate and implement strategic decisions while in the presence of CB contamination.

ECBC's mission and vision are supported by the Center's three Directorates of Research and Technology (R&T), Engineering, and Program Integration. The R&T Directorate provides integrated science and technology (S&T) solutions that address CB defense knowledge gaps and vulnerabilities. Basic science research at ECBC contributes valuable information to the fundamental science knowledgebase, enabling the development of technologies that directly benefit the Warfighter and further strengthen the Army's S&T mission. ECBC's unique set of core research and technology capabilities position it to be the Army's fundamental source of research in chemistry and biology.

A Soldier dons gloves during a Chemical, Biological, Radiological, Nuclear training exercise. (DoD photo by Staff Sgt. Steven Colvin, U.S. Army/Released)



ECBC ILIR Project Selection and Evaluation Process

The purpose of the ILIR program is to fund innovative basic research projects that are high risk and have high potential payoff for fulfilling future Army capability needs. The DoD defines basic research as “the systematic study directed toward greater knowledge or understanding of the fundamental aspects of phenomena and of observable facts without specific applications toward processes or products in mind.” The ILIR program is also specifically designed to foster increased innovation within ECBC. ECBC views the program as a critical part of its efforts to ensure a high level of quality in basic science; to foster innovation in the areas of chemistry and biology; to mentor junior investigators in the art and practice of laboratory science; and to explore new technological innovations and phenomenology at the boundaries of chemistry, biology, mathematics, or physics to expand the state-of-the-possible in support of CBRNE defense missions.

The ILIR program solicits the Center’s principal investigators for innovative proposals that correspond to topics highlighted in the ECBC R&T Directorate’s Strategic Roadmap. The FY15 ILIR topics are: *Rational Molecular Synthesis and Nano-system Design, Synthetic Biology, Nano Chemical and Biological Sensing, Panomics and Molecular Toxicology, Aerosol Sciences, Algorithm Design and Development, and Surface Science*. Proposals are first reviewed internally by the Branch and Division Chiefs for their technical innovation, alignment to Army/ECBC S&T topic areas, and programmatic completeness. The proposals are then reviewed and critiqued by a panel comprised of resident and external Department of the Army Senior Technologists (ST), Senior Scientists from other DoD organizations, and civilian and military faculty members at the United States Military Academy.

The review panel evaluates each proposal on its scientific objective, the scientific methods proposed, the qualifications of the investigator, and the budget; with the scientific objective and methods weighted as the most important criteria. The proposals are then ranked according to merit. Only proposals deemed by the panel as basic research are considered for funding. Quality comments from the reviewers are compiled and used, with the numerical score, as a critical assessment of the proposal. This written feedback is essential for ECBC’s mentoring of researchers and for justifying the elimination of research programs that are not competitive.

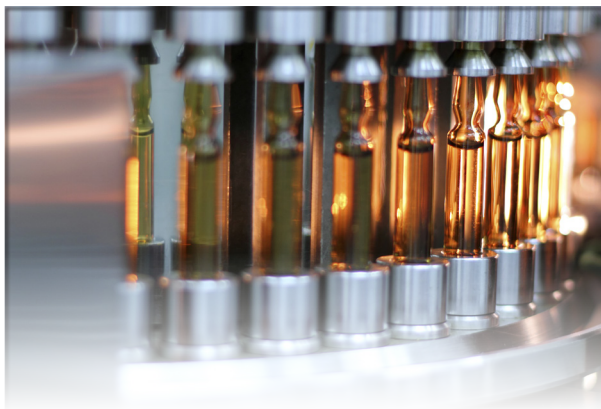
Quarterly reviews of project performance provide guidance to the program’s participants, ensuring that projects meet significant milestones and that substantive new knowledge is being produced and transferred to ECBC and the broader scientific community. An external Technical Advisory Board (TAB), comprised of senior research scientists from across academia and government organizations, convenes annually in the fourth quarter of the program to assess year-to-date performance of the funded basic science research projects. Comments and feedback from the TAB Review Panel are used as a guide for shaping the overall mission of the ILIR program and to improve the overall quality of ECBC’s basic science research projects into subsequent years.

This cyclical review and assessment process was used to select and monitor the progress of six ILIR projects. Internal funds were also used to support five basic research projects under the SSI program and seven “Seedling” projects, which are smaller-scale projects of high risk, high reward basic research. This Proceedings Report contains the technical reports from all 18 ECBC produced ILIR/SSI/Seedling-funded projects.

FY15 Innovation Program Highlights

ECBC R&T hosted its annual Technical Advisory Board (TAB) Review of select R&T basic science programs on 1 and 2 September, 2015. The TAB Review gives ECBC the opportunity to obtain an unbiased, external assessment of the content, quality, innovation, accomplishments, and relevance of select research programs from a panel of distinguished personnel.

This year, the TAB evaluated 11 projects from the FY15 ILIR and SSI programs, and 16 projects from the internally-funded Seedling and Section 219 Innovation Programs over two days. On the first day, principal investigators from the ILIR and SSI projects each made 30 minute presentations to the TAB on a variety of topics, ranging from, "*Characterization of the Host Proteome within Virion Particles from the Alphaviridae and Flaviviridae Viral Families*," to "*Plasmon-Exciton Coupling in Multilayered Nanostructures*." Seedling and Section 219 projects were evaluated in a separate poster session on the second day of the review.



The review concluded with the TAB formally presenting their assessment of the projects to the ECBC Director and ECBC R&T Director. The projects were evaluated against four criteria: scientific objectives; opportunity and significance; research methodology; its connections to the broader community, and overall capabilities and metrics. The TAB provided recommendations on how best to refine each project for success. The TAB's feedback helps to guide the projects and shapes the overall quality and mission of ECBC's basic science research programs.

This year, the TAB consisted of experts from both the Department of Defense and Department of Homeland Security:

- Donald Bansleben, Ph.D., Acting Branch Chief, Chem-Bio Research and Development Branch, Department of Homeland Security Science and Technology Directorate
- Charlene Mello, Ph.D., Chief Scientist, Macromolecular Science Team, US Army Natick Soldier Research, Development and Engineering Center
- Dawanne Poree, Ph.D., Chemical Sciences Division, Polymer Chemistry Research Area, US Army Research Office
- Christian Whitchurch, Ph.D., Devices Branch Manager, Diagnostics, Detection and Disease Surveillance Division, Defense Threat Reduction Agency
- J. Kenneth Wickiser, Ph.D., Assistant Professor, Department of Chemistry and Life Science, United States Military Academy

Overall, the TAB commended solid collaborations and high productivity amongst the strongest, most successful of the ILIR and SSI projects. In addition, the strongest projects had incorporated comments and suggestions from previous TAB review panels to improve their scientific rigor from year-to-year. The TAB was also excited to see that several of the Seedling and Section 219 projects were addressing important, unique challenges in CB defense such as novel sample collection methodologies and new mathematical models for surface deposition. The panel agreed that many of these efforts had generated promising data and results with a relatively small amount of investment over a short period of time.

Presentations and Proceedings:

Beginning in FY17, ECBC's ILIR program topics will be updated to reflect recent updates to the Joint Program Executive Office for Chemical and Biological Defense (JPEO-CBD) 30 year plan and the Joint Long-range Investment Requirements Analysis (LIRA). The 30 year plan, developed by the JPEO-CBD in conjunction with the Defense Threat Reduction Agency (DTRA) Joint Science and Technology Office (JSTO), was developed to visualize how current and future S&T Efforts progress and transition to fulfill Warfighter capability gaps. Similarly, the LIRA serves as the baseline to inform the DoD Chemical and Biological Defense Program's investment decisions in the Sense, Shape, Shield, and Sustain capability areas.

Additionally, the Center is continuing to expand the Innovative Development of Employee Advanced Solutions (IDEAS) program (formerly the Section 219 program). This program was authorized in Section 219 of the FY09 National Defense Authorization Act (NDAA) and extended in the FY12 NDAA through FY16. This public law authorizes laboratory directors to use up to 3% of available funds for the purpose of technology development, transition of technology developed by the laboratory, workforce development, and minor construction for enhancement of laboratory capabilities. ECBC uses internal funding to provide a platform for innovative ideas that are intended to push technology to meet customer needs and expedite transitions to the Warfighter. To date, these short-term, small investments (~\$50K) have yielded several innovations addressing unique Warfighter challenges. Recently highlighted in several media outlets is the Integrated Respiratory and Eye Protective Scarf (IREPS), a protective mask for specialized operators (e.g., users with facial hair, or must operate with other unique head-borne equipment). Since FY13, the R&T Directorate has reviewed the Innovation projects at the annual TAB review. Year after year, the TAB panel continues to remark how this program is producing innovative solutions to real Army problems, within fiscally constrained parameters.

- Cabalo, Jerry. "Study of the effect of chromophore environment on UV-resonance Raman scattering spectroscopy of tyrosine-containing short peptides", *Chemical and Biological Defense Science and Technology (CBD S&T) Conference*, **MAY 2015**. St. Louis, MO.
- Hsu, C. W., Shen, Y., Zhen, B., Ye, D., Qiu, W., Celanovic, I., Shapira, O., DeLacy, B. G., Johnson, S.G., Joannopoulos, J.D., Soljagic, M., "Novel phenomena in nano-photonics systems of macroscopic sizes", *Proceedings of SPIE 9162, Active Photonic Materials VI*, **SEP 2014**. DOI: 10.1117/12.2061092
- Knox, Craig. "Understanding how exosporium hairs affect spore adhesion on simple surfaces", *Chemical and Biological Defense Science and Technology (CBD S&T) Conference*, **MAY 2015**. St. Louis, MO.
- Mantooth, Brent. "Mechanisms and enhancement of VX decontamination from rubbery polymer substrates", *Chemical and Biological Defense Science and Technology (CBD S&T) Conference*, **MAY 2015**. St. Louis, MO.
- McElhiney, M., Mirotznik, M., Zander, Z., DeLacy, B.G., "Aluminum-based plasmonic arrays using nanosphere lithography", *META 2015*, **AUG 2015**. New York, NY.
- Prugh, Amber. "Role of acetylcholinesterase in the regulation of mesenchymal stem cell proliferation and differentiation", *Chemical and Biological Defense Science and Technology (CBD S&T) Conference*, **MAY 2015**. St. Louis, MO.



Peer Reviewed Publications

- Adames, N.R.; Wilson, M.L.; Fang, G.; Lux, M.W.; Glick, B.S.; Peccoud, J. "GenoLIB: a database of biological parts derived from a library of common plasmid features", *Nucleic Acids Research*, **MAY 2015**. 43(10), p4823-4832. DOI: 10.1093/nar/gkv272 ISSN: 0305-1048 eISSN: 1362-4962
- Angelini, D.J.; Moyer, R.A.; Cole, S.; Willis, K.L.; Oyler, J.; Dorsey, R.M.; Salem, H. "The Pesticide metabolites paraoxon and malaoxon induce cellular death by different mechanisms in cultured human pulmonary cells", *International Journal of Toxicology*, **SEP 2015**. 34(5), p433 441. DOI: 10.1177/1091581815593933 ISSN: 1092 874X
- Anquillare, E. L.; Miller, O. D.; Hsu, C. D.; DeLacy, B. G.; Joannopoulos, J. D.; Soljačić, M. "Efficient broad-and tunable-bandwidth optical extinction via aspect-ratio-tailored silver nanodisks", *arXiv:1510.01768 [physics.optics]*, **SEP 2015**.
- Cabalo, J.B.; Saikin, S.K.; Emmons, E.D.; Rappoport, D.; Aspuru-Guzik, A. "State-by-state investigation of destructive interference in resonance Raman spectra of neutral tyrosine and the tyrosinate anion with the simplified sum-over-states approach", *Journal of Physical Chemistry A*, **OCT 2014**. 118(41), p9675 9686. DOI: 10.1021/jp506948h
- DeLacy, B.G.; Hsu, C.W.; Miller, O.; Zander, Z.; Yagloski, R.; Lacey, S.; Johnson, S.; Joannopoulos, J.; Soljačić, M.; "Coherent plasmon-exciton coupling in silver platelet-J-aggregate nanocomposites", *Nano Letters*, **FEB 2015**. 15(4), p2588-2593. DOI: 10.1021/acs.nanolett.5b00157
- Fleischmann, C.; Gopez, J.; Lundberg, P.; Ritter, H.; Killops, K.L.; Hawker, C.J.; Klinger, D. "A Robust platform for functional microgels via thiol-ene chemistry with reactive polyether-based nanoparticles", *Polymer Chemistry*, **MAR 2015**. 6(11), p2029-2037. DOI: 10.1039/c4py01766h ISSN: 1759-9954 eISSN: 1759-9962
- Jiang, Y.V.; Freyer, J.L.; Cotanda, P.; Brucks, S.D.; Killops, K.L.; Bandar, J.S.; Torsitano, C.; Balsara, N.P.; Lambert, T.H.; Campos, L.M. "The Evolution of cyclopropenium ions into functional polyelectrolytes", *Nature Communications*, **JAN 2015**. 6(5950). DOI: 10.1038/ncomms6950 ISSN: 2041 1723
- Killops, K.L.; Brucks, S.D.; Rutkowski, K.L.; Freyer, J.L.; Jiang, Y.V.; Valdes, E.R.; Campos, L.M. "Synthesis of robust surface-charged nanoparticles based on cyclopropenium ions", *Macromolecules*, **APR 2015**. (48)8, p2519-2525. DOI: 10.1021/acs.macromol.5b00403 ISSN: 0024-9297 eISSN: 1520 5835
- Killops, K.L.; Rodriguez, C.G.; Lundberg, P.; Hawker, C.J.; Lynd, N.A. "A Synthetic strategy for the preparation of sub-100 nm functional polymer particles of uniform diameter", *Polymer Chemistry*, **MAR 2015**. 6(9), p1431-1435. DOI: 10.1039/c4py01703j ISSN: 1759-9954 eISSN: 1759-9962
- Miller, O. D.; Polimeridis, A. G.; Reid, M. T.; Hsu, C. W.; DeLacy, B. G.; Joannopoulos, J. D.; Soljačić, M.; Johnson, S. G. "Fundamental limits to the optical response of lossy media", *arXiv:1503.03781 [physics.optics]*, **MAR 2015**.
- Tran, H.; Ronaldson, K.; Bailey, N.A.; Lynd, N.A.; Killops, K.L.; Vunjak-Novakovic, G.; Campos, L.M. "Hierarchically ordered nanopatterns for spatial control of biomolecules", *ACS Nano*, **NOV 2014**. 8(11), p11846-11853. DOI: 10.1021/nn505548n ISSN: 1936-0851 eISSN: 1936-086X
- Tripathi, A.; Emmons, E. D.; Fountain III, A. W.; Guicheteau, J. A.; Moskovits, M.; Christesen, S.D. "Critical role of adsorption equilibria on the determination of surface-enhanced Raman enhancement", *ACS Nano*, **DEC 2014**. 9(1), p584-593. DOI: 10.1021/nn5058936
- Xu, B.; Gonella, G.; DeLacy, B. G.; Dai, H. L. "Adsorption of anionic thiols on silver nanoparticles", *Journal of Physical Chemistry C*, **FEB 2015**. 119(10), p5454-5461. DOI: 10.1021/jp511997w

Table of Contents

In-House Laboratory Independent Research (ILIR) Projects

1 Characterization of the host proteome within virion particles from the *Alphaviridae* and *Flaviviridae* viral families

*Andrew Kilianski, Amanda Piper, Jennifer Kookan, Raquel Hernandez, Trevor Glaros**

This new project analyzed the protein content of purified virions from the *Alphaviridae* and *Flaviviridae* families by liquid chromatography–mass spectrometry to identify host proteins packaged by these viruses with the goal of examining their roles in the viral life cycle and providing a basis by which new strategies could be developed for viral origin, characterization, detection, and treatment.

11 Role of acetylcholinesterase in the regulation of mesenchymal stem cell proliferation and differentiation

*Amber Prugh, Stephanie Cole, Daniel Angelini**

This project examined whether cholinesterase reactivators would reduce the toxic effects of organophosphates on cellular differentiation and proliferation by inhibiting AChE activity through exposure to parathion and paraoxon. The final year of this effort focused on determining potential binding partners for AChE in MSCs and performing 2-PAM reactivation and knockdown studies.

20 The persistence of microbial memory: An exploration of the potential of bacteria as an information storage medium

*James Myslinski, Sarah Katoski, Michael Kim, Frank Kragl, Matthew Lux**

The second year of this project continued to assess the feasibility of storing data in living bacteria cells and determine if the use of intelligent encoding strategies would enable recovery of stored information in the face of selective pressures by synthesizing DNA encoding a 3D-printable model file and examining the integrity of the message in evolving populations after insertion and passaging in *E. coli*.

27 Examination of the effects of botulinum neurotoxins on *Caenorhabditis elegans*

*Edward Hofmann, James Myslinski, Edward Emm, Patricia Buckley**

The final year of this effort examined *C. elegans* SNAP-25 and VAMP-2 orthologous proteins to determine the effects of botulinum neurotoxin (BotNT) in the *C. elegans* system, exploring the model's use as a potential in vivo diagnostic assay for toxin testing and help to establish the *C. elegans* as an intermediate model to the mouse lethality assay for BotNT.

36 Microbial wargaming: Modeling the contributions to fitness of bacteria encoding deployable genetic weaponry

*Aleksandr Miklos, Matthew Lux, Vanessa Funk, Steven Yee, Henry Gibbons**

The final year of this project visualized colicin promoter induction in adjacent bacterial colonies, determined if ColA and ColE1 producing strains displace non-producers in a colony-competition assay, and disabled immunity and lysis protein from GFP expressing strains to test the relative fitness of a non producing strain in the absence of the immunity protein.

44 Experimental and theoretical investigation of liquid droplet break-up induced by supersonic shock waves

Jerry Cabalo, Daniel Weber, Daniel Wise, Clayton Moury, Alejandro Queiruga, Tarek Zohdi*

This new project applied a combined theoretical and experimental approach to understanding the shockwave-induced break up of aerosol particles through abrupt nonisotropic heating and pressure. This study aims to predict particle size distribution, as a function of agent physical and chemical properties, and how far a chemical or biological agent travels during a release.

Surface Science Initiative (SSI) Projects

54 Fano resonance in a gold nanosphere with a J-aggregate coating

Andrew Fales, Stephen Norton, Bridget Crawford, Brendan DeLacy, Tuan Vo-Dinh*

The final year of this effort to fabricate unique nanostructures focused on plasmon-exciton coupling in plasmonic nanostructures and plexcitonic particles or arrays and sought a fundamental understanding of the differences between the plasmon-organic exciton system and the plasmon-inorganic system.

62 Adsorption of anionic thiols on silver nanoparticles

Bolei Xu, Grazia Gonella, Brendan DeLacy, Hai-Lung Dai*

This new effort began to interrogate the simultaneous use of plasmonic and excitonic structures to synergistically enhance the charge injection efficiency and rate from a given molecule into silver (Ag) nanoparticles. This charge injection is fundamental to understanding and improving photovoltaic and photocatalytic processes.

74 Understanding the effect of substrate material and solvation on surface-enhanced Raman spectroscopy enhancement

*Jason Guicheteau, Ashish Tripathi, Erik Emmons, Augustus Fountain, III, Steven Christesen**

This new project began the study of different SERS substrate geometries and metal alloy combinations to determine whether the product of the analytical enhancement factor and the maximum number of molecules per unit area on the surface ($G \times n_{max}$) depends on substrate. Additionally, the effect of solvation on binding and SERS enhancement was investigated.

80 Determination of mechanisms and transport enhancement in liquid-phase extraction of penetrants from polymers

Brent Mantooth, Mark Varady, Thomas Pearl, Craig Knox, Jerry Cabalo, John Escarsega, Robert Lambeth*

This new effort focused on studying the influence of solvents on the subsurface mass transport of molecular species in the bulk of polymer films with a multifaceted combination of computational and experimental approaches. Understanding the mechanisms at play during this process enables optimization of decontaminants and coating materials to enhance or restrict chemical transport in and extraction from surfaces.

90 Understanding how exosporium hairs affect spore adhesion on surfaces

Jana Kesavan, Craig Knox, Erica Valdes, Vipin Rastogi, Pamela Humphreys, Paul DeLuca, Guzeliya Korneva, Robert Latour*

The second year of this project continued analyses to provide insight into the role of the Bacillus exosporium in spore adhesion and determine stickiness factors to predict agent fate of bio-threats in the environment. SEM/TEM, BET theory, and modeling per-area adhesion results were used to determine if exosporium hairs respond to chemical environments and mediate spore adhesion via contact area and orientation.

Seedling Projects

101 The nature of CWA adsorption on graphene

*Harold Banks**

This study focused on the zig-zag and armchair edges of graphene, the region where the bulk of the chemistry and physics occurs, by proposing computationally optimized models for graphene, testing the credibility of self-passivated structures, and determining the adsorption energy of sarin by placing it at various edge positions and within the bulk of the aromatic structure.

- 108** **Assessing the biological threat from suicide bombers**
Jerry Cabalo, Katelynn Stafford, Cristian Maldonado-Figueroa, Daniel McGrady*
This effort investigated the viability of organisms and the dispersion and aerosolization of spores in the post-detonation fragments of a suicide bomber by performing three progressively larger explosive charge sizes using mannequins filled with ballistics gel mixed with *Bg* or *Bt* spores along with a fluorescent tracer.
- 118** **Tunable color filters using aluminum based nano-sandwiches**
*Zion Aranda, Mathew Zablocki, Mark Mirotznik, Zach Zander, Brendan DeLacy**
This effort utilized electromagnetic computations to design Al-SiO₂-Al thin films then fabricated the structures using physical vapor deposition (PVD) and chemical vapor deposition (CVD) techniques, varying the cavity thickness of the silica layer to generate different colors of light, and measured the spectral properties of the transmitted light with a visible spectrophotometer.
- 124** **Paper-based sequence detection with minimal sample preparation**
*James Myslinski, Vanessa Funk, Steve Blum, Matthew Lux**
This project established the capacity to produce paper-based gene networks at ECBC, demonstrated paper-based detection of RNA specific to *Bacillus thuringiensis var. kurstaki*, and tested the robustness of these RNA sensor circuits to the presence of cellular lysates produced both mechanically and chemically in order to incorporate cellular lysis mechanisms into a paper-based gene-network system.
- 129** **Estimating threat agent concentration through state-space analysis**
Erin Shelly, Fiona Narayanan, Michael Kierzewski, Thomas Ingersoll*
This effort utilized state-space modeling to estimate concentration from presence/absence data when many sensors are deployed in unison by validating estimates from presence/absence sensor data against known concentrations from historic aerosol sensor data. Computer code developed in the statistical language R was adapted for use under laboratory and field conditions.
- 138** **A novel bio-hydrogel-based sampling approach**
Lisa Smith, Laura Burton, Pooja Rastogi, Kristina Parman, Vipin Rastogi*
This effort investigated the use of a bio-hydro gel as an alternative sampling approach to generally inefficient surface sampling approaches on porous surfaces by developing a water-based gel that dries into a thin film and is then pulled off the surface, encapsulating and preserving bio-agent and other contaminants which are then recovered by a simple one-step process of hydration.
- 143** **Exploring aerosol charge characteristics due to explosive disseminations**
Daniel Wise, Elias Yoon, Daniel Weber*
This effort created and functioned experimental explosive devices, filled with conductive and non-conductive materials in the sub-micron range, to characterize the resulting aerosol. The results were compared to various non-explosive disseminations of the same payload materials to provide perspective to the characteristics of the electrical charge resulting from the explosive device.



ILIR PROJECTS

Characterization of the host proteome within virion particles from the *Alphaviridae* and *Flaviviridae* viral families

Andy Kilianski^a, Amanda Piper^b, Jennifer Kookan^a, Raquel Hernandez^b, Trevor Glaros^{a*}

^aU.S. Army Edgewood Chemical Biological Center, Research and Technology Directorate,
5183 Blackhawk Rd, Aberdeen Proving Ground, MD 21010

^bNorth Carolina State University, 346 Polk Hall, Raleigh, NC 27695

ABSTRACT

Due to the significant impact viruses pose to public health, the economy, and for their potential to be used as biological weapons, novel non-traditional methods are needed to characterize emerging viruses. As virus particles bud from an infected cell, they contain not only virus-specific proteins and nucleic acid, but also incorporate host proteins. While this phenomenon has been observed for a handful of viruses, it remains unclear if host proteins are specifically packaged and if they are critical to the viral life cycle. In this study, the protein content of purified virions from the *Alphaviridae* and *Flaviviridae* families will be analyzed by liquid chromatography mass spectrometry to determine if host proteins are specifically packaged by these viruses and if these host proteins are critical for the viral life cycle. The purified virions will first be propagated and purified from the same host cells, thus giving a common background and identical set of host proteins for bioinformatic comparison both within and between viral families. If virus particles package specific host proteins and there are identifiable patterns of host proteins within or between viral families, then these molecular signatures could provide a basis by which new strategies could be developed for viral origin, characterization, detection, and treatment.

Keywords: Proteomics, biomarkers, viral proteomics, host proteins, mass spectrometry

1 INTRODUCTION

The continuing emergence of novel and re-emergent viral pathogens creates risks to public health and endangers our deployed Warfighters. To prevent and respond to these risks, the biodefense community needs to utilize new methods and technology for pathogen characterization. These techniques can answer questions regarding the composition of viral particles and how viruses interact with host cells. This type of information is necessary for the design of new detection assays, countermeasures, and forensic techniques related to virus infection. Two families of viruses, *Alphaviridae* and *Flaviviridae*, are especially capable of threatening the Warfighter. Both families are enveloped, positive-sense RNA viruses that cause vector-borne disease. Notable members of these families include Chikungunya virus, Dengue virus, West Nile virus, and Zika virus. Also of note are the biodefense-relevant alphaviruses Venezuelan Equine Encephalitis virus and Eastern Equine Encephalitis virus, which are able to cause disease through aerosol routes. Many of these pathogens from zoonotic reservoirs lack any effective vaccines and antivirals. Host-based therapeutics are thought to be attractive avenues, but identifying targets for this approach requires a detailed understanding of how these viruses interact with host factors throughout the replication cycle. In addition to being attractive countermeasure targets, host proteins give potential signatures related to pathogen growth conditions, background, and location. These signatures can be used in forensic applications when searching for information related to pathogen attribution. Central to either of these applications is the necessity for understanding the interactions between viral pathogens and the host cells they require to replicate. To uncover these types of interactions, this research project focused on host proteins within virus particles and any functional relevance these identified proteins might have to the viral lifecycle.

Alphaviruses enter host cells at the plasma membrane through fusion with membrane components or by receptor attachment and internalization. This mode of entry is known as receptor mediated endocytosis (Figure 1A). This process often involves the formation of clathrin-coated pits. Numerous other mechanisms have been described including clathrin-independent pathways such as the caveolar/raft pathway and less understood pathways involving small GTPases.¹ Recently, the mode of entry for alphavirus has been revisited. Studies performed in conditions that do not allow for endocytosis or any vesicular transport have shown that the viral genome still enters the host cells.

Additionally, when drugs are used to inhibit cellular functions thought to be essential for viral entry, viral RNA is still delivered into the host cells. Collectively, this new evidence suggests that alphaviruses are able to infect cells by direct penetration through the formation of a pore structure composed of viral, and potentially, host proteins (Figure 1B).² Regardless of the mode of host cell entry, the general mechanism for viral replication is the same (Figure 1A).

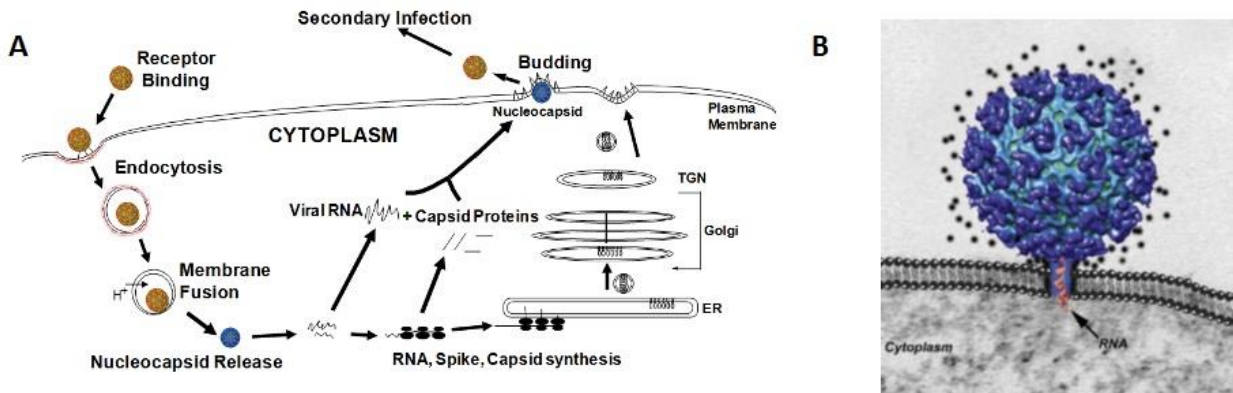


Figure 1. Schematic of the alphavirus host cell entry and life cycle. A) Virus particles enter the host cell via endocytosis. The viral membrane then fuses with the endosomal membrane in a pH-dependent manner, which results in the release of the virus particle/genome. The viral genome and proteins are then synthesized, assembled, and released from the host cells. Figure was adapted from Margaret Kielian's laboratory at Yeshiva University-Albert Einstein College of Medicine. B) Direct penetration through the formation of a pore structure. Figure adapted from Hernandez et al., 2015.²

In this study, highly pure Sindbis virus (SINV) preparations were analyzed using liquid chromatography with tandem mass spectrometry (LC-MS/MS) to determine if host proteins were specifically packaged into virus particles. Detailed analysis of these particles has resulted in the discovery of more than 45 unique host proteins when the virus is replicated in a human background using HEK293 cells. When the background was changed to a different species, hamster BHK21 cells, more than 50 host proteins were discovered. Functional analysis of these host protein identifications suggests that they may play a molecular role in nucleic acid binding and catalysis. When the host protein profiles between species were cross compared, six proteins were found to be in common. In FY16, this basic research study will aim to expand our understanding of the roles these six conserved host proteins may play in viral replication. Will the virus be able to produce an active infection when these host proteins are knocked out? Will they be able to produce new progeny? Will these new progeny be able to produce a new secondary infection? In addition, we will expand our characterization of virions by examining the host proteomes of other alphaviruses and flaviviruses.

2 METHODS

2.1 Virus preparation and purification

Heat-resistant SINV (SVHR) was grown in BHK21 cells (hamster), HEK293 cells (human), and C710 cells (mosquito), which were all obtained from American Type Culture Collection (ATCC®; Manassas, VA). Culture medium from each cell line was harvested and served as a negative control. Virus and negative controls were harvested from four T75 flasks (Corning®). Cells were infected at a multiplicity of infection ratio of 100 pfu/mL and allowed to replicate for a single cycle. The resulting virus was twice purified in linear potassium tartrate gradients by ultracentrifugation (Beckman Coulter® SW-28 rotor for 18 hours at 24,000 rpm). The resulting band of purified virus was collected and washed once by pelleting the virus in phosphate buffered saline (PBS) and washing the pellet to remove residual salts. The purified population was then run over Sephadex® gravity filtration columns (Sigma-Aldrich®), followed by elution and protein quantification for sample normalization.

2.2 Protein extraction and digestion

Viral preparations and their respective negative controls were processed for liquid chromatography tandem mass spectrometry (LC-MS/MS) analysis using the filter-aided sample preparation (FASP) method as previously described.³ Briefly, following purification, the total protein concentration was determined using the bicinchoninic acid (BCA) assay. All preparations were then normalized using sterile PBS to 0.5 µg/µL, aliquoted in 10 µg fractions, and

stored at -80 °C. A total of 10 µg of total protein (20 µL) was mixed 1:1 with mammalian protein extraction reagent (M-PER™; Thermo Scientific™, Cat. #: 78501) supplemented with 50 mM of dithiothreitol, and heated to 95 °C for 10 minutes. Once cooled to room temperature, the samples were mixed with 200 µL of urea buffer (UA; comprised of 8 M urea and 100 mM Tris HCl at pH 8.5) and placed over a 30 kDa filter spin column (Millipore Ultracel® YM-30), and centrifuged at 14,000 x g for 30 minutes at room temperature to collect all proteins on the filter membrane. Denatured and reduced proteins were then alkylated by adding 100 µL of IAA solution (0.05 M iodoacetamide in UA) to each filter and incubating at room temperature in the dark for 20 minutes. Following alkylation, the samples were centrifuged at 14,000 x g for 20 minutes to remove the alkylation solution. Next, each sample was washed three times with 100 µL of UA and then three times with 100 µL of 100 mM triethylammonium bicarbonate (TEAB). Centrifugation at 14,000 x g for 30 minutes was used to remove each wash including the final wash. To digest the captured protein, 100 µL of a trypsin digestion solution (10 µg/mL in TEAB) was placed on each membrane and incubated in a sealed tube overnight at 37 °C with shaking. After incubation, the peptides were collected for LC-MS/MS analysis in a clean tube by centrifuging each tube for 30 minutes at 14,000 x g. The membrane was washed by centrifugation one time with 50 µL TEAB and once with 50 µL of 0.5 M NaCl. All washes were collected and pooled with the final peptide elute. Each sample was then acidified using 10% trifluoroacetic acid (TFA) until the final pH is roughly 2-3. Prior to MS analysis, each sample was desalted using Pierce™ C18 desalting columns (Thermo Scientific™, Cat. # 89870) according to the manufacturer's directions.

2.3 Liquid chromatography mass spectrometry analysis

Tryptic peptides were analyzed on an Orbitrap Elite™ Hybrid Ion Trap-Orbitrap Mass Spectrometer coupled with the EASY-nLC™ II liquid chromatography (LC) pump system. Dried peptides were reconstituted in 3% acetonitrile/0.1% formic acid and resolved on a PicoFrit® 15 cm x 75 µm ID high performance liquid chromatography (HPLC) column packed with 5 µm BioBasic® C18 particles 300 Å (New Objective; Woburn, MA) using a 130-minute multistep gradient (i.e., 0-5 minutes: 5-10% B; 6-110 minutes: 10-35% B; and 111-130 minutes: 35-95% B). For the gradient, the A buffer is 3% acetonitrile/0.1% formic acid and the B buffer is 95% acetonitrile/0.1% formic acid. Orbitrap™ MS1 scans were performed at a resolution of 120,000 at 400 m/z, with a scan range of 110-2000 m/z. The top 20 precursors were selected for MS2 data-dependent fragmentation. MS2 spectra were acquired using the iontrap scanning in normal mode (Top 20 method). The minimum signal required to trigger a data-dependent scan was 5,000. Collision induced dissociation (CID) was used to generate MS2 spectra with the following settings: normalized collision energy 35%, default charge state 2, isolation width 2 m/z, and activation time of 10 milliseconds. AGC target was set to 1×10^6 for MS and 5×10^4 for MS/MS with a maximum accumulation time of 200 milliseconds. Dynamic exclusion was set for 60 seconds for up to 500 targets with a 5 ppm mass window. A lock mass of 445.120025 was used for internal calibration to improve mass accuracy.

2.4 Mass spectrometry data processing

Spectra data was processed using Proteome Discoverer 1.4 with the SEQUEST search algorithm against a merged database for *Homo sapiens* RefSeq database (Tax ID: 10116) with Sindbis virus polyprotein (Uniprot ID: P03317) or *Cricetulus griseus* (Chinese hamster) RefSeq database (TaxID: 10029) with Sindbis virus polyprotein (Uniprot ID: P03317). Dynamic modifications were set for carbamidomethylation of cysteine (+57.02 Da), oxidation of methionine (+15.99 Da), phosphorylation of serine, threonine, or tyrosine (+79.966), and N-terminal acetylation (+42.011). MS/MS spectra were search with a precursor mass tolerance of 10 ppm and a fragment mass tolerance of 0.6 Da. Trypsin was specified as the protease with a maximum number of missed cleavages set to 2. A false discovery rate was calculated using PERCOLATOR and was set at < 1% to score high confidence peptide identifications. For comparative purposes, a significant protein identification was based upon one or more high confidence peptide identifications. Grouping and functional analysis was performed using the PANTHER classification system using each protein ID's gene name (human background only).

3 RESULTS

3.1 Highly pure viral preparation

To effectively analyze the host protein content with viral particles, ultra-pure preparations of virions had to be created. Host background contamination from other cellular vesicles or cell debris needs to be accounted for to validate host proteins identified in the viral preparations. This was accomplished using a two-step purification procedure with negative controls being run through in parallel. First, virus was grown and supernatant collected from infected and

non-infected cells. Virus particles were then concentrated by floating on density gradients, followed by elution over gravity filtration columns. Again, negative control fractions were run through the same process as virus-containing fractions. To determine if this purification scheme (Figure 2A) resulted in pure preparations of virus particles, fractions were visualized using electron microscopy (Figure 2B). The electron micrographs of the two-step purified SINV preparations show extremely pure virus preparations, with no cell debris or other cell-associated membrane-bound vesicles visible.

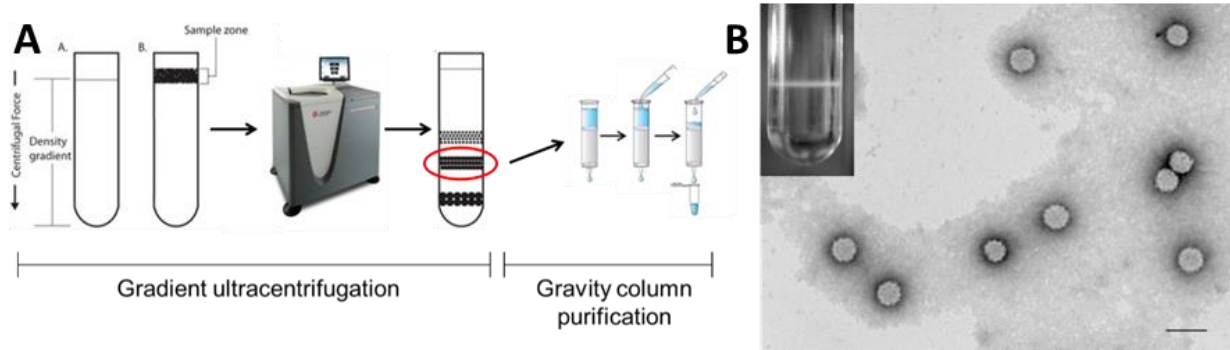


Figure 2. Schematic of the SINV virion purification strategy and production timeline. A) A two-step purification strategy was utilized; the virus preparations were first spun over density gradients using an ultracentrifuge then eluted using gravity columns. Negative controls were processed in parallel with the virus preparations. B) Electron micrographs of the purified virions to determine that the two-step virus purification strategy provided pure preparations of virions for downstream MS analysis.

Adapted from Hernandez et al. 2015.¹

3.2 Host protein identification in purified SINV virions

The visualization of the purified viral preparations indicated that no contaminating particles were present, so SINV preparations were analyzed, in parallel with negative control fractions, using LC-MS/MS. Viral preparations and negative controls from BHK21 (hamster, *C. griseus*), C710 (mosquito, *Aedes albopictus*), and HEK293 (human) cell backgrounds were run to determine if specific host proteins could be detected. This analysis was performed using an Orbitrap Elite™ Hybrid Ion Trap-Orbitrap Mass Spectrometer (Thermo Scientific™). Each sample was analyzed in triplicate on a virgin C18 HPLC column. By using a new column for each sample we are able to ensure that carry over from sample to sample would not result in false host protein identifications. After running the samples, the data was analyzed using Proteome Discoverer™ 1.4 (Thermo Scientific™) to identify peptides and align them to known host proteins from each background.

Each purified viral preparation yielded unique host protein identifications with only a limited number of host proteins being identified in the negative controls. Keratin was often identified in the negative control. This identification was ignored for functional interpretation and likely introduced during sample processing. BHK cells yielded over 50 unique protein IDs from the LC-MS/MS analysis, and are partially displayed below in Table 1.

Table 1. Top 25 viral and host proteins from purified SINV virions grown from BHK21 cells.

Description	Σ Coverage	Σ # Unique Peptides	Σ # PSMs
Structural polyprotein	64.50	75	1664
Desmosplakin	9.17	23	63
Non-structural polyprotein	2.63	6	25
Junction plakoglobin	10.98	9	24
Junctional adhesion molecule C	17.13	6	22
Claudin	10.05	3	19
Cellular nucleic acid-binding protein	19.77	3	11
Annexin	18.03	4	10
SH3 and multiple ankyrin repeat domains proteins	0.62	1	6
Sorting nexin-5	3.11	1	5
Ubiquitin	32.68	2	5
Hemoglobin subunit alpha	10.56	1	4
Desmocollin-1	2.39	1	3
Hemoglobin subunit epsilon-Y2	6.80	1	3
Skin-specific protein 32	2.92	1	3
Vascular non-inflammatory molecule 3	1.86	1	3
Heat shock cognate 71 kDa protein	11.00	2	2
Putative RNA-binding protein 3	10.65	1	2
Putative uncharacterized protein	11.54	1	2
Slit-like 3 protein	4.26	1	2
Transcriptional adapter 2-beta	2.13	1	2
UV radiation resistance-associated gene protein	1.17	1	2
26S proteasome non-ATPase regulatory subunit	5.32	1	1
Actinin receptor type-2A	2.53	1	1
Note: Σ Coverage describes the total percent coverage of the full length protein. Σ # Unique Peptides refers to the total number of unique peptides identified for a given protein. Σ # PSMs refers to the total number of peptides sequenced for that protein.			

While BHK21 cell host proteins are used as the example here, an additional 44 host proteins were identified from the HEK293 human background and 27 proteins from the C710 mosquito background. Both hamster and human genomes and proteomes are well characterized; however, the same level of characterization does not exist in the mosquito host *A. albopictus*, as the complete genome sequence was very recently published.⁴ To analyze the raw data obtained from the C710 cell background, we relied on a draft proteome created by Jose Ribiero at the NIH. This draft proteome of ~6,000 proteins aided with the identification of the 27 proteins here. This data will be used to create functional relevance to their annotations, as many of the proteins identified in the C710 background classify in similar functional categories to the proteins identified in the mammalian backgrounds. As not much is known about the cellular processes involved in vector propagation of emerging viral diseases, these datasets will prove useful for probing those molecular pathogen-host interactions.

The proteins identified in each host background cover a wide range of molecular functions and protein classes that are summarized in Figure 3. Proteins identified in the BHK21 background have functions such as nucleic acid and protein binding, catalytic activity, regulator activity, receptor activity, and transporter activity. They are members of classes such as chaperones, kinases, membrane traffic proteins, and signaling molecules.

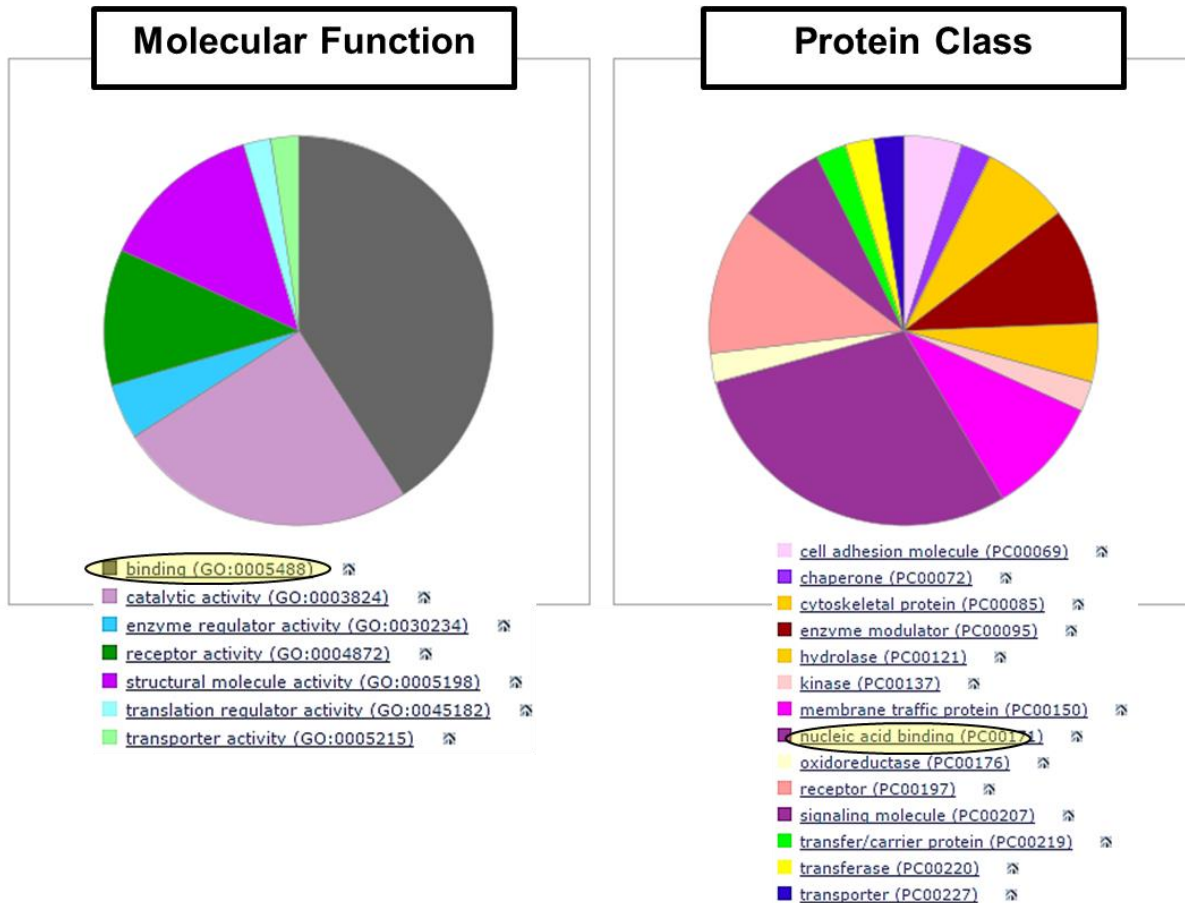


Figure 3. Functional analysis of host protein identification from SINV virions. The functional classification of all the host proteins identified within virions from human backgrounds were determined using the PANTHER Classification System. The function and classification of potential target proteins for functional characterization are highlighted.

3.3 Conserved host protein signatures between human and hamster backgrounds

When comparing replicate virus preparations to each other (same host background), we identified four proteins that had multiple peptides identified (Figure 4A). Given that the limiting factor that dictates detection is dynamic range and instrument sensitivity, the host proteins which were commonly detected between separate preparations were also likely in the highest abundance within these virus particles. In addition to comparing preparations within hosts, we also compared the host proteins identified between species. Using this strategy we identified six protein signatures that were conserved between both host backgrounds (Figure 4B). Since these protein signatures are serving as the foundation for all future functional studies, the fragmentation spectrum which resulted in peptide identifications is presented in Figure 5.

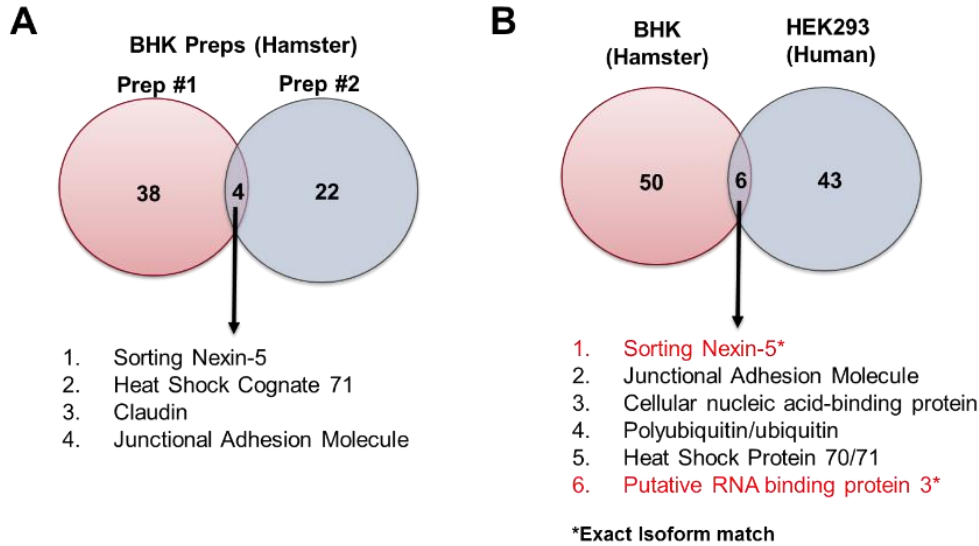


Figure 4. Host protein comparison for experimental replicates and species. A) Two separate viral preparations were analyzed by LC-MS/MS. The host proteome was then compared between each prep. B) The total host proteome identified for all SINV preps were compared at the species level; six proteins were found to be conserved.

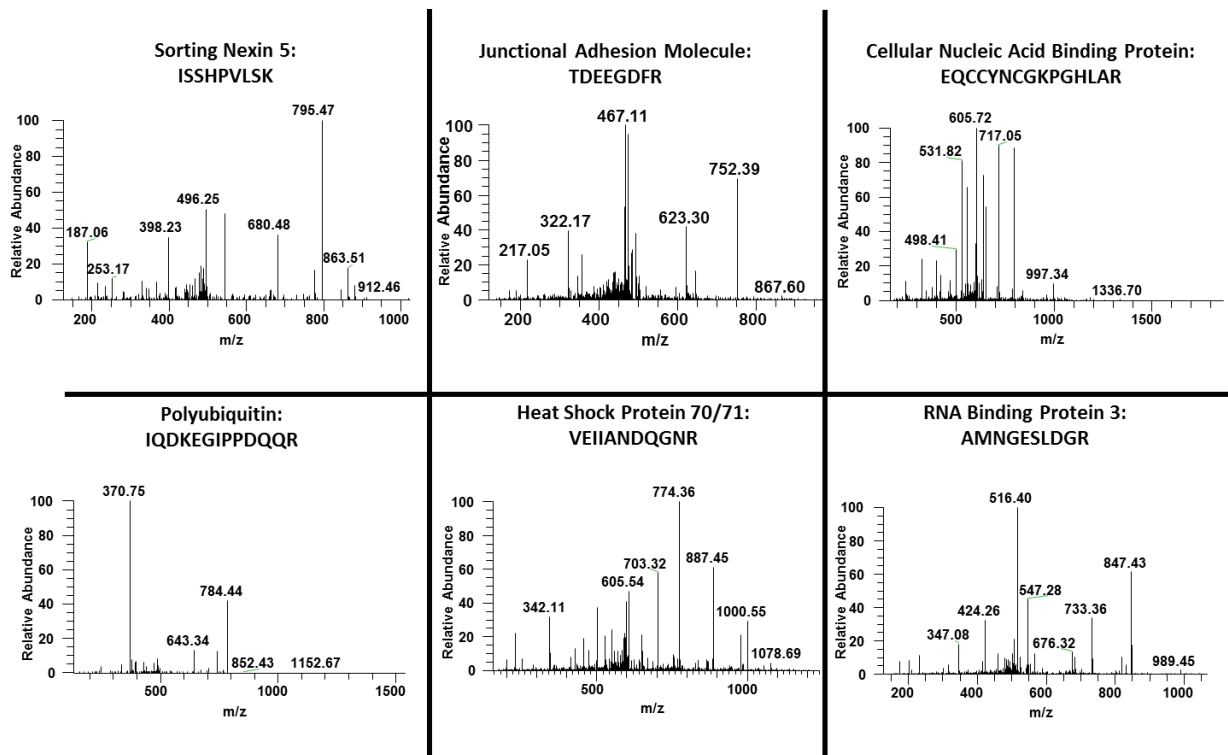


Figure 5. Species conserved proteins: MS/MS spectrum used for peptide identification.

The role that these host proteins may play in the viral life cycle will be the subject of future studies. Initially, we will use a siRNA approach to determine how these virus replication when the host protein is knocked down. However, since we were unable to acquire antibodies that were evaluated to work against hamster proteins, we purchased and evaluated polyclonal antibodies raised against each protein’s human homolog. All three of the anti-human polyclonal antibodies successfully detected the hamster homologs (Figure 6).

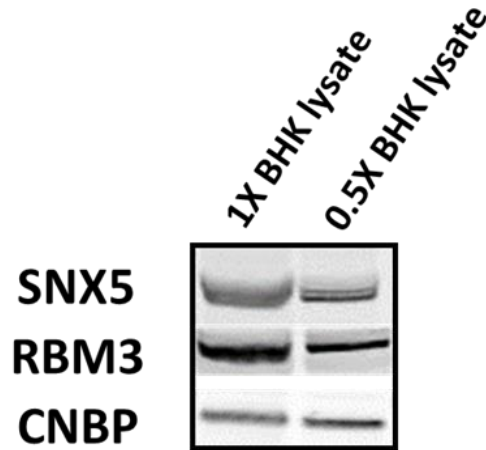


Figure 6. Western blot images of BHK21 cellular lysate using polyclonal antibodies raised against human homologs.

4 DISCUSSION

The development of antivirals, vaccines, and investigative tools for viruses remains a major gap in the ability to protect public and Warfighter health from emerging diseases. Basic understandings of virus-host biology remain central to these products, and must harness new techniques and capabilities to increase this basic science knowledge. Here, LC-MS/MS was utilized to determine if the prototypical alphavirus, Sindbis virus, specifically packaged host proteins into its virus particles. Using a two-stage purification process for SINV virions, followed by FASP for sample preparation and mass spectrometry analysis revealed a variety of host proteins incorporated into SINV particles in each host background (Table 1). The mosquito proteome is not well annotated, and the characterization of MS data from the C710 background required our collaboration with groups currently annotating mosquito databases. Despite this limitation, the functional role of these proteins being associated with SINV replication will lend experimental validation of their proteomic annotation. As mosquito proteins are being targeted as a way of interrupting vector transmission of disease, this annotation is useful. Of note, in the mammalian backgrounds, is the identification of a core group of conserved host proteins (Figure 4B). These proteins will serve as the first set of proteins interrogated for their functional relevance during the SINV life cycle.

Sorting Nexin 5 (SNX5) forms part of the retromer complex within host cells, playing an important role in trafficking membranes between the plasma membrane and Golgi apparatus. These membrane movement events are required to recycle receptors and other plasma membrane components during normal cellular processes. Recently, a pair of studies has elucidated a role for SNX5 as a restriction factor for pathogen infection. The intracellular bacteria *Chlamydia* requires membrane structures to replicate and produce infectious progeny within host cells. Both Aeberhard et al.⁵ and Mirrashidi et al.⁶ determined that SNX5 can negatively impact the membrane rearrangements required by *Chlamydia* to replicate efficiently. To counter this restrictive effect, *Chlamydia* sequesters SNX5 in replicative bodies and prevents its action on membrane rearrangements. SINV also requires extensive membrane rearrangement for replication, and assembles virus particles at the plasma membrane. SNX5 might be hijacked by SINV during particle assembly to induce events necessary for infectious particles to be formed. It is also possible that SNX5 can restrict SINV infection via a mechanism similar to *Chlamydia*, so the sequestration of SNX5 at sites of SINV particle formation is a virus-induced countermeasure.

While SNX5 has been definitively implicated in the pathogenesis of infectious agents, the other conserved proteins have a less-clear potential role in SINV replication. Junctional adhesion molecule (JAMC) has roles in cancer biology⁷ and pathogenic immune responses⁸ related to cell adhesion and homing, but has no defined role in virus biology. SINV rearranges the plasma membrane to exit the cell at specific sites conducive to virus budding,⁹ so it is possible that JAMC is enriched at this site and helps create a supportive environment for SINV budding. Cellular nucleic acid binding protein (CNBP) and RNA binding protein 3 (RBM3) both have the ability to bind single stranded RNA,¹⁰ the species of RNA encoding the SINV genome. These RNA-binding proteins could protect viral RNA from host cell antiviral sensors while also promoting translation of viral polyproteins upon progeny virus entry into the host cell

cytoplasm. Ubiquitin and HSP70/71 are important throughout the viral life cycle,^{11,12} although it remains unclear if these molecules play a role by incorporation into alphavirus and SINV virions.

The identification of multiple host factors within SINV particles allows opportunities to continue exploring how these proteins influence the production of infectious virions by SINV. This novel characterization also included the conserved identification of SINV non-structural proteins. Alphavirus non-structural proteins are important for virus replication, but are not traditionally thought to form any structural components of the virus particle. Further examination of the coverage obtained by LC-MS/MS determined that SINV nonstructural protein 2 (nsP2) was being incorporated into virus particles in each host background. This is a novel discovery, as nsP2 has not been identified within virus particles. This is also significant because of the myriad functions that SINV nsP2 has; it is a viral protease¹³ with functions ranging from trans cleavage of viral polyproteins to innate immune evasion early in viral replication.¹⁴⁻¹⁷ SINV incorporating nsP2 into progeny virions could give viral polyprotein cleavage and innate immune antagonism at the earliest stages of viral entry, before translation of the plus-stranded viral RNA occurs. This would give SINV a head start on evading and blocking host responses to viral replication, allowing SINV to productively infect susceptible cells.

Overall, this study has produced results that significantly contribute to the understanding of alphavirus-host biology. LC-MS/MS analysis of highly pure viral particles determined that SINV specifically incorporates host proteins into progeny virus particles. These proteins have a variety of functions that can be investigated for a role in SINV replication, with a core group of proteins conserved in multiple host backgrounds serving as a logical starting point. This research also aids vector annotation, with the recently sequenced *A. albopictus* serving as a host background here. Finally, the novel discovery of SINV nsP2 incorporation into virus particles suggests a specific interaction and role for nsP2 in progeny infection. By interrogating SINV particles for the host background proteome, a better understanding of the virus-host interactions necessary for alphavirus entry, replication, progeny production, and budding can be established.

ACKNOWLEDGMENTS

The authors would like to acknowledge U.S. Army funding provided through the Edgewood Chemical Biological Center's In-House Laboratory Independent Research Program.

REFERENCES

- [1] Leung, J.Y.-S.; Ng, M.M.-L.; and Chu, J.J.H., "Replication of alphaviruses: A review on the entry process of alphaviruses into cells." *Advances in Virology*, **2011**, p1-9.
- [2] Vancini, R.; Hernandez, R.; and Brown, D., "Alphavirus entry into host cells." *Progress in Molecular Biology and Translational Science*, **2015**, 129, p33-62.
- [3] Wiśniewski, J.R. *et al.*, "Universal sample preparation method for proteome analysis." *Nature Methods*, **2009**, 6, p359-362.
- [4] Dritsou, V. *et al.*, "A draft genome sequence of an invasive mosquito: an Italian *Aedes albopictus*." *Pathogens and Global Health*, **2015**, 109(5), p207-220.
- [5] Aeberhard, L. *et al.*, "The proteome of the isolated *Chlamydia trachomatis* containing vacuole reveals a complex trafficking platform enriched for retromer components." *PLOS Pathogens*, **2015**, 11(6), e1004883.
- [6] Mirrashidi, K.M. *et al.*, "Global mapping of the inc-human interactome reveals that retromer restricts *Chlamydia* infection." *Cell Host and Microbes*, **2015**, 18(1), p109-121.
- [7] Langer, H.F. *et al.*, "A novel function of junctional adhesion molecule C in mediating melanoma cell metastasis." *Cancer Research*, **2011**, 71(12), p4096-4105.
- [8] Ballet, R. *et al.*, "Blocking junctional adhesion molecule C enhances dendritic cell migration and boosts the immune responses against *Leishmania major*." *PLOS Pathogens*, **2014**, 10(12), e1004550.
- [9] Martinez, M.G. *et al.*, "Imaging the alphavirus exit pathway." *Journal of Virology*, **2014**, 88(12), p6922-6933.

- [10] Wright, C.F.; Oswald, B. W.; and Dellis, S., "Vaccinia virus late transcription is activated in vitro by cellular heterogeneous nuclear ribonucleoproteins." *Journal of Biological Chemistry*, **2001**, 276(44), p40680-40686.
- [11] Jiang, X. and Chen, Z.J. "The role of ubiquitylation in immune defense and pathogen evasion." *Nature Reviews*, **2011**, 12(1), p35-48.
- [12] Nagy, P.D. *et al.*, "Emerging picture of host chaperone and cyclophilin roles in RNA virus replication." *Virology*, **2011**, 411(2), p374-382.
- [13] Shin, G. *et al.*, "Structural and functional insights into alphavirus polyprotein processing and pathogenesis." *Proceedings of the National Academy of Sciences*, **2012**, 109(41), p16534-16539.
- [14] Russo, A.T.; White, M.A.; and Watowich, S.J., "The crystal structure of the Venezuelan equine encephalitis alphavirus nsP2 protease." *Structure*, **2006**, 14(9), p1449-1458.
- [15] Akhrymuk, I.; Kulemzin, S.V.; and Frolova, E.I., "Evasion of the innate immune response: the Old World alphavirus nsP2 protein induces rapid degradation of Rpb1, a catalytic subunit of RNA polymerase II." *Journal of Virology*, **2012**, 86(13), p7180-7191.
- [16] Frolova, I. *et al.*, "Random insertion mutagenesis of Sindbis virus nonstructural protein 2 and selection of variants incapable of downregulating cellular transcription." *Journal of Virology*, **2009**, 83(18), p9031-9044.
- [17] Fros, J.J. *et al.*, "Chikungunya virus nonstructural protein 2 inhibits type I/II interferon-stimulated JAK-STAT signaling." *Journal of Virology*, **2010**, 84(20), p10877-10887.

Role of acetylcholinesterase in the regulation of mesenchymal stem cell proliferation and differentiation

Amber M. Prugh^a, Stephanie D. Cole^b, Daniel J. Angelini^{a*}

^aU.S. Army Edgewood Chemical Biological Center, Research & Technology Directorate,
5183 Blackhawk Rd, Aberdeen Proving Ground, MD 21010

^bExcet, Inc., 8001 Braddock Rd, Suite 303, Springfield, VA 22151

ABSTRACT

Mesenchymal stem cells (MSC) are multipotent cells located in various adult tissues. Recently, it has been reported that human bone marrow-derived MSCs express active acetylcholinesterase (AChE) and that disruption of AChE activity by organophosphate (OP) chemicals affects the ability of MSCs to differentiate into osteoblasts. It is currently unknown what role AChE plays in regulating MSC proliferation and differentiation. In this study, we found that OPs decrease AChE activity in MSCs, which consequently reduces the proliferation and/or differentiation potential of these cells. In addition, we established MSC toxicity profiles of two cholinesterase reactivators and the efficacy of each in recovery of cellular viability following exposure to OP chemicals. To examine the role for AChE in MSC differentiation, we used a genome-editing strategy (CRISPR/Cas9) to attempt to knockdown AChE expression in MSCs. Finally, we performed His-tagged AChE pulldowns to determine potential AChE binding partners followed by protein identification using mass spectrometry. Understanding the pathways associated with MSC proliferation and differentiation could lead to the development of future MSC-based tissue repair therapies.

Keywords: Acetylcholinesterase, differentiation, mesenchymal stem cells, organophosphates, paraoxon, parathion, tissue repair

1 INTRODUCTION

Mesenchymal stem cells (MSC) can be isolated from various adult tissues and play a significant role in tissue maintenance and repair. *In vitro*, these cells are capable of self-renewal and, under the appropriate culture conditions, can be differentiated into bone, cartilage, and fat.^{1,2} More recent studies have demonstrated that MSCs are capable of differentiating into other cell types, including alveolar epithelium, hepatocytes, myocytes, and neurons.² The mechanisms of MSC differentiation are poorly understood, but recent studies have demonstrated that MSCs derived from bone marrow express acetylcholinesterase (AChE).^{3,4} These same researchers also found that AChE activity levels affect the ability of MSCs to differentiate into osteoblasts.⁴ The main function of AChE in the body is regulating the levels of acetylcholine located at synaptic junctions within the neuromuscular system; without AChE activity, these neurons would be in a constant state of stimulation. Many organophosphate (OP) chemicals, including pesticides and chemical warfare agents (CWA), directly target the enzymatic action of AChE. It is very interesting that AChE located in MSCs may play a non-traditional role in these cells and it is certainly possible that OPs could affect the ability of MSCs to differentiate and/or proliferate through the disruption of AChE. This is significant to the Army's mission because service members in the field are at risk of exposure to a host of toxic chemicals, including OPs. Exposure to these chemicals could affect MSC ability to proliferate and/or differentiate, therefore reducing the ability to recover from any injuries sustained during assignments. Also, tissue repair is essential to the long-term health of individuals exposed to CWA. Previously published experimental findings lead us to propose the following hypothesis: OPs reduce AChE activity in MSCs, therefore reducing the proliferation and/or differentiation potential of these cells. Our long-term objective is to determine the signaling pathways associated with MSC proliferation and differentiation and how these pathways relate to MSC-mediated tissue repair.

2 BACKGROUND AND SIGNIFICANCE

2.1 Mesenchymal stem cells

MSCs, also known as marrow stromal cells, were initially described in 1968 by Friedenstein and colleagues.⁵ In their studies, MSCs were isolated from bone marrow due to their characteristic ability to attach to tissue culture flasks. Once attached, these cells displayed a fibroblast-like morphology. Since their initial discovery in bone marrow, MSCs have been isolated from several other tissues including the umbilical cord, Wharton's jelly of the umbilical cord, placenta, adipose tissue, dental pulp, as well as from the lungs of lung transplant patients.² MSCs are capable of self-renewal and can be maintained in a multipotent state *in vitro*.⁶ Since no single marker is available to identify MSCs, the International Society for Cell Therapy has published a consensus statement regarding identification requirements.¹ According to this definition, MSCs must display the following properties: 1) adherence to plastic under routine cell culture conditions; 2) expression of the cellular markers CD73, CD90, and CD105; 3) lack of expression of CD11b, CD14, CD19, CD34, CD45, CD79a, and human leukocyte antigen (HLA); and 4) the capacity for *in vitro* differentiation into osteoblasts, adipocytes, and chondroblasts.

2.2 MSC proliferation pathways

It has been reported that MSC growth occurs in three distinct phases; these phases include a lag phase (3-5 days in culture), a rapid proliferation phase, and a stationary phase.² It has been demonstrated that the Wnt signaling cascade plays a critical role in this process, and it is likely that there are many other signaling pathways associated with MSC proliferation yet to be identified. It is possible that AChE may play a role in this process.

2.3 Current understanding of MSC differentiation

Even though MSCs have been traditionally thought of as multipotent progenitors for bone, cartilage, and adipose tissue, recent investigations have revealed that MSCs have the ability to differentiate into other cell types including astrocytes, neurons, alveolar epithelial cells, and hepatocytes.² Currently, only a few genes have been identified that play critical roles in MSC differentiation. These genes include, but are not limited to Wnt, Runt-related transcription factor 2 (Runx2), transforming growth factor- β (TGF β), peroxisome proliferator-activated receptor γ (PPAR γ), osterix, and brain-derived neurotrophic factor (BDNF). For example, Runx2 acts as a master gene for the regulation of osteogenic differentiation.² Up-regulation of this gene product promotes both osteogenic and chondrogenic differentiation, while inhibiting adipogenic differentiation. Even though AChE has been shown to be expressed in MSCs, the exact role it plays in MSC differentiation is currently unknown.

3 MATERIALS AND METHODS

3.1 Human MSC culture

Primary human bone marrow-derived MSCs were obtained from Lonza (Walkersville, MD) and cultured in Mesenchymal Stem Cell Growth Medium (MSCGM) supplemented with Mesenchymal Stem Cell Growth Supplement (MSCGS), L-glutamine, gentamicin, and amphotericin-B (all supplements from Lonza) as described.^{7,8} Only MSCs from passages 4 through 8 were examined for these studies.

3.2 Preparation of the OP chemicals

Stock solutions of the organophosphate pesticide parathion and its metabolite, paraoxon, (both from ULTRA Scientific; N. Kingstown, RI) were prepared in 100% ethanol (EtOH) and stored at 4°C.

3.3 Preparation of reactivator

The cholinesterase reactivator pralidoxime (2-pyridine aldoxime methylchloride or 2-PAM) obtained from Sigma-Aldrich® (St. Louis, MO) was prepared in sterile deionized water to a 1 M stock solution. Working stocks of lower concentrations were prepared from this stock in sterile deionized water as needed. All stocks were stored at 4 °C in the dark. The cholinesterase reactivator obidoxime chloride (Sigma-Aldrich®) was prepared in sterile deionized water to a 0.1 M stock solution. Working stocks of lower concentrations were prepared from this stock in sterile deionized water as needed. All stocks were stored at -80 °C. Thawed stocks were used within one week (stored at 4 °C in the dark) to ensure reactivator potency.

3.4 MSC cholinesterase reactivator toxicity studies

To evaluate the toxicity of the cholinesterase reactivator obidoxime chloride alone on MSCs, 1×10^4 cells per well were plated in 96-well tissue culture plates and allowed to attach for 24 hours. Then, MSCs were exposed to increasing concentrations (1 μ M, 10 μ M, 50 μ M, 100 μ M, 150 μ M, 200 μ M, 250 μ M) of obidoxime chloride for 24 hours and 48 hours. Cellular viability in the presence of this reactivator was determined by the MTT assay (Roche Applied Science; Indianapolis, IN).

3.5 MSC cholinesterase reactivator proliferation studies

To evaluate the effects of obidoxime chloride alone on MSC proliferation, 1×10^3 cells per well were plated in 96-well tissue culture plates and allowed to attach for 24 hours. Then, MSCs were exposed to increasing concentrations (1 μ M, 10 μ M, 50 μ M, 100 μ M, 150 μ M, 200 μ M, and 250 μ M) of obidoxime chloride for 24 hours and 48 hours. MSC proliferation in the presence of this reactivator was determined by the BrdU Cell Proliferation Assay (Roche Applied Science).

3.6 Evaluation of cholinesterase reactivator in the presence of OP

Based on results from the studies described in Sections 3.4 and 3.5, as well as the 2-PAM results, reactivator concentration(s) with no significant effects on cellular viability or proliferation over 48 hours were chosen for experiments with paraoxon. To evaluate cholinesterase reactivation, the stated viability and proliferation assays were performed in the presence or absence of media alone, vehicle (EtOH), obidoxime chloride (1 mM, 5 mM, 10 μ M) or 2-PAM (0.25 mM), paraoxon (100 μ M, 300 μ M, 1,000 μ M, 3,000 μ M, 5,000 μ M, 10,000 μ M), or paraoxon with reactivator. To test pre-treatment of cells with reactivator, some experiments underwent a 15-minute pretreatment with each well's respective reactivator concentration prior to the stated exposure.

3.7 MSC differentiation studies

3.7.1 Adipogenic differentiation

To evaluate adipogenic differentiation, MSCs were plated in 96-well tissue culture plates at 5×10^3 cells per well and allowed to grow to confluence in the presence of MSCGM. Once the cells reached confluence, the media was replaced with Human MSC Adipogenic Induction Medium (Lonza) and Adipogenic Maintenance Medium (Lonza) with or without vehicle (EtOH), OP chemical, and/or reactivator in cycles in accordance with the manufacturer's recommended protocol. The cells were cultured for 14 days. At the end of the differentiation period, the cells were stained using the AdipoRed Assay Reagent (Lonza) protocol and measured using a microplate fluorescence spectrophotometer.

3.7.2 Osteogenic differentiation

For osteogenic differentiation, MSCs were plated in 96-well tissue culture plates at 1×10^3 to 2.5×10^3 cells per well. After attachment but prior to confluence (24-72 hours), the media was replaced with Osteogenic Differentiation Medium (Lonza) with or without vehicle (EtOH), OP chemical, and/or reactivator. This medium was replaced every 3-4 days for 14-21 days. At the end of each differentiation period, cells were fixed with absolute EtOH or 4% paraformaldehyde (PFA) for 30 minutes then stained using the OsteoImage™ Mineralization Assay (Lonza) protocol and measured using a microplate fluorescence spectrophotometer.

3.8 Clustered regularly-interspaced short palindromic repeats (CRISPR)/Cas9 knockout of AChE

The transfection protocol was adapted from the Ultra-Cruz® Transfection Reagent (Santa Cruz Biotechnology®; Dallas, TX) specification sheet. MSCs were plated at a density of 2×10^5 cells per well in antibiotic-free medium in 6-well plates. After 24 hours, transfection complex solutions were prepared in antibiotic-free medium in accordance with the manufacturer's recommendations using a concentration of 1 μ g plasmid (either non-targeting control or AChE knockout) per 10 μ L transfection reagent and incubated with cells for 72 hours, with antibiotic-free medium refreshment after 24 hours and 48 hours. MSCs were lysed 72 hours post-transfection and collected in 1X RIPA buffer (Cell Signaling Technology®, Inc.; Danvers, MA), centrifuged, and the supernatants assayed for protein concentration with the Pierce™ 660nm Protein Assay (Thermo Scientific™; Waltham, MA). The samples were resolved using the 4-12% gradient Bolt® Bis-Tris Plus Gel according to the manufacturer's instructions (Life Technologies™; Grand Island, NY) and transferred onto polyvinylidene fluoride (PVDF) membranes (Life Technologies™) using the iBlot® 7-Minute Blotting System (Life Technologies™). The membranes were blocked, incubated with mouse anti-AChE monoclonal antibodies (Santa Cruz Biotechnology®, Inc.), and incubated with anti-mouse IgG antibodies conjugated to alkaline phosphatase using the iBlot® Western Blot System (Life Technologies™) according to the manufacturer's

instructions. Finally, the membranes were developed using the iBlot® Western Detection Chromogenic Kit (Life Technologies™).

3.9 Determination of AChE activity in MSCs

AChE activity within the MSCs was measured using the colorimetric Acetylcholinesterase Assay Kit (Abcam®; Cambridge, MA) according to the manufacturer's recommended protocol. Prior to the AChE activity assay MSCs were exposed to media with or without paraoxon (100 µM and 3000 µM), 2-PAM (0.25 mM and 0.5 mM), or paraoxon and 2-PAM together for 24 hours and lysates were collected using dPBS + 1% Triton™ X-100 (Sigma-Aldrich®) and a cell scraper. AChE activity was reported as a percentage of control AChE activity.

3.10 AChE binding partners in MSCs

3.10.1 Determination of potential AChE binding partners in MSC

The Pierce™ Pull-Down PolyHis Protein:Protein Interaction Kit (Thermo Scientific™) was used according to the manufacturer's recommended protocol. Briefly, previously prepared His-tagged AChE protein was incubated with MSC lysates for 1 hour at room temperature. These mixtures were placed on filter columns, washed, and protein eluted (column flow-through was kept from each step for analysis). The eluted protein and the initial flow-through were then prepared for sodium dodecyl sulfate polyacrylamide gel electrophoresis (SDS-PAGE) and bands visualized using SimplyBlue™ Safe Stain (Life Technologies™). Band preparation for identification by mass spectrometry (MS) was completed using the In-Gel Tryptic Digestion Kit (Thermo Scientific™) with destaining.

3.10.2 Confirmation of binding partner by co-immunoprecipitation (Co-IP)

The immunoprecipitation protocol was adapted from the Protein A/G PLUS-Agarose Immunoprecipitation Reagent (Santa Cruz Biotechnology®) specification sheet. MSCs were lysed, collected, and assayed for protein concentration as described above (Section 3.8). Lysate samples were diluted in 1X RIPA to within the concentration range suggested in the protocol. Lysates were pre-cleared with protein A/G-agarose beads (Santa Cruz Biotechnology®) for 30 minutes at 4 °C with rotation, followed by centrifugation and supernatant collection. Rabbit polyclonal anti-vinculin antibodies (Santa Cruz Biotechnology®) were added to the supernatant followed by overnight incubation at 4 °C with rotation. A/G-agarose beads were added to the tube again with overnight incubation at 4 °C with rotation. Bead pellets were then washed several times with PBS, re-suspended in sample buffer, prepared for SDS-PAGE, and processed for immunoblotting as described above (Section 3.8) with mouse monoclonal anti-AChE antibodies (Santa Cruz Biotechnology®).

3.11 Statistical analysis

A Student's *t*-test was used to compare mean responses between individual experimental and control groups. Analysis of variance (ANOVA) was used to compare the mean responses among experimental and control groups in experiments with multiple groups. The Tukey's test was used to determine significant differences between groups. A *p*-value < 0.05 was considered significant for all experiments.

4 RESULTS

4.1 Human bone marrow-derived MSC culture

Human bone marrow-derived MSCs were grown on tissue culture-treated plastic in MSCGM. MSCs attach to tissue culture-treated plastic and display a fibroblast-like morphology. Figure 1 is a phase contrast photomicrograph of MSCs cultured in our laboratory at passage 5.



Figure 1. A representative phase contrast image of cultured, undifferentiated human MSCs.

4.2 Evaluation of the cholinesterase reactivator obidoxime chloride

Prior to introducing obidoxime chloride into any of our viability, proliferation or differentiation studies, it was essential to determine its toxicity in MSCs. The following experiments address these issues.

4.2.1 Effect of obidoxime chloride on MSC viability

MSCs were plated at a density of 1×10^4 in 96-well tissue culture plates with 24-hour attachment, then exposed to increasing concentrations (1 μM , 10 μM , 50 μM , 100 μM , 150 μM , 200 μM , and 250 μM) of obidoxime chloride for either 24 hours (Figure 2A) or 48 hours (Figure 2B) and evaluated using the MTT Viability Assay (Roche Applied Science). There was no significant reduction in cellular viability following a 24-hour or 48-hour exposure to either 1 μM or 10 μM obidoxime chloride. A dose-dependent reduction in viability is seen as obidoxime chloride concentration is increased.

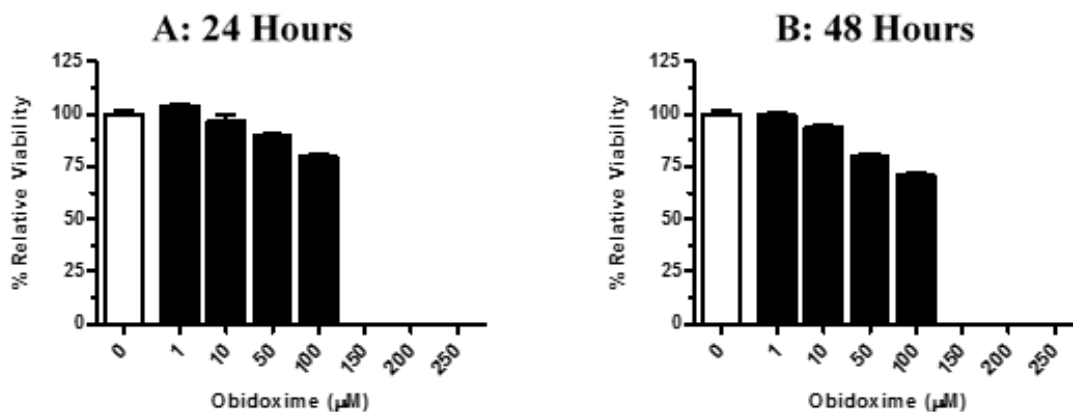


Figure 2. Effects of obidoxime chloride on the viability of cultured human MSCs. MSCs were exposed to increasing concentrations (1 μM , 10 μM , 50 μM , 100 μM , 150 μM , 200 μM , and 250 μM) of obidoxime chloride (closed bars) or media alone (open bars) for either (A) 24 hours or (B) 48 hours, after which they were assayed for viability using the MTT Cell Viability Assay. The results are reported as mean \pm the standard error of the mean (SEM) of % Relative Viability; $n = 12$ for each condition tested.

4.2.2 Effect of obidoxime chloride on MSC proliferative ability

MSCs were plated at a density of 1×10^3 cells in 96-well tissue culture plates with 24-hour attachment, then exposed to increasing concentrations (1 μ M, 10 μ M, 50 μ M, 100 μ M, 150 μ M, 200 μ M, and 250 μ M) of obidoxime chloride for either 24 hours (Figure 3A) or 48 hours (Figure 3B) and evaluated using the BrdU Cell Proliferation Assay (Roche Applied Science).

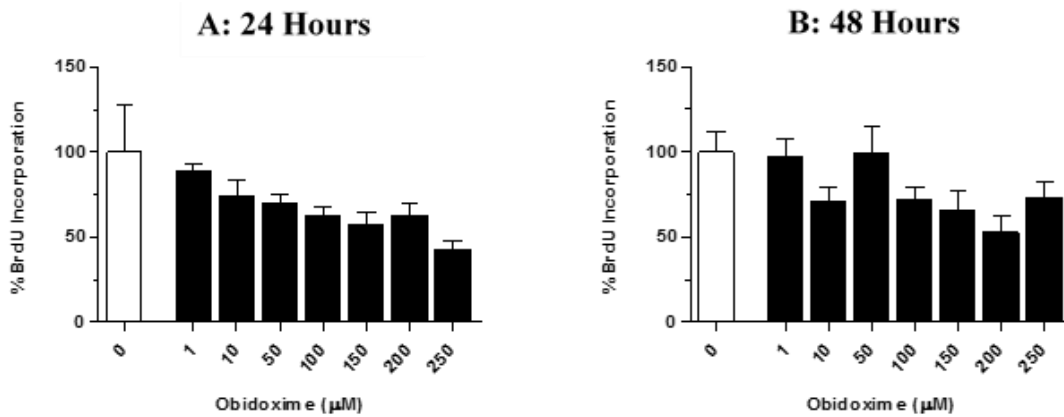


Figure 3. Effects of obidoxime chloride on the proliferative ability of cultured human MSCs. MSCs were exposed to increasing concentrations (1 μ M, 10 μ M, 50 μ M, 100 μ M, 150 μ M, 200 μ M, and 250 μ M) of obidoxime chloride (closed bars) or media alone (open bars) for either (A) 24 hours or (B) 48 hours equivalent, after which they were assayed for proliferation using the BrdU Cell Proliferation Assay. The results are reported as mean \pm SEM of % BrdU Incorporation; $n = 4$ for controls and $n = 12$ for experimental conditions.

4.2.3 Evaluation of cholinesterase reactivator in the presence of OP

Reactivator concentration(s) with no significant effects on cellular viability or proliferation over 48 hours were chosen for experiments with paraoxon. Based on the viability and proliferation assay data above, further experiments utilized 1 μ M, 5 μ M, or 10 μ M obidoxime chloride. To evaluate cholinesterase reactivation, the stated viability and proliferation assays were performed in the presence or absence of media alone, vehicle (EtOH), obidoxime chloride (1 μ M, 5 μ M, 10 μ M) or 2-PAM (0.25 mM) (Year 2 data), paraoxon (100 μ M, 300 μ M, 1,000 μ M, 3,000 μ M, 5,000 μ M, and 10,000 μ M), or paraoxon with reactivator. To test pre-treatment of cells with reactivator, in some experiments the final stated exposure followed a 15-minute pre-treatment with each well's respective reactivator concentration. With or without pre-treatment of cells, no consistent viability or proliferation data was obtained to prove significant rescue by either reactivator following exposure to any concentration of paraoxon ($n = 4$ for controls, $n = 3-8$ for experimental conditions; data not shown).

4.3 MSC differentiation studies

4.3.1 Adipogenic differentiation in the presence of OP and/or reactivator

MSCs were plated in 96-well tissue culture plates at a density of 5×10^3 cells per well and allowed to grow to confluence in the presence of MSCGM. Once the cells reached confluence, the media was replaced with MSC Adipogenic Induction Medium (Lonza) and Adipogenic Maintenance Medium (Lonza) with or without vehicle (EtOH), OP, and/or reactivator in cycles in accordance with the manufacturer's recommended protocol. The cells were cultured for 14 days. At the end of the differentiation period, the cells were stained using the AdipoRed™ Assay Reagent (Lonza) protocol and measured using a microplate fluorescence spectrophotometer. Cells in the presence of both paraoxon (100 μ M) and obidoxime chloride (5 μ M) had a reduction in differentiation comparable to that of cells in the presence of paraoxon alone. Cells in the presence of both parathion (100 μ M) and obidoxime chloride (5 μ M) also had a reduction in differentiation than cells exposed to parathion alone ($n = 8$ for each condition tested; data not shown).

4.3.2 Osteogenic differentiation in the presence of OP and/or reactivator

MSCs were plated in 96-well tissue culture plates at a density of 1×10^3 to 2.5×10^3 cells per well. After attachment but prior to confluence (24-72 hours), the media was replaced with Osteogenic Differentiation Medium (Lonza) with or without vehicle (EtOH), OP, and/or reactivator. This medium was replaced every 3-4 days for 18 days. At the end of

each differentiation, period cells were fixed with absolute EtOH or 4% PFA for 30 minutes then stained using the OsteoImage™ Mineralization Assay (Lonza) protocol and measured using a microplate fluorescence spectrophotometer. Cells in the presence of both paraoxon (100 μ M) and obidoxime chloride (5 μ M) had a reduction in differentiation comparable to that of cells in the presence of paraoxon alone. Cells in the presence of both parathion (100 μ M) and obidoxime chloride (5 μ M) had a further reduction in differentiation than cells exposed to parathion alone; further studies would need to be completed to assess significance ($n = 8$ for each condition tested; data not shown; 14-day and 21-day differentiation data for continued time courses with OPs not discussed because results are similar to those seen in Year 2).

4.4 CRISPR/Cas9 knockout of AChE

MSCs were plated in 6-well plates at a density of 2×10^5 cells per well in antibiotic-free medium and allowed to attach overnight. The cells were then transfected with a solution of 1 μ g plasmid (either non-targeting control or AChE knockout) per 10 μ L transfection reagent. At 72 hours post-transfection, MSCs were lysed and processed for immunoblotting as previously described (Section 3.8). Both plasmids tested, and to a lesser degree, the transfection reagent had a visibly toxic effect on the MSCs over the 72 hour post-transfection period. There was an observable reduction in AChE expression following the transfection, but this reduction was incomplete (data not shown).

4.5 Determination of AChE activity in MSCs

MSCs were cultured in the presence of media, paraoxon (100 μ M and 3000 μ M), 2-PAM (0.25 mM and 0.5 mM), or paraoxon and 2-PAM together for 24 hours, then assayed for AChE activity. Results were inconsistent; further studies would need to be completed to assess significance ($n = 3$ for each condition tested; data not shown).

4.6 AChE binding partners in MSCs

4.6.1 Determination of potential AChE binding partners in MSCs

Pulldown assays using the Pierce™ Pull-Down PolyHis Protein:Protein Interaction Kit (Thermo Scientific™) were further optimized (more pure His-tagged protein in appropriate buffer) after Year 2. Optimized results yielded a single band (~117 kDa in rows 5 and 6 in Figure 4) associated with AChE (~68 kDa in Figure 4).

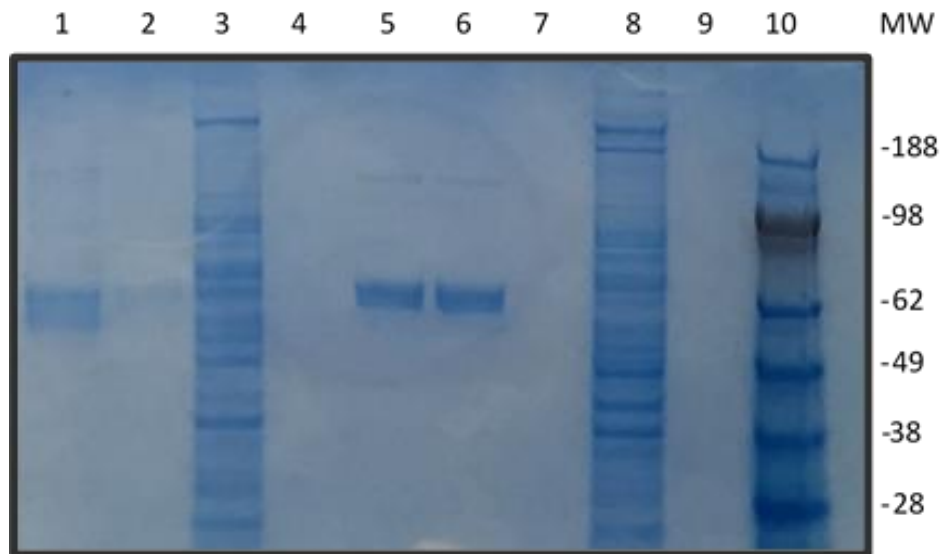


Figure 4. Identification of potential AChE binding partners in human MSCs. Following the protein interaction kit protocol, the gel was stained using SimplyBlue™ Safe Stain (Life Technologies™). The resulting band at ~117 kDa in sample lanes 5 and 6 is a potential binding partner for AChE (~68 kDa in sample lanes 5 and 6). The protein was identified using MS as vinculin, a focal adhesion protein.

Lane 1: His-tagged AChE protein, Lane 2: His-tagged AChE protein bound to agarose beads,

Lane 3: MSC whole-cell lysate, Lane 4: initial eluate (negative control), Lane 5: second eluate (experimental), Lane 6: third eluate (experimental), Lane 7: blank, Lane 8: MSC whole-cell lysate, Lane 9: blank, and Lane 10: molecular weight (MW) standard.

4.6.2 Confirmation of binding partner by Co-IP

The Co-IP protocol, adapted from Santa Cruz Biotechnology®, was optimized using polyclonal rabbit anti-vinculin antibodies for IP and monoclonal mouse anti-AChE antibodies for IB. Figure 5 is a representative result of this Co-IP.

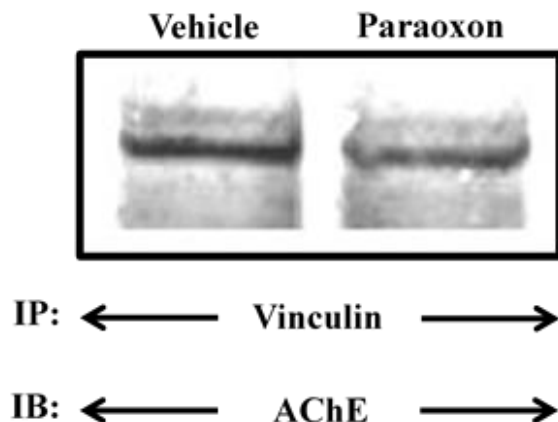


Figure 5. Association of AChE with the focal adhesion protein vinculin in human MSCs. Human MSCs were exposed to either paraoxon or equivalent amounts of vehicle control (EtOH) for 24 hours. The MSCs were lysed and immunoprecipitated with anti-vinculin antibodies, resolved by SDS-PAGE, and transferred to PVDF membranes. The membranes were then incubated with anti-AChE antibodies followed by AP-conjugated secondary antibodies and then developed. The blot shown is representative of three independent experiments.

5 CONCLUSIONS

During the first and second years of this project, our results indicated that OPs affect the cellular viability (IC_{50} : Paraoxon – 2,000 μ M; Parathion \geq 10,000 μ M), proliferative ability (Paraoxon \geq 300 μ M; Parathion \geq 100 μ M), and differentiation potential of MSCs. We demonstrated that the OPs, parathion and paraoxon, reduced the cellular viability as well as the proliferative ability of MSCs in a dose-dependent manner. We also demonstrated the ability to differentiate MSCs into several different cell types including adipocytes, osteoblasts, and neurons (determined by morphology analysis over the last 2 years). Next, we examined three time points during adipogenic and osteogenic differentiation using a quantitative fluorescence-based assay. Treatment with either parathion or paraoxon reduced MSCs ability to differentiate into both osteoblasts and adipocytes. During the second and third years of this project, we introduced the cholinesterase reactivators 2-PAM and obidoxime chloride into our studies to determine a possible role for AChE. After we determined reactivator concentrations that did not disrupt the normal cell viability or proliferative potential, we introduced these into our paraoxon/parathion toxicity studies. Our protein interaction studies suggested that AChE binds to the focal adhesion protein vinculin in MSCs; this interaction may be key to regulating the proliferation and differentiation of these cells. Overall, results suggest that OPs could be altering the normal function of MSCs by disrupting the normal pathways associated with AChE in MSCs (e.g., association with vinculin); these altered pathway(s) could be responsible for inducing cellular death as well as altering the normal proliferative and differentiation functions of MSCs.

ACKNOWLEDGMENTS

The authors would like to acknowledge U.S. Army funding provided through the Edgewood Chemical Biological Center's In-House Laboratory Independent Research Program. The authors would also like to thank Dr. Augustus W. Fountain, Ms. Rebecca Braun, and Ms. Stacey Broomall for continued scientific and administrative support.

REFERENCES

- [1] Dominici, M. *et al.*, "Minimal criteria for defining multipotent mesenchymal stromal cells. The International Society for Cellular Therapy position statement." *Cytotherapy*, **2006**, 8(4), p315-317.
- [2] Rastegar, F. *et al.*, "Mesenchymal stem cells: Molecular characteristics and clinical applications." *World Journal of Stem Cells*, **2010**, 2(4), p67-80.
- [3] Hoogduijn, M.J.; Cheng, A.; and Genever, P.G., "Functional nicotinic and muscarinic receptors on mesenchymal stem cells." *Stem Cells and Development*, **2009**, 18(1), p103-112.
- [4] Hoogduijn, M.J.; Rakonczay, Z.; and Genever, P.G., "The effects of anticholinergic insecticides on human mesenchymal stem cells." *Toxicological Sciences*, **2006**, 94(2), p342-350.
- [5] Friedenstein, A.J. *et al.*, "Heterotopic of bone marrow. Analysis of precursor cells for osteogenic and hematopoietic tissues." *Transplantation*, **1968**, 6(2), p230-247.
- [6] Pittenger, M.F. *et al.*, "Multilineage potential of adult human mesenchymal stem cells." *Science*, **1999**, 284(5411), p143-147.
- [7] Angelini, D.J. *et al.*, "Hypoxia-induced mitogenic factor (HIMF/FIZZ1/RELM alpha) recruits bone marrow-derived cells to the murine pulmonary vasculature." *PLOS One*, **2010**, 5(6), e11251.
- [8] Kolosova, I.A. *et al.*, "Resistin-like molecule alpha stimulates proliferation of mesenchymal stem cells while maintaining their multipotency." *Stem Cells and Development*, **2013**, 22(2), p239-247.

The persistence of microbial memory: An exploration of the potential of bacteria as an information storage medium

James M. Myslinski^a, Sarah Katoski^b, Michael Kim^c, Frank J. Kragl^c, Matthew W. Lux^{c*}

^aExcet, Inc., 8001 Braddock Rd, Suite 303, Springfield, VA 22151

^bLeidos, Inc., P.O. Box 68, Gunpowder Branch, Aberdeen Proving Ground, MD 21010

^cU.S. Army Edgewood Chemical Biological Center, Research and Technology Directorate,
5183 Blackhawk Rd, Aberdeen Proving Ground, MD 21010

ABSTRACT

The ability of DNA to store large amounts of information in a small amount of space is remarkable. Combined with the plummeting costs to both read and write DNA, the notion of DNA as a viable data storage material has recently emerged. Existing efforts have focused on *in vitro* DNA for storage; however, in this study, we investigate storing data in living bacteria cells. In addition to demonstrating data storage in bacteria, we use the system to assess two fundamental scientific questions regarding “non-functional” DNA: (a) the relative mutation rate of non-functional data-storing DNA versus genomic DNA; and (b) the stability of a mixed population of functionally identical but genetically different strains. We first implement an encoding strategy robust to the types of errors expected in living cells, namely mutations, insertions, deletions, and recombinations. We use this algorithm to encode into DNA a 3D-printable model of the Death Star. We also perform preliminary work to assess our experimental system for accumulating mutations in a population in a continuous flow environment. Future work will assess our ability to recover the data in the face of actual mutation accumulation by testing data-containing strains in our experimental system, the relative error rates, and stability of mixed populations.

Keywords: DNA storage, synthetic biology, mutation rates

1 INTRODUCTION

1.1 DNA as a storage medium

With the recent costs of synthesis and sequencing of DNA plummeting, the notion of storing data in DNA has become of interest and was demonstrated by two studies storing a significant amount of digital data in DNA (*in vitro*).^{1,2} The incredible density of information per volume and the natural stability of DNA offer a potential solution to the enormity of today’s data storage needs. The obvious shortfalls are very slow read/write times and destructive reads, which targets the emerging technology towards archival storage applications. Indeed, at the current stage of development and price point, it is estimated that DNA can already compete with existing technology in the most extreme cases where access is roughly once per ten years.¹ In this work, we investigate the use of bacteria as a host to store DNA encoded with digital information. Working *in vivo* offers several advantages and disadvantages. In practical archival storage applications, storing in bacteria offers the ability to rapidly reproduce data for redundancy or to circumvent destructive read issues, but at the cost of higher storage demands, higher error rates, and lower density. Beyond archival storage, storage in bacteria allows the data to survive in natural environments. Applications include covert transmission of information and embedding source information into engineered or biological threat organisms for attribution of potential downstream releases.

1.2 Mutation rate of non-functional DNA

Computing the *in vivo* mutation rate of organisms has long been an area of research.³⁻⁶ One of the complicating factors in studying mutation rates is the inherent functional bias, whereby impacts on the fitness resulting from a mutation influence the prevalence of that mutation in a population. As it is impossible to assess the impact on function of an individual base pair *a priori*, genomes are far too large to test exhaustively, and many “functions” may only present themselves under certain conditions, it is impossible to label any individual base pair as “nonfunctional”. Moreover, the definition of “function” is hotly contested.⁷ The insertion of large amounts of synthetic data-storing DNA into bacteria offers an opportunity to address this issue from a different angle by making the assumption that this

data-storing DNA will be “random” and have no function. Of course, function can occur by chance, thereby undermining the assumption. However, the odds of significant function occurring by chance are low and can be made lower by scanning the DNA bio-informatically for predicted function. At the least, assessing the mutation rate of data-storing DNA should provide a reasonable estimate for *in vivo* DNA replication errors that is less influenced by functional bias than is genomic DNA. This baseline estimate of *in vivo* rates has uses in understanding natural evolution, predicting the stability of information encoded into living organisms, and as a baseline rate for mutation of functional DNA.

1.3 Competition between functionally identical strains

The roles of microbial communities in health and environmental concerns have been rapidly emerging.⁸⁻¹⁰ Understanding how the genetic makeup of these populations and their interactions impact outcomes is a daunting task. Complex competition and cooperation between species and subspecies, in both time and space, makes the work especially challenging. Indeed, even isogenic strains have been shown to produce variable population structures.¹¹ Here, by splitting data among multiple strains and growing them together, we are naturally able to ask questions about the stability of mixed populations of functionally equivalent but genetically diverse strains over time.

2 METHODOLOGY

2.1 Software and 3D printing

All described software is written in MATLAB® (MathWorks®; Natick, MA). RS encoding/decoding used built-in MATLAB® functions. *In silico* simulations leveraged infrastructure housed at the U.S. Army Research Laboratory (ARL) as part of the Department of Defense (DoD) Supercomputing Resource Center. Multifile compression is performed by the unix zip utility. Hexdumps performed by the unix xxd utility. We created the 3D model using ZEdit™ software and saved the file in .zpr format. The model was printed using ZPrint software and a SOLIDWORKS 3D printer. File compression was done with the open source utility 7-zip, set to the highest compression setting.

2.2 DNA synthesis, assembly, and cloning

DNA blocks are manufactured as gBlocks™ from IDT®; all primers are produced by IDT®. The Gibson Assembly® Kit is provided by New England BioLabs®, Inc. PCR amplification is performed using GQ5® High-Fidelity PCR Master Mix (New England BioLabs®, Inc.). Primers are automatically generated using custom software written in MATLAB®. With a user-defined target melting temperature and maximum primer length, the software generates primer sets for each block such that all amplifications can be performed simultaneously. The software also allows the user to flag blocks that were modified to pass repetitiveness scans (see above) such that the additional sequences are ignored. The bacterial artificial chromosome (BAC) vector used is CopyRight® v2.0 pEZ™ BAC (Lucigen®). Hosts are DH5α, CopyRight® optimized competent cells (Lucigen®), and XL1-Red mutator cells (Agilent Technologies).

2.3 Batch and continuous flow cultures

Batch culture experiments are performed in a 20 L reactor containing Luria-Bertani (LB) medium and appropriate antibiotics. Continuous flow experiments are also performed in a 20 L reactor with a flow rate that is adjusted by experiment. For the 20 L batch culture, cells were grown overnight, added to the reactor, and samples taken at $t = 0$ hours and $t = 6.7$ hours after inoculation. For the 250 mL flask culture, cells were grown overnight in 50 mL conical tubes, 1 mL of each mixed into 50 mL of fresh LB, and grown overnight.

3 DATA

3.1 Encoding and decoding algorithms

The first step in using bacteria as a data storage medium is to encode the information into a string of virtual DNA base pairs. In contrast to *in vitro* efforts^{1,2} where synthesis and sequencing errors are the only significant source of errors, challenges to information stability are potentially very high in cells and error correcting methods are crucial. Error handling is a field rich in digital design and communications, providing many tools ripe for adaptation. A noticeable difference, however, is that unlike digital applications where the runtime of the encoder/decoder is typically of critical importance, we are effectively unconstrained by runtime because the time spent in the bacteria is the rate-limiting step

of the communication channel. We use a modular, multilayer approach to maximize our chances of recovering the data. Our architecture is designed such that by adjusting input parameters for the encoding algorithm, the system can be tuned to be robust to different error rates for different error types, such as point mutations, insertions, etc. We use *in silico* simulations based on our experimental set up to select values that should be robust to expected *in vivo* error rates.

Table 1. Conversion table between binary and base pairs.

Binary	00	01	10	11
Base Pair	A	T	C	G

3.1.1 Data blocks

The primary functional unit in our strategy is designated as a “block” of length b and is divided into three subsections: the address (length a), the data (length d), and the error-correcting code (ECC; length e). The address determines the location of the data contained in the block in relation to all other blocks. The ECC enables recovery of both the data and address subsections in the face of mutations anywhere in the block. The ECC uses Reed-Solomon (RS) encoding, which breaks up a message sequence into k symbols of m bits and adds additional symbols to create a code word of length n symbols such that a corresponding decoder is capable of correcting t symbols and detecting $2*t$ symbol errors. Here, we set $b=m*n$ such that each block is one code word. RS encoders are constrained by two inequalities:

$$t \leq \frac{n - k}{2} \quad (1)$$

and

$$n \leq 2^m - 1 \quad (2)$$

By choosing values for b , m , and t , these constraints result in an ECC length of $e=2t*m$. By additionally choosing a value of a , the data length can be computed as $d=b-a-2t*m$. See Table 2 for the values selected in this work.

To encode a set of arbitrary data, the algorithm is pointed to a folder, which it compresses into a single file. The resulting file is then hex dumped, and the hex sequence converted to binary. Using the value of d an arbitrary binary sequence can be divided into appropriate sized blocks. Incrementally increasing binary addresses are then appended to the front of each block, and the address plus data sequence is passed through an RS encoder to create a full block with the ECC appended to the end. Since the total amount of data is unlikely to be divisible by d , the leftover data is padded by a single 1 followed by enough 0's to make a full-sized block. These blocks of binary sequence are then converted to a DNA sequence as shown in Table 1.

3.1.2 Data drives and redundant array of independent disks (RAID)

Blocks are subsequently arranged into larger units called “drives”. Each drive represents an individual bacterial strain containing encoded data. Each drive contains a sequence of blocks separated by stop codons. The stop codons serve two purposes: (1) to provide a marker for the decoding algorithm to separate blocks, and (2) to help reduce the probability of random functionality arising from the encoded DNA. The blocks are arranged across drives by striping in a RAID 6 implementation. The outcome of this RAID 6 approach is that two additional drives are added to the pool, the blocks are spread amongst the drives, and the overall system becomes tolerant to the complete or partial loss of up to two full drives. This approach protects against the situation where one or two strains lose large chunks of data through recombination or otherwise, or disappear from the population entirely.

Generation of the RAID drives uses the same RS theory described above. Here, however, the message sequence is the symbol from each data drive in a given position, and thus has length $D=k_{RAID}$ equal to the number of data drives. Unlike in the ECC case, when data is missing during RAID recovery the position of missing data is known. In this special case, RS decoders can recover these ‘erasures’ at double the rate of the case where the position is unknown, allowing recovery of up to $T=t_{RAID}$ symbols, where $t_{RAID}=n_{RAID}-k_{RAID}$, $n_{RAID}=D+R$, and R is the total number of RAID drives. See Table 2 for our choice of these parameters in this work.

Table 2. Values used for various encoding parameters.

Block Parameters			Drive Parameters		
Total Block Size	b	2000 bits	# of Data Drives	D	8 drives
Address Size	a	10 bits	# of RAID Drives	R	2 drives
ECC Symbol Length	m	10 bits	RAID Code Word Length	M	10 bits
Correctable Symbols per Code Word	t	4 symbols	Correctable Drives per Stripe	T	2 symbols

To generate RAID drives, data drives are first divided such that the block in each position across drives is in the same group, called a stripe. For each symbol position of each stripe, a RAID RS encoder is used to generate symbols to recover from errors within stripes. However, this process is only applied for address and data symbol positions. For the ECC positions, the ECC RS is applied to the generated RAID data to complete the RAID block. This approach allows for recovery from point mutations before applying RAID. At this stage, the data is fully encoded into DNA blocks and assembled into drives.

3.1.3 Synthesis keys

An additional consideration in encoding the data into DNA is the ability to actually synthesize the DNA. *In vitro* efforts have used large pools of DNA oligos, which simplifies synthesis significantly compared to the much larger assembled DNA molecules required here. For oligo synthesis, the only barrier to high fidelity synthesis is that error rates increase significantly with length for homopolymer runs. Thus, previous efforts have used encoding strategies that preclude homopolymer runs completely. In this work, we use newly available commercial services to order DNA in 1 kbp chunks, exactly the size of the data blocks. These chunks are produced commercially by synthesizing overlapping oligos that can be assembled directly into the desired chunk. However, this process enforces rules on the sequence of the chunk to prevent complications in the assembly process, most notably rules limiting receptiveness. By encoding the DNA to preclude homopolymer repeats, the odds of a block passing the repetition screens drops dramatically. Therefore, in this work we do not enforce any homopolymer restrictions.

Even without homopolymer restrictions, blocks can be rejected for repetition. This repetition can occur by random chance or because the actual binary data is low complexity; the use of padding of the final block can introduce long stretches of low complexity. To avoid this issue, we use an encryption key to perturb the sequence in a reversible way. The encryption breaks the sequence into W words of size w base pairs, then perturbs each word by a randomly generated key value, k , where $0 < k < 4^w$. The perturbation occurs by converting the word back to binary (see Table 1) and adding the binary of the current key value (disregarding any carry) to create a new word. The same set of K key values, where $K = W/w$, is applied to all blocks. In this way, by passing the key along to the decoder, the process can be reversed and original block sequence recovered. Here, we use $w=4$.

The encryption key method does not, however, guarantee that a block will pass the repetition screen because even randomly generated sequences will fail with some probability. For the special case of repetitive sequences occurring on the block ends, two randomly generated 8 bp sequences that do not occur in the block in forward or reverse can be generated and appended to each end. Such blocks are noted for special processing later. Otherwise, if a set of drives contains blocks that still fail the repetition screens after encryption, a new random encryption key can be generated and applied and the blocks rescreened. Thus, by looping until a successful key is found, the repetition screens can be passed without modifying the encoding process.

3.1.4 Simulated passaging

In order to assess the efficacy of our encoding strategy *in silico* beforehand, we created software that simulates cells evolving in a continuous-flow environment. In a continuous-flow reactor, cells flow out of the reactor at a rate equal to their growth rate. Though in reality the population is asynchronous, this can be modeled by taking a population, duplicating it, and then randomly removing half of the individuals from the new double-sized population. By introducing errors in the duplication process based on literature values, we can assess the likely mutation accumulation in a population based on realistic experimental conditions. The values in Table 2 were informed by this analysis.

3.1.5 Encoded contents

We used the above described algorithm to encode a 3D-printable model file of a “Death Star” (see Methodology). The model file was compressed to the smallest size possible and then zipped together with a readme file. This file was then used as input to the encoding algorithm, resulting in 364 blocks spread across 10 drives totaling 364,000 base pairs.

The final file size was 63 kB, yielding ~1.4 bits/bp or ~70% encoding efficiency. The encoding efficiency is highly dependent on choice of encoding parameters.

3.1.6 Decoding

The decoding algorithm is essentially the inverse of the encoding procedure. Assembled contigs from sequencing data are treated as drives and scanned for stop codons spaced by the size of the blocks. In cases where an expected stop codon is not found, the scan looks +/- 5 bps from the expected location and also checks for single base pair mutations from the expected stop codon. Based on these stop codons, potential blocks are passed through the ECC RS decoder to check for errors. Blocks that have too many errors for correction are flagged, and blocks that are successfully decoded are arranged by their respective address value. Based on which blocks are present or absent, RAID is applied to recover any missing blocks as necessary. For example, if only a RAID block is missing from a stripe, that block is not recovered as the data for that stripe is already present. If any data blocks cannot be recovered by RAID, the algorithm reports a failure. Otherwise, the algorithm assembles the data blocks into a single sequence, converts the sequence to a file, and unzips the file.

3.2 Drive synthesis

3.2.1 Assembling blocks into drives

Two alternative strategies were employed to assemble the ten drives. For Drive 1, the individual blocks were assembled by PCR amplifying each block with specially designed primers that contain overhangs complementary to the sequence of the neighboring block (see Methodology). These products were then assembled using Gibson Assembly¹² into groups of 6, transformed into *Escherichia coli* cells, and extracted (see Methodology). Extensive attempts to PCR amplify the product directly from the Gibson Assembly product worked very inconsistently, motivating a switch to the transformation approach. Drives 5-10 were synthesized into larger chunks of around 1.5 kbp that contained built-in overlaps, and are currently being assembled into groups of five. Drives 2-4 are still to be synthesized.

3.2.2 Barcodes

The use of multiple data drives allows us to ask fundamental questions about functionally equivalent but genetically different strains. While the mutation rates will be assessed by next-generation sequencing of samples of growing cultures, this data is only roughly able to approximate the relative quantities of the DNA in a sample. A more quantitative approach is the use of quantitative real-time polymerase chain reaction (qPCR), which with properly designed assays is capable of giving relatively accurate estimates of the number of copies of a specific DNA sequence present in a sample. Rather than designing new assays for each drive, we repurposed computationally designed and experimentally verified genetic barcode sequences that can be added to the drive (data not yet published). Using these barcodes, we can quickly assess the relative abundance of each drive in a growing population.

3.2.3 Inserting data into cells

The assembled blocks were inserted into a BAC using Gibson Assembly, and transformed into *E. coli*. Three strains were used: the commonly used DH5 α , a BAC-optimized strain called CopyRight®, and a mutator strain deficient in a proofreading enzyme called XL1-Red. See Methodology for more detail.

3.3 Passaging of strains

3.3.1 Mutation accumulation experiments

In order to test the ability of the algorithm to recover data in the face of *in vivo* mutations and analyze the mutation rates of nonfunctional DNA, experimental accumulation of mutations is necessary. To accomplish this, we are processing mixed cultures of cells in a continuous flow reactor. Over time, samples are collected for next-generation sequencing and mutational analysis. More frequently, samples are taken for qPCR analysis to assess the stability of the population. We have established growth rates of control strains in fermenter conditions to inform continuous flow reactor settings. Trial runs of the continuous flow set up are in progress.

3.3.2 Preliminary stability assessment of mixed cultures

We have tested mixed populations of cells containing 10 different genetic barcodes. The tests were performed under two experimental conditions: a 20 L batch culture and a 250 mL flask (see Methodology). Table 3 summarizes the results. Interestingly, the relative proportions of each barcode were not particularly stable. These results suggest that either (a) the barcode sequence confers some unexpected impact on fitness, or (b) that competition between

phenotypically identical cells is significantly impacted by noise. Further tests to assess the reproducibility of the success or lack thereof of each barcode in this experimental design, as well as testing a strain containing no barcode, should resolve the source of the change in relative proportion. Additionally, these experiments will inform the predicted stability of our encoded data and address the fundamental question of the stability of phenotypically identical but genetically diverse populations.

Table 3. Stability of mixed population.

Barcode	% of Total Population			
	20 L Batch Culture, not normalized		250mL Flask Culture, normalized	
	0 hour	6.7 hours	0 hour	16 hour
1	7.07%	17.87%	10%	9.86%
2	6.69%	4.89%	10%	6.06%
3	9.38%	6.22%	10%	7.63%
4	n/d*	n/d*	n/d*	n/d*
5	14.60%	9.99%	10%	13.46%
6	n/a**	n/a**	n/a**	n/a**
7	20.33%	31.50%	10%	17.69%
8	n/a**	n/a**	n/a**	n/a**
9	10.83%	7.94%	10%	11.38%
10	9.51%	5.61%	10%	8.88%
11	11.24%	8.46%	10%	15.12%
12	10.35%	7.52%	10%	9.93%

*Barcode 4 assays failed for unknown reason, returning no data.
 **Barcodes 6 and 8 from the original set of 12 were not used here due to poor performance.

3.4 Mutation analysis

Samples were sequenced using next-generation sequencing to achieve high read coverage. Mutation rates were assessed using a Bayesian approximation method that leverages the distribution of read coverage at each individual base pair. This approach allows estimation of overall mutation rates and comparison of rates for nonfunctional and genomic DNA, and leverages the information present in read variability that is typically lost by building consensus sequences.¹³

4 RESULTS

4.1 Encoding and decoding algorithms

The encoding and decoding algorithms have been successfully implemented and tested thoroughly using the *in silico* simulator. Using these tools and reasonable values from the literature on mutation rates in *E. coli*, error correction and other parameters were selected to provide appropriate robustness to expected perturbations to the DNA encoded message. A 3D-printable model of the Death Star was selected as the digital data to encode for the project, and the binary representation encoded into DNA sequences for synthesis and assembly.

4.2 Drive synthesis

The original synthesis strategy of PCR amplifying products of Gibson Assembly reactions proved to have low success rates, necessitating a change in assembly strategy. Instead of direct PCR amplification, we turned to transformation and extraction of Gibson Assembly reactions, which has proven to work with much higher reliability. With the new strategy, full-scale assembly of the drives has proceeded rapidly.

4.3 Passaging of strains

Preliminary experiments demonstrated that there are fluctuations in mixed populations of cells that differ only in the sequence of nonfunctional DNA carried by the cells. It remains to be determined the degree of this variability, and whether the variability is purely stochastic or somehow related to the sequence contained in each strain.

5 CONCLUSIONS

We have successfully developed a custom encoding/decoding algorithm specifically for the domain of storing data in bacterial DNA. Using these algorithms, we have encoded data for 370 kbp of DNA, which we have partially assembled into ten data “drives” that can be propagated in cells to answer basic science questions about basal mutation rates *in vivo* and competition between microbial strains that differ only in the sequence of nonfunctional DNA. With the impending completion of the assembly of these strains, we expect that key results addressing these questions will be produced in the near future.

ACKNOWLEDGMENTS

The authors would like to acknowledge U.S. Army funding provided through the Edgewood Chemical Biological Center’s In-House Laboratory Independent Research Program. We would also like to thank Will Burlew for support with 3D printing and model file design. We would also like to thank Alex Miklos, Sandy Gibbons, Kelley Betts, and Peter Emanuel for fruitful discussions about the project.

REFERENCES

- [1] Goldman, N. *et al.*, "Towards practical, high-capacity, low-maintenance information storage in synthesized DNA." *Nature*, **2013**, 494(7435), p77-80.
- [2] Church, G.M. *et al.*, "Next-generation digital information storage in DNA." *Science*, **2012**, 337(6102), p1628.
- [3] Lee, H., *et al.*, "Rate and molecular spectrum of spontaneous mutations in the bacterium *Escherichia coli* as determined by whole-genome sequencing." *Proceedings of the National Academy of Science*, **2012**, 109(41), E2774-E2783.
- [4] Drake, J., "Contrasting mutation rates from specific-locus and long-term mutation-accumulation procedures." *Genes Genomes Genetics*, **2012**, 2(4), p483-485.
- [5] Ochman, H., "Neutral mutations and neutral substitutions in bacterial genomes." *Molecular Biology and Evolution*, **2003**, 20(12), p2091-2096.
- [6] Wielgoss, S. *et al.*, "Mutation rate inferred from synonymous substitutions in a long-term evolution experiment with *Escherichia coli*." *Genes Genomes Genetics*, **2011**, 1(3), p183-186.
- [7] Graur, D. *et al.*, "On the immortality of television sets: “Function” in the human genome according to the evolution-free gospel of ENCODE." *Genome Biology and Evolution*, **2013**, 5(3), p578-590.
- [8] Joscelyn, J. and Kasper, L., "Digesting the emerging role for the gut microbiome in central nervous system demyelination." *Multiple Sclerosis Journal*, **2014**, 20(12), p1553-1559.
- [9] Bultman, S., "Emerging roles of the microbiome in cancer." *Carcinogenesis*, **2014**, 23(2), p249-255.
- [10] Sandek, A. *et al.* "The emerging role of the gut in chronic heart failure." *Current Opinion in Clinical Nutrition and Metabolic Care*, **2008**, 11(5), p632-639.
- [11] Coward, C. *et al.*, "Competing isogenic *Campylobacter* strains exhibit variable population structures *in vivo*." *Applied Environmental Microbiology*, **2014**, 80(21), p3857-3867.
- [12] Gibson, D. *et al.*, "Enzymatic assembly of DNA molecules up to several hundred kilobases." *Nature Methods*, **2009**, 6(5), p343-345.
- [13] Schuh, A. *et al.*, "Monitoring chronic lymphocytic leukemia progression by whole genome sequencing reveals heterogeneous clonal evolution patterns." *Blood*, **2012**, 120(20), p4191-4196.

Examination of the effects of botulinum neurotoxins on *Caenorhabditis elegans*

Edward R. Hofmann^a, James M. Myslinski^a, Edward J. Emm^b, Patricia E. Buckley^{c*}

^aExcet, Inc, 8001 Braddock Rd, Suite 303, Springfield, VA, USA 22151

^bLeidos, Inc., P.O. Box 68, Gunpowder Branch, Aberdeen Proving Ground, MD 21010

^cU.S. Army Edgewood Chemical Biological Center, Research and Technology Directorate,
5183 Blackhawk Rd, Aberdeen Proving Ground, MD 21010

ABSTRACT

Botulinum neurotoxin (BotNT) remains one of the deadliest substances known to man, yet few methods for neutralizing the BotNT toxin exist today, and side effects associated with these antidotes are often debilitating and less than efficacious. Previously, we were able to employ an *in vitro* model, BE(2)-M17 neuroblastoma cells, to use as a primary screen for blocking the cleavage of SNAP-25, the primary target for BotNT A activity. Currently, methods for developing treatments for exposure or efficient models for identifying BotNT inhibitors continue to rely heavily on animal lethality testing. An intermediate *in vivo* model that “bridges the gap” between *in vitro* testing and full-fledged animal studies would serve as an invaluable tool. In this new study, we propose the use of the model organism *Caenorhabditis elegans* as an intermediate model to the mouse lethality assay in order to determine whether previous *in vitro* results can be repeated in an *in vivo* model that is not only scalable, but also reproducible and automatable. This effort investigates the ability of BotNT to cleave *C. elegans* homologous proteins in an *in vivo* system, without the use of mice as the model organism.

Keywords: *C. elegans*, botulinum neurotoxin exposure, SNAP-25, VAMP2, SNB-1, RIC-4B, protein cleavage

1 INTRODUCTION

There are many bacteria that are known to cause disease in humans, but there are few that produce as deadly an effect as *Clostridium botulinum*. The neurotoxins that are produced by *C. botulinum*, and some strains of *C. butyricum*, and *C. baratii*, have been declared Category A agents on the scale for “Critical biological agent categories for public health preparedness.”¹ The category A agents on this list have the greatest potential for adverse public health impact, and have a moderate to high potential for large-scale dissemination, or the ability to invoke mass fear in the general population due to their heightened recognition to cause death.¹

Botulinum neurotoxin (BotNT), as one of the deadliest substances known to man and a Category A threat agent, has the potential to be used in a terrorist event,^{2,3} yet its paralyzing effects have been exploited for the treatment of neurological diseases^{4,5} and cosmetic therapy.⁶ The current method for neutralizing BotNT toxin is to inject human⁷ or equine antisera into the affected individual.⁸ The side effects associated with these antidotes are often debilitating, and less than therapeutically desired.⁷ Thus, there is an increased demand for finding better treatment methods to treat exposure and to find efficient models for measuring and identifying BotNT inhibitors.^{9,10} The goal of this effort is to investigate the practicality of using the nematode *Caenorhabditis elegans* as an *in vivo* model for mediating the translocation of BotNT across the cell membrane using antibodies that prevent the subsequent intracellular catalytic cascade; thus neutralizing BotNT. We hypothesize that the intrinsic biology of *C. elegans* can be used as an *in vivo* model for predicting BotNT toxicity and, consequently, can be developed as a new method for screening/testing therapeutic interventions for BotNT poisoning.

There are seven serotypes of toxin (BotNT A-G) produced by these bacteria, categorized based upon their immunological properties and amino acid variations.¹¹ Out of these seven serotypes, there are four toxin types known to cause deaths in humans: BotNT A, B, E, and F.^{2,12-15} All seven of the Botulinum neurotoxins are zinc metalloproteases that inactivate specific cellular proteins.¹³ They are produced as 150-kDa, single-chain proteins comprising three functional domains: *N*-terminal catalytic domain (light chain, LC), an internal translocation domain (heavy chain translocation, HCT), and a *C*-terminal receptor binding domain (heavy chain receptor, HCR).¹⁶ The HCR

can then be further subdivided into an *N*-terminal (HCR_N) and *C*-terminal (HCR_C) domains. The LC targets the soluble *N*-ethylmaleimide-sensitive factor attachment protein receptor. Specifically the LC of BotNT A, C, and E cleave nine amino acids from the *C*-terminal peptide of the synaptosome associated 25-kDa protein SNAP-25;^{13,16-18} whereas, the LC of BotNT B, D, F, and G all cleave synaptobrevin 2 (VAMP2).^{13,14,19,20} The HCR is responsible for the binding and translocation of the toxin *in vivo*.^{16,20} Both chains, bound by a single interchain disulfide bond, are required for toxicity (Figure 1).¹⁵

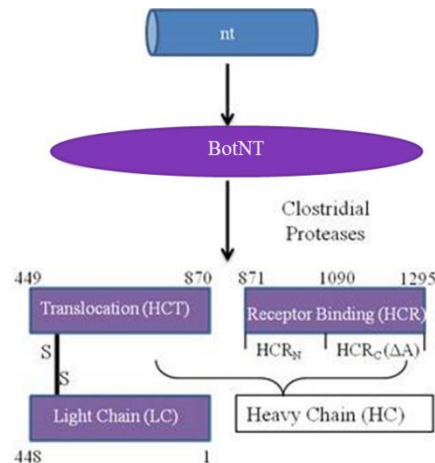


Figure 1. Model of BotNT (adapted from Baldwin¹⁶). The neurotoxin gene (nt) produces BotNT, which is cleaved by clostridial proteases into a dichain toxin, whose LCs and HCs are linked by a disulfide bond. The *N*-terminal light chain is a zinc protease. The *C*-terminal heavy chain includes a translocation domain (HCT), and a *C*-terminal receptor binding domain which can be subdivided into an *N*-terminal (HCR_N) and *C*-terminal domain (HCR_C(ΔA)).

Previous studies have shown that exposing the nematode *C. elegans* to various drugs produces electrophysiologically comparable results to vertebrate neurons.²¹ Furthermore, a number of human stress responses are conserved in *C. elegans*.²¹ *C. elegans* is well-established as a model system to elucidate molecular mechanisms involved in toxicological responses relevant to human intoxication.²¹⁻²³ The nematode model system has a neuromuscular junction with similar proteins of interest that, when disrupted, exhibit the same phenotypical results as human BotNT intoxication;^{24,25} therefore, the animal activity, before and after BotNT exposure, is predictive of the activity or inhibition of the toxin. Both SNAP-25 (RIC-4B homologue) and VAMP2 (SNB-1 homologue), the substrates of BotNT cleavage (Figure 2), are conserved in many lower organisms including the cleavage site in the nematode *C. elegans* (Figure 3). Indeed, these orthologues function in neurotransmitter secretion in *C. elegans* and mutant animals demonstrate various dysfunctional neurotransmitter phenotypes from arrested development to paralysis depending on the nature of the mutation.²⁵ Sequence alignment of the orthologues to these proteins in *C. elegans* suggests the cleavage sites of these proteins are conserved and therefore should be sensitive to proteolytic cleavage by BotNT.

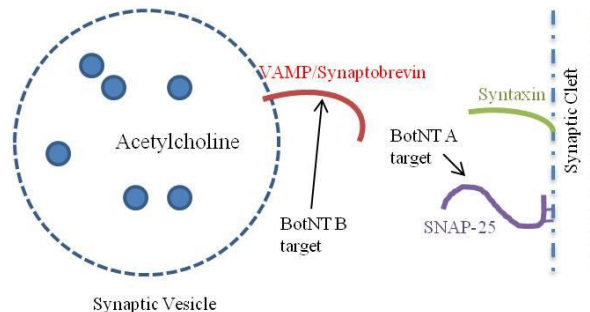


Figure 2. Model of BotNT activity (adapted from Barr¹³). BotNT blocks the cholinergic transmission from the synaptic vesicle to the synaptic cleft. BotNT A degrades SNAP-25 and BotNT B degrades VAMP, which prevents the vesicle from being bound to the membrane. This leads to flaccid muscle paralysis and nerve destruction, followed by difficulties in breathing and swallowing, leading to death.

2.3 Optimizing protein production

To select the highest protein-producing colonies, protocols were adapted from Li et al.²⁹ First, an appropriate plasmid was transformed into chemically competent DH5 α cells by incubating the cells (100 μ L) with the plasmid (1 μ L, 50.1 ng/ μ L) for 30 minutes at 0 °C, followed by 30 seconds at 42 °C, whereupon SOC media (250 μ L) was added and then placed in a 37 °C shaking incubator (200 rpm) for 1 hour. LB plates were spread with two volumes (50 μ L and 150 μ L) of the transformed cells, and incubated at 37 °C overnight. Three colonies from each plate were then selected and used to inoculate 2 mL LB cultures (Carbenicillin 100 μ g/mL), which were placed in a shaking incubator at 37 °C overnight. To evaluate the expression, three 300 mL Erlenmeyer flasks containing TB Overnight Express™ media (50 mL) were inoculated with each culture (1 mL), and were incubated at 37 °C in a shaking incubator (200 rpm) overnight. A glycerol stock was prepared from each culture, and the remainder was centrifuged at 4,000 x g for 15 minutes, the supernatant was discarded, and the pellet was re-suspended in sodium dodecyl sulfate (SDS) lysis buffer and incubated at 95 °C for 10 minutes. The lysed solutions were analyzed by SDS-PAGE (polyacrylamide gel electrophoresis) (Bio-Rad Criterion™ XT 4-12%) to evaluate the expression, and the culture that appeared to have the highest expression was carried forward, repeating the above process to select for the highest expressing culture.

The optimum incubation time for expression was evaluated by growing a culture in TB Overnight Express™ media (50 mL) at 30 °C in a shaking incubator (200 rpm) where aliquots (1 mL) were taken at approximately 2-hour intervals, according to the manufacturer's directions (QIAGEN, Valencia, CA). A fresh LB plate was streaked and incubated at 37 °C overnight. An LB culture (2 mL) was inoculated with a single colony and incubated at 37 °C for 8 hours in a shaking incubator (200 rpm); whereupon additional LB (50 mL) was added, and incubation continued for 17 hours. Each of four baffled Erlenmeyer flasks containing TB Overnight Express™ media (500 mL) were inoculated with 2 mL of the aforementioned 50 mL culture, and incubated at 30 °C for 24 hours in a shaking incubator (200 rpm); which was determined to be the optimal expression protocol.

2.4 Expressed protein purification

The cultures expressing protein were centrifuged at 4,000 x g for 15 minutes, the supernatant discarded, and the pellet was re-suspended in buffer (20 mM sodium phosphate, 0.5 M NaCl, 20 mM imidazole, pH 7.4). This re-suspended pellet was then lysed using a microfluidizer, and the cell debris was removed by centrifugation (14,000 rpm) and filtration (22 μ m). The resulting solution was purified on an ÄKTAexpress fast protein liquid chromatography (FPLC) system (GE Healthcare Life Sciences) using a HisTrap HP 1 mL column and a gradient elution, where buffer A was 20 mM phosphate buffered saline (PBS) containing 20 mM imidazole and buffer B was 20 mM PBS containing 520 mM imidazole. Using the Experion™ Lab-On-Chip system, samples of the protein were analyzed under non-reducing conditions in order to determine molecular weight of the proteins, which represents the detection of degradation products as well as contaminants within the sample.

2.5 Optimizing *C. elegans* protein extraction

To select the method that produces the greatest quantity of proteins, two different methods of preparing *C. elegans* were evaluated. For both methods, starved worms were collected in M9 buffer and centrifuged (16,000 x g). Using the freeze-thaw method required the worm pellet to be re-suspended in 200 μ L of M9 buffer and alternately snap frozen in LN₂ and thawed at room temperature for 5 cycles. The lysed material was centrifuged (16,000 x g) for 5 minutes, the sample decanted to 25 μ L, and 10 μ L of 2X SDS gel loading buffer was added. The sample was then sonicated in a sonication bath (VWR® Scientific, Aquasonic 50HT) for 2 minutes and immediately incubated at 95 °C for 5 minutes. The sample was then analyzed by SDS-PAGE (Bio-Rad Criterion XT 4-12%) using standard procedures. Alternatively, using the immersion sonication method, the supernatant was discarded and the worm pellet was re-suspended in an isotonic HEPES solution (360 mM sucrose and 12 mM HEPES). The worms were then sonicated on ice at maximum power using four, 5-second pulses (Cole-Parmer® 4710 Series Ultrasonic Homogenizer). The lysed material was centrifuged (16,000 x g) for 5 minutes and the supernatant was analyzed by SDS-PAGE (Bio-Rad Criterion™ XT 4-12%) using standard procedures; which was determined to be the optimal extraction protocol.

2.6 *In vitro* toxin exposure

In order to determine if recombinant RIC-4B N-His from *C. elegans* is susceptible to cleavage by BotNT A or BotNT B, 64.6 μ M purified protein was incubated with 660 nM BotNT A or BotNT B diluted in the optimized³⁰ sample buffer (0.2 mg/mL BSA, 0.25 mM ZnCl₂, 5 mM DTT, 50 mM HEPES, pH 7.4) at 37 °C for 1 hour. Recombinant human SNAP-25 and synaptobrevin were used as positive cleavage controls for BotNT A or BotNT B. Using the Experion™ Lab-On-Chip system, samples of the protein were analyzed under non-reducing conditions in

order to determine the molecular weight of the proteins, which represents the detection of degradation products as well as contaminants within the sample.

In order to determine if recombinant SNB-1 C-His from *C. elegans* is susceptible to cleavage by BotNT A or BotNT B, 5 μ M purified protein was diluted in the optimized sample buffer and incubated with 3 nM and 0.3 nM of each toxin at 37 °C for 24 hours. Aliquots of each sample were combined with SDS-PAGE gel loading buffer, heated to 95 °C for 5 minutes, run on an 18% Criterion™ XGT SDS-PAGE gel (Bio-Rad), and electrophoretically transferred to a nitrocellulose filter for Western blotting using standard procedures. Blots were probed with Mouse anti-SNB-1 (Developmental Studies Hybridoma Bank at the University of Iowa) in 1X milk diluent blocking buffer (KPL, Gaithersburg, MD), washed and incubated with Goat anti-Mouse HRP (KPL). The blots were then developed using a GE Amersham Western Development Kit according to the manufacturer's instructions, and read on a Bio-Rad Gel Doc system.

2.7 *In vivo* toxin exposure

Synchronized *C. elegans* CZ333 worms were washed from their plates with water, collected and distributed into microcentrifuge tubes. The worms were then centrifuged at 1,300 x g for 1 minute, the majority of the liquid was removed, and 80 μ l of the remaining concentrated material was pipetted into a 96-well plate. After counting and diluting, roughly 20-40 worms were aliquoted and incubated with Trisialoganglioside GT_{1b} for 2 hours at room temperature. After incubation, the worms were washed with water to remove the gangliosides and exposed to BotNT complex A or B by adding 700 nM of each toxin complex to a well containing the synchronized *C. elegans* CZ333. Worms were exposed to the toxins at room temperature for 1 hour. Samples were then plated onto NGM plates containing 1 mM aldicarb and incubated at room temperature and assessed every 20 minutes for 1 hour. Determination of paralysis was based on probing the worms three times on the anterior and posterior ends and watching for movement. Sluggish, atypical, partial movement was also included as paralysis.

3 RESULTS

3.1 Purified expressed proteins

Both of the recombinant homologous *C. elegans* proteins, RIC-4B and SNB-1, were produced and purified for this study. Large quantities of each protein were produced and analyzed on an SDS-PAGE gel in order to determine the molecular weights of the proteins produced (Figure 4).

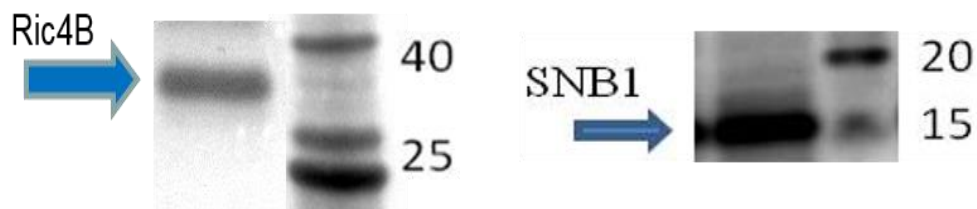


Figure 4. SDS-PAGE (4-12%) gel of FPLC (HisTrap, 1 mL column) purified RIC-4B N-His (left) and SNB-1 (right) C-His proteins. Numbers indicate molecular weights of control ladder proteins.

3.2 *In vitro* toxin exposure

Since the purified recombinant RIC-4B was a relatively pure protein, it was selected for determination of cleavage by BotNT A or BotNT B. Figure 5 depicts the molecular weights of the proteins in the presence or absence of toxin. If the protein was cleaved by the toxin, the molecular weight would decrease. There is no conclusive shift in the RIC-4B band, which indicates that cleavage of RIC-4B did not occur. However, there was also no conclusive shift in the control protein bands; therefore, either of the BotNT may not have had a high enough active concentration to cleave its targets.

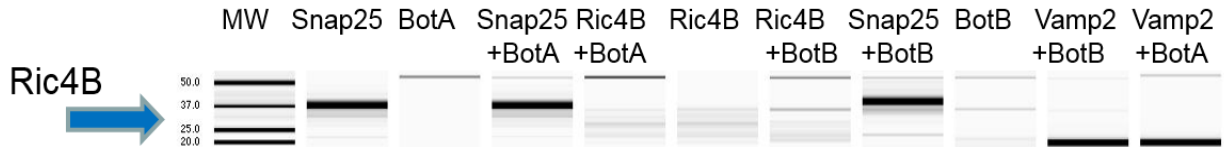


Figure 5. Western blot of RIC-4B exposed to BotNT A or BotNT B. MW contains the ladder. SNAP-25 and VAMP2 are control proteins for BotNT A and BotNT B, respectively.

There is a commercially available antibody that recognizes *C. elegans* SNB-1. This antibody was used in a Western blot to detect the molecular weight of the protein. There is no conclusive shift in the SNB-1 band, which indicates that cleavage did not occur (data not shown).

3.3 *In vivo* toxin exposure

Aldicarb is an inhibitor of acetylcholinesterase and induces hypercontracted paralysis in worms; therefore, exposed worms were placed on aldicarb plates to determine the effects of *C. elegans* exposure to BotNT. Observation of the worms after exposure indicated that there was little difference between the control worms and the exposed worms (Figure 6). All samples were checked 2 hours post exposure to confirm that there was not a delayed recovery aspect to the exposure. At 2 hours post exposure all worms were paralyzed and most likely dead.

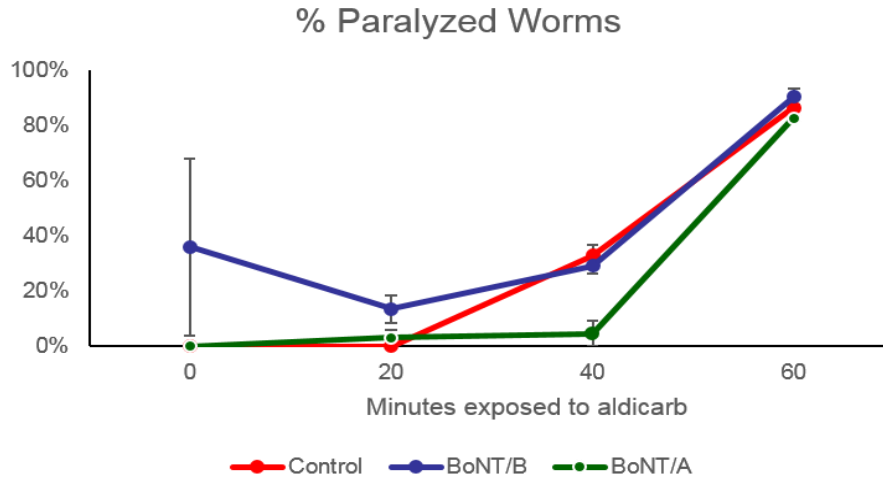


Figure 6. Scoring of *C. elegans* after 1-hour exposure to 700 nM BotNT complex A or B. Data points represent an average of three exposure experiments. Time 0 for one BotNT complex B sample was an anomalous situation whereby all of the worms were in a stunned state when removed from the well but recovered rapidly over the first 20 minutes.

4 CONCLUSION

There is a pressing need for the development of better therapies that can inhibit the toxicity of BotNT. There have been many studies showing the neutralizing effect of monoclonal,³¹⁻³⁴ recombinant oligoclonal,³⁵ and chimeric antibodies,³⁶ and the screening test most often regarded as the “gold standard” for testing BotNT activity is the mouse LD₅₀ method. However, as scientific research evolves, there is a push towards eliminating animals for lethal testing.⁹ Therefore, a more practical model for measuring BotNT toxicity must be chosen that adequately mimics toxin binding to a neuronal cell *in vivo*. This study was designed to determine the efficacy of using *C. elegans* as an *in vivo* model for studying BotNT exposure. Previous studies have shown that exposing the nematode *C. elegans* to various drugs produces electrophysiologically comparable results to vertebrate neurons.²¹ There are a number of human stress responses that have been conserved in *C. elegans*,²¹ and there have also been studies that indicate synaptobrevin (*snb-1*) is expressed in the *C. elegans* nervous system.²⁵ Furthermore, there is a large body of work supporting the measuring of SNAP-25 cleavage as an indicator of BotNT activity.³⁷⁻⁴¹ Although functional assays such as the

neurotransmitter release assay could also be used, SNAP-25 cleavage is the most time efficient and sensitive assay for inhibitor screenings.⁹ With the aim to utilize this cleavage, the present investigation was designed to determine if the homologous *C. elegans* proteins react similarly to SNAP-25 in the presence of BotNT. All of the experiments performed in conjunction with this project have produced inconclusive evidence. We were unable to verify BotNT cleaves the *C. elegans* proteins RIC-4B or SNB-1, and also unable to verify that BotNT toxicity produces a measurable effect on live worms. Further studies are underway to determine conclusively if *C. elegans* can be used to measure the toxic effect of BotNT exposure.

ACKNOWLEDGMENTS

The authors would like to acknowledge U.S. Army funding provided through the Edgewood Chemical Biological Center's In-House Laboratory Independent Research Program.

REFERENCES

- [1] Rotz, L.D. *et al.*, "Public health assessment of potential biological terrorism agents." *Emerging Infectious Diseases*, **2002**, 8(2), p225-230.
- [2] Arnon, S.S. *et al.*, "Botulinum toxin as a biological weapon: medical and public health management." *Journal of the American Medical Association*, **2001**, 285(8), p1059-1070.
- [3] Wein, L.M. and Liu, Y., "Analyzing a bioterror attack on the food supply: the case of botulinum toxin in milk." *Proceedings of the National Academy of Science*, **2005**, 102(28), p9984-9989.
- [4] Arimitsu, H., *et al.*, "Purification of fully activated Clostridium botulinum serotype B toxin for treatment of patients with dystonia." *Infection and Immunity*, **2003**, 71(3), p1599-1603.
- [5] Atassi, M.Z. *et al.*, "Molecular recognition of botulinum neurotoxin B heavy chain by human antibodies from cervical dystonia patients that develop immunoresistance to toxin treatment." *Molecular Immunology*, **2008**, 45(15), p3878-3888.
- [6] Brin, M.F., "Basic and clinical aspects of BOTOX." *Toxicon*, **2009**, 54(5), p676-682.
- [7] Arnon, S.S. *et al.*, "Human botulism immune globulin for the treatment of infant botulism." *New England Journal of Medicine*, **2006**, 354(5), p462-471.
- [8] Black, R.E. and Gunn, R.A., "Hypersensitivity reactions associated with botulinal antitoxin." *American Journal of Medicine*, **1980**, 69(4), p567-570.
- [9] Kiris, E. *et al.*, "Embryonic stem cell-derived motoneurons provide a highly sensitive cell culture model for botulinum neurotoxin studies, with implications for high-throughput drug discovery." *Stem Cell Research*, **2011**, 6(3), p195-205.
- [10] Lee, J.O. *et al.*, "M17 human neuroblastoma cell as a cell model for investigation of botulinum neurotoxin A activity and evaluation of BotNT/A specific antibody." *The Botulinum Journal*, **2008**, 1(1), p135-152.
- [11] Smith, T.J. *et al.*, "Analysis of the neurotoxin complex genes in Clostridium botulinum A1-A4 and B1 strains: BoNT/A3, /Ba4 and /B1 clusters are located within plasmids." *PLOS One*, **2007**, 2(12), e1271.
- [12] Baldwin, M.R. *et al.*, "Subunit vaccine against the seven serotypes of botulism." *Infection and Immunity*, **2008**, 76(3), p1314-1318.
- [13] Barr, J.R. *et al.*, "Botulinum neurotoxin detection and differentiation by mass spectrometry." *Emerging Infectious Diseases*, **2005**, 11(10), p1578-1583.
- [14] Evans, E.R.; Skipper, P.J.; and Shone, C.C., "An assay for botulinum toxin types A, B, and F that requires both functional binding and catalytic activities within the neurotoxin." *Journal of Applied Microbiology*, **2009**, 107(4), p1384-1391.

- [15] Montecucco, C. and Schiavo, G., "Mechanism of action of tetanus and botulinum neurotoxins." *Molecular Microbiology*, **1994**, 13(1), p1-8.
- [16] Baldwin, M.R. *et al.*, "Characterization of the antibody response to the receptor binding domain of botulinum neurotoxin serotypes A and E." *Infection and Immunity*, **2005**, 73(10), p6998-7005.
- [17] Adekar, S.P. *et al.*, "Neutralization of botulinum neurotoxin by a human monoclonal antibody specific for the catalytic light chain." *PLOS One*, **2008**, 3(8), e3023.
- [18] Schiavo, G. *et al.*, "Botulinum neurotoxins serotypes A and E cleave SNAP-25 at distinct COOH-terminal peptide bonds." *FEBS Letters*, **1993**, 335(1), p99-103.
- [19] Cheng, L.W. *et al.*, "Antibody protection against botulinum neurotoxin intoxication in mice." *Infection and Immunity*, **2009**, 77(10), p4305-4313.
- [20] Kalb, S.R. *et al.*, "Extraction and inhibition of enzymatic activity of botulinum neurotoxins/A1, /A2, and /A3 by a panel of monoclonal anti-BoNT/A antibodies." *PLOS One*, **2009**, 4(4), e5355.
- [21] Leung, M.C. *et al.*, "Caenorhabditis elegans: An emerging model in biomedical and environmental toxicology." *Toxicological Sciences*, **2008**, 106(1), p5-28.
- [22] Nass, R. and Hamza, I., "The nematode *C. elegans* as an animal model to explore toxicology in vivo: Solid and axenic growth culture conditions and compound exposure parameters." *Current Protocols in Toxicology*, **2007**, Chapter 1, Unit 1.9.
- [23] Kaletta, T. and Hengartner, M.O., "Finding function in novel targets: *C. elegans* as a model organism." *Nature Reviews Drug Discovery*, **2006**, 5(5), p387-398.
- [24] Saifee, O.; Wei, L.; and Nonet, M.L., "The *Caenorhabditis elegans* unc-64 locus encodes a syntaxin that interacts genetically with synaptobrevin." *Molecular Biology of the Cell*, **1998**, 9(6), p1235-1252.
- [25] Nonet, M.L. *et al.*, "Synaptic transmission deficits in *Caenorhabditis elegans* synaptobrevin mutants." *Journal of Neurosciences*, **1998**, 18(1), p70-80.
- [26] Mahoney, T.R.; Luo, S.; and Nonet, M.L., "Analysis of synaptic transmission in *Caenorhabditis elegans* using an aldicarb-sensitivity assay." *Nature Protocols*, **2006**, 1(4), p1772-1777.
- [27] Nguyen, M. *et al.*, "Caenorhabditis elegans mutants resistant to inhibitors of acetylcholinesterase." *Genetics*, **1995**, 140(2), p527-535.
- [28] Eisenmann, D.M., "WormBook." The *C. elegans* Research Community WormBook. **2005**; Available from: www.wormbook.org.
- [29] Sivashanmugam, A. *et al.*, "Practical protocols for production of very high yields of recombinant proteins using *Escherichia coli*." *Protein Science*, **2009**, 18(5), p936-948.
- [30] Mizanur, R.M.; R.G. Stafford; and S.A. Ahmed, "Cleavage of SNAP-25 and its shorter versions by the protease domain of serotype A botulinum neurotoxin." *PLOS One*, **2014**, 9(4), e95188.
- [31] Wang, H. *et al.*, "A new neutralizing antibody against botulinum neurotoxin B recognizes the protein receptor binding sites for synaptotagmins II." *Microbes and Infection*, **2010**, 12(12-13), p1012-1018.
- [32] Yang, G.H. *et al.*, "Isolation and characterization of a neutralizing antibody specific to internalization domain of *Clostridium botulinum* neurotoxin type B." *Toxicon*, **2004**, 44(1), p19-25.
- [33] Yu, R. *et al.*, "Neutralizing antibodies of botulinum neurotoxin serotype A screened from a fully synthetic human antibody phage display library." *Journal of Biomolecular Screening*, **2009**, 14(8), p991-998.
- [34] Zhao, H. *et al.*, "Characterization of the monoclonal antibody response to botulinum neurotoxin type A in the complexed and uncomplexed forms." *Japanese Journal of Infectious Diseases*, **2012**, 65(2), p138-145.
- [35] Nowakowski, A. *et al.*, "Potent neutralization of botulinum neurotoxin by recombinant oligoclonal antibody." *Proceedings of the National Academy of Sciences*, **2002**, 99(17), p11346-11350.
- [36] Prigent, J. *et al.*, "Production and characterisation of a neutralizing chimeric antibody against botulinum neurotoxin A." *PLOS One*, **2010**, 5(10), e13245.

- [37] Aplan, J.P.; Adler, M.; and Oyler, G.A. "Inhibition of neurotransmitter release by peptides that mimic the N-terminal domain of SNAP-25." *Journal of Protein Chemistry*, **2003**, 22(2), p147-153.
- [38] Aplan, J.P. *et al.*, "Peptides that mimic the carboxy-terminal domain of SNAP-25 block acetylcholine release at an Aplysia synapse." *Journal of Applied Toxicology*, **1999**, 19(Suppl 1), S23-S26.
- [39] Ferrer-Montiel, A.V. *et al.*, "The 26-mer peptide released from SNAP-25 cleavage by botulinum neurotoxin E inhibits vesicle docking." *FEBS Letters*, **1998**, 435(1), p84-88.
- [40] Binz, T. *et al.*, "Proteolysis of SNAP-25 by types E and A botulin neurotoxins." *Journal of Biological Chemistry*, **1994**, 269(3), p1617-1620.
- [41] Blasi, J. *et al.*, "Botulinum neurotoxin A selectively cleaves the synaptic protein SNAP-25." *Nature*, **1993**, 365(6442), p160-163.

Microbial wargaming: Modeling the contributions to fitness of bacteria encoding deployable genetic weaponry

Aleksandr Miklos^{a,b}, Matt Lux^a, Vanessa Funk^a, Steven Yee^{a,c}, Henry S. Gibbons^{a*}

^aU.S. Army Edgewood Chemical Biological Center, Research and Technology Directorate,
5183 Blackhawk Rd, Aberdeen Proving Ground, MD 21010

^bExcet, Inc., 8001 Braddock Rd, Suite 303, Springfield, VA 22151

^cDefense Threat Reduction Agency, 2800 Bush River Rd, Aberdeen Proving Ground, MD 21010

ABSTRACT

Recent advancement in synthetic biology tools has enabled the modeling of simple *in vitro* systems of complex community dynamics. In this study, we developed a simple *in vitro* model system for inter-community warfare using bacterial strains equipped with antibacterial colicin and/or phage weapons and test carriage, along with deployment of weapons affecting strain fitness in model ecosystems. These systems were developed and employed with a range of experimentally tunable frequencies in order to test defined hypotheses regarding the emergence of warfare in a simple and infinitely permutable model system.

Keywords: Colicin, competition, evolution, synthetic biology, niche maintenance, competitive exclusion

1 INTRODUCTION

This study proposed a novel approach to studying the emergence of warfare in large populations: a Petri plate-based wargaming system in which opposing bacterial communities were equipped with weapons existing in either a fully evolved state or in a cryptic, resting state awaiting development or deployment. Using this simple modeling system with defined and interchangeable genetic components, we aimed to quantify the contribution to fitness of bacterial communities of model weapon systems.

Recent research has revealed that bacteria, despite their relatively simple unicellular structure and small size, engage in a number of striking collective behaviors, including altruism, cooperation, restricted growth, and self-policing.¹⁻⁴ While bacterial communities can be observed to follow paths in which the whole community benefits from the actions of its individual parts, this is not always the case at the level of individual bacterial cells and bacteria have been observed to cheat,⁵⁻⁷ that is to exploit the activity of the community without contributing to a common good; pollute,⁷ and participate in other individual deviant behavior. Likewise, cooperative communities have been shown to evolve strategies to suppress cheater populations.⁸ Together, these represent both collective survival strategies combined with bet-hedging strategies on the level that, in spite of the divergent and antisocial behavior of a small minority, benefit the species by ensuring maximal likelihood of survival should growth conditions rapidly become unfavorable.

Bacterial communities employ both offensive weaponry and defensive measures to take and hold territory. Bacteria have been engaging in competitive behaviors for billions of years, and have evolved highly diversified strategies to achieve superiority within a niche relative to their interspecies and intraspecies rivals. These include strategies that are analogous to human wartime behaviors and include offensive, defensive, counteroffensive, intelligence, and counterintelligence strategies. Offensive strategies include the synthesis of antibacterial compounds (antibiotics, bacteriocins); defensive measures include modifications to cell walls and the acquisition of resistance cassettes or degradative enzymes; intelligence strategies include utilizing quorum-sensing signals from opposing communities to “read the enemy’s mail,” and so forth. The diversity of methods employed in the microbial world suggests that these simple organisms might serve as model systems for complex social human behaviors, most especially warfare (Table 1). Bacteriocins in particular have been shown to play roles in competitive exclusion (“taking and holding territory”) against invading strains.⁹

The signals driving communal behaviors are becoming better understood and are being employed as interchangeable tools for engineering complex social behaviors among microbial communities.¹⁰⁻¹¹ Communal behavior is driven by quorum-sensing mechanisms, which rely on secreted diffusible small molecules to monitor bacterial population

density. Offensive weapons are often driven by population density, proximity (antibiotics can themselves be considered quorum-sensing molecules), or contact with the enemy,⁹ while defensive measures can be either pre-emptive (regulated based on the ambient environmental conditions rather than a direct encounter), or triggered by encounter with an enemy's offensive weapons, or both.¹² The effector molecules and regulatory systems are well-characterized and can serve as model systems to study the deployment of tactical and strategic weaponry including weapons of mass destruction by individuals or states (Table 1). Interestingly, as with defense budgets for human societies, deployment of colicins and defensive measures incurs a significant energetic cost that must be carefully balanced with the evolutionary gains lest it become a fitness disadvantage.¹³

Table 1. Bacterial components as models for human weapons classes.

Class	Characteristics	Weapon	Model system	Costs to produce	Defense	Costs to defend
Strategic	Transmissible, mass casualty	Plague, smallpox	Cryptic lytic bacteriophage	Metabolic burden, host cell lysis	Target modification	Nutrient loss due to target function changes
Tactical	Non-contagious, diffusible	Anthrax, chemicals, artillery	Bacteriocins (e.g., colicins), antibiotics	Metabolic costs of production, efflux	Outer membrane modification; target modification; degradation; immunity	Decreased permeability to nutrients; efflux effort
Individual	Single-victim, contact	Ricin	Contact-dependent inhibition toxins ¹⁴		Target modification	Nutrient loss due to target function changes

We envisioned three distinct model scenarios in which bacterial communities might mimic nation-state weapons development or recapitulate the emergence of individual/small group terrorism. In this study, we focused on the tactical model system of colicin protein toxins, which offer an ideal platform for the development of simple *in vitro* competition systems for Gram-negative bacteria. Broadly, colicins belong to a wide family of bacteriocidal proteins that are produced and secreted by bacteria. Cidal activities of bacteriocins can either exhibit broad or narrow host ranges depending on the nature of the toxin and can even in some cases suppress the growth of competitive eukaryota. Specifically, colicins are secreted by Enterobacteriaceae, notably *Escherichia coli* for which they are named. Most wild-type isolates of *E. coli* and almost all pathogenic *E. coli* strains encode at least one colicin module, suggesting prominent roles for these genetic elements in establishing and maintaining the presence of a given strain within an ecological niche.

In general, colicins target a specific protein localized in the outer membrane which facilitates entry and uptake into the host cell by means of one or more ABC transporter. Colicins are generally internalized by this process and then exhibit a toxic behavior toward the target strain.¹⁵ Different colicins have different enzymatic or inhibitory functions, such as nuclease activity, the ability to depolarize membranes, or inhibition of peptidoglycan synthesis. Colicins are typically encoded as three-gene modules containing the colicin itself, an immunity protein, and a lysis protein. The immunity protein protects the host strain from the effects of the colicin while the lysis protein functions to break open expressing cells to discharge the colicin payload into the environment.

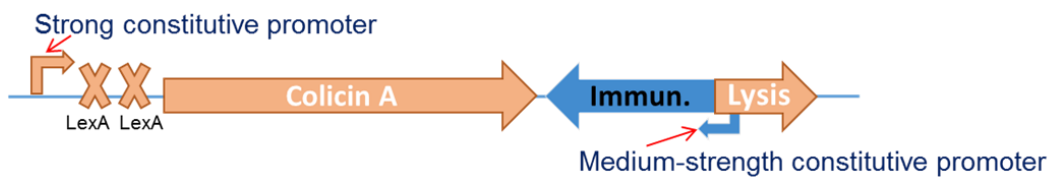


Figure 1. Colicin A locus showing Colicin A, immunity, and lysis protein genes with LexA repressor binding sites and promoters. The colicin itself is the toxic secreted product, the immunity protein protects the host population, while the lysis protein causes a subpopulation of the host strain to lyse, liberating the colicin proteins into the culture medium.

2 METHODS

2.1 Bacterial strains

E. coli W3110 (ATCC® 27325™), *E. coli* (ATCC® 14763™), *Pseudomonas aeruginosa* (ATCC® 25360™), and *P. aeruginosa* (ATCC® 25360™) were acquired from American Type Culture Collection (ATCC®; Manassas, VA). Colicin-producing *E. coli* strains BZB 1011, BZB 1030, BZB 1191, BZB 2101, BZB 2102, BZB 2103, BZB 2104, BZB 2125, BZB 2149, PAP 308, and PAP 702 (Table 2) were obtained from Institut Pasteur (Paris, France).

2.2 Strain fitness assay

Luria-Bertani (LB) broth (Sigma-Aldrich®; St. Louis, MO) and Tryptic Soy (TS) broth (EMD Chemicals, Inc.; Gibbstown, NJ) were prepared according to the manufacturer's instructions. Non-swarming agar plates were prepared using either 1.5% bacto-agar (Sigma-Aldrich®) in LB or TS broth. Swarming agar plates were prepared using 0.75% or 0.5% bacto agar, or 0.5% 'Eiken' agar (EIKEN CHEMICAL Co., Ltd.; Tokyo, Japan) in either LB or TS broth. Cultures were grown overnight from glycerol stocks in either LB or TS broth at 37 °C with shaking at 180 rpm on an Innova® 4200 Incubator Shaker (New Brunswick™ Scientific; Edison, NJ). Inocula were normalized to OD₆₀₀ < 0.1 using a SPECTRONIC® 21 Spectrophotometer (Milton Roy Co.; Ivyland, PA) and plated on (swarming or non-swarming) agar plates using a sterile toothpick in a 1-to-1 competition style of some combination of pyocin-susceptible or pyocin-producer *P. aeruginosa* and/or colicin-susceptible or colicin-producer *E. coli*. These competition-style plates were quartered with the upper quadrants reserved for controls and the bottom quadrants reserved for a single inocula susceptible or producer strain surrounded by three inoculums of susceptible or producer strains. Plates were incubated at 37 °C in a humidified Innova® 4200 for up to 21 days. Colony growth photographs were taken at various times using a Color QCount® automatic colony counter with ColorCount™ (Version 2.3) software (Spiral Biotech, Inc.; Norwood, MA). Alternatively, time-lapse images were collated from plates incubated at 37 °C in an Innova® 4330 incubator shaker (New Brunswick™ Scientific; Edison, NJ) and scanned hourly using an Epson Perfection V600 Photo Scanner (Seiko Epson®; Long Beach, CA) with Rap-ID Software (Specific Technologies; Mountain View, CA).

2.3 Colicin induction

Following normalization, inocula were heated in an Isotemp™ 215 water bath (Fisher Scientific™ International, Inc.; Hampton, NH) at 37 °C for up to 1 hour and then plated on swarming agar plates and incubated as above.

2.4 Synthetic green fluorescent protein (GFP)-reporter construct

A sequence based on the Colicin A operon (Figure 1) was designed in which the *sfGFP* gene replaced the *colA* gene and was placed under a tetracycline-inducible promoter was designed and synthesized (DNA2.0; Menlo Park, CA) in a low-copy expression vector. The plasmid was introduced into *E. coli* W3110 by standard transformation methods. Expression of sfGFP was monitored by fluorescence on agar plates (Figure 2).

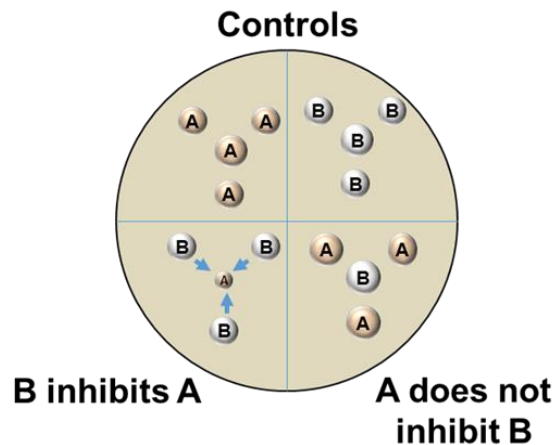


Figure 2. Two strains A and B are plated in arrangements to allow the comparison of colony size. Growth inhibition manifests as a decrease in size of the central colony in one or both of the lower quadrants relative to the same strain in the upper quadrants. The top quadrants represent controls to ensure that colony size difference of the middle colony are not due to auto-inhibition.

We began development of a simple *in vitro* competition assay using a number of colicin-expressing strains obtained from the Institut Pasteur (Table 2). These strains, initially described by Pugsley and co-workers¹⁶ express a variety of colicins and are resistant to a number of colicins produced by other strains within the collection, making these an ideal set of initial tester strains for the development of simple competition scenarios.

Table 2. Colicin-producing strains utilized in this study.

CIP idx	Strain	PRODUCES	RESISTS	Mechanism	Receptor	Translocation
105643	BZB2101	colA	colA	Pore Forming	BtuB	OmpF/TolQRAB
105642	BZB2102	colB	colB	Pore Forming	FepA	?/TonB, ExbBD
105641	BZB2103	colD	colD	tRNase	FepA	?/TonB, ExbBD
105640	BZB2104	colE1	colE1	Pore Forming	BtuB	OmpF/TolQRAB
105644	BZB2125	colE2	colE2	DNase	BtuB	OmpF/TolQRAB
105646	BZB2149	colE3	colE3	16s rRNase	BtuB	OmpF/TolQRAB
105664	BZB1011	--	--			
105637	BZB1191	--	--			
105665	BZB1030	--	(A),(E1),E2,E3			
105669	PAP308	--	A,E2-8 tol.			
105671	PAP702	--	--			

2.5 *In vitro* competition assay

The 0.5% agar plates were inoculated with spot cultures of each strain using a toothpick or inoculation loop such that a single colony of a “target” strain would be surrounded by three colonies of the producer strain.

3 RESULTS

In order to demonstrate that we could visualize colicin-mediated growth inhibition, we developed a simple growth assay on low-concentration agar plates that allow greater strain mobility on the plate surface. Colicin strains were plated in a spatial scheme noted in Figure 2 that was modified such that only two surrounding colonies were utilized instead of three. In this assay system, colicin-mediated growth inhibition manifests itself as the formation of smaller colonies at the centers of the triangular arrangements, or as distorted colony shapes in the colonies at the apices.

We demonstrated that we could observe growth inhibition at interfaces between colicin-producing and non-producing organisms (Figure 3). In this system, a tetracycline inducible promoter governs the expression of GFP in the non-producing strain, whereas the colicin immunity gene remains under the control of the colony growth of the non-producing strain (green or partially green colonies), is inhibited by the producing strain, and appears as if the colony itself were being driven away by the producing strain. In addition, the colonies of the non-producing strain were not consistently labeled with GFP, which should be produced consistently given the presence of the inducer (anhydrotetracycline) in the medium. However, non-producing strains consistently produced high levels of GFP expression when plated next to or in between colonies of strains expressing Colicin A (Figure 3). We believe this to represent preliminary evidence of colicin-mediated selection, as non-producing strains that harbor the immunity protein to Colicin A would be predicted to have a growth advantage in the presence of Colicin A secreted by the producing strains; this would not be the case against strains that produce other colicins (e.g., Colicin B). Non-producing colonies formed sectored colonies when plated next to producers of other colicins, indicating instability of the plasmid that would result either from metabolic burdens conferred by GFP expression or by the expression of the lysis protein from the Colicin A operon, which is retained in this expression construct.

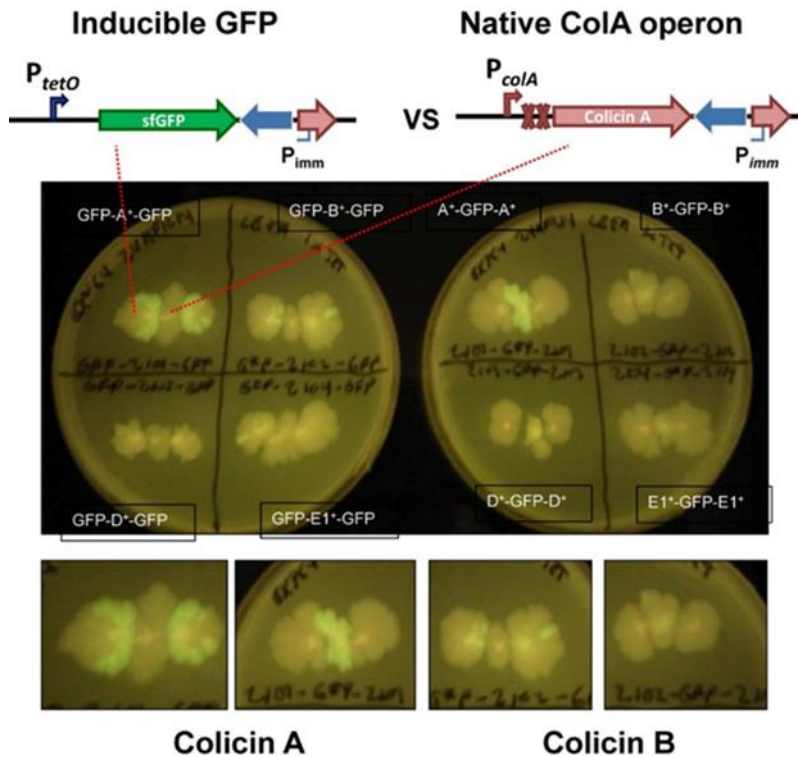


Figure 3. Forced maintenance of GFP reporter plasmid indicates colicin-mediated selection of strains expressing ColA immunity protein. Producer strains expressing native colicin operon and non-producer strains were inoculated between colonies of the other strain and were allowed to grow on Eiken agar for several days.

In order to obtain more quantitative readouts of the colony growth and to be able distinguish fluorescent from non-fluorescent colonies over time, we constructed an imaging system that synchronized the operation of a transilluminator with a camera outfitted with filters for assessment of GFP expression (Figure 4). In this system, a standard microbiological incubator was configured with a blue-light transilluminator, a camera, and appropriate emission filters to register the GFP fluorescence (Figure 4A). Bleaching of fluorescence due to constant illumination was avoided by synchronizing the transilluminator output with the camera, which was actuated on a timer switch (Figure 4B). The final configuration of the system is shown in Figure 4C.

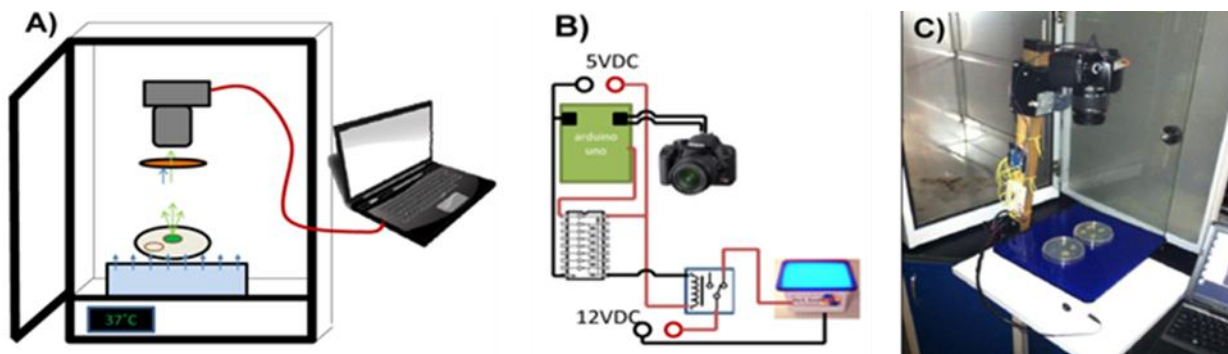


Figure 4. System configuration. A) Schematic showing a bacterial incubator configured with a transilluminator, fluorescence filter, camera, and computer controller for imaging of colonies. B) Process control of time-lapse imaging. When the camera is signaled (by the computer) to take a picture, the shutter-release signal is read by the Arduino microcontroller. Upon this signal, the Arduino microcontroller sets an output pin high (via a Darlington transistor bridge) to close a relay, switching on the lightbox. The microcontroller holds the pin high for 2 seconds after initial signal to ensure the light is on long enough for a full exposure, then the system resets (with the lightbox off) until the next photo is taken. C) Imaging system removed from the incubator compartment.

Using this imaging technique, we generated time-lapse images of growing colonies on plates and utilized this to show the fluorescence of non-producing strains grown in the presence of colicin-producing strains (Figure 5). As found in previous results, the non-producing strain maintained its fluorescence across the entire colony throughout the time-lapse series in the presence of a strains producing Colicin A, which indicated that the plasmid expressing the modified colicin operon was under selection. This makes sense given that the strain maintains the expression of the native immunity protein to Colicin A. This also provided unambiguous evidence of colicin-mediated antagonism in this system, and set the stage for the future work that would utilize synthetic colicin operons in isogenic strain backgrounds. We attempted to visualize the antagonism directly by utilizing a DNA-reactive fluorophore (SYBR® Safe stain, Invitrogen™) that was incorporated into the plates.

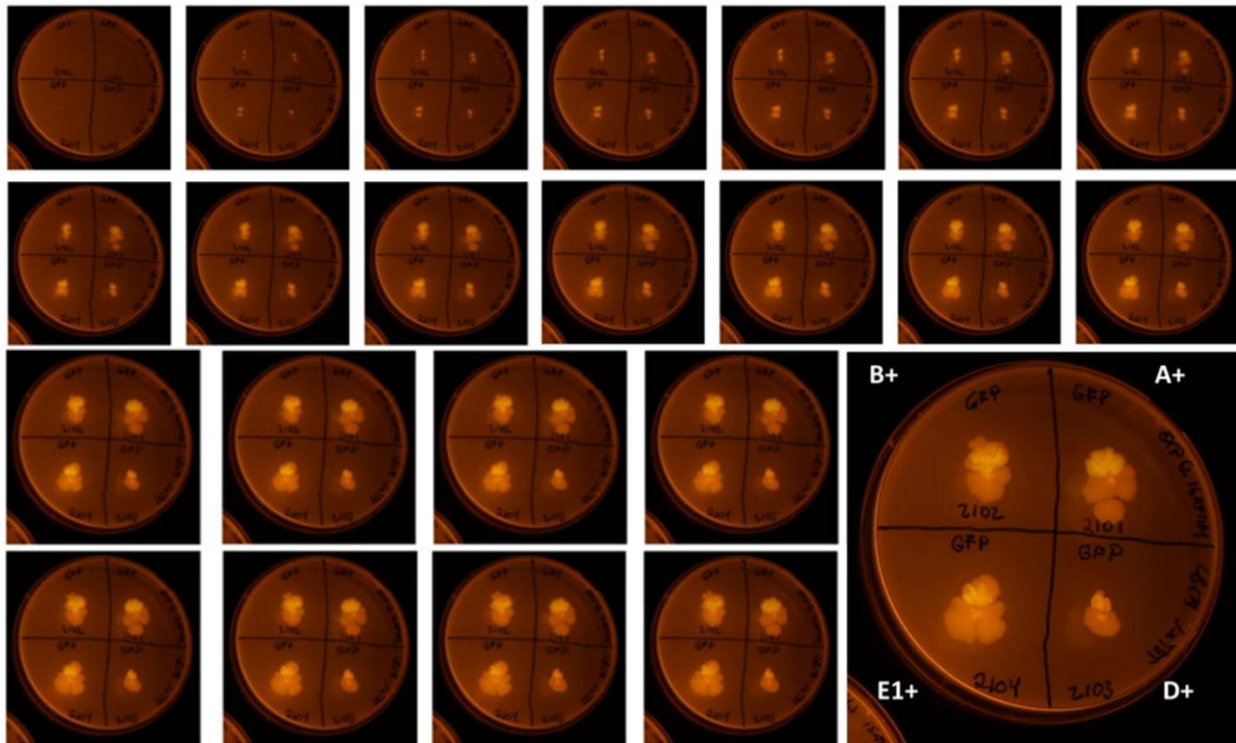


Figure 5. Time-lapse imagery of *E. coli* colony-level antagonism mediated by colicin expression. Strains expressing the indicated colicin protein that were competed against W3110 transformed with a plasmid expressing GFP. Plates were photographed every 30 minutes for time-lapse movies. Static images spaced 2.5 hours apart are shown here.

Our reasoning was that microbial death resulting from colicin-mediated lysis would manifest as zones of more intense fluorescence across the plates; however high backgrounds, presumably due to constitutive strain lysis even in the non-expressing strains prevented any interpretable data from emerging from these studies (not shown). To ensure that all strains were in similar vector backbones so that they can be placed into isogenic strain backgrounds to normalize for promoter strength, plasmid copy number, and host strain heterogeneity, (which would complicate any direct comparison of the competition assays), several of the Colicin A and Colicin E expression constructs we re-engineered into identical vector backbones (Figure 6).

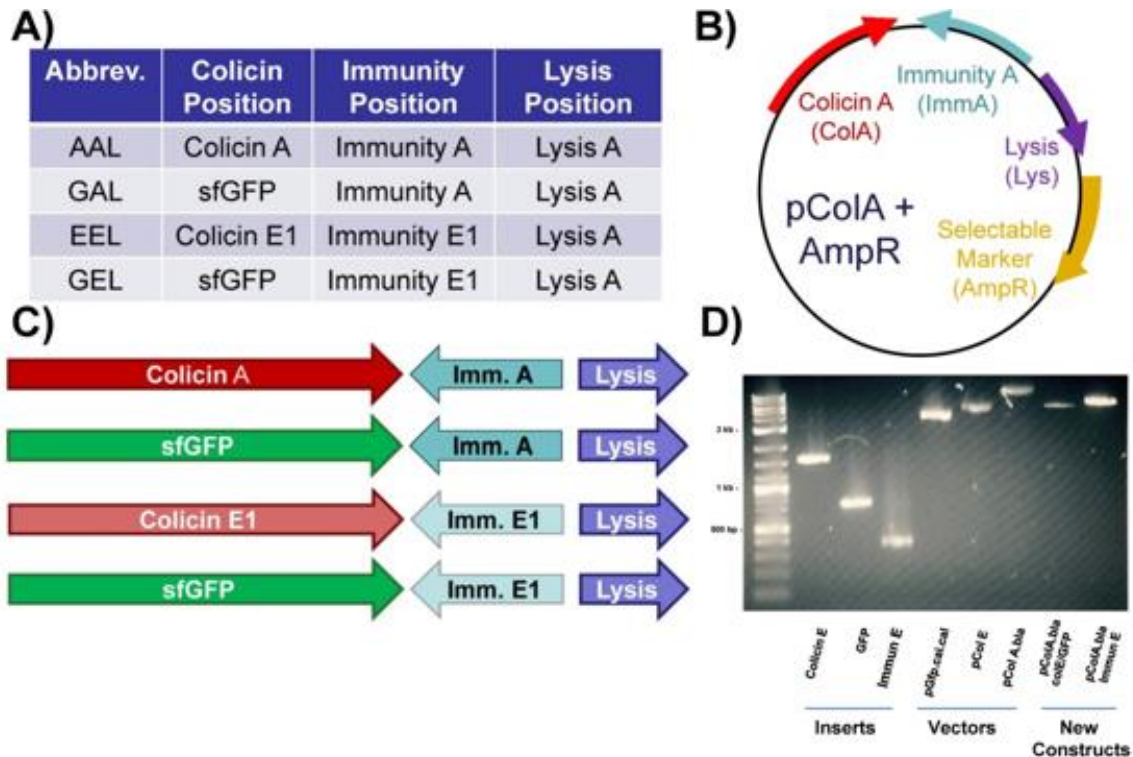


Figure 6. Redesign and isogenization of colicin expression constructs. All colicin expression constructs are being re-cloned into a single expression background with cognate immunity proteins but with identical lysis proteins to control for efficiency of host cell lysis, as well as for the efficiency of the immunity gene promoters, which reside within the lysis gene. A) Nomenclature table; B) plasmid schematic; C) organization of redesigned operons; and D) gel electrophoresis of new constructs showing integration of immunity and GFP genes into pColA (AmpR).

The final phase of this project consisted of re-engineered expression constructs being completed and cloned into isogenic (pColA) vector backbones. These expression constructs were 1) pColA/GFP/ImmA, 2) pColA/GFP/ImmE, and 3) pColA/ColE/ImmE. After the isogenic plasmid backbones were constructed, assays were performed to determine whether producing strains displaced the non-producing strain in a colony-competition assay. This would answer the hypothesis of whether the disappearance of GFP-producing strains in the colony competition assay in the absence of immunity protein is the result of invasion and/or displacement of the resulting strain by colicin-producing bacteria. Competition assays using swarming Eiken agar plates and broth cultures were performed, however, after several attempts to visualize competition amongst the expression constructs, no such competition was seen.

4 CONCLUSIONS

Unfortunately, despite numerous attempts to visualize the competition between bacteria on a plate, it has not been possible to reliably detect overt evidence of killing or competition in the assay system selected. It is possible that the medium selected did not promote sufficient motility to allow the competition to be visible, or that the constructs did not express the colicins as planned. Further verification of expression using quantitative real-time PCR (qRT-PCR) would be necessary to ascertain whether the colicin genes are transcribed in this assay system and if so, when. If the work is to be continued, colicin expression from these constructs should be verified. In addition, simple *in vitro* growths in liquid culture should establish the dynamics of inter-strain competition.

ACKNOWLEDGMENTS

The authors would like to acknowledge U.S. Army funding provided through the Edgewood Chemical Biological Center's In-House Laboratory Independent Research Program.

REFERENCES

- [1] Wintermute, E.H. and Silver, P.A., "Emergent cooperation in microbial metabolism." *Molecular Systems Biology*, **2010**, 6, p407.
- [2] Hosoda, K. et al., "Cooperative Adaptation to Establishment of a Synthetic Bacterial Mutualism." *PLOS One*, **2011**, 6(2), e17105.
- [3] Tan, C.; Marguet, P.; and You, L.C., "Emergent bistability by a growth-modulating positive feedback circuit." *Nature Chemical Biology*, **2009**, 5(11), p842-848.
- [4] Xavier, J.B., "Social interaction in synthetic and natural microbial communities." *Molecular Systems Biology*, **2011**, 7, p483.
- [5] Fiegna, F. and Velicer, G.J., "Competitive fates of bacterial social parasites: persistence and self-induced extinction of *Myxococcus xanthus* cheaters." *Proceedings of the Royal Society B: Biological Sciences*, **2003**, 270(1523), p1527-1534.
- [6] Sandoz, K.M.; Mitzimberg, S.M.; and Schuster, M., "Social cheating in *Pseudomonas aeruginosa* quorum sensing." *Proceedings of the National Academy of Sciences*, **2007**, 104(40), p15876-15881.
- [7] Maharjan, R.P.; Seeto, S.; and Ferenci, T., "Divergence and redundancy of transport and metabolic rate-yield strategies in a single *Escherichia coli* population." *Journal of Bacteriology*, 2007, 189(6), p2350-1358.
- [8] Manhes, P. and Velicer, G.J., "Experimental evolution of selfish policing in social bacteria." *Proceedings of the National Academy of Sciences*, **2011**, 108(20), p8357-8362.
- [9] Majeed, H. et al., "Competitive interactions in *Escherichia coli* populations: the role of bacteriocins." *The ISME Journal*, **2011**, 5(1), p71-81.
- [10] Li, C.H.; Wang, E.; and Wang, J., "Potential Landscape and Probabilistic Flux of a Predator Prey Network." *PLOS One*, **2011**, 6(3), e17888.
- [11] Prindle, A. et al., "A sensing array of radically coupled genetic 'biopixels'." *Nature*, **2012**, 481(7379), p39-44.
- [12] Prost, L.R. and Miller, S.I., "The *Salmonellae* PhoQ sensor: Mechanisms of detection of phagosomal signals." *Cellular Microbiology*, **2008**, 10(3), p576-582.
- [13] Chao, L. and Levin, B.R., "Structured habitats and the evolution of anticompetitor toxins in bacteria." *Proceedings of the National Academy of Sciences*, **1981**, 78(10), p6324-6328.
- [14] Aoki, S.K. et al., "Contact-dependent inhibition of growth in *Escherichia coli*." *Science*, **2005**, 309(5738), p1245-1248.
- [15] Cascales, E. et al., "Colicin biology." *Microbiology and Molecular Biology Reviews*, **2007**, 71(1), p158-229.
- [16] Pugsley, A.P., "*Escherichia coli* K12 strains for use in the identification and characterization of colicins." *Journal of General Microbiology*, **1985**, 131(2), p369-376.

Experimental and theoretical investigation of liquid droplet break-up induced by supersonic shock waves

Jerry Cabalo^{a*}, Daniel Weber^a, Daniel Wise^a, Clayton Moury^a, Alejandro Queiruga^b,
Tarek Zohdi^b

^aU.S. Army Edgewood Chemical Biological Center, Research and Technology Directorate,
5183 Blackhawk Rd, Aberdeen Proving Ground, MD 21010

^bDepartment of Mechanical Engineering, University of California, 6117 Etchevery Hall,
MC 1760, Berkeley, CA 94720

ABSTRACT

The aerosolization of liquid or solid particles by explosives or shock waves is a process of great importance to the study of break-up of liquid fuels for propulsion, as well as in chemical and biological defense. To reduce the complexity of the problem to a manageable level, we focus on the interaction of shock waves and liquid particles. We use a dual experimental and theoretical approach to understand the break-up process. Particle image velocimetry (PIV) is used to image the side scatter signal from liquid particles after the passage of a shock wave. Using our apparatus, we have recorded images showing both agglomeration with very high concentrations of liquid particles, and fragmentation of particles. Histograms of the distribution particle intensities show a shift due to fragmentation. Particle modeling shows that drag and initial spacing of particles are critical to shock induced agglomeration.

Keywords: Shock wave, surface tension, aerosol particles, fragmentation, PIV

1 INTRODUCTION

1.1 Objective

A basic understanding of the explosive dissemination of particles is of immense relevance to the Army's mission. The physical processes involved relate to chemical-biological defense as well as dissemination of obscurants. For chemical and biological defense, a key task is to predict the extent of threats, that is, how much active threat material is delivered, how far it goes, and the length of time the material remains a threat. The key to predicting the behavior of chemical or biological weapons clouds from explosive dissemination is knowing the resulting particle size distribution. The capability to predict particle size distribution as a function of agent physical and chemical properties is essential to predicting how far a chemical (or biological) travels and how extensive the contamination zone is. Properties of agents themselves, or additives (potentially both solid and liquid) to the agent, or chemical breakdown products influence the particle size distribution. Biological and chemical agent cloud neutralization has also been considered using high explosive-induced shock waves, or by explosively disseminated particles capable of catalytic degradation of agent.

The explosive dissemination of particles, however, is a complex, multiscale problem. First, there is the heat and pressure resulting from detonation of the high explosive. Then, there is the interaction of the heat and pressure on the liquid or packed particle payload. This interaction is truly multi-scale, including the resulting micrometer sized aerosol particles or packed particles in the payload of a device. There are a number of significant technical barriers to addressing all these issues simultaneously, and so we simplify the problem to make it experimentally and theoretical feasible.

We focus on the phenomenon of shock waves interacting with aerosol particles and we neglect the break-up of bulk material in the early stages of a dissemination event. This allows us to consider the effects of pressure and heat separately. This approach is reasonable because shock waves communicate pressure at speeds many times greater than sound, and can push aerosol particles far ahead of the heat and rapid chemistry of the detonation fireball. Another advantage to this approach is that we can reduce the system study to a one dimensional problem. We expect that a basic understanding of how shock waves interact with aerosol particles not only can impact the understanding of how explosives aerosolize condensed materials, but also has broader applicability. It should be noted that the interaction

of shock waves and condensed phase particles is also relevant to the semiconductor manufacturing industry, where laser induced shock waves are under consideration for removal of particulate contaminants from substrates.¹ In addition, shock wave impaction has been used in the creation of nano-composites.² As a result, we contend that the interaction of shock waves and particulates is worthy of study.

The interaction of condensed matter with shock waves is a physically interesting phenomenon. Shock waves involve an abrupt change in pressure resulting in rapid heating of up to ~1,000 kelvin (K), and have been used for decades as a means of studying fast gas phase chemistry. Even more interestingly, the temperature behind a shock must be described as a tensor because the distribution of gas molecule velocities along the direction of shock propagation and the directions perpendicular are different.³ As a result, we expect shock wave heating to be unevenly distributed over an object as a shock wave passes. For condensed phase particles suspended as an aerosol, this could mean uneven heating. The surface energy, or surface tension in the case of liquids, of the condensed phase has a significant temperature dependence. As a result, we expect shock induced temperature gradients on the particles to control atomization of larger particles to smaller ones. For shock waves interacting with condensed matter particles, we hypothesize that non-isotropic gas dynamic heating controls the break up process through non-uniform surface energy on the particles, and ultimately, the final size distribution of the aerosol.

1.2 Background

The focus of our study is greatly different from previous work. The bulk of the state of the knowledge in the field centers on the break-up of liquid and solid materials in the lower energy regime encountered with liquid atomization by sprays and powder dissemination.⁴ However, a number of studies have been reported for shock waves interacting with particulates. Theofanous et al.⁵⁻⁷ have performed studies that combine highly detailed imagery of millimeter sized droplets interacting with shock waves, and two-phase fluid dynamics simulations. Much of this type of work is highly relevant to the atomization of fuels and combustion. Yet these studies do not include small particles or microturbulence. Due to our interest in chemical and biological agents, it may be necessary to expand studies to droplet sizes in the human respirable range. Gates et al.⁸⁻¹⁰ demonstrated a loss of viability for *Bacillus atropheus* (BG) spores exposed to shock wave heating, but they did not study the mechanism of spore inactivation in detail. Furthermore, because the BG particles consisted of heterogeneous material, it is quite difficult to relate experimental results to particular phenomena. Yann et al.¹¹ investigated the dispersion of solid particles by high explosives comparing particle morphology before and after dispersion. Kudryashova reported¹² an explosive aerosol disperser that favored cavitation in the liquid feed. Even a number of experimental studies reporting interaction of particles with shock waves have been reported.¹³ These studies focused on the effect of particles on the shock wave itself, but not the effect of shock waves on the particles. However, we intend to study the shock induced break-up of aerosol particles as a function of surface tension and gas dynamic heating.

To test the hypothesis, a combined theoretical and experimental approach was applied to understanding the fundamental problem of shock wave-induced break up of materials. For experimental measurements of shock wave-particle interaction, a standard shock tube was used, with optical access ports to monitor particle change with laser light scattering. A shock tube presents a number of advantages: 1) simple symmetry allows reduction of the experiment and model to one dimension, 2) precise control of the shock wave amplitude, 3) ability to use an inert suspension gas to exclude the added complexity of chemical change, 4) optical access for laser light scattering measurements, and 5) the ability to fill the tube with monodisperse aerosol. While an electrodynamic trap coupled with optical microscopy could theoretically give detailed data on drop morphology changes, we considered that configuration incompatible with shock waves.

Modeling is an important component for this study because it is not possible to image the particles in our size range of interest in the same direct way as Theofanous et al.⁵⁻⁷ Instead, we experimentally measure the size of aerosols in the shock tube before and after a shock wave. These serve as validation points for the model. The validated model in turn gives the detailed information on what is happening to the particles on a microscopic scale. For modeling of the interaction of the condensed phase drop, we intend to utilize discrete element-based computation, which has emerged in multiple fields, and is ideal for the simulation of particle-based systems. They are advantageous in dealing with domains that break apart, as compared to traditional continuum based finite difference and finite element methods which have severe limitations. Discrete element-based computations are faithful to underlying physics through the imposition of conserved quantities (such as mass momentum, etc.). Surface energy (surface tension) can be modeled as the cohesive potential between the discrete elements in the simulation. The shock wave can be simulated using a standard finite element model interacting with the discrete element model of the drop, with the non-isotropic

temperature accounted for in the finite element model. The models will be validated against the degree of particle fragmentation observed as a function of properties of the shock wave, as well as any observed particle deformation.

2 EXPERIMENTAL PROCEDURE

2.1 Overview

This study employs both experimental and theoretical approaches to the understanding of the interaction of shock waves and liquid aerosol droplets in the respirable size range. For experimental measurements, a shock tube is used in conjunction with a particle image velocimetry (PIV) device. The PIV enables us to optically record the positions and side-scatter intensity of particles that we have pumped into the shock tube before and after exposure to a shock wave. The image data enables us to observe changes that a shock wave imposes on the aerosol. Discrete particle modeling, described above, is validated with the before and after shock wave data. The entire validated simulation allows us to make conclusions about the continuous phase fluid interacting with the discrete particle models of the aerosols.

2.2 The shock tube and aerosol generation

We based the shock tube design on that reported by Wagner et al.^{14,15} The shock tube cross section is a 3-inch x 3-inch square with a wall thickness of 0.5 inches. The tube consists of modular sections, with each section having a square flange sealed with a gasket on each end. Figure 1 shows the side view of the shock tube, including the location of the pressure transducers. The third pressure transducer port is collocated with the PIV camera window, 0.25 m upstream of that location is the second transducer location. The first transducer is 1.59 m upstream of the second transducer and initiates all measurements and timing electronics. For measurements with the PIV, we had to remove the third transducer and replace it with a black-painted blank because the transducer was highly reflective of stray laser light. We utilized piezo-electric differential pressure transducers (model 113B; PCB Piezotronics, Inc.; Depew, NY) with a sensitivity of 10 mV/psig to detect the passage of the shock front. A model 483C05 signal conditioner (PCB Piezotronics, Inc.) powers the sensors and performs current-to-voltage conversion. The output is directed to a TDS5104B digital oscilloscope (Tektronix®; Beaverton, OR) for recording. The shock speed is measured using the time difference between signals and the known distance between the pressure transducers.

Burst disks are used to generate the shock waves. The burst disks are cut from disposable aluminum baking pans. The high pressure plenum was attached to the shock tube via a flange fitted to the shock tube and 2-inch PVC pipe. A 2-inch PVC union is used to hold the burst disk in place. A high pressure reservoir of 3.7 L volume is formed from a 6-foot length of PVC schedule 40 pipe, terminated with a connection to a high pressure cylinder. The PVC section is rated to 250 psig, while the aluminum portion has been tested up to 500 psig, and should be capable of withstanding 1,000 psig. The pressure in the reservoir is ramped up until the burst disk fails, resulting in the generation of a shock wave. The thickness of the aluminum was chosen to fail at 150 psig. The original design of this experiment utilized an air gun to generate shock waves to reduce cost and simplify the experimental procedure. However, the piston in the air gun moved too slowly to generate shocks, and this approach had to be abandoned.

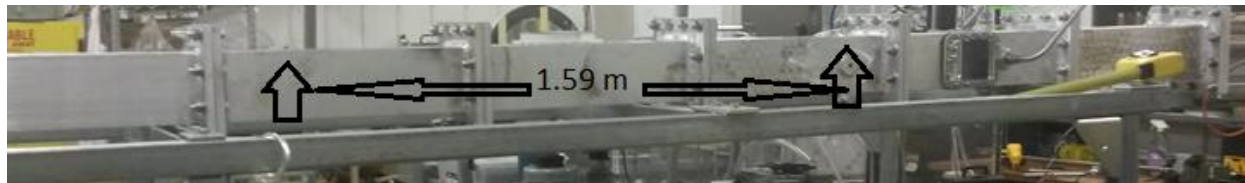


Figure 1. Side view of the shock tube. Locations of pressure transducers are shown.

Figure 2 shows the side view of the experimental section of the shock tube, including the windows, and optics for the PIV system. Two 5-inch x 3-inch windows made of plexiglass allow the entrance and exit of the PIV laser sheet. These are designed to match the 1,000 psig pressure limit of the metal tube, and so are made to be 3/4-inch thick, mounted in the sides of the tube. A 2-inch diameter, 3/8-inch thick quartz window mounted on the top of the tube serves as the viewport for the PIV camera. A black anodized tube between the window and the PIV camera reduces stray light from the room.

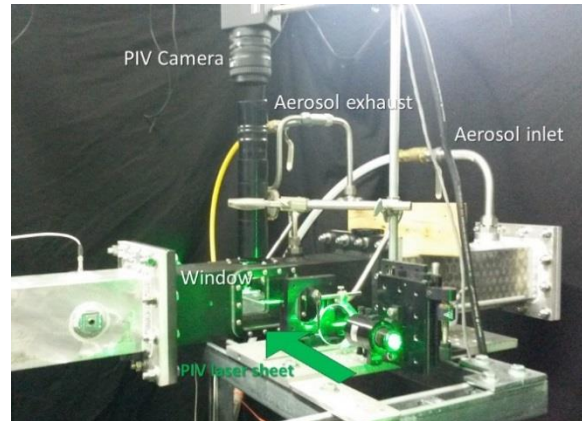


Figure 2. View of shock the tube experimental section with PIV camera and optics.

A 3/4-inch diameter tube introduces aerosols into the back end of the shock tube. In order to reduce contamination of the shock tube windows by the aerosol material, the exhaust ports are placed near the windows as shown in Figure 2. This forms a “dead” zone by the windows where aerosols become temporarily trapped. To isolate the exhaust pump and aerosol source from the pressure jump of the shock wave, ball valves are placed inline. A number of methods are used to generate aerosols. For large number concentrations, a paint sprayer is used. For controlled, monodisperse aerosols, an ultrasonic sprayer (Sono-Tek Corp.; Milton, NY) is used. This device uses a piezoelectric actuator driven with radio frequency white noise to ensure uniform breakup of the liquid feed. Particle size is controlled by changing the relative concentrations of a low vapor pressure liquid, such as Oleic acid, and a high pressure solvent, such as isopropyl alcohol. The aerosols are introduced into a 1 m³ plexiglass drying chamber with a mixing fan. Aerosols are drawn from the drying chamber into the shock tube. For the initial tests performed, the mass mean diameter of the aerosol was set to 7 μm.

2.3 PIV imaging

For imaging of the particles in the shock tube before and after passage of the shock wave, a two-dimensional PIV (TSI® Inc.; Shoreview, MN) is used. This consists of a Gemini dual Nd:YAG laser system (New Wave Research; Bozeman, MT) capable of producing two overlapping laser shots with user-set delays between. The laser shots provide intense and precisely timed illumination for a specialized digital camera. To illuminate a planar region of flow corresponding to the focal plane of the PIV camera, the laser is focused to a sheet with a 250 mm diverging concave cylindrical lens, and then focused to a thin sheet with a 200 mm lens. The camera is capable of recording two distinct frames from both laser shots. Under normal operating conditions, a fluid flow is seeded with particles, and the difference between particle positions viewed in the two picture frames determine the local flow field. For these experiments, the camera frames are intended to compare the side scatter of particles before and after the passage of a shock wave. For the burst disk materials selected, we get good consistency in burst pressure, and thus a consistent shock wave speed. We use the pressure transducer signal to fire the PIV at the right time to capture the effect of shocks on particles. The shock speed is measured from a burst disk given disk thickness, and is used to set a fixed delay. The first transducer signal is then fed to an amplifier so that it is always detectable by the digital delay generator. The delay generator sends a Transistor-Transistor Logic (TTL) pulse to the PIV Synchronizer to fire the laser flashlamps, Q-switches, and PIV camera.

To measure the changes that the shock wave passage induces on the particles, we measure the number of particles and their side-scatter intensity in the images. For a given laser sheet intensity and camera sensitivity, we record background images and subtract these from images containing particles. This post processing is necessary because we are unable to completely eliminate stray scattered light from the PIV laser. The images are loaded into MATLAB® (MathWorks®; Natick, MA) and then processed further. The peak finding routine calculates the x and y components of the derivatives in signal intensity at each pixel location in the image. Since numerical derivation is performed, the derivative of a given Cartesian component is calculated approaching the pixel from the plus and minus directions. An inflection point, or maximum due to the present of a particle, is held to occur when for when both x and y components, the values for the plus and minus directions, change numerical sign. To account for numerical noise, a threshold in intensity change per pixel is imposed. To limit the influence of stray light further, a region of interest is imposed to limit contributions from noise. The coordinates of each particle in the image is recorded, and the signals are integrated

for intensity for a fixed number of pixels (a total of 9 pixels), with the most intense reading at the middle of a 3 x 3 pixel square.

2.4 Schlieren imaging

Schlieren interferometric photography is used to verify the form of the shock wave. To generate the schlieren images, a bright white (100 W incandescent) light source is focused onto a slit and passed to a 12-inch diameter collimating mirror. The light beam passes through the experimental section of the shock tube through a second slit, and then onto a 12-inch focusing mirror and lens that condenses the image of the experimental section onto the active area of a high speed 8,000 frame/second camera.

2.5 Raman thermal measurements

Although the transient temperature in the shock wave can be calculated from the speed, we intended to experimentally measure the molecular rotational temperature of N_2 and O_2 from their rovibrational Raman. Using a focused 6 W continuous wave (CW) Nd:YAG laser, we were able to measure the N_2 and O_2 rovibrational peaks using an Ocean Optics USB2000 fiber optic spectrometer. A 1-inch diameter, 20 mm focal length lens was used to condense the Raman scattering into the F#5 spectrometer. Because the slit in the USB2000 was cemented into place, we could not improve the resolution, which was unsatisfactory. We then used the same condenser optics to focus scattering onto the slit of an Oriel® Instruments 77250 1/8 m Monochromator, with a charge-coupled device (CCD) camera as a detector. The camera exposure time was operated at minimum and synchronized with the pulsed laser. To maximize signal, the laser was focused to a spot rather than a sheet.

2.6 Computational modeling using discrete particles

Although the ground work has been laid for modeling the fragmentation of particles due to shock wave interaction, these approaches are not reported until more experimental data is available to validate results. To date, modeling has focused on the forced interaction of particles induced by the shock wave. To that end, very simple equations of motion were used to investigate the conditions leading to coagulation. A simple system was considered, with two particles at rest, and hit with a shock wave along the axis defined by the distance between the two. Only Stokes' drag forces and weak attraction between particles, initial separation between particles, and shock speed were considered.

3 RESULTS AND DISCUSSION

3.1 Shockwave measurement and characterization

To date, our current shock tube design and configuration have successfully demonstrated supersonic shock waves of up to Mach 1.37. A rupture of given burst disks occurs at 130 psig, resulting in the pressure transducer readings in Figure 3.

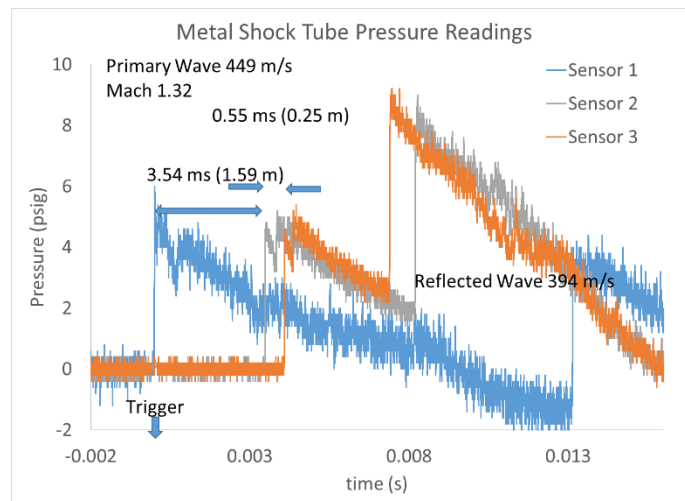


Figure 3. Oscilloscope readings of transducer output during the passage of a shock wave.

There are a number of features in Figure 3 that show the characteristic of a shock wave. First, there is an abrupt change in pressure that is essentially the definition of a shock wave. In addition, the pressure transducers show responses sequentially depending on their location from the burst disk. The timing of the arrival of the shock front at each transducer corresponds to 449 m/s, which is faster than sound. Because of the end plate on the shock tube, there is a reflected wave, and the transducers then respond in a reverse sequence. As expected, the reflected wave has lost energy and has a reduced velocity of 394 m/s. In the previous configuration using the air gun, although up to 500 psig backing pressures were used in the gun, no abrupt change in pressure was observed. In fact, the pressure of all three transducers rose pretty much simultaneously over 10 milliseconds before reaching equilibrium. In contrast, Figure 3 shows passage of both the primary and reflected shock fronts occurring within that timeframe. Schlieren images of the shock wave serve as additional evidence for a planar, supersonic shock wave. Figure 4 shows still frames from the high speed video of the passage of the shock wave. The shock wave is planar and travels faster than sound. The images correspond to the passage of abrupt pressure jumps recorded at the third transducer. Thus, we demonstrate the capability to generate shocks.

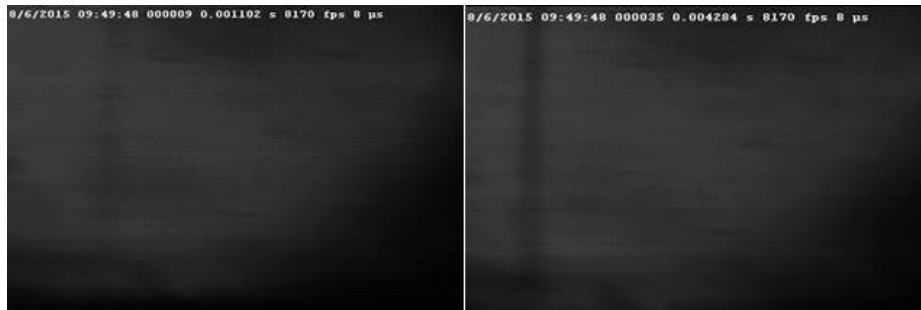


Figure 4. Schlieren images of the primary and reflected shock waves. The shock front appears as a vertical line in the image. The acquisition of high speed camera frames was triggered by the first pressure transducer, and the images appear at the correct frame where we would expect the supersonic shock wave.

In addition to speed and schlieren measurements, we attempted to perform direct Raman measurements of rotational temperature using the rotational lines superimposed on the vibrational lines for O₂ and N₂. For the configuration attempted, we could not get measurable signal without tightly focusing the CW laser beam. When we transitioned to the pulsed laser that had the same average power as the CW laser, where we would have expected the same number of Raman photons, we detected primarily laser induced breakdown emission from air. We expect that we need faster optics for the monochromator and an improved detector to successfully perform these measurements, so that more signal is collected, and the excitation laser can be defocused until no breakdown occurs.

3.2 PIV Imaging

Data from the PIV suggests shock wave induced change has occurred. Several tests using a paint sprayer were used for the purpose of range finding due to the ease of viewing change to the resulting large numbers of particles.

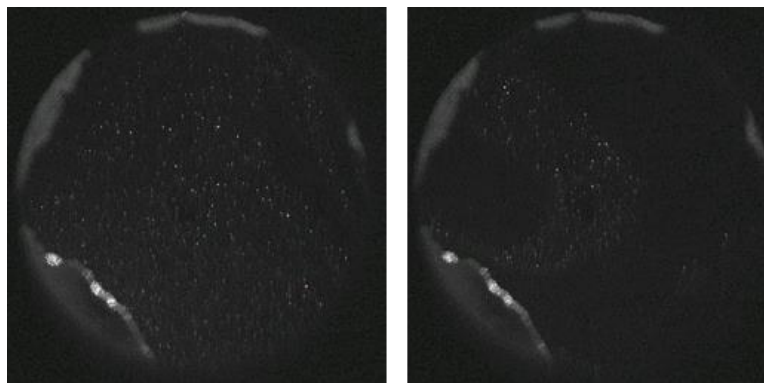


Figure 5. PIV images of 5 μm polystyrene latex (PSL) beads before (left) and after (right) passage of a shock wave.

From the first test, Figure 5 compares the image recorded from 5 μm PSL beads before and after passage of a shock. For the solid PSL beads, there is no observable change in the intensity of the individual particles post-shock. There appear to be particle rarified regions in the image; a number of possibilities exist to explain these images. We may not have permitted the particles sufficient time to diffuse down the shock tube. The result is that if there is poor mixing between particle-rich and particle-poor regions, the shock may push a poorly mixed volume of air into the viewable region. The fact that the side scatter intensities in the image don't change much suggest the particles have remained unchanged themselves, and the effect of the shock wave was just to move them.

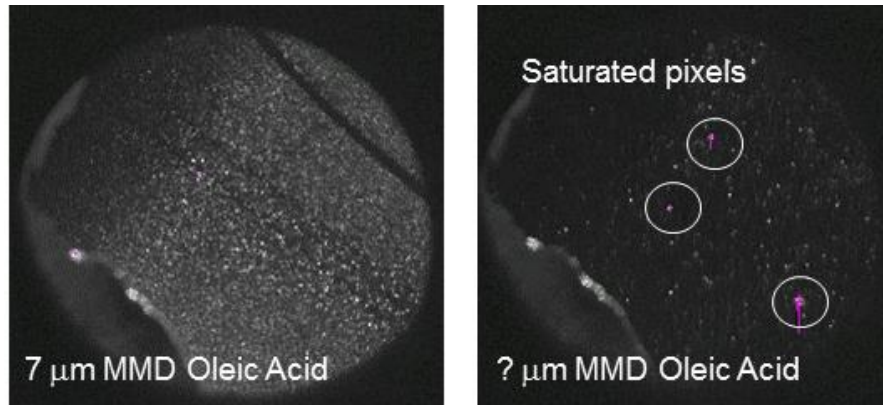


Figure 6. PIV images of oleic acid aerosols before (left) and after (right) the passage of a shock wave. After the passage of the shock, more intense side scatter intensities from the particles are observed, suggesting agglomeration and formation of larger droplets.

A second test was performed using liquid oleic acid particles. Oleic acid has the consistency of a light oil, and was aerosolized with the same paint sprayer as the 5 μm PSL beads. Very large concentrations on the order of 10^5 particles/L were obtained, resulting in the dense particle image in Figure 6. Following the passage of the shock, significantly fewer particles are visible. However, individual particle intensities appear much more intense in the right hand image in Figure 6. We reason that although it is possible the shock moved particles, it could not create more intense side scatter without creating larger particles. When a particle size calibration has been performed, it should be possible to convert side scatter intensity in the image to particle size. Given the known density of the aerosol material, the number and size can be converted to mass, and a mass balance can be compared in both images.

The discrete particle modeling (not yet validated) shows some suggestive trends that could explain what is happening in the image. As described above, the simulation looked at the contact between two particles some distance apart, with the shock wave approaching along the axis defined by the distance between the particles. At particle diameters greater than some critical size (0.025 microns in the model), the shock front fails to accelerate the first particle before it picks up the second close particle and both are moved at the same velocity. For particles less than the critical size, the shock wave can pick up the first particle before it accelerates the second particle, and bring both particles into contact; for liquid particles, this results in agglomeration. Based on these trends, we expect agglomeration to be heavily dependent on the initial concentration of particles, as well as the shock intensity.

For smaller number concentrations, the spacing between particles is greater, and there must be enough drag on particles so that the shock wave accelerates particles into other particles. For the right conditions, we expect the shock wave to fragment particles. The left image in Figure 7 shows 7 μm oleic acid particles generated with a Sono-Tek sprayer. After the passage of the shock wave, a greater number of particles are visible. To measure particle intensities, we processed the images with a MATLAB® script, counted the particles in the image, and determined the number of counts in each particle spot. To create histograms, the intensity scale was binned, and the number of particles in each bin were counted. Figure 8 shows the histograms with the distribution of particle side scatter intensities. Because we have not yet calibrated the side scatter to particle size, the histograms do not currently show the change in size distribution.

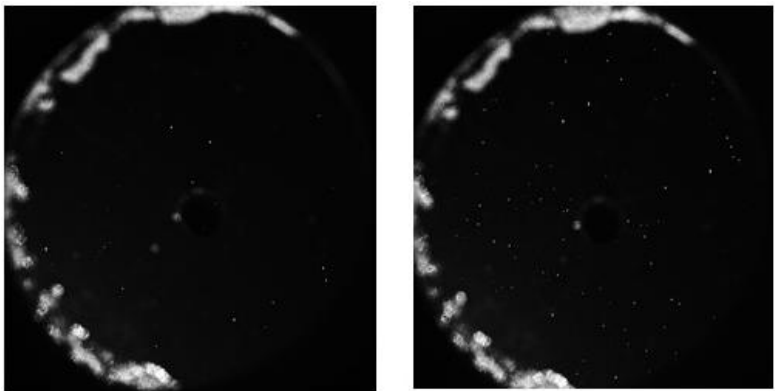


Figure 7. Oleic acid particles (7 μm) produced from a Sono-Tek sprayer, showing before (left) and after (right) the passage of a shock wave. A greater number of particles are apparent after the shock (right).

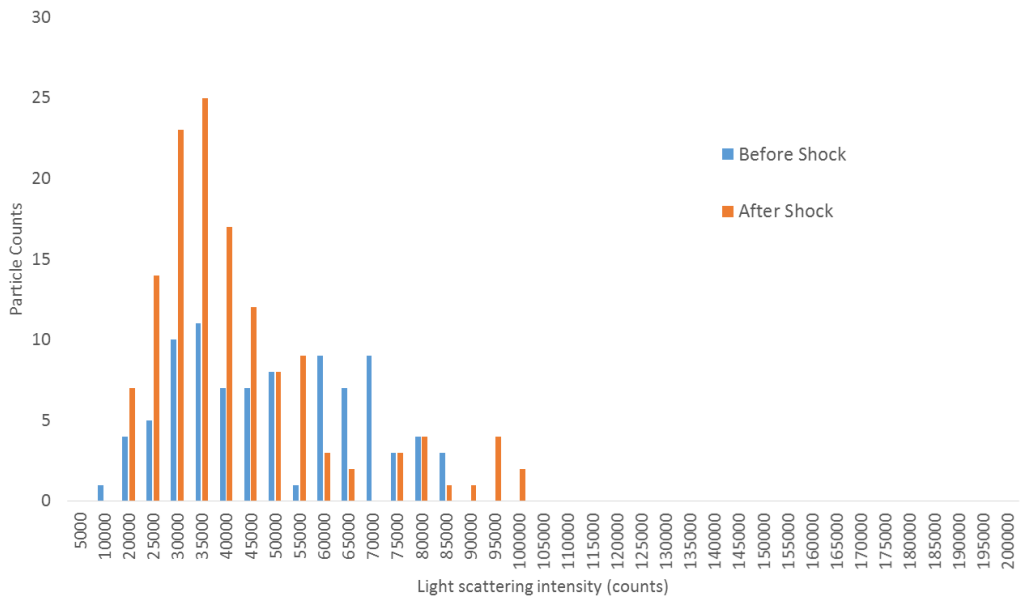


Figure 8. Histograms of the distribution particle intensities in the before shock and after shock images (from Figure 7).

What we see in Figure 8 is a change in the distribution of particle side scattering intensity induced by the shock. Prior to the shock, the distribution has more weight for the higher intensities. After the shock, not only has the distribution shifted towards smaller particle signals, that is, smaller particles, but there are more particles. This strongly suggests that the shock wave has fragmented droplets. A few particles appear in the distribution after the shock that are larger than those before the shock. We attribute this to the stochastic nature of the measurement, so that many more measurements are necessary to average out fluctuations in the size of particles. Nevertheless, the shape of the distribution has changed, thus suggesting a change in size distribution.

Although we have demonstrated the ability to observe particle fragmentation and agglomeration, many more measurements need to be completed in order to see trends in break up or agglomeration as a function of experimental conditions such as particle surface tension, concentration, or shock intensity. Although the groundwork for highly detailed modeling of the interaction of shock waves and particles has been laid, validation work is necessary. Ultimately, we expect the model to predict particle behavior based on shock intensity and surface tension.

4 CONCLUSIONS

In order to test our hypothesis on the interaction of liquid droplets in the respirable range and shock waves, a shock tube/wind tunnel has been constructed to allow the viewing of aerosols in the tube with a PIV. Using both schlieren imaging and the pressure as a function of time, we have demonstrated moderate shock waves up to Mach numbers of 1.35. The PIV provides pairs of images with ~10 ns time resolution so that no particle movement occurs during the image exposure time. Using high droplet concentrations generated with a paint sprayer, we have observed shock induced agglomeration. For sparser particle concentrations, we observed particle fragmentation. Thus, we have successfully demonstrated the experimental and theoretical tools for studying the agglomeration and break-up of aerosol particles. However, more measurements investigating the influence of initial particle size, shock intensity, and particle surface energy are necessary to fully explore the validity of our hypothesis on the shock-particle interaction.

ACKNOWLEDGMENTS

We acknowledge a number of contributors and entities without whom this work could not have been performed. We acknowledge funding provided by the In-house Laboratory Independent Research Program administered by Dr. Augustus W. Fountain, as well as support provided by the U.S. Army Research Laboratory Army High Performance Computing Research Center (AHPCRC) administered by Dr. Raju Namburu.

REFERENCES

- [1] Peri, M.D.M.; Devarapalli, V.K.; and Cetinkaya, C., "Selective removal of 10-40-nm particles from silicon wafers using laser-induced plasma shock waves." *Journal of Adhesion Science and Technology*, **2007**, 21(3-4), p331-337.
- [2] Kim, Y.; Hokamoto, K.; and Itoh, S., "A study on the consolidation of Cu, Ni / graphite powder using shock compaction method." *Material Science Forum*, **2008**, 566, p345-350.
- [3] Hoover, W.G. and Hoover, C.G., "Tensor temperature and shock-wave stability in a strong two-dimensional shock wave." *Physical Review E: Statistical, Nonlinear, and Soft Matter Physics*, **2009**, 80(1 Pt 1), e011128.
- [4] Zohdi, T.I., "Numerical simulation of the impact and deposition of charged particulate droplets." *Journal of Computational Physics*, **2013**, 233, p509-526.
- [5] Theofanous, T.G. and Li, G.J., "On the physics of aerobreakup." *Physics of Fluids*, **2008**, 20, e052103.
- [6] Theofanous, T.G.; Mitkin, V.V.; and Ng, C.L., "The physics of aerobreakup. III. Viscoelastic liquids." *Physics of Fluids*, **2013**, 25, e032101.
- [7] Theofanous, T.G. *et al.*, "The physics of aerobreakup. II. Viscous liquids." *Physics of Fluids*, **2012**, 24, e022104.
- [8] Gates, S.D. *et al.*, "Extension of Bacillus endospore gas dynamic heating studies to multiple species and test conditions." *Journal of Applied Microbiology*, **2011**, 111(4), p925-931.
- [9] Gates, S.D. *et al.*, "Bacillus endospore resistance to gas dynamic heating." *Journal of Applied Microbiology*, **2010**, 109(5), p1591-1598.
- [10] McCartt, A.D. *et al.*, "Response of Bacillus thuringiensis Al Hakam endospores to gas dynamic heating in a shock tube." *Zeitschrift für Physikalische Chemie (Muenchen, Germany)*, **2011**, 225, p1367-1377.
- [11] Gregoire, Y. *et al.*, "Investigation of the behavior of solid particles dispersed by high explosive." *40th Annual International Conference of ICT (Karlsruhe, Germany)*, 23-26 June **2009**.
- [12] Kudryashova, O.B. *et al.*, "Physicomathematical modeling of explosive dispersion of liquid and powders." *Propellants, Explosives, Pyrotechnics*, **2011**, 36(6), p524-530.
- [13] Brandt, O.; Rajathurai, A.M.; and Roth, P., "First observations on break-up of particle agglomerates in shock waves." *Experiments in Fluids*, **1987**, 5(2), p86-94.

- [14] Wagner, J.L. *et al.*, "Shock tube investigation of quasi-steady drag in shock-particle interactions." *Physics of Fluids*, **2012**, 24, e123301.
- [15] Wagner, J.L. *et al.*, "A multiphase shock tube for shock wave interactions with dense particle fields." *Experiments in Fluids*, **2012**, 52(6), p1507-1517.



SSI PROJECTS

Fano resonance in a gold nanosphere with a J-aggregate coating

Andrew M. Fales^{a,b}, Stephen J. Norton^{a,b}, Bridget M. Crawford^{a,b}, Brendan G. DeLacy^{d*},
Tuan Vo-Dinh^{a,b,c}

^aFitzpatrick Institute for Photonics, Duke University, Durham, NC 27708

^bDepartment of Biomedical Engineering, Duke University, Durham, NC 27708

^cDepartment of Chemistry, Duke University, Durham, NC 27708

^dU.S. Army Edgewood Chemical Biological Center, Research & Technology Directorate,
5183 Blackhawk Rd, Aberdeen Proving Ground, MD 21010

ABSTRACT

We present a facile method to induce J-aggregate formation on gold nanospheres in colloidal solution using polyvinylsulfate. The nanoparticle J-aggregate complex results in an absorption spectrum with a split lineshape due to plasmon-exciton coupling (i.e., via the formation of upper and lower plexcitonic branches). The use of nanoparticles with different plasmon resonances altered the position of the upper plexcitonic band while the lower band remained at the same wavelength. This splitting was investigated theoretically, and shown analytically to arise from Fano resonance between the plasmon of the gold nanoparticles and exciton of the J-aggregates. A theoretical simulation of a J-aggregate coated and uncoated gold nanosphere produced an absorption spectrum that showed good agreement with the experimentally measured spectra.

Keywords: Plexcitons, plasmons, excitons, nanoshells, J-aggregates, scattering dark state

1 INTRODUCTION

Coupling of the exciton resonance of a J-aggregate coating with the localized surface plasmon resonance (LSPR) of the metallic core of a plasmonic nanoparticle gives rise to an asymmetric resonance exhibiting the characteristic Fano lineshape. Fano resonances generated by composite nanostructures have been proposed for biomolecular sensing because of the sensitivity of the Fano phenomenon to the local environment.¹ There are various hybrid systems coupling plasmon and exciton resonances to generate hybridized energy states, referred to as plexcitons, for a wide variety of applications.²⁻¹¹ These hybridized energy states are manifested in the formation of a blue-shifted peak (upper plexcitonic branch), and a red-shifted peak (lower plexcitonic branch). Here we report absorption measurements of a J-aggregate compound coating a gold nanosphere that displays the characteristics of Fano interference. The Fano lineshape can be described as a consequence of the coupling between a sharp resonance, in this case the J-aggregate response, and a broader resonance, here provided by the plasmon response.^{12, 13} This coupling between the two modes produces a partial “quenching” of the plasmon response by the J-aggregate resonance, or equivalently, an induced-transparency in the absorption cross section of the particle.¹⁴ Evidence of the latter is a “Fano dip” in the extinction spectrum near the J-aggregate resonance. As shown below, the spherical symmetry of the metallic core with the J-aggregate layer is sufficiently simple to show analytically that their interaction produces the classic Fano lineshape. Letting ω_b and ω_s denote, respectively, the broad and sharp resonances and γ_b and γ_s their corresponding line widths, this Fano response takes the form:

$$F(\omega) = \frac{(\kappa + q)^2}{\kappa^2 + 1}, \quad (1)$$

where $\kappa = (\omega^2 - \omega_s^2 - \omega_s \Delta) / \Gamma$, $q = (\omega_s^2 - \omega_b^2) / \gamma_b \omega_s$, $\Delta = (\omega_s^2 - \omega_b^2) / \omega_s$ and $\Gamma = \gamma_s \omega_s$.¹⁵ Here we have assumed that $\gamma_s \ll \gamma_b$. We show in a later section that the response of the J-aggregate on the gold particle can be placed in the form of (1) thus confirming the experimental results with theoretical studies.

2 METHODOLOGY

2.1 Materials

All chemicals were purchased from Sigma-Aldrich® (St. Louis, MO, USA) at the highest purity available unless otherwise specified. Ultrapure water (18 MΩ-cm) was used in all preparations. Glassware and stir bars were cleaned with aqua regia before use.

2.2 Instrumentation

Ultraviolet-Visible (UV-Vis) spectra were recorded on a FLUOstar® Omega plate reader (BMG LABTECH; GmbH, Germany). Transmission electron microscope (TEM) micrographs were acquired on a Tecnai™ G2 Twin TEM (FEI™; Hillsboro, OR).

2.3 Gold nanoparticle (AuNP) synthesis

The gold nanospheres were synthesized using a modified Turkevich method. A 100 mL solution of 0.25 mM HAuCl_4 was brought to a rolling boil under vigorous stirring. The reduction process was initiated by injecting 0.7 mL of 1% citrate solution. The solution immediately turned clear, followed by a slow transition to dark grey and then deep red. After this point, the solution was kept boiling for another 30 minutes, maintaining the initial volume, before being cooled to room temperature. This resulted in particles with a plasmon peak at 540 nm. The nanoparticles with plasmons at 532 nm and 520 nm were produced by altering the amount of citrate added to 1 mL and 2 mL, respectively.

2.4 PIC sample preparation

A 0.5 mM stock solution of 1,1-Diethyl-2,2-cyanine iodide (PIC) was prepared in 0.1 M phosphate buffer, pH 6.0. PIC J-aggregate formation was induced by diluting the stock solution into 5 M NaCl; when diluted into water, no J-aggregate formation is observed. For J-aggregate formation on the gold nanoparticles, the particles were first coated with a polymer, poly(vinylsulfonic acid) sodium salt solution (PVSA), at 0.02% w/v to stabilize them against aggregation. The PIC stock solution could then be added at the desired concentration to the PVSA-coated gold nanospheres (AuNP-PVSA).

3 DATA AND RESULTS

The formation of J-aggregates by PIC has been well documented in the literature.²⁻¹¹ A simple method to induce J-aggregate formation is by increasing the salt concentration of the dye solution. As shown in Figure 1, when the PIC stock solution is diluted into water, no J-aggregates are observed. When 5 M NaCl is used in place of water, the J-aggregate peak can be seen at 575 nm. The interaction of these J-aggregates with gold nanospheres was studied by adding aliquots of the PIC stock solution to PVSA-coated gold nanoparticles.

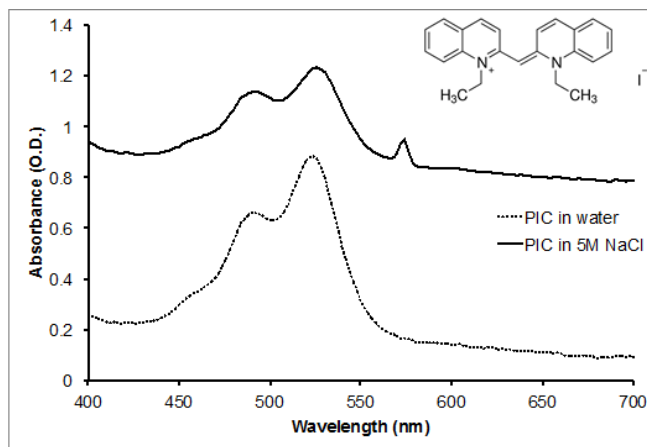


Figure 1. UV-Vis absorption spectra of 20 μM PIC in water (dotted) and in 5 M NaCl (solid). The new peak observed at about 575 nm indicates the presence of J-aggregates in the solution. The chemical structure of PIC is shown at the top right.

The PVSA was used to serve two purposes in this study. First, the gold nanoparticles were protected against aggregation in the presence of PIC. Without the polymer coating, the color of the nanoparticle solution changed immediately upon addition of PIC and the particles began to settle out of solution. Second, the negatively-charged PVSA aided in electrostatic interaction with the positively charged PIC. To determine the optimal amount of PIC for interaction with the gold nanoparticles, a range of PIC concentrations were added to AuNP-PVSA before UV-Vis spectra were recorded. Figure 2 shows the extinction spectra of the AuNP-PVSA and PIC complexes. As shown, the magnitude of the induced transparency at around 580 nm levels off after the concentration of PIC reaches 20 μM . This concentration was then selected for further investigation.

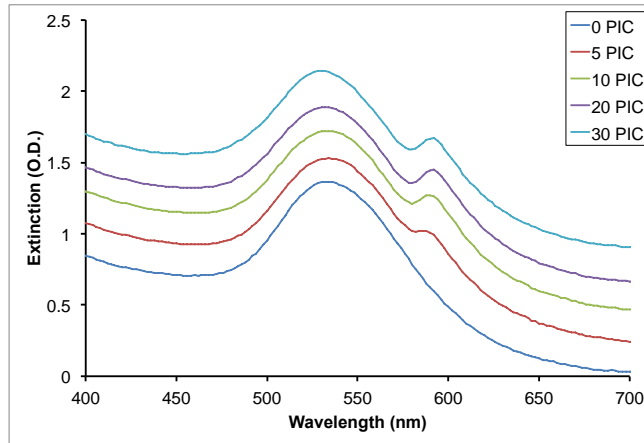


Figure 2. UV-Vis spectra of AuNP-PVSA with different concentrations (in μM) of PIC. The spectra have been offset for clarity.

Three different sizes of nanoparticles were prepared to see what effect, if any, this would have on the Fano lineshape. By keeping the concentration of gold constant and varying the amount of citrate, gold nanoparticles with a plasmon resonance of 520 nm, 532 nm, and 540 nm were produced (Figure 3A-B). This corresponds to nanoparticle sizes of approximately 15 nm, 40 nm, and 60 nm, respectively (Figure 3C-E). All three sizes of nanoparticles were shown to produce the Fano lineshape after forming a complex with PIC, consisting of a spectral dip at about 580 nm and a new peak at approximately 593 nm. The original surface plasmon resonance wavelength of the sample is retained as the upper band in the split lineshape.

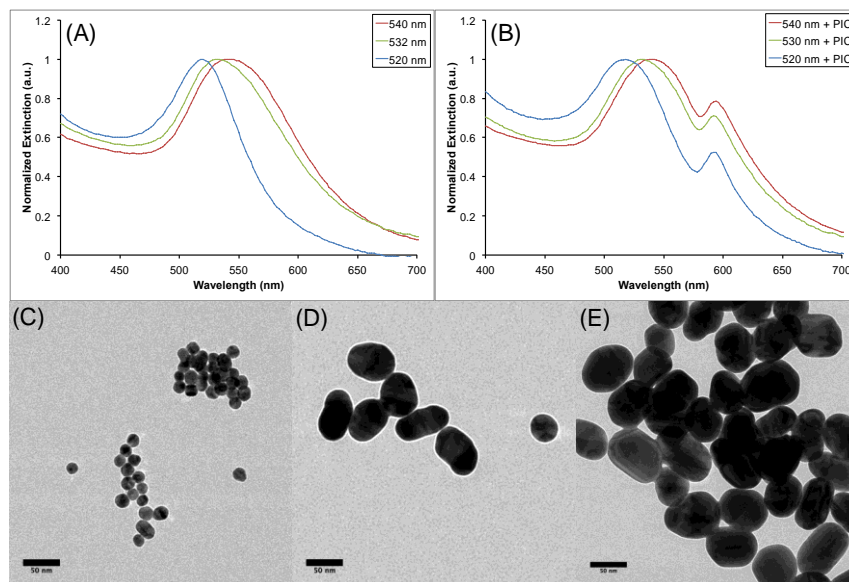


Figure 3. (A) Normalized extinction spectra of the three different nanosphere samples, labeled by their peak plasmon resonance. (B) Normalized extinction spectra of the nanosphere + 20 μM PIC samples. (C-E) TEM images of the 520 nm, 532 nm, and 540 nm samples, respectively. Scale bars are 50 nm.

The unnormalized extinction spectra of the AuNP-PVSA and AuNP-PVSA + PIC complexes are shown in Figure 4. After addition of PIC, there is a decrease in the extinction maxima at the plasmon resonance wavelength, accompanied by an increase in extinction at 593 nm, with a dip between the two peaks occurring at 580 nm. In all three cases, the lower band remains at 593 nm, while the upper band position is dependent on the initial surface plasmon resonance wavelength of the nanoparticles. Thus, the 520 nm plasmon particles have the largest gap between the upper and lower plexcitonic branches at 73 nm, and the 540 nm plasmon particles have the smallest gap at 53 nm.

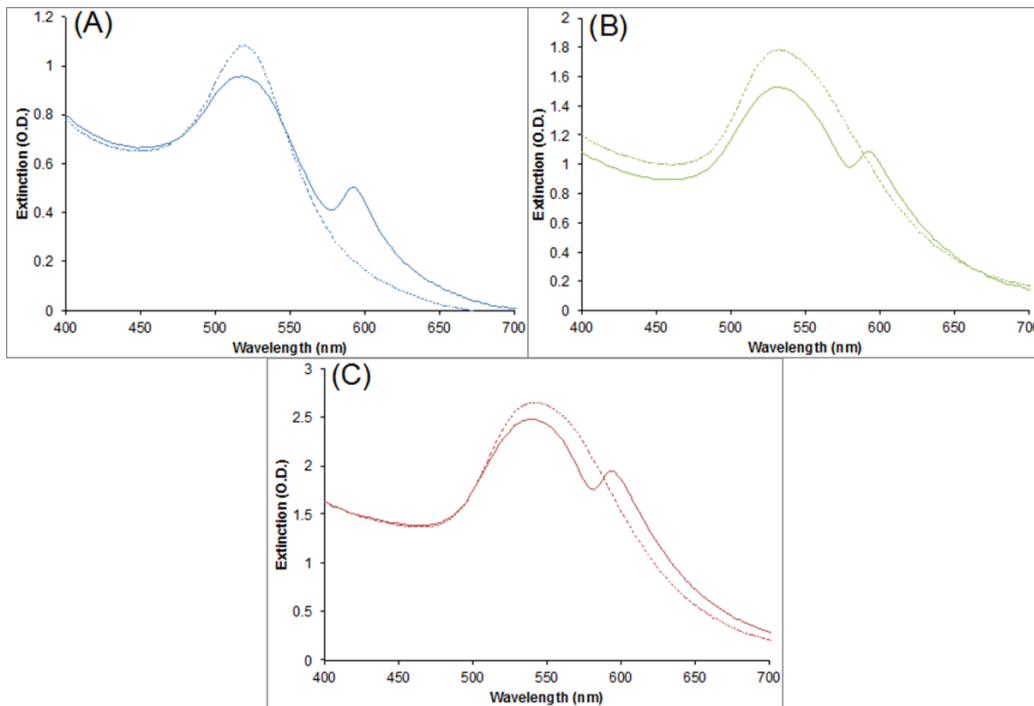


Figure 4. Extinction spectra of the AuNP-PVSA (dotted) and AuNP-PVSA + PIC complex (solid) for the (A) 520 nm, (B) 532 nm, and (C) 540 nm plasmon samples.

To better visualize the splitting between the upper and lower plexcitonic branches, an energy diagram was created (Figure 5). As previously observed, the upper band of the split lineshape closely follows the initial surface plasmon resonance of the nanoparticles, while the lower band is essentially unchanged between the three samples. The energy difference between the upper and lower bands for the 520 nm, 532 nm, and 540 nm plasmon nanoparticles was determined to be 306, 236, and 200, respectively. These values are in line with those reported in previous works.^{5,11,16-18}

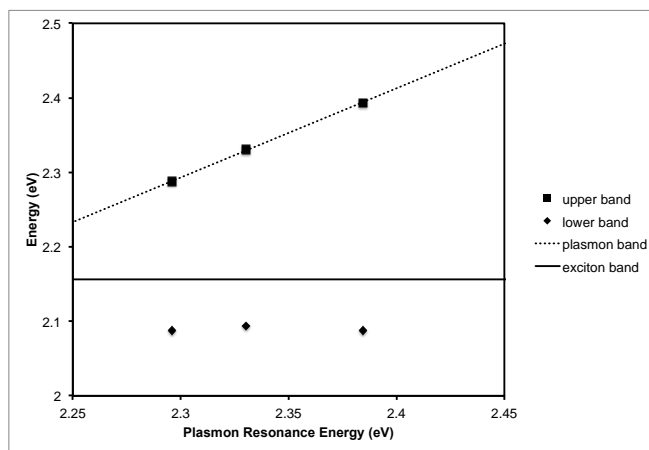


Figure 5. Energy diagram of the upper and lower plexcitonic branches for the three different nanoparticle samples, extracted from the spectra in Figure 4.

4 THEORETICAL METHODS

We show in this section that the coupling between the plasmonic resonance of the gold core and the J-aggregate layer gives rise to a Fano resonance that can be expressed in the standard Fano form. Denote the layer and core dielectric constants by $\dot{\epsilon}_j$ and $\dot{\epsilon}_{au}$, respectively, and the background dielectric constant by $\dot{\epsilon}_m$. We model the response of the J-aggregate compound using a Lorentzian lineshape of the form

$$\dot{\epsilon}_j(\omega) = \dot{\epsilon}_{j\infty} + \frac{f\omega_0^2}{\omega_0^2 - \omega^2 - i\omega\gamma_j}, \quad (2)$$

where ω_0 is the primary J-aggregate transition line, f is the oscillator strength and γ_j is the resonance linewidth.

We employ a simple Drude model for the dielectric constant of the gold core:

$$\dot{\epsilon}_{au}(\omega) = \dot{\epsilon}_\infty - \frac{\omega_p^2}{\omega^2 + i\omega\gamma_{au}}, \quad (3)$$

where ω_p is the plasmon frequency for gold and γ_{au} is the plasmon linewidth. Let R and R_c denote respectively the radius of the coated particle and the radius of the gold core. The layer thickness is then $t = R - R_c$, where we assume the thickness is much less than the particle radius ($t \ll R$). We also assume that the particle is much smaller than the optical wavelength so that the quasistatic approximation can be employed. The polarizability of the particle is then given by

$$\alpha = 3V \left[\frac{(\dot{\epsilon}_j - \dot{\epsilon}_m)(2\dot{\epsilon}_j + \dot{\epsilon}_{au}) + (2\dot{\epsilon}_j + \dot{\epsilon}_m)(\dot{\epsilon}_{au} - \dot{\epsilon}_j)(R_c/R)^3}{(\dot{\epsilon}_j + 2\dot{\epsilon}_m)(2\dot{\epsilon}_j + \dot{\epsilon}_{au}) + 2(\dot{\epsilon}_j - \dot{\epsilon}_m)(\dot{\epsilon}_{au} - \dot{\epsilon}_j)(R_c/R)^3} \right], \quad (4)$$

where V is the particle volume. The scattering and absorption cross sections are

$$\sigma_s = \frac{k^4}{6\pi} |\alpha|^2 \quad (5)$$

$$\sigma_a = k \text{Im}\{\alpha\}, \quad (6)$$

where k is the wavenumber in the host medium. We can simplify (4) under the assumption of a thin layer. Expanding $(R_c/R)^3$ to first order in the thickness t by writing $(R_c/R)^3 = (1 - t/R)^3 \approx 1 - 3t/R$ and substituting into (4) gives

$$\alpha = 3V \left[\frac{\dot{\epsilon}_j(\dot{\epsilon}_{au} - \dot{\epsilon}_m) - \tau(2\dot{\epsilon}_j + \dot{\epsilon}_m)(\dot{\epsilon}_{au} - \dot{\epsilon}_j)}{\dot{\epsilon}_j(\dot{\epsilon}_{au} + 2\dot{\epsilon}_m) - 2\tau(\dot{\epsilon}_j - \dot{\epsilon}_m)(\dot{\epsilon}_{au} - \dot{\epsilon}_j)} \right] \quad (7)$$

where $\tau \equiv t/R$. This approximation can be avoided for thicker layers by replacing τ everywhere with $\tau - \tau^2 + \tau^3/3$.

To show how Fano interference arises in this system, we neglect for simplicity the J-aggregate damping in (2) by setting $\gamma_j = 0$. This can usually be justified by noting that typically $\gamma_j \ll \gamma_{au}$. To further simplify the analysis, we shall consider the case in which $\dot{\epsilon}_{j\infty} = \dot{\epsilon}_\infty = \dot{\epsilon}_m$ in (2) and (3). It is convenient to define $\tilde{\omega}_0 \equiv \omega_0 \sqrt{1 + f/\dot{\epsilon}_m}$ and $\tilde{\omega}_{au} \equiv \omega_p / \sqrt{3\dot{\epsilon}_m}$, where the frequency $\tilde{\omega}_{au}$ corresponds to the plasmon resonance of the gold core in the absence of the layer (when $\tau = 0$). Substituting (2) and (3) into (7) and multiplying numerator and denominator by $(\omega_0^2 - \omega^2)(\omega^2 + i\omega\gamma_{au})$ results in

$$\alpha = - \left(\frac{V\omega_p^2}{\dot{\epsilon}_m} \right) \frac{\omega^2 - \tilde{\omega}_0^2 + \tau P}{(\omega^2 - \tilde{\omega}_0^2)(\omega^2 - \tilde{\omega}_{au}^2 + i\omega\gamma_{au}) - \tau Q}, \quad (8)$$

where

$$P \equiv 3(f\omega_0^2 / \omega_p^2 - 1)\omega^2 + (3 + 2f / \dot{\epsilon}_m)\omega_0^2 \quad (9)$$

$$Q \equiv 2f\omega_0^2\tilde{\omega}_{au}^2. \quad (10)$$

In deriving (9) and (10), we have dropped terms of order f^2 , since typically $f \ll 1$, and terms of order $f\gamma_{au}/\omega$.

The response is quenched for the value of $\omega = \omega_q$ for which the numerator of (8) vanishes. Setting the numerator to zero, we find the following:

$$\omega_q^2 = \frac{\tilde{\omega}_0^2 - \tau\omega_0^2(3 + 2f / \dot{\epsilon}_m)}{1 + 3\tau(f\omega_0^2 / \omega_p^2 - 1)}.$$

We note that only partial quenching will occur when the J-aggregate linewidth γ_j , is nonzero. The resonances are determined by the zeros of the real part of the denominator of (8), or the solution to

$$(\omega^2 - \tilde{\omega}_{au}^2)(\omega^2 - \tilde{\omega}_0^2) - 2\tau f \omega_0^2 \tilde{\omega}_{au}^2 = 0.$$

Assuming that the term proportional to τf is small compared to $|\tilde{\omega}_{au}^2 - \tilde{\omega}_0^2|$, the resonant frequencies $\tilde{\omega}_{au}$ and $\tilde{\omega}_0$ are shifted slightly. To first order in τf the plasmon resonance $\tilde{\omega}_{au}$ is shifted to $\bar{\omega}_{au}$, given by

$$\bar{\omega}_{au}^2 = \tilde{\omega}_{au}^2 + \frac{2\tau f \omega_0^2 \tilde{\omega}_{au}^2}{\tilde{\omega}_{au}^2 - \tilde{\omega}_0^2}.$$

The J-aggregate resonance is also shifted by an amount proportional to τf , which we denote by $\bar{\omega}_0$:

$$\bar{\omega}_0^2 = \tilde{\omega}_0^2 - \frac{2\tau f \omega_0^2 \tilde{\omega}_{au}^2}{\tilde{\omega}_{au}^2 - \tilde{\omega}_0^2}.$$

To show how Fano behavior is manifested by this system, we follow an approach used by Gallinet and Martin in their analysis of two coupled harmonic oscillators as an illustration of Fano interference in a mechanical system.¹⁹ In our case, the product τf plays the role of the coupling parameter. We begin by expanding the denominator of (8) about the J-aggregate resonance $\tilde{\omega}_0$. When ω is near $\tilde{\omega}_0$, the factor $\omega^2 - \tilde{\omega}_{au}^2 - i\omega\gamma_{au}$ in the denominator is slowly varying and we replace it with $C \equiv \tilde{\omega}_0^2 - \tilde{\omega}_{au}^2 - i\tilde{\omega}_0\gamma_{au}$. On evaluating $|\alpha|^2$ and $\text{Im}\{\alpha\}$, we find that the cross sections become after some manipulation:

$$\sigma_s = A \frac{(\kappa + p)^2}{\kappa^2 + 1} \quad (11)$$

$$\sigma_a = B \frac{(\kappa + q)^2 - b}{\kappa^2 + 1}, \quad (12)$$

where

$$\kappa = \frac{1}{\Gamma} \left[\omega^2 - \tilde{\omega}_0^2 + \frac{\tau Q (\tilde{\omega}_{au}^2 - \tilde{\omega}_0^2)}{|C|^2} \right]$$

$$\Gamma = \frac{\tau Q \tilde{\omega}_0 \gamma_{au}}{|C|^2}$$

$$p = \frac{\tilde{\omega}_0^2 - \tilde{\omega}_{au}^2}{\tilde{\omega}_0 \gamma_{au}} + \frac{P |C|^2}{Q \tilde{\omega}_0 \gamma_{au}}$$

$$q = \frac{\tilde{\omega}_0^2 - \tilde{\omega}_{au}^2}{\tilde{\omega}_0 \gamma_{au}} + \frac{P |C|^2}{2Q \tilde{\omega}_0 \gamma_{au}}$$

and $A = (k^2 V \omega_p^2 / \dot{\omega}_m |C|)^2 / 6\pi$, $B = -kV \omega_p^2 / \dot{\omega}_m |C|$, and $b = (\tau P / 2\Gamma)^2$. Equation 11 is in the classic Fano form given by Equation 1, but both Equation 11 and Equation 12 display the characteristic asymmetric resonance arising from the ‘‘Fano dip’’ which occurs when $\kappa + p \approx 0$ in (11) and when $(\kappa + q)^2 - b \approx 0$ in Equation 12.

4.1 Simulation

Figure 6 shows a calculation of the absorption cross-section using (4) and (12) with the values $\dot{\omega}_m = 1.77$, $R = 20$ nm, $R_c = 19$ nm, and in (2) $\omega_0 = 2\pi c / \lambda_0$ with $\lambda_0 = 540$ nm, $\gamma_j = 0.02\omega_0$, and $f = 0.02$. For this choice of parameters, one can show that the scattering cross section is insignificant compared to the absorption cross section. The dielectric constant for gold, $\dot{\omega}_{au}(\omega)$, was derived from data published in the Handbook of Optical Constants of Solids.²⁰ The dip in the absorption cross section at about 530 nm corresponds to the ‘‘quenching’’ or induced-transparency of the particle absorption due to the J-aggregate layer.

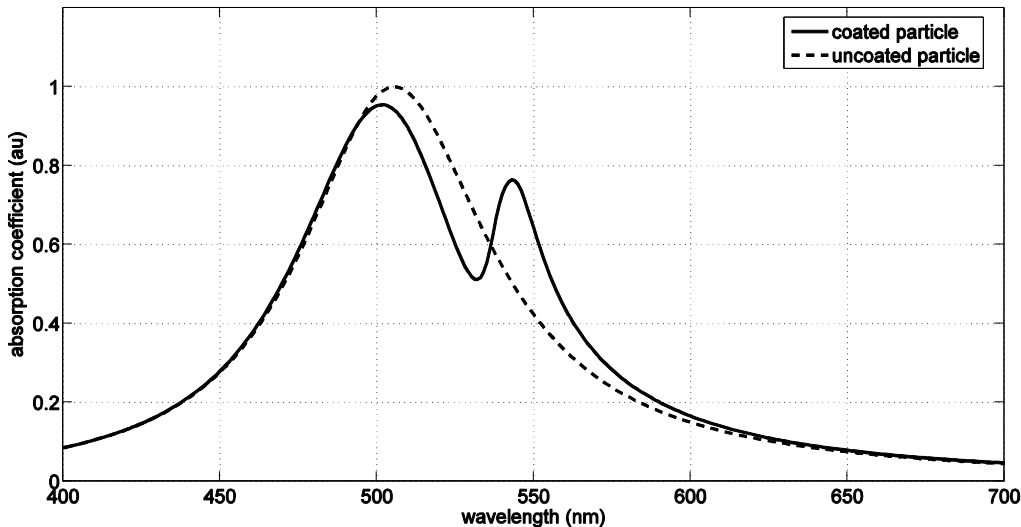


Figure 6. Calculation of the absorption cross section with and without the J-aggregate coating.

5 CONCLUSION

Polymer coated gold nanospheres were shown to promote J-aggregate formation of PIC dye on the nanoparticle surface. Coupling between the plasmon of the nanoparticles and exciton of the J-aggregates produced a Fano lineshape, showing an upper and lower plexcitonic band. The size of nanoparticles used affected the position of the upper plexcitonic band, but had no effect on the lower band. The largest splitting energy was found to be 306 meV, for the gold nanoparticles with a plasmon resonance at 520 nm. The observed splitting was shown analytically to be due to Fano resonance between the gold nanoparticle and J-aggregates. A simulated absorption spectrum of a J-aggregate coated gold nanosphere showed good agreement with the experimentally measured spectra.

ACKNOWLEDGMENTS

This research was funded by the Department of the Army Basic Research Program and sponsored by the Edgewood Chemical Biological Center. Support was also provided by the U.S. Army Research Office under contract W911NF-13-D-0001.

REFERENCES

- [1] Wu, C. *et al.*, "Fano-resonant asymmetric metamaterials for ultrasensitive spectroscopy and identification of molecular monolayers." *Nature Materials*, **2012**, 11(1), p69-75.
- [2] Wiederrecht, G.P.; Wurtz, G.A.; and Hranisavljevic, J., "Coherent coupling of molecular excitons to electronic polarizations of noble metal nanoparticles." *Nano Letters*, **2004**, 4(11), p2121-2125.
- [3] Yoshida, A.; Uchida, N.; and Kometani, N. "Synthesis and spectroscopic studies of composite gold nanorods with a double-shell structure composed of spacer and cyanine dye J-aggregate layers." *Langmuir*, **2009**, 25(19), p11802-11807.
- [4] Achermann, M. "Exciton-plasmon interactions in metal–semiconductor nanostructures." *The Journal of Physical Chemistry Letters*, **2010**, 1(19), p2837-2843.
- [5] Fofang, N.T. *et al.*, "Plexciton dynamics: Exciton-plasmon coupling in a J-aggregate-Au nanoshell complex provides a mechanism for nonlinearity." *Nano Letters*, **2011**, 11(4), p556-1560.

- [6] Zengin, G. *et al.*, "Approaching the strong coupling limit in single plasmonic nanorods interacting with J-aggregates." *Scientific Reports*, 2013, 3, p3074.
- [7] Murphy, C.J., Peer Reviewed: "Optical Sensing with Quantum Dots." *Analytical Chemistry*, **2002**, 74(19), 520A-526A.
- [8] Govorov, A.O. and Carmeli, I., "Hybrid structures composed of photosynthetic system and metal nanoparticles: Plasmon enhancement effect." *Nano Letters*, **2007**, 7(3), p620-625.
- [9] Artuso, R.D. and Bryant, G.W., "Optical response of strongly coupled quantum dot-metal nanoparticle systems: Double peaked fano structure and bistability." *Nano Letters*, **2008**, 8(7), p2106-2111.
- [10] DeLacy, B.G. *et al.*, "Layer-by-layer self-assembly of plexcitonic nanoparticles." *Optics Express*, **2013**, 21(16), p19103-19112.
- [11] DeLacy, B.G. *et al.*, "Coherent plasmon-exciton coupling in silver platelet-J-aggregate nanocomposites." *Nano Letters*, **2015**, 15(4), p2588-2593.
- [12] Miroshnichenko, A.E.; Flach, S.; and Kivshar, Y.S., "Fano resonances in nanoscale structures." *Reviews of Modern Physics*, **2010**, 82(3), p2257-2298.
- [13] Satanin, A.M. and Joe, Y.S. "Fano interference and resonances in open systems." *Physical Review B*, **2005**, 71(20), p205417.
- [14] Wu, X.; Gray, S.K.; and Pelton, M., "Quantum-dot-induced transparency in a nanoscale plasmonic resonator." *Optics Express*, **2010**, 18(23), p23633-23645.
- [15] Gallinet, B. *et al.*, "Fano resonant plasmonic systems: Functioning principles and applications." *AIP Conference Proceedings*, **2012**, 1475(1), 18-20.
- [16] Lekeufack, D.D. *et al.*, "Core-shell gold J-aggregate nanoparticles for highly efficient strong coupling applications." *Applied Physics Letters*, **2010**, 96(25), p253107.
- [17] Schlather, A.E. and *et al.*, "Near-field mediated plexcitonic coupling and giant Rabi splitting in individual metallic dimers." *Nano Letters*, **2013**, 13(7), p3281-3286.
- [18] Melnikau, D. *et al.*, "Strong plasmon-exciton coupling in a hybrid system of gold nanostars and J-aggregates." *Nanoscale Research Letters*, **2013**, 8(1), p134.
- [19] Gallinet, B. and Martin, O.J.F., "Ab initio theory of Fano resonances in plasmonic nanostructures and metamaterials." *Physical Review B*, **2011**, 83(23), p235427.
- [20] Palik, E.D., *Handbook of Optical Constants of Solids*, Ed. Academic Press: Burlington, VT, **1997**.

Adsorption of anionic thiols on silver nanoparticles

Bolei Xu^a, Grazia Gonella^a, Brendan G. DeLacy^{b*}, Hai-Lung Dai^a

^aDepartment of Chemistry, Temple University, Philadelphia, PA 19122

^bU.S. Army Edgewood Chemical Biological Center, Research & Technology Directorate,
5183 Blackhawk Rd, Aberdeen Proving Ground, MD 21010

ABSTRACT

The adsorption of negatively charged 3-mercaptopropanesulfonate (MPS) on the surface of citrate-stabilized silver nanoparticles (Ag NP) in water is investigated using colloidal particle surface sensitive techniques. The adsorption of this negatively charged thiol appears to be qualitatively different from that of neutral thiols, and highlights the importance of repulsive interactions of electrostatic and steric origins pertaining to charged thiols. For the charged MPS thiol, the adsorption process occurs in two phases. At low surface coverage, where the intermolecular repulsion is negligible and the adsorption is dominated by the formation of the S–Ag bond, MPS molecules need to overcome an activation energy barrier $E_a = (7.5 \pm 0.9)$ kcal/mol with an associated free energy change $\Delta G_{\text{ads}} = -(14.3 \pm 0.3)$ kcal/mol, and behave similar to neutral thiols. On the other hand, at high surface coverage where the repulsive interactions among MPS molecules cannot be neglected, the adsorption is characterized by a higher $E_a = (12.4 \pm 0.5)$ kcal/mol and lower $\Delta G_{\text{ads}} = -(7.4 \pm 0.1)$ kcal/mol.

Keywords: Second harmonic generation, light scattering, charged thiols, negative thiols, silver nanoparticles

1 INTRODUCTION

Colloids containing particles with size ranging from micrometers to nanometers are of great technological interests. Many of the unique properties of colloids originate from the high ratio between the number of atoms at the surface and that in the bulk. In general, as the particles become smaller, the surface characteristics become more deterministic of the colloidal properties. Among the various colloidal particles, noble-metal particles, such as those made of gold and silver, have continued to attract a great deal of interest because of the large number of applications in fields spanning from optics to energy, catalysis, and biomedicine.¹⁻⁶

In many of the applications utilizing colloidal particles there is a need to modify the particle surface either to provide the particles with new functionalities by attaching specific molecular groups (active functionalization), or to reduce/eliminate undesirable interactions of the particles with their surroundings (passive functionalization). For metallic particle surfaces, even though new routes, such as the use of N-heterocyclic carbenes,^{7,8} have been proposed, so far the most versatile method for functionalizing the metallic particle surface is through thiolation.⁹⁻¹¹ Molecules containing a sulfhydryl group, which has high affinity with noble metals, present an efficient route for surface modification.¹² As thiolation constitutes an important and frequently used surface modification step, a mechanistic understanding of the reactions between thiols and metallic particle surfaces is of great importance for the control of the particle surface properties and the development of new surface modification methods.^{7,13,14} The adsorption of charged thiols has been used, for instance, to alter the surface charge properties and therefore enable specific applications of metallic nanoparticles. An example is the case in which cationic thiols have been used to promote J-aggregation of anionic cyanines on the surface of Au nanoparticles (NP).¹⁵

Despite the importance of understanding molecular interactions at the surface of metallic particles, studies carried out on metallic nanoparticle surfaces are few especially when compared to their planar surface counterpart, and there is an even smaller number of studies investigating Ag compared to Au. This is because, when compared to the planar surface case, characterizing the metallic particle surface in the colloidal environment is experimentally more complex. For instance, a peculiar problem with colloidal particles is aggregation. In order to prevent particles from aggregating, stabilizers, such as citrate, are routinely used to treat the particle surface. Furthermore, there is a need for *in situ* surface-sensitive methods that are capable of probing the surface of these nanometer-size particles buried in the colloidal solution.

The effectiveness of second harmonic light scattering (SHS) for detecting molecules at the surface of micrometer-size particles in the colloidal environment was first demonstrated by Eisenthal and coworkers.¹⁶ Our group, along with others, has demonstrated that SHS is capable of probing the surface of nanometer size particles in the colloidal environment. In particular, we have shown that the surface of metallic nanoparticles (NP) can be examined.^{17-19,20-24,25-28} SHS refers to the process in which the coherent second harmonic (SH) signal generated by a particle is scattered by the particle itself because its size is comparable to, or smaller than, the wavelength used in the experiment. As a coherent second-order optical process, second harmonic generation (SHG) is intrinsically interface sensitive. In the electric dipole approximation, when the bulk presents a center-of-inversion symmetry, the surface is the sole source of SHG.

In the past, SHG has been used extensively to study adsorption of molecules to planar metallic surfaces, including polycrystalline gold surfaces in aqueous solutions.²⁹⁻³⁴ In earlier works, our group has shown that adsorption and reaction of thiol molecules on the surface of metallic particles in colloidal solutions can be characterized by SHS.²⁵⁻²⁶ The SH signal detected in those experiments has been shown to be predominantly from the surface layer of atoms of the Ag NPs.²⁵ With the surface origin of the SH signal established, SHS was then used to probe the adsorption reaction of a neutral thiol, 1,2-benzenedithiol, on Ag NPs and to determine the adsorption free energy, saturation density, and reaction activation energy.²⁶

In this paper, we report the characterization of the adsorption reaction of (negatively) charged thiols onto citrate-stabilized Ag NPs. An alkanethiol molecule with a sulfonate end group (SO^{3-}), such as 3-mercaptopropanesulfonate (MPS), has low pKa ($\text{pKa} \leq 1$).³⁵ In our experimental conditions, the pH of the Ag NP-containing solution is 6.6 (which only decreases slightly after thiol adsorption) at which little to no MPS is in neutral form.³⁶ Through SHS measurements, supported by results from other complementary techniques, we demonstrate that this sulfonated thiol is able to chemisorb to the Ag NP surface and further stabilize the Ag NPs by replacing the physisorbed citrate ions and thus increasing the amount of negative charges on the surface. The higher stability may facilitate the use of MPS-adsorbed Ag NPs as more effective intermediates for surface modification. Most importantly, it is shown that, due to the presence of charges, the mechanism of adsorption of charged thiols is much different from that of neutral thiols.^{25, 26} Knowledge of how the nature of the end group affects the adsorption of a molecule on the particle surface can therefore be used to guide the particle modification. In general terms, thiolation of molecules is increasingly used in concert with the use of metallic nanoparticles for many different technological applications. As an example, thiolation of small molecules, peptides, and proteins is used for therapeutic applications, and thus it becomes very important to know to which extent these molecules can actually adsorb to the surface of said nanoparticles because of repulsive or steric intermolecular interactions induced by the presence of certain end groups.³⁷

2 METHODOLOGY

2.1 Chemicals

Sodium citrate dehydrate (99%) and sodium 3-mercaptopropanesulfonate (MPS, 90%) were purchased from Sigma-Aldrich®. Deionized water (18.2 M Ω) was prepared in the laboratory using a Barnstead™ E-Pure™ Ultrapure Water Purification system (Thermo Scientific™; Waltham, MA).

2.2 Silver nanoparticles synthesis

A modified procedure by Lee and Meisel was used to prepare silver nanoparticles.³⁸ Approximately 110 mg of AgNO_3 were dissolved in 400 mL of deionized water (18M Ω -cm) and placed in a 1-liter 3-neck flask. Separately, 10 mL of 1% by weight trisodium citrate solution was placed in an addition funnel, which was attached to a second neck of the flask. Additionally, in order to minimize evaporation losses, a condenser tube was placed on the center neck of the flask. The solution was then heated to 100 °C using a heating jacket and temperature controller (Glas-Col; Terre Haute, IN), while magnetically stirring and refluxing. Upon reaching the boiling point, the trisodium citrate solution was added drop-wise. Heating continued for an additional hour at 100 °C. Finally, the heating jacket was removed and the solution was stirred for an additional hour at room temperature. The concentration of the silver colloid was estimated to be 0.3 mg/mL.

2.3 Extinction spectra

Ultraviolet-Visible spectra have been recorded at room temperature using a UV-1800 spectrophotometer (Shimadzu Scientific Instruments; Columbia, MD).

2.4 Transmission electron microscope

The morphology of the Ag NPs has been examined by transmission electron microscope (TEM) (JEOL JEM-1400). One drop of the sample was dried on the surface of a Cu grid covered with a formvar carbon film. TEM images were taken at an accelerating voltage of 120 kV.

2.5 Dynamic light scattering and zeta potential measurements

Hydrodynamic size and zeta potential (ζ) of Ag NPs have been measured by dynamic light scattering (DLS) using a Zetasizer Nano ZSP (Malvern; Worcestershire, UK) with disposable folded capillary cells. Measurements were conducted at (25.0 ± 0.1) °C with the 632.8 nm laser output. A total of three measurements were acquired for each sample, and their average value is reported in this work.

2.6 Ag NPs colloid preparation

Before the experiments, the Ag NPs colloidal solutions were pretreated with dialysis to remove the chemicals left over from the synthesis. It has been experimentally observed that as citrate concentration increases, the ζ becomes more negative up to $[\text{citrate}] = 30 \mu\text{M}$, above which no further change in $\zeta = (-37.2 \pm 1.4)$ mV is observed. Hence, we chose to stabilize our stock solution using a citrate concentration equal to $30 \mu\text{M}$. For dialysis, a sulfur-free Spectra/Por® 7 regenerated cellulose (RC) membrane (Spectrum® Laboratories, Inc.; Rancho Dominguez, CA) was used (MWCO 2000). After soaking for 30 minutes with high volumes of deionized water, the dialysis membrane was loaded with Ag NPs, and then placed in the dialysis buffer, $30 \mu\text{M}$ citrate solution, at a volume equal to 200 times of the original sample. A clean magnetic stir bar was used to stir the entire solution. Every 30 minutes the dialysis buffer was refreshed and the whole procedure repeated 8 times. The dialysis treatment appeared not to influence the UV-Vis and two-photon emission spectra of the Ag NPs. Unless otherwise specified, all Ag NPs in this work were used after diluting 40 times this stock solution. We have compared the two-photon emission spectra as well as UV-Vis spectra of dialyzed and undialyzed samples and concluded that dialysis does not influence the optical properties of the Ag NP colloidal solution.

2.7 Second harmonic scattering

The experimental setup used in this work has been described previously.^{25,26} Briefly, the fundamental light at a wavelength of ~ 800 nm was provided by a femtosecond Ti:Sapphire laser (oscillator only, Micra-5™, Coherent®; Santa Clara, CA) whose average output was 300 mW with 130 fs pulse duration and a 78 MHz repetition rate. The laser was focused down to a spot size of $\sim 40 \mu\text{m}$ into the sample. The sample was either contained inside a Starna quartz cell (1-cm path length) and stirred with a magnetic bar methods or continuously flown by a micropump producing a liquid-jet column of ~ 1 mm diameter. In both cases, the signal was collected within $\sim \pi/4$ solid angle around the forward (fundamental beam propagation) direction. A long pass filter was used to remove higher harmonic contributions from the fundamental beam before the sample and a band pass filter (Schott, BG39, 340-600 nm) was used to remove the fundamental contribution in the scattered light detected from the sample. The detection system included a spectrometer (Acton SP2300, Princeton Instruments; Trenton, NJ), photomultiplier tube (PMT) (R1527, Hamamatsu), fast preamplifier (350MHz, SR445A, Stanford Research Systems; Sunnyvale, CA), and a photon counting system (SR400, Stanford Research Systems). All data were recorded employing an ad-hoc LabVIEW (National Instruments®; Austin, TX) program. Since in our spectra the SH emission peak has always been superimposed to a broad two-photon fluorescence background, in order to extract the pure SHS signal, the emission spectrum was fitted using the sum of a squared Gaussian function for the 400 nm (SH) peak and a regular Gaussian function for the two-photon fluorescence for the determination of the SH intensity.

2.8 Isothermal adsorption experiments

Since MPS adsorption on citrate-stabilized Ag NPs is very slow, the experiments measuring SH signal as a function of thiol concentration were performed as follows. 800 mL of Ag NPs solution was equally distributed into 40 test tubes, each containing a final volume equal to 20 mL. An aqueous stock solution of MPS was prepared at a concentration of 2.5 mM, and different aliquots of this stock solution were added to the 40 tubes so that the final MPS concentration in the tubes ranged from 0 to $50 \mu\text{M}$. The tubes were shaken at 100 rpm at 25 °C for 12 hours. The SHS

data showed no further change in the signal intensity after 12 hours. The content of each tube was then used to fill the reservoir of our liquid jet setup.

2.9 Temperature controlled time-resolved experiments

To control the temperature precisely, a quartz fluorimeter cell (1-cm path length 62F-Q-10 from Starna Cells, Inc.) was employed. By tuning the temperature of the water flowing through the cell jacket, it was possible to precisely control the temperature of the sample from 20-60 °C. The actual temperature of the solution was measured using a thermocouple. At a given temperature, 1.5 mL of the Ag NPs colloidal solution was added into the cell. The SHS signal intensity as a function of time at the SH wavelength was collected after the addition of an aliquot of MPS stock solution chosen in such a way that the final concentration of MPS in the cell equaled 50 μM . A magnetic bar was used to stir the sample continuously during the experiment.

3 DATA AND RESULTS

The spectrum of the scattered light from citrate-stabilized Ag NP colloidal solutions detected upon 800 nm light excitation is known to contain two distinct contributions: A peak at 400 nm assignable to the SH signal and a much broader peak at longer wavelengths attributed to the two-photon excitation induced fluorescence (TPF).²⁵ The SH wavelength (400 nm) is in resonance with the localized surface plasmon (LSP) of Ag NPs in the size range used in this experiment and provides resonant enhancement for the SH signal. Similar to previous studies on neutral thiols, the surface origin of the SHS signal can be experimentally confirmed by the observation of a decrease in the SH intensity upon adsorption of thiols on the Ag NP surface.²⁵ Such decrease, up to 78% in the case of the MPS thiol, can be attributed to the localization of the NP surface electrons upon formation of the Ag-S bond and consequent reduction of the second order polarization.

As previously demonstrated, the adsorption of thiols on noble metal NPs can be characterized by the adsorption isotherm measured using SHS. Figure 1A shows the dependence of the SH intensity as a function of the concentration of MPS in the colloidal solution. The magnitude of the SH intensity can be related to the thiol coverage on the surface.³⁹ Previous studies of the neutral thiol 1,2-benzenedithiol showed the typical Langmuir adsorption behavior as revealed by the monotonic, exponential-like decay of the SHS signal as the thiol concentration in the colloidal solution is increased.²⁵ The SHS adsorption isotherm in the case of MPS is, however, dramatically different. The SH signal decreases by 56% when [MPS], the bulk MPS concentration, is initially increased from 0 μM to 0.12 μM . Further increase of [MPS] up to 1.0 μM induces no detectable change in the SHS signal. However, when [MPS] is increased between ~ 1 μM and 10 μM , the SH intensity appears to decrease by another 22% until saturation is finally reached.

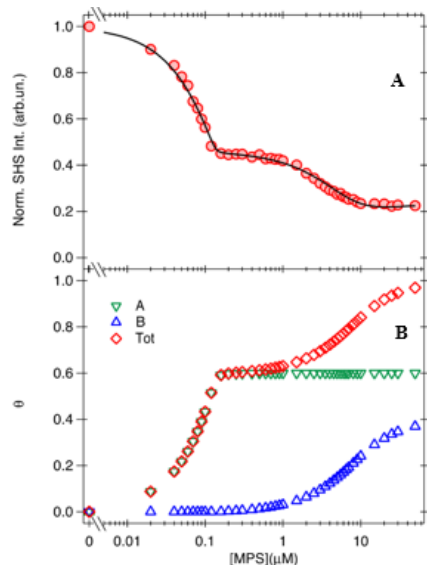


Figure 1. A) The SHS intensity, set as unity for the intensity detected with no MPS, measured as a function of the MPS concentration. B) θ_A (blue points), θ_B (green), and the total coverage θ (red) obtained from the best fit, shown in A) as the solid line, of the SHS intensity to Equation 3.

The observed behavior of the SHS signal strongly suggests that the adsorption of MPS on the Ag NP surface proceeds through a two-step mechanism as the surface MPS coverage changes in response to the changing MPS concentration. To verify the speculation that there are two stages in the adsorption process from the appearance of the adsorption isotherm, we examine the kinetics associated with the MPS adsorption. Time-dependent observation of the SH intensity, which can be quantitatively related to the thiol surface coverage, at a fixed [MPS] reveals how fast the thiol can adsorb onto the particle surface. The temperature dependence of this adsorption rate process allows the determination of the activation energy of the adsorption reaction. Figure 2A shows the SH intensity response as a function of time following the addition of a fixed amount of MPS to the colloidal solution corresponding to a 50 μM bulk concentration. Briefly, the SH intensity rapidly decays at first and then continues decreasing at a much slower rate. As the analysis below shows, these measurements made over a wide range of MPS concentrations are consistent with a two-stage mechanism for the adsorption of MPS.

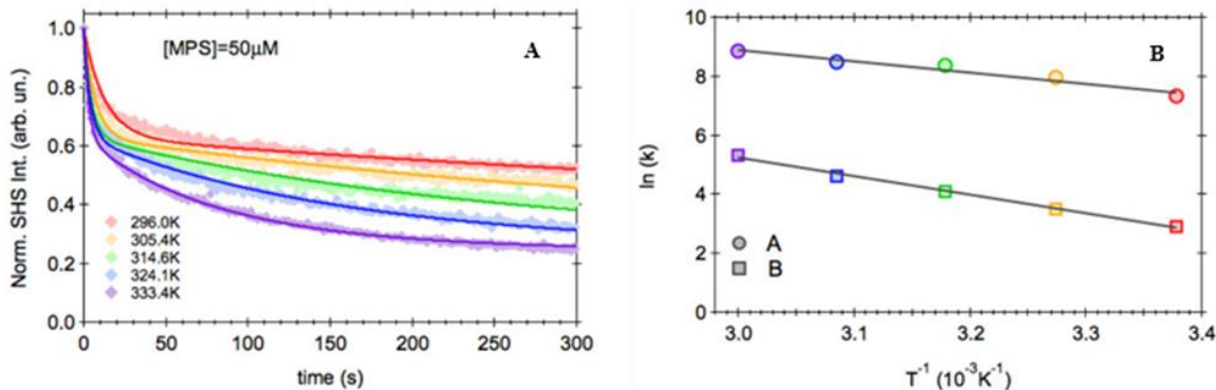


Figure 2. A) The normalized SHS intensity as a function of time following the addition at $t = 0$ of [MPS] = 50 μM recorded at the specified constant temperature: (red) 296.0 ± 0.1 K, (yellow) 305.4 ± 0.1 K, (green) 314.6 ± 0.1 K, (blue) 324.1 ± 0.1 K, and (purple) 333.4 ± 0.1 K. Continuous lines are the best simultaneous fit to Equation 5. B) Arrhenius plot of the adsorption rate constants: circle points are related to $k_{A,1}$ and squares $k_{B,1}$, while the continuous lines are the best fit to the Arrhenius Equation.

The ζ of the particles is measured to characterize the surface charges. Since MPS and citrate are both anions, it is important to understand the role of citrate in the MPS adsorption process. First, for comparison purposes, ζ was measured for colloidal solutions with different citrate concentrations but without MPS (see Methodology). Next, ζ was measured as a function of [MPS] for the Ag colloidal solutions stabilized using two different citrate concentrations: 30 μM , the one also used to stabilize the Ag NPs in Figure 1A, and 0.5 μM , at which the surface charge density of Ag NPs is expected to be lower. As illustrated in Figure 3A, ζ varies with the citrate concentration. At [citrate] = 30 μM , the surface is saturated with citrate (see Methodology), $\zeta = -(32.9 \pm 0.6)$ mV before the MPS addition. For [citrate] = 0.5 μM , also without MPS, $\zeta = -(17.2 \pm 0.3)$ mV, reflecting less citrate on the particle surface. Besides an offset in the absolute value of ζ , the two sets of data measured as a function of [MPS] show very similar behaviors. For $0 < [\text{MPS}] < 0.1$ μM , the ζ value becomes more negative with increasing [MPS]; for [MPS] > 0.1 μM , the ζ value fluctuates but appears unchanged until [MPS] > 5 μM , where ζ shifts to more positive values. The change of the ζ value as a function of [MPS] mirrors the differences in the adsorption isotherm in the three [MPS] ranges. The ζ measurements also suggest different adsorption behaviors in the two [MPS] regions, below ~ 0.1 μM and higher than ~ 1 μM , where adsorption occurs.

The SHS adsorption isotherm is also measured at these two citrate concentrations, 30 μM and 0.5 μM , for comparison. The results are shown in Figure 3B. The two SHS adsorption isotherms appear to be very similar despite the substantial difference in the citrate concentration and absolute values of ζ .

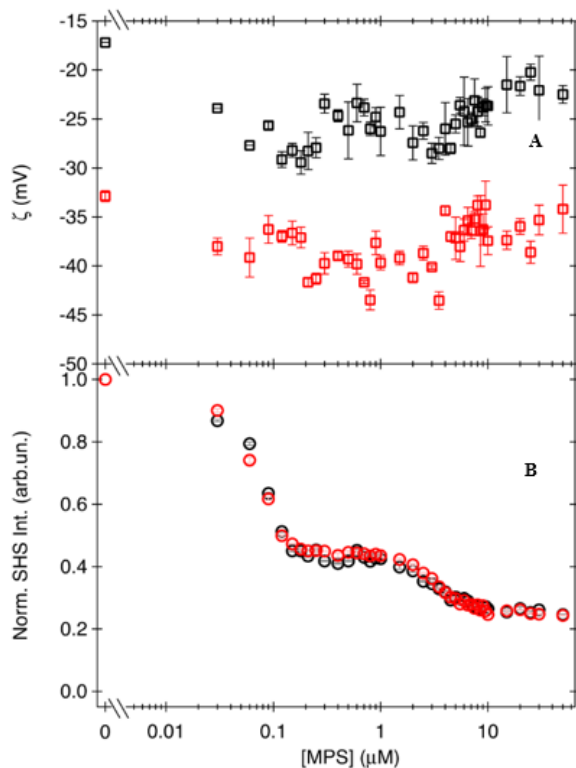


Figure 3. A) Zeta potential (ζ) of the Ag NP colloidal solution measured as a function of the MPS concentration with the citrate concentration set at 0.5 μM (black points) and 30.0 μM (red). B) The corresponding SHS intensities (with the intensities measured for the MPS = 0 solutions set as unity).

As the experimental results strongly suggest that the charged thiols adsorb with two different mechanisms in different concentrations, we model the adsorption as a sum of two reactions, each associated with a specific site with its own adsorption characteristics – density, free energy change, and activation energy:



In Equation 1, MPS (T) adsorbs onto empty surface sites (ES_i) on the Ag NP surface (where $i = A, B$), resulting in a MPS-occupied i site (TS_i). The relation between $[\text{MPS}]$ and the amount of surface adsorbed thiol determined through the two adsorption reactions can be mathematically described using two distinct Langmuir adsorption processes. Here, the depletion of MPS in the bulk solution is taken into account.¹⁶ The two equilibrium constants can be expressed as:

$$K_A = \frac{\theta_A N_{max}}{N_{max}(\theta_{Amax} - \theta_A)(x - \theta N_{max})} \quad (2a)$$

$$K_B = \frac{\theta_B N_{max}}{N_{max}(\theta_{Bmax} - \theta_B)(x - \theta N_{max})} \quad (2b)$$

where x is the $[\text{MPS}]$, K_i is the equilibrium constants corresponding to the reactions in (1), N_{max} is the maximum number density of bonding sites available to MPS (including both A and B sites), and θ_i is the fraction of the i sites covered by MPS ($\theta = \theta_A + \theta_B$), while θ_{imax} (with $\theta_{imax} + \theta_{imax} = 1$) is the maximum fraction of i sites at surface saturation.

Considering the change in the surface nonlinear response of the Ag NPs is proportional to the surface coverage of thiols, the SH intensity can be expressed as:^{25,30,34,39,40}

$$I(2\omega) \propto |\chi_{Ag} - \chi_{SAT}(\theta_A + \theta_B)e^{i\theta}|^2 \quad (3)$$

where χ_{Ag} represents the susceptibility of the bare Ag NP, χ_{SAT} is the decrease in Ag surface susceptibility induced by thiol adsorption at the saturation coverage, and, φ , the phase difference between these two susceptibilities, is present here because the two susceptibilities carry different contributions: χ_{Ag} represents both surface and possibly bulk contributions from the Ag NP, while χ_{SAT} has a pure surface origin and is influenced by the chemisorption of thiols.²⁸ With respect to observables in a time-dependent experiment, the rate equations below are used for the description of the amount of thiols on the surface:

$$\frac{d\theta_A}{dt} = k_{A,1}(\theta_{Amax} - \theta_A)C - k_{A,-1}\theta_A \quad (4a)$$

$$\frac{d\theta_B}{dt} = k_{B,1}(\theta_{Bmax} - \theta_B)C - k_{B,-1}\theta_B \quad (4b)$$

where $k_{i,1}$ and $k_{i,-1}$ ($i = A, B$) are the rate constants for adsorption and desorption at the surface site i , respectively. $C = [\text{MPS}]$ is a constant since at very high concentration, depletion of the thiols in the solution due to surface adsorption is negligible. By solving Equation 4, we obtain the analytical expression of the surface coverage θ_i as a function of time:

$$\theta_A = \theta_A (1 - e^{-(k_{A,1}C + k_{A,-1})t}) \quad (5a)$$

$$\theta_B = \theta_B (1 - e^{-(k_{B,1}C + k_{B,-1})t}) \quad (5b)$$

where θ_i ($i = A, B$) is the final coverage for site i at $[\text{MPS}] = C$. Given the fact that $k_{i,1} \ll k_{i,-1}$, $k_{i,-1}$ can be ignored, and it is thus possible to plot $k_{i,1}$ as a function of the reciprocal of the temperature.²⁶ Equation 3, after substituting θ_A and θ_B from Equation 2, can be used to fit the experimental SHS adsorption isotherm shown in Figure 1A. The parameters from a nonlinear least-squares fitting of the data, K and $\theta_{max} N_{max}$, together with some derived quantities such as the Gibbs free energy change, ΔG_{ads} , and the molecular surface density defined as $\Gamma_{max} = N_{max}\theta_{max}/(4\pi R^2\eta)$ (with R the average NP radius and η the particle density in the colloid), are listed in Table 1.

Table 1. Parameters (θ_{max} , N_{max} , K , E_a) extracted from the nonlinear fitting and the derived quantities the molecular surface density (Γ_{max}) and Gibbs free energy change (ΔG_{ads}).

Parameter	Site A	Site B
$\theta_{max} N_{max}$ (μM)	0.13 ± 0.01	0.10 ± 0.01
Γ_{max} (cm^{-2})	$(2.2 \pm 0.2) \times 10^{14}$	$(1.6 \pm 0.2) \times 10^{14}$
K (M^{-1})	$(5.8 \pm 2.8) \times 10^{10}$	$(3.1 \pm 0.4) \times 10^5$
ΔG_{ads} (kcal/mol)	-14.3 ± 0.3	-7.4 ± 0.1
E_a (kcal/mol)	7.5 ± 0.9	12.4 ± 0.5

ΔG_{ads} for A and B sites are (-14.3 ± 0.3) kcal/mol and (-7.4 ± 0.1) kcal/mol, respectively. Note that the large difference in the two ΔG_{ads} , 6.9 kcal/mol, can be attributed to the effects of electrostatic and steric repulsions at the two adsorption sites (see below). The A- and B-site surface densities at saturation coverage are $(2.2 \pm 0.2) \times 10^{14}$ MPS/cm² and $(1.6 \pm 0.2) \times 10^{14}$ MPS/cm², respectively. The calculated coverage θ_i , for both A and B sites, as well as the total coverage θ as a function of [MPS], calculated using the parameters from the fitting, are shown in Figure 1B. Our calculation is based on the assumption that all Ag NPs have a spherical shape with a diameter of exactly 80 nm. In reality, however, the size of the particles measured by dynamic light scattering (DLS) is (80 ± 20) nm and TEM images indicate a polyhedral shape. Therefore, in our calculations we underestimate the total surface area of the particles and this, in turn, produces an overestimation of the surface coverage. This can explain why our $\Gamma_{Tot max} = \Gamma_{Amax} + \Gamma_{Bmax}$ is larger than the value of 2.20×10^{14} molecules/cm² found for the sodium 2-mercaptoethane sulfonate monolayer on rough Au thin film.⁴¹ However, the value of $\Gamma_{Tot max}$ found for MPS in this work is still smaller than the one reported for a densely packed self-assembled monolayer (SAM) of ethanethiolate on Ag(111), namely 4.7×10^{14} molecules/cm², and what our group previously obtained, 7×10^{14} molecules/cm², for 1,2-benzenedithiol on Ag NPs.^{25,42,43} Note that both ethanethiolate and 1,2-benzenedithiol are neutral molecules. By the simultaneous fit of the time dependent SHS data in Figure 2A with Equation (3), after substituting for θ_i the expression in Equation (5), it is possible to obtain $k_{i,1}$ at each temperature. $k_{i,1}$ as a function of the inverse of the absolute temperature can be analyzed using the Arrhenius equation (Figure 2B) for the determination of the activation energy of chemisorption to A and B sites as (7.5 ± 0.9) kcal/mol and (12.4 ± 0.5) kcal/mol, respectively (Table 1).

It is important to note that the adsorption model proposed must be consistent with these observations: In the low MPS concentration regime the adsorption has a larger free energy change (in magnitude) but smaller activation energy, and the particle surface becomes more negatively charged as [MPS] increases. In the higher concentration regime, the second stage of adsorption, the free energy change is smaller in magnitude but the activation energy larger and the particle surface is less negatively charged. We propose a mechanism based on the effect of electrostatic and steric repulsion by adsorbed charged thiols and the presence of the surfactant citrate at the particle surface.

The adsorption of *n*-alkanethiols on metal surfaces has been studied both in ultra-high vacuum and in solution conditions.^{11,44-47} In a solution, adsorption is proposed to occur through a sequence of steps: (i) physisorption with displacement of original surfactants off the surface, (ii) formation, in the absence of strong hydrophobic effects and lateral chain interactions, of disordered sub monolayers at low coverage, and finally, (iii) the increase in coverage induces a rapid increase in intermolecular interactions, and eventually leads to a formation of an ordered full monolayer.¹¹ Because of the amphiphilic nature of *n*-alkanethiolates, the intermolecular interaction includes both attractive (i.e., lateral forces between hydrocarbon chains) and repulsive (i.e., sulfonate endgroup repulsion) forces. Depending on the coverage, further adsorption of a thiol is either favored when attraction forces dominate, or disfavored when repulsion dominates.^{42,43} In this study, the short chain ($n = 3$) and negatively-charged terminus of MPS present unique considerations for the adsorption. Consequently, we propose a different adsorption mechanism for MPS. MPS has a short chain and intense repulsive interaction: The sulfonate endgroup provides not only a long-range electrostatic repulsion, but also a short-range steric repulsion.⁴¹

The nearly constant SHS signal observed for the range $0.12 \mu\text{M} < [\text{MPS}] < 1.0 \mu\text{M}$, in between the two adsorption regimes, can be best described by assuming that MPS adsorption on Ag NPs comes to a halt because the molecules have to overcome a large energy barrier compared to what is required at lower coverage in order to bind to the Ag NP surface. We thus postulate that the intermolecular electrostatic and steric repulsion is the origin of such barrier.^{42,43,48} The model schematically depicted in Figure 4 reflects the evolution of the surface environment upon the adsorption of short-chain, negatively charged thiol molecules.

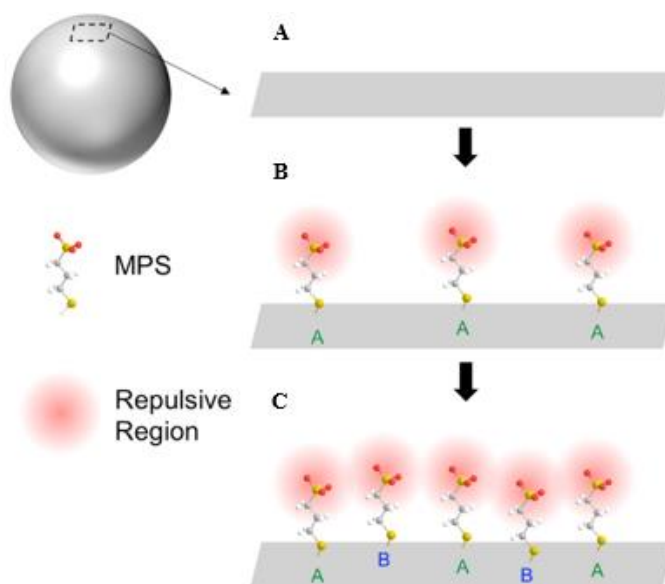


Figure 4. Schematic representation of the two adsorption stages of the negatively-charged thiol MPS on a Ag NP surface.

At low coverage, the intermolecular distance among adsorbed thiols at the A sites (see Figure 4) is large enough so that the repulsive interaction is negligible. However, the surface coverage will build up until a critical coverage where the intermolecular repulsion prevents further adsorption is reached. When the MPS concentration in solution increases above a critical value, sufficient driving force is generated and further surface adsorption on B sites (Figure 4) occurs.

The Gibbs free energy (ΔG_{ads}) for charged thiol adsorption on metal surfaces in aqueous solution is affected by its solvation in the liquid, intermolecular interactions at the surface that have both attractive and repulsive contributions, and the formation of the metal-S bond.^{9,12,43} In addition, displacement of surfactants (water, citrate, etc.) also

contributes to ΔG_{ads} .⁴³ In contrast, the activation energy is associated with the particular step that contributes most to the energy barrier for the chemisorption process.

At low coverage, the MPS molecules are, on average, far apart and the interaction between adjacent MPS molecules is negligible. Hence, inter-thiol repulsion is minimized and its impact on the activation energy is relatively low. On the other hand ΔG_{ads} is dominated by the energy of formation of the Ag-S bond and, subsequently, the magnitude of the free energy is larger.

When the surface coverage is higher, intermolecular interactions have to be taken into account. It is reasonable to anticipate that the repulsion is larger than the attraction at the higher coverage. Compared with the A site, the B site's free energy change magnitude will be smaller. The reduction in $|\Delta G_{\text{ads}}|$ between A and B sites by 6.9 kcal/mol represents the contribution from the repulsive interactions (i.e., the sum of electrostatic and steric repulsions minus the change induced by the increased concentration of MPS in the solution). In contrast, the repulsion will cause the activation energy to be higher (increase from (7.5 ± 0.9) kcal/mol to (12.4 ± 0.5) kcal/mol) as it prevents the incoming charged thiol molecule getting close to the surface for the bond formation.

The measured relative values of the adsorption free energy and the activation energy are consistent with the proposed model. It should also be pointed out that the adsorption of MPS on the NP surface does not deplete the nearby thiols in the solution, at least for the higher concentrations, so that diffusion is not the rate-determining step and not the source of the activation energy.²⁶ The activation energy for the neutral 1,2-benzenedithiol on Ag NPs was previously found to be (8.4 ± 0.3) kcal/mol.²⁶ The adsorption of decanethiol on Au(111) from ethanol has been reported to have an activation energy of 7.1 kcal/mol,⁴⁹ while an activation energy of 6.9 kcal/mol has been observed for several alkanethiol groups on Au(111) in ultrahigh vacuum conditions.⁵⁰ It is interesting to note that the activation energies for neutral and anionic thiol adsorptions to A sites are measured to be similar. The process that relates to this activation energy involves solvation, diffusion, intermolecular interactions including electrostatic and van der Waals interactions, near the surface, and molecule-surface interactions including charge/image-charge forces. To discern what is the exact activated process requires proper characterization of each of these interactions and may need molecular dynamics simulation for this complex system, and is beyond the scope of this paper.

One important difference between colloidal systems and the more widely studied flat surfaces is the presence of the electrolytes in the solution because of the need to stabilize the particles in the colloid. Ions like citrate physisorb onto the particle surface and create an electric double layer (EDL) that prevents the particles from aggregating. Since we are studying negatively-charged thiol, the influence of co-ions has to be taken into account. For instance, MPS adsorption has been found to be significantly slower, at least by two orders of magnitudes, than neutral thiols.^{25,26} This is primarily due to the existence of EDL from the citrate co-ion. The competition for adsorption at the particle surface can be revealed from the zeta potential measurements.

In our system, after dialysis (described in details in the Experimental Section), the ions existing in the solution (pH ~6.6) are Na^+ , Cit^{3-} and MPS^- . A one-to-one replacement of Cit^{3-} by MPS^- would produce a less negatively charged particle surface, while replacement of water with MPS^- will lead to an increase of the negative charges of the particle. In the low MPS concentration regime (i.e., the first adsorption phase), the zeta potential measurements indicate that the particle surface is becoming more negatively charged. It is therefore reasonable to conclude that the exchange between water and MPS^- dominates in this phase. As the coverage increases until all sites occupied by water only are filled, exchange between Cit^{3-} and MPS^- takes place and the total surface charge becomes less negative.

The role of citrate on adsorption can be inferred from Figure 3B in which the SHS intensities detected as a function of the MPS concentration in the colloidal solution with two dramatically different citrate concentrations, namely 0.5 μM and 30 μM , are essentially identical. The surface citrate coverages at the two different citrate concentrations are very different, but the adsorption of the thiols occurs at the same rate. It appears evident then that the replacement of citrate does not have major bearing on the adsorption rates and energetics. This seems reasonable based on the fact that citrate is physisorbed and its presence does not significantly affect the S-Ag bonding, which is the origin of the decrease in the SHS signal. The same conclusions can be drawn for the less strongly bonded water on the surface.

Another consideration to keep in mind is that the observed SHS behavior cannot be due to the adsorption of multiple layers. To begin with, adsorption of multilayers of molecules with the same charge is highly unlikely. The adsorption of the first layer will cause the nonlinear polarizability of the metal surface to decrease, while the following layers will have negligible effect on the metal surface nonlinear polarizability. There should not be a two-stage of decreases in SHS as more and more MPS is adsorbed on the Ag NP surface. Furthermore, multi-layer adsorption should cause

a continuous decrease in the ζ , which is not the case. As shown in Figure 3A after an initial decrease, a turning point in ζ is observed and, at higher [MPS], starts increasing.

4 CONCLUSIONS

In summary, the surface sensitive second harmonic light scattering has enabled the characterization of the chemisorption of negatively charged thiol molecule MPS on the surface of Ag colloidal nanoparticles. It is found that the chemisorption of this charged thiol occurs in two different regimes in contrast to that of neutral thiols that show a single Langmuir adsorption isotherm. This two-step adsorption is primarily a result of the charge-charge repulsion among the anionic thiols adsorbed on or near the surface. At low MPS concentration (below 0.1 μM), a low coverage of the charged thiols can be adsorbed onto the surface: The repulsion among adsorbed MPS molecules is small so that the activation energy (7.5 ± 0.9 kcal/mol) is lower and the magnitude of the free energy of adsorption (-14.3 ± 0.3 kcal/mol), dominated by the energy of formation of the Ag-S bond, is relatively large. The adsorbed thiols do not displace the citrate ions physisorbed on the surface, so the particle becomes more negatively charged. The adsorption of thiols stops when the coverage becomes sufficiently high so that the inter-thiol repulsion prohibits further adsorption. As the concentration increases to above 1 μM , sufficient driving force is built up to overcome the inter-thiol repulsion and chemisorption continues. Here, due to increased repulsion the activation energy is bigger, (12.4 ± 0.5) kcal/mol, and the magnitude of the free energy change, (-7.4 ± 0.1) kcal/mol, is smaller. As the thiols now display the more negatively charged citrate, the particle becomes less negatively charged. This study illustrates the importance of repulsive interactions, both electrostatic and steric in origin, in the chemisorption of charged thiols on metallic nanoparticles.

ACKNOWLEDGMENTS

The authors would like to acknowledge U.S. Army funding provided through the Edgewood Chemical Biological Center's Surface Science Initiative Program.

REFERENCES

- [1] Daniel, M.-C. and Astruc, D., "Gold nanoparticles: Assembly, supramolecular chemistry, quantum-size-related properties, and applications toward biology, catalysis, and nanotechnology." *Chemical Reviews*, **2003**, 104, p293-346.
- [2] Halas, N.J. *et al.*, "Plasmons in strongly coupled metallic nanostructures." *Chemical Reviews*, **2011**, 111, p3913-3961.
- [3] Mayer, K.M. and Hafner, J.H., "Localized surface plasmon resonance sensors." *Chemical Reviews*, **2011**, 111, p3828-3857.
- [4] Rycenga, M. *et al.*, "Controlling the synthesis and assembly of silver nanostructures for plasmonic applications." *Chemical Reviews*, **2011**, 111, p3669-3712.
- [5] Rosi, N.L. and Mirkin, C.A. "Nanostructures in biodiagnostics." *Chemical Reviews*, **2005**, 105, p1547-1562.
- [6] Eckhardt, S. *et al.*, "Nanobio silver: Its interactions with peptides and bacteria, and its uses in medicine." *Chemical Reviews*, **2013**, 113, p4708-4754.
- [7] Crudden, C.M. *et al.*, "Ultra stable self-assembled monolayers of N-heterocyclic carbenes on gold." *Nature Chemistry*, **2014**, 6, p409-414.
- [8] Weidner, T. *et al.*, "NHC-based self-assembled monolayers on solid gold substrates." *Australian Journal of Chemistry*, **2011**, 64, p1177-1179.
- [9] Love, J.C. *et al.*, "Self-assembled monolayers of thiolates on metals as a form of nanotechnology." *Chemical Reviews*, **2005**, 105, p1103-1170.

- [10] Nuzzo, R.G. and Allara, D.L., "Adsorption of bifunctional organic disulfides on gold surfaces." *Journal of the American Chemical Society*, **1983**, 105, p4481-4483.
- [11] Schreiber, F., "Structure and growth of self-assembling monolayers." *Progress in Surface Science*, **2000**, 65, p151-257.
- [12] Ulman, A., "Formation and structure of self-assembled monolayers." *Chemical Reviews*, **1996**, 96, p1533-1554.
- [13] Volkert, A.A. *et al.*, "Salt-mediated self-assembly of thioctic acid on gold nanoparticles." *ACS Nano*, **2011**, 5, p4570-4580.
- [14] Stewart, A. *et al.*, "Controlling assembly of mixed thiol monolayers on silver nanoparticles to tune their surface properties." *ACS Nano*, **2012**, 6, p3718-3726.
- [15] Yoshida, A.; Yonezawa, Y.; and Kometani, N., "Tuning of the spectroscopic properties of composite nanoparticles by the insertion of a spacer layer: Effect of exciton-plasmon coupling." *Langmuir*, **2009**, 25, 6683-6689.
- [16] Wang, H. *et al.*, "Second harmonic generation from the surface of centrosymmetric particles in bulk solution." *Chemical Physics Letters*, **1996**, 259, p15-20.
- [17] Jen, S.-H. and Dai, H.-L., "Probing molecules adsorbed at the surface of nanometer colloidal particles by optical second-harmonic generation." *Journal of Physical Chemistry B*, **2006**, 110, p23000-23003.
- [18] Jen, S.-H.; Gonella, G.; and Dai, H.-L., "The effect of particle size in second harmonic generation from the surface of spherical colloidal particles. I: Experimental observations." *Journal of Physical Chemistry A*, **2009**, 113, p4758-4762.
- [19] Jen, S.-H.; Dai, H.-L.; and Gonella, G., "The effect of particle size in second harmonic generation from the surface of spherical colloidal particles. II: The nonlinear Rayleigh-Gans-Debye model." *Journal of Physical Chemistry C*, **2010**, 114, p4302-4308.
- [20] Eisenthal, K.B., "Second harmonic spectroscopy of aqueous nano- and microparticle interfaces." *Chemical Reviews*, **2006**, 106, p1462-1477.
- [21] Ray, P.C., "Size and shape dependent second order nonlinear optical properties of nanomaterials and their application in biological and chemical sensing." *Chemical Reviews*, **2010**, 110, p5332-5365.
- [22] Brevet, P.F., "Second harmonic generation in nanostructures." In: *Handbook of Nanoscale Optics and Electronics*, 1st ed., Wiederrecht, G.P. (ed.). Elsevier: Amsterdam, Massachusetts. **2010**. p77-105.
- [23] Roke, S. and Gonella, G., "Nonlinear light scattering and spectroscopy of particles and droplets in liquids." *Annual Review of Physical Chemistry*, **2012**, 63, p353-378.
- [24] Gomopoulos, N. *et al.*, "Label-free second harmonic and hyper Rayleigh scattering with high efficiency." *Optics Express*, **2013**, 21, p815-821.
- [25] Gan, W. *et al.*, "Reactions and adsorption at the surface of silver nanoparticles probed by second harmonic generation." *Journal of Chemical Physics*, **2011**, 134(4), e041104.
- [26] Gan, W.; Xu, B.; and Dai, H.-L., "Activation of thiols at a silver nanoparticle surface." *Angewandte Chemie International Edition*, **2011**, 50, p6622-6625.
- [27] Gonella, G. *et al.*, "The effect of composition, morphology, and susceptibility on nonlinear light scattering from metallic and dielectric nanoparticles." *Journal of Physical Chemistry Letters*, **2012**, 3, p2877-2881.
- [28] Gonella, G. and Dai, H.-L., "Second harmonic light scattering from the surface of colloidal objects: Theory and applications." *Langmuir*, **2013**, 30, 2588-2599.
- [29] Corn, R.M. and Higgins, D.A., "Optical second harmonic generation as a probe of surface chemistry." *Chemical Reviews*, **1994**, 94, 107-125.
- [30] Camillone, N., "Diffusion-limited thiol adsorption on the gold(111) surface." *Langmuir*, **2004**, 20(4), p1199-1206.

- [31] Dounce, S.M.; Yang, M.; and Dai, H.-L., "Physisorption on a metal surface probed by surface state resonant second harmonic generation." *Surface Science*, **2004**, 565, p27-36.
- [32] Heskett, D. *et al.*, "Oxygen and pyridine on Ag(110) studied by second harmonic generation: Coexistence of two phases within monolayer pyridine coverage." *Surface Science*, **1988**, 197, p225-238.
- [33] Karpovich, D.S. and Blanchard, G.J., "Direct measurement of the adsorption kinetics of alkanethiolate self-assembled monolayers on a microcrystalline gold surface." *Langmuir*, **1994**, 10, p3315-3322.
- [34] Dannenberger, O.; Buck, M.; and Grunze, M., "Self-assembly of n-alkanethiols: A kinetic study by second harmonic generation." *Journal of Physical Chemistry B*, **1999**, 103, p2202-2213.
- [35] Guthrie, J.P., "Hydrolysis of esters of oxy acids: pKa values for strong acids; Brønsted relationship for attack of water at methyl; free energies of hydrolysis of esters of oxy acids; and a linear relationship between free energy of hydrolysis and pKa holding over a range of 20 pK units." *Canadian Journal of Chemistry*, **1978**, 56, p2342-2354.
- [36] Campen, R.K. *et al.*, "Linking surface potential and deprotonation in nanoporous silica: Second harmonic generation and acid/base titration." *Journal of Physical Chemistry C*, **2010**, 114, p18465-18473.
- [37] Davis, M.E.; Chen, Z.; and Shin, D.M., "Nanoparticle therapeutics: An emerging treatment modality for cancer." *Nature Reviews: Drug Discovery*, **2008**, 7, p771-782.
- [38] Lee, P.C. and Meisel, D., "Adsorption and surface-enhanced Raman of dyes on silver and gold sols." *Journal of Physical Chemistry*, **1982**, 86(17), p3391-3395.
- [39] Wang, H.F. *et al.*, "Energetics and population of molecules at microscopic liquid and solid surfaces." *Journal of Physical Chemistry B*, **1998**, 102, p4446-4450.
- [40] Campen, R.K. *et al.*, "Second harmonic generation as a probe of multisite adsorption at solid-liquid interfaces of aqueous colloid suspensions." *Journal of Physical Chemistry C*, **2007**, 111, p8805-8813.
- [41] Rouhana, L.L.; Moussallem, M.D.; and Schlenoff, J.B., "Adsorption of short-chain thiols and disulfides onto gold under defined mass transport conditions: Coverage, kinetics, and mechanism." *Journal of the American Chemical Society*, **2011**, 133, p16080-16091.
- [42] Hatchett, D.W. *et al.*, "Electrochemical oxidative adsorption of ethanethiolate on Ag(111)." *Journal of the American Chemical Society*, **1997**, 119, p6596-6606.
- [43] Hatchett, D.W. *et al.*, "Electrochemical measurement of the free energy of adsorption of n-alkanethiolates at Ag(111)." *Journal of the American Chemical Society*, **1998**, 120, p1062-1069.
- [44] Schreiber, F. *et al.*, "Adsorption mechanisms, structures, and growth regimes of an archetypal self-assembling system: Decanethiol on Au(111)." *Physical Review B*, **1998**, 57(19), p12476-12481.
- [45] Bain, C.D. *et al.*, "Formation of monolayer films by the spontaneous assembly of organic thiols from solution onto gold." *Journal of the American Chemical Society*, **1989**, 111, p321-335.
- [46] Laibinis, P.E. *et al.*, "Comparison of the structures and wetting properties of self-assembled monolayers of n-alkanethiols on the coinage metal surfaces, copper, silver, and gold." *Journal of the American Chemical Society*, **1991**, 113, p7152-7167.
- [47] Schlenoff, J.B.; Li, M.; and Ly, H., "Stability and self-exchange in alkanethiol monolayers." *Journal of the American Chemical Society*, **1995**, 117, p12528-12536.
- [48] Calvente, J.J. *et al.*, "Desorption of spontaneously adsorbed and electrochemically readsorbed 2-mercaptoethanesulfonate on Au(111)." *Langmuir*, **1996**, 12, p5696-5703.
- [49] Han, Y. and Uosaki, K., "Effects of concentration and temperature on the formation process of decanethiol self-assembled monolayer on Au(111) followed by electrochemical reductive desorption." *Electrochimica Acta*, **2008**, 53, p6196-6201.
- [50] Lavrich, D.J. *et al.*, "Physisorption and chemisorption of alkanethiols and alkyl sulfides on Au(111)." *Journal of Physical Chemistry B*, **1998**, 102, p3456-3465.

Understanding the effect of substrate material and solvation on surface-enhanced Raman spectroscopy enhancement

Jason Guicheteau^a, Ashish Tripathi^b, Erik Emmons^a, Augustus W. Fountain, III^a,
Steven Christesen^{a*}

^aU.S. Army Edgewood Chemical and Biological Center, Research & Technology Directorate,
5183 Blackhawk Rd, Aberdeen Proving Ground, MD 21010

^bLeidos, Inc., P.O. Box 68, Gunpowder Branch, Aberdeen Proving Ground, MD 21010

ABSTRACT

Surface-enhanced Raman spectroscopy (SERS) is a useful technique for probing analyte-noble metal interactions and determining thermodynamic properties such as their surface reaction equilibrium constants and binding energies. However, in order to predict the SERS activity of molecules, it is important to understand the nature of the binding of these compounds to the noble metal surface. In this effort we have studied the binding of several nitrogen containing aromatic chemicals to nanostructured gold surfaces from aqueous media. These studies have revealed that a complex equilibrium state exists between the molecules and the gold surface that cannot be explained by a simple Langmuir isotherm. The peak area of selected Raman features versus concentration data of each of the chemical analyzed suggests two equilibrium states. The two equilibrium states could be attributed to concentration dependent arrangements/orientation and/or two types of adsorption sites: Nucleophilic and Electrophilic.

Keywords: SERS, Langmuir isotherm, dual site, enhancement factor

1 INTRODUCTION

Surface-enhanced Raman spectroscopy (SERS), the enhancement of the Raman signal resulting from analyte adsorption onto nano-structured metallic surfaces, has been studied for almost 40 years.¹⁻³ This research, however, has not yet transformed SERS into a tool for routine chemical analysis. While most of the SERS enhancement can be explained by the enhanced electric field produced by the metallic nanostructures, the effect of molecular properties on the binding and SERS enhancement is less well understood. Understanding these effects are important in understanding why certain molecules exhibit very large SERS enhancements while other molecules, on the same substrate, yield little to no enhancement of the Raman signal.

The key to comparing the SERS activity of different molecules is the definition of a SERS enhancement factor. Traditionally, the SERS enhancement factor, G , is defined by:⁴

$$G = \frac{I_S N_R}{I_R N_S} \quad (1)$$

where I_S and I_R , are, respectively, the SERS intensity due to N_S "participating" molecules, and the ordinary Raman intensity due to N_R of the same molecules in solution. However, G has proved difficult to calculate reliably as a consequence of the fact that it depends on at least one, and often more than one, hard to determine parameters. Most often it is N_S that cannot be accurately determined because it is difficult to know the exact surface area on a molecular scale or how tightly the molecules pack together when adsorbed onto the surface. Additionally, the surface concentration of the analyte will follow an isotherm, which is a function both of the analyte's concentration in solution and on the surface's chemical affinity for that molecule.

As part of an earlier defense project effort, we developed a prescriptive approach to determining SERS enhancement we termed the SERS Enhancement Value (SEV or F).⁵ This measure corrects operationally for the aforementioned difficulty of determining N_S , and also for the spatial inhomogeneity of the enhancement of many SERS substrates. The SEV is defined as the ratio of the two analyte concentrations c_R and c_S producing the same Raman or SERS intensity. We define c_R as the concentration of the analyte in solution in the absence of the SERS substrate and c_S as the concentration of the analyte in the solution from which the analyte was adsorbed (at equilibrium) onto the SERS

substrate. It is clear that there are an infinite number of pairs of concentrations that satisfy this condition. One approach to determine c_R and c_S is by measuring Langmuir isotherms and selecting the intensity that is 90% of the maximum SERS value ($\alpha=0.9$). This approach has the benefit that F is defined entirely in terms of measurable and definable factors, such as concentrations, without having to make assumptions regarding the numbers of molecules that contribute to the SERS or ordinary Raman intensities. In other words, F not only includes the traditional SERS enhancement factor, G , but also the thermodynamics of adsorption parameter, the equilibrium constant.

Although F and G represent different definitions of SERS enhancement, it can be shown that the two are related:

$$F_\alpha = G n_{max} \frac{(1-\alpha)^A}{V} K \quad (2)$$

where A is the focal area and V is the focal volume, which are dependent on the collection optics of the Raman instrument. Rearranging Equation 1, we obtain:

$$\ln(F_\alpha) = \ln \left\{ G \frac{(1-\alpha)n_{max}A}{V} \right\} + \ln(K) \quad (3)$$

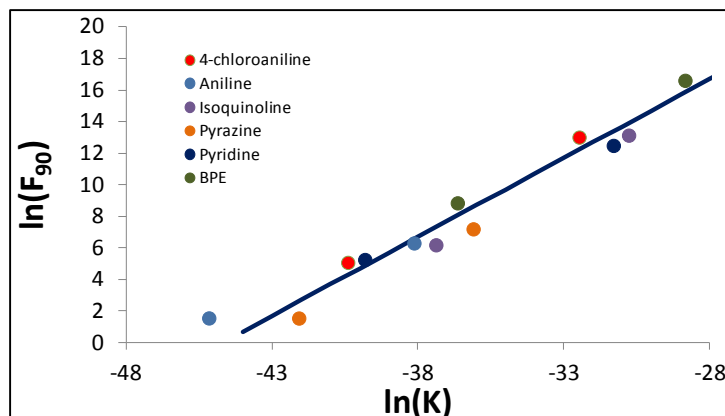


Figure 1. Plot of $\ln(F_{90})$ versus $\ln(K)$ for six reversibly bound analytes. Each analyte produces two values for K and F_{90} due to the dual Langmuir fits of the data.

A plot of $\ln(F_\alpha)$ versus $\ln(K)$ yields a straight line of unit slope with an intercept proportional to $G \times n_{max}$ (Figure 1). This implies that the product of the analytical enhancement factor and the packing density on the surface is a function of the substrate only and is independent of the particular analyte. This product can be interpreted as a SERS enhancement per unit area.

1.1 Influence of binding energy

From the law of mass action, the equilibrium constant, K , is a function of difference in the Gibbs free energy, ΔG , of products in the form of chemisorbed reactant analyte on the planar substrate from the reactants in the solution state along with the clean planar substrate at a temperature T . The following equation shows K as a function of ΔG and T :

$$K = e^{-\Delta G/RT} \quad (4)$$

where, R is the ideal gas constant, and T is the temperature. Substituting Equation 3 in Equation 2 we obtain:

$$\ln(F_\alpha) = \ln \left\{ G \frac{(1-\alpha)n_{max}A}{V} \right\} - \Delta G/RT \quad (5)$$

The change in free energy occurs when the analyte is “unsolubilized” from the solvent and reacts with the surface. Thus:

$$\Delta G = \Delta G_{rxn} - \Delta G_{solvation} \quad (6)$$

where ΔG_{rxn} is the change in Gibbs free energy due to the reaction of the adsorbate to adsorbent and $\Delta G_{solvation}$ is Gibbs free energy of dissolution of the adsorbent in the solvent. Substituting Equation 6 in Equation 5, we obtain:

$$\ln(F_\alpha) = \underbrace{\ln \left\{ G \frac{(1-\alpha)n_{max}A}{V} \right\}}_{\text{Fn of substrate and detector}} - \underbrace{\frac{\Delta G_{rxn}}{RT}}_{\text{Fn of reaction parameters}} + \underbrace{\frac{\Delta G_{solvation}}{RT}}_{\text{Fn of solvation}} \quad (7)$$

The right hand side of Equation 7 can be viewed as a summation of three functions. The first term (red) is a function of the product of G and n_{max} . Both of these values are functions of substrate (material and design) and, based on our previous studies, appear to be independent of the bound analyte. The second term (green) comprises the thermodynamic parameters of the reaction that are independent of the substrate design and a function only of the substrate material (Au for Klarite) and the analyte. The third term (blue) is a function Gibbs free energy of dissolution of adsorbent into the solvent and the temperature of the solution. The molecular factors that may influence the solvation process include differences in the dipole moment of the solute and solvent, the localized dipole moment of solute and solvent, the ability of the solute and solvent to form hydrogen bonds, etc.

The goal of this work is to break down each function of Equation 7 into experimental tasks in order fully understand the SERS effect aimed at an improved predictability of the SERS activity of molecules of interest. From initial results in building the relationship between F and G (Figure 1), we observed that the concentration dependence of the SERS intensity for some of the reversibly bound chemicals is best fit to a dual Langmuir equation (Figure 2)⁶ as opposed to the traditional single Langmuir model.

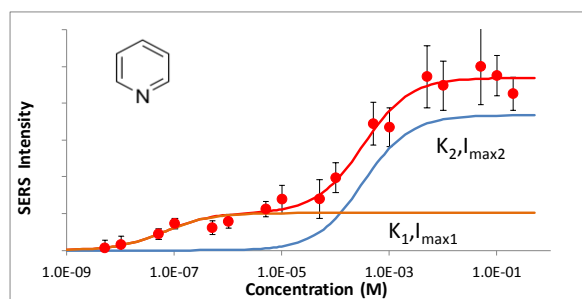


Figure 2. Dual Langmuir fit of pyridine data. The red circles are experimental data, the red curve is the combined dual Langmuir fit, and the blue and orange curves are the single Langmuir components of the red curve.

The nature of this fit was not understood and it suggests that there are at least two different types of binding sites on the nanometallic substrate. It could not be ruled out, however, that the deviation from a single Langmuir dependence was due to rearrangement of the molecules on the surface at high concentrations. This year we studied this effect further, to determine the nature of this observed phenomenon.

2 EXPERIMENTAL METHODS

2.1 Materials

1,2-di(4-pyridyl)ethylene (BPE), ethanol, acetonitrile, sodium hydroxide, and hydrochloric acid were purchased from Sigma-Aldrich® and used without further purification. Solutions were prepared in deionized water in the range of 5×10^{-9} M to 0.1 M concentrations. All the experiments were performed at room temperature (23 °C). Commercially available gold SERS substrates (Klarite®, KLA-312, Renishaw Diagnostics Ltd.; UK) were used for this work. The substrates provide adequately strong and reproducible SERS enhancement when 785 nm excitation is used.^{8,11}

2.2 Raman microscopy

The Raman measurements were performed with a JASCO NRS-3200 dispersive Raman microscope system operating at 785 nm excitation with approximately 4 mW power incident on the sample. A 10X microscope objective was used both to focus the laser on the substrate and to collect the Raman scattered light. The relatively modest laser power and magnification were used to minimize any laser-induced heating of the substrate. The laser spot size was not measured but is estimated to be in the range of 1-5 μm . The Raman scattered light was dispersed with a 600 grooves/mm diffraction grating (blazed at 750 nm) and a spectrometer entrance slit width of 100 μm was used to obtain a spectral resolution of approximately 8 cm^{-1} . All the Raman spectra were acquired with 25 second integration time and averaged over three co-additions. The Raman scattered light was detected with a thermoelectrically cooled charge-coupled device (CCD) camera (Andor; Belfast, UK). The strong Rayleigh scattered light was suppressed with a notch filter (Semrock; Rochester, NY). Raman spectral mapping of the substrate was performed by selecting a 36 location grid, in a rectangular 6x6 format, on the substrate and obtaining a Raman spectrum at each of the locations.

3 RESULTS AND DISCUSSION

We acquired SERS-based adsorption isotherms for five azarenes and four analines with Klarite® as the substrate and deionized water as the solvent.⁶ Two examples are shown in Figure 3.

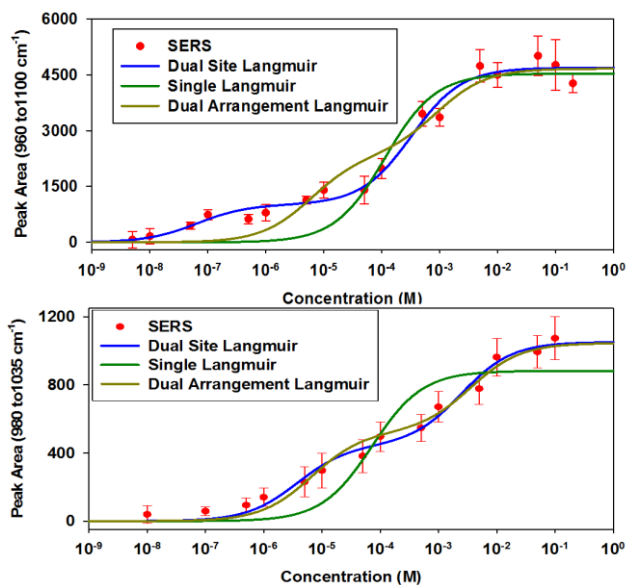


Figure 3. Representative examples demonstrating multiple Langmuir isotherm fitting terms.

Concentration dependent isotherms resulting from SERS have traditionally been fit to a Single Langmuir Isotherm (SLI), Equation 8:

$$I_{C_S} = I_{max} \left(\frac{K C_S}{1 + K C_S} \right) \quad (8)$$

where K is the equilibrium constant, C_s is the analyte concentration, I_{C_s} is peak area of a spectral feature at the concentration C_s , and I_{max} is the maximum observed peak area of that spectral feature. Figure 3 shows the SLI fit for both chemicals and it can be observed that it does not fit the data well. In Langmuir's original paper describing the theory of adsorption on planar surfaces, the above equation is described as the simple adsorption example.⁷ However, he goes on to describe additional scenarios which he termed multiple elementary spaces. These additional scenarios extended the simple isotherm to account for the surface containing different kinds of "elementary spaces" or binding sites that are some fraction of the entire surface. In the scenario allowing the adsorbent to bind in a different type of site with a different orientation and/or density, Equation 8 is transformed to:

$$I_{C_S} = I_{max} \left(\frac{\beta_1 K_1 C_S}{1 + K C_S} + \frac{\beta_2 K_2 C_S}{1 + K C_S} \right) \quad (9)$$

where β_1 and β_2 are the fractions representing each additional elementary space. If necessary, β can be extended to more than two terms. For the case of two term, this relation is called the Dual Site Langmuir Isotherm (DSLII).

Langmuir further assumed that there may be more than one molecule occupying the same "elemental space", which could lead to rearrangement of molecules resulting in higher packing density at higher concentrations. In this case, Equation 8 is transformed to:

$$I_{C_S} = I_{max} \left(\frac{K_1 C_S + 2K_1 K_2 C_S^2}{1 + K_1 C_S + K_1 K_2 C_S^2} \right) \quad (10)$$

This term has been labeled the Dual Arrangement Langmuir Isotherm (DALI). Again, looking at the data from Figure 3 it is observed that the DSLII equation best represents the observed data. However, DALI can't be ruled out as a better fit due to an extra fitting term in DSLII may be skewing the fit. To further explore whether the observed phenomena is dual site or dual arrangement additional experiments were performed.

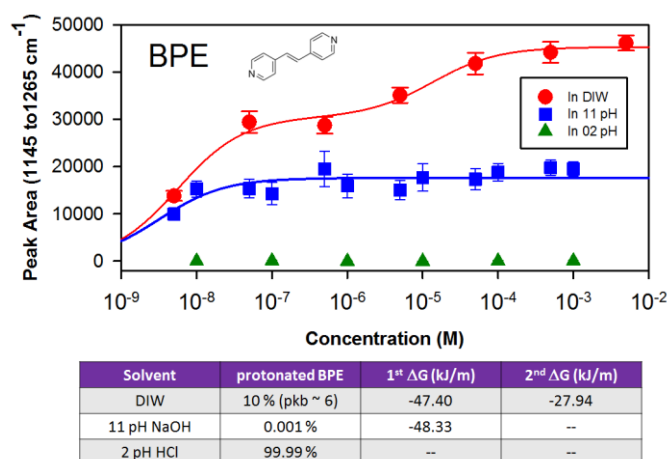


Figure 4. Concentration dependent isotherm of BPE in deionized water, 11 pH, and 2 pH with resulting binding energies.

Figure 4 shows an additional data collection of BPE in deionized water, acidic (2 pH), and alkaline (11 pH) solution. In deionized water, BPE can be found in both protonated and non-ionized states. The BPE in deionized water isotherm, shown by the red circles in Figure 4, is best fit with DSLI. Consider the isotherm of BPE in 11 pH where 99.999% of the molecules are non-ionic. We observe a single Langmuir isotherm (blue curve). If one were to attribute the complex isotherms observed with deionized water as the solvent (red curve) to the dual arrangement scheme, then we should have observed a similar complex isotherm for BPE at 11 pH. Crowding of adsorbed BPE molecules should have caused the rearrangement and the curve should have exhibited a secondary binding energy. This leads us to attribute the observed isotherms to existence of two types of sites: one that accepts non-ionized BPE and a second that accepts protonated BPE. However, there was no observed BPE spectral response at 2 pH showing binding of the supposed protonated BPE. While we are exploring the reasons for this, initially we believe the ethylene bridge is being cleaved by the excess HCl and changing or producing major and minor products that are described by Markovnikov's rule that are different from the original BPE molecule.⁸

In order to circumvent this potential reaction and demonstrate dual site adsorption, we saturated a Klarite® substrate with 10^{-4} M thiophenol and then equilibrated with BPE solution (10^{-7} M to 10^{-3} M) in deionized water, as shown in Figure 5. It has been established that the attachment of azarenes (of which BPE is a type) to Au-SERS substrates occurs via the lone pair of electrons present in the nitrogen atom.³ Thus, the sites that accept non-ionized BPE molecules should be electrophilic in nature. Thiophenol, which is an acid, will bind to electrophilic sites.

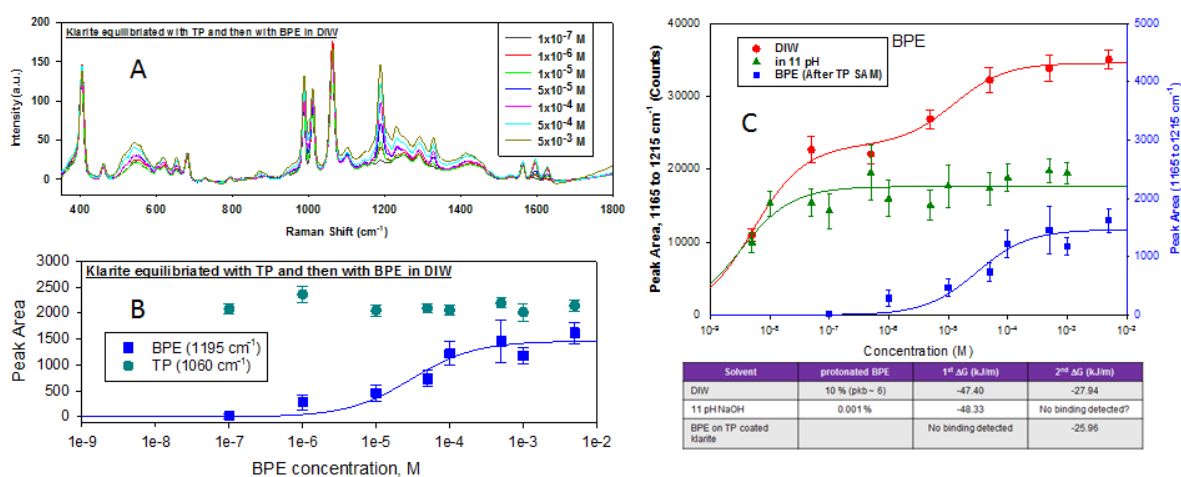


Figure 5. A) SERS spectra, B) absorption isotherm peaks, and C) associated binding energies for Klarite® substrate equilibrated with thiophenol and BPE.

Figure 5A shows the unique spectral bands of thiophenol ($1,000\text{ cm}^{-1} - 1,100\text{ cm}^{-1}$) and BPE ($1,200\text{ cm}^{-1}$). As stated above, a SAM was established for thiophenol ensuring complete adsorption to all available electrophilic sites. After which, BPE was added and allowed enough time to equilibrate at each concentration between 10^9 M and 10^{-3} M . What is immediately noticeable is the emergence of the BPE vibrational bands, which leads to the observed adsorption isotherm that is well explained by the SLI model (Figure 2B). It is clear that BPE attachment is not due to the detachment of adsorbed thiophenol because the thiophenol signal strength does not change. This leads to the conclusion that BPE attachment is occurring at sites that are not and could not be occupied by thiophenol, but in fact binding to the available nucleophilic sites which are available to protonated BPE. Finally, in Figure 5C we compare the absorption isotherms and resulting binding energies between the above experiments (BPE at pH 11, and the BPE addition after the thiophenol SAM was established). The DSLI fit and resulting binding energies agree very well with that of BPE in deionized water, the agreement with the DSLI model of BPE in deionized water is very good. We believe these experiments strongly suggest that Klarite® is a substrate that is made up of both electrophilic and nucleophilic sites.

4 CONCLUSION

Our study has revealed that a DSLI can be used to explain the complex equilibrium states between absorbing molecules and gold nanometallic structured surfaces. This leads us to believe that planar array surfaces, such as Klarite®, which are made up of various nano-roughened structures, contain both electrophilic and nucleophilic binding sites. Future studies into this task will investigate the geometrical nature of the identified dual sites which will lead to enhanced substrate design and a better understanding of the SERS effect.

ACKNOWLEDGMENTS

The authors acknowledge financial support from the Edgewood Chemical Biological Center's Surface Science Initiative Program.

REFERENCES

- [1] Fleishmann, M.; Hendra, P.J.; and Mcquillan, A.J., "Raman spectra of pyridine adsorbed at a silver electrode." *Journal of Physical Chemistry*, **1974**, 26, p163-166.
- [2] Albrecht, M.G. and Creighton, J.A., "Anomalously intense Raman spectra of pyridine at a silver electrode." *Journal of the Analytical Chemistry Society*, **1977**, 99(15), p5215-5217.
- [3] Jeanmaire, D.L. and Van Duyne, R.P., "Surface Raman electrochemistry. Part 1. Heterocyclic, aromatic and aliphatic amines adsorbed on the anodized silver electrode." *Journal of Electroanalytical Chemistry*, **1977**, 84(1), p1-20.
- [4] Le Ru, E.C. *et al.*, "Surface enhanced Raman scattering enhancement factors: A comprehensive study." *Journal of Physical Chemistry C*, **2007**, 111(37), p13794-13803.
- [5] Guicheteau, J.A. *et al.*, "Surface enhanced Raman scattering (SERS) evaluation protocol for nanometallic surfaces." *Applied Spectroscopy*, **2013**, 67(4), p396-403.
- [6] Tripathi, A. *et al.*, "Critical role of adsorption equilibria on the determination of surface-enhanced Raman enhancement." *ACS Nano*, **2015**, 9, p584-593.
- [7] Langmuir, I., "The adsorption of gases on plane surfaces of glass, mica, and platinum." *Journal of the Analytical Chemistry Society*, **1918**, 40(9), p1361-1403.
- [8] Markownikoff, W., "Ueber die abhängigkeit der verschiedenen vertretbarkeit des radicalwasserstoffs in den isomeren buttersäuren." *European Journal of Organic Chemistry (Weinheim, Germany)*, **1870**, 153(2), p228-259.

Determination of mechanisms and transport enhancement in liquid-phase extraction of penetrants from polymers

Brent A. Mantooth^{a*}, Mark J. Varady^b, Thomas P. Pearl^b, Craig K. Knox^c, Jerry B. Cabalo^a,
John A. Escarsega^d, Robert H. Lambeth^d

^aU.S. Army Edgewood Chemical Biological Center, Research and Technology Directorate,
5183 Blackhawk Rd, Aberdeen Proving Ground, MD 21010

^bOptiMetrics, 100 Walter Ward Blvd, Abingdon, MD 21009

^cLeidos, Inc., P.O. Box 68, Gunpowder Branch, Aberdeen Proving Ground, MD 21010

^dU.S. Army Research Laboratory, 4600 Deer Creek Loop, Aberdeen Proving Ground, MD 21005

ABSTRACT

Several relevant practical processes utilize transport of species across liquid-solid boundaries, including material decontamination, membrane separation, and transdermal drug delivery. Identification of mechanisms associated with liquid-phase extraction of absorbed species (penetrants) from polymers, specifically how absorbing solvents promote bulk penetrant diffusion is critical to understanding and optimizing these processes. Based on prior research on transport in polymers, we hypothesize three mechanisms for extraction rate enhancement: 1) increase in free volume due to plasticization, 2) increase in polymer chain mobility, and 3) relative strength of chemical interaction between penetrant, solvent, and polymer molecules. This work has focused on the third hypothesized mechanism and understanding how isolated penetrant and solvent species interacted with polyurethanes. Gravimetric uptake experiments were performed and the results used to fit Flory interaction parameters and Maxwell-Stefan diffusivities. Molecular dynamics simulations were used to compute self-diffusivities of single species, elucidating clear trends with strength of chemical interaction with the polymer. Further molecular dynamics simulations are underway to study how penetrant diffusivities change in the presence of solvent molecules. Systems that display measurable changes as a function of composition will be selected for further experimental study in which the penetrant extraction rate will be quantified using bulk flow cell and infrared spectroscopy techniques.

Keywords: Multicomponent transport, liquid-phase extraction, Maxwell-Stefan, Flory-Huggins, molecular dynamics, polymer, decontamination

1 INTRODUCTION

The rate at which chemical species (i.e., penetrants) absorbed in a polymer (i.e., in solution where the penetrant is the solute and the polymer is the solvent) can be extracted into an adjacent liquid is often limited by diffusive transport in the bulk-phase. As shown in Figure 1, the absorbed penetrant must migrate from the bulk to the phase interface where it partitions into the liquid-phase according to local thermodynamic equilibrium. This configuration has practical applications in decontamination of chemical warfare agents from absorbing materials,¹⁻³ leaching of organics from solid waste material,⁴⁻⁶ and controlled transdermal drug delivery.⁷⁻⁹ Another closely related practical application is membrane separations processes in which a feed consisting of a gaseous or liquid mixture of species is passed over a polymeric membrane and one of the species is selectively transported across the membrane due to differences in solubility and/or diffusivity.¹⁰⁻¹²

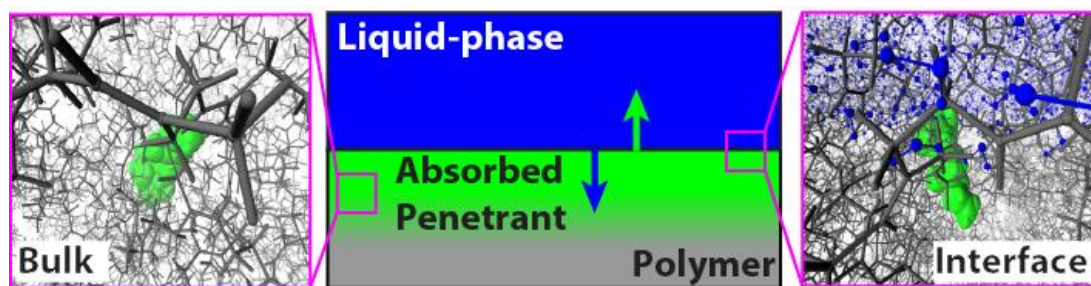


Figure 1. Schematic of liquid-phase extraction at macroscale showing the transport of both liquid and penetrant across the phase boundary along with molecular scale depictions of penetrant within the bulk of the polymer (left) and penetrant across the phase boundary (right).

In each of the above mentioned applications, it is common to have multiple species diffusing simultaneously within the polymer material. A mathematical description of the multicomponent transport process at the continuum level is provided by the Maxwell-Stefan diffusion model.¹³⁻¹⁴ In polymeric substrates, the driving force for transport of species in the absence of external forces (e.g., applied electric field) is the gradient in chemical potential. Two widely used models for the chemical potential of a species in solution in a polymer are the Flory-Huggins and Flory-Rehner models.¹⁵ These thermodynamic mixing models have been extended to account for more than one species in solution in a polymer,¹⁶⁻¹⁷ and have been coupled with the Maxwell-Stefan formulation to model transport of multiple species in a polymer. The vast majority of work on this front has centered on the application of steady-state transport across membranes,¹⁸⁻²⁰ although the theory is sufficiently robust to describe transient processes such as penetrant extraction where the spatial distribution of concentration is continuously evolving over time.

In any continuum model, such as the Maxwell-Stefan model, phenomenological parameters such as diffusivity and Flory interaction parameter must be known, and these often don't have a clear connection to the molecular scale mechanisms that drive these processes (e.g., polymer-penetrant interactions). One of the primary goals of this work is to develop a multiscale modeling approach in which the phenomenological parameters are informed by atomistic simulations of the transport processes, thereby developing a mechanistic understanding of the observed macroscale transport rates. This provides a path toward a more rational formulation of extraction liquids depending on the particular polymer-penetrant system. Much progress has been made over the past two decades in simulating diffusion in polymers using atomistic methods, particularly molecular dynamics (MD).²¹⁻²⁴ Such studies have yielded a fundamental mechanistic understanding of the diffusion process for several systems of practical relevance. Some examples include the separation of ethanol and water using pervaporation through a polydimethyl siloxane (PDMS) membrane,²⁵ the diffusion of model diesel components through polymer membranes for desulfurization,²⁶ and the influence of hydrogen bonding interactions in the observed differences between water and benzene transport in polyvinyl alcohol (PVA).²⁷

Experimental studies on the multicomponent transport in polymers have ranged from simple gravimetric uptake aimed at informing phenomenological model parameters to detailed spectroscopic studies with the goal of monitoring how specific chemical interactions evolve throughout the diffusion process. For example, the equilibrium sorption of ethanol/water mixtures of varying composition in PDMS was measured to inform the composition dependence of interaction parameters in the Flory-Huggins equation.²⁸ Time-resolved sorption of methanol/toluene mixtures into polyvinyl acetate (PVAC) was measured using a magnetic suspension balance, and the data used to fit the diffusivities of both species.²⁹ Musto et al. used transmission Fourier transform infrared spectroscopy (FTIR) to determine that water diffusing in poly(ϵ -caprolactone) (PCL) exists as either a single species or as a dimer interacting with the polymer backbone.³⁰ Infrared spectra of water and methanol in a Nafion® membrane (DuPont™; Wilmington, DE) in intimate contact with an attenuated total reflectance (ATR) cell were collected during a transient sorption experiment to conclude that swelling of the membrane during methanol sorption was the primary contributing factor to high methanol crossover in direct methanol fuel cells.³¹

Of particular interest in this work is the augmentation of the transport rate of penetrants contained within a polymer due to the presence of an adjacent liquid-phase. It has been observed in work performed by the Edgewood Chemical Biological Center (ECBC) Decontamination Sciences Branch that the transport rate across the phase boundary cannot be solely accounted for by thermodynamic considerations (i.e., the solubility of the penetrant in the adjacent liquid-phase). Figure 2 shows the experimentally observed time-resolved extraction of O-ethyl S-[2-(diisopropylamino)ethyl] methylphosphonothioate (VX, penetrant) absorbed in silicone elastomer

(polymer) into both pure water (blue circles) and a water/methanol mixture (red squares). A continuum model not accounting for solvent interaction with the polymer provides a good prediction for pure water (curve a), while it underpredicts the extraction rate into the water/methanol mixture (curve b). This suggests that in some cases molecules from the liquid-phase enter into the polymer phase, enhancing the diffusion rate of the penetrant through the polymer. Modifying the model to account for the interaction of methanol with the silicone and using a phenomenological description of the corresponding influence on VX diffusivity in silicone, the observed extraction rate is well-predicted (curve c).

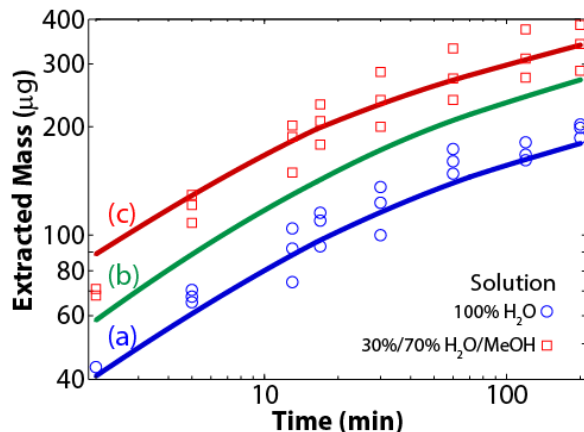


Figure 2. Time evolution of extracted VX mass from silicone using water (circles) and a mixture of 30% water/70% methanol (squares). Also shown are model results of the extraction process for (a) best fit to experimental data using 100% water, (b) 30%/70% water/methanol assuming that absorbed methanol has no influence on the bulk transport of VX in silicone, and (c) best fit to experimental data using the water/methanol mixture, accounting for increased diffusivity of VX in silicone due to absorbed methanol.

The goal of this work is to develop a fundamental molecular level understanding of the mechanisms responsible for increased penetrant transport rate in polymers exposed to certain solvents. Emphasis is placed on the influence of polymer-penetrant, polymer-solvent, and penetrant-solvent interactions; how these evolve over the course of a dynamic extraction process; and how the penetrant mobility correspondingly changes. This will be accomplished by developing a consistent multiscale modeling framework using well-established continuum formulations in conjunction with atomistic methods to provide interpretation of phenomenological parameters and better understanding of fundamental transport mechanisms. Experimental techniques focus on gaining an understanding of transport of single species (i.e., penetrant and solvent independently) in the polymer using gravimetric techniques. Experiments will also measure the rate of penetrant extraction rate using a flow cell apparatus developed by the ECBC Decontamination Sciences Branch, and spectroscopic techniques will be used to study the specific chemical interactions during the extraction process.

2 METHODOLOGY

2.1 Polymer synthesis and characterization

Structurally analogous polyurethane (PU) and polyhydroxyurethane (PHU) polymers, shown in Figure 3 were prepared to examine how the presence of pendant hydroxyl groups effects penetrant and solvent transport. The model polyurethane polymer was prepared using standard polyol-isocyanate chemistry. The model PHU was prepared by an Army Research Laboratory-developed organocatalytic cyclic carbonate-amine polymerization. The backbones of the two polymers are identical differing only in the pendant hydroxyl group present in the PHU structure, providing different hydrogen bonding environments for absorbing species.

Polymer samples were characterized using size exclusion chromatography (SEC), dynamic scanning calorimetry (DSC), and thermal gravimetric analysis (TGA). Residual solvent from the casting process was quantified using proton nuclear magnetic resonance (¹H NMR). Understanding the properties and characteristics of the synthesized polymers is vital to ensure consistency of samples for experimentation, and to inform MD and continuum modeling efforts.

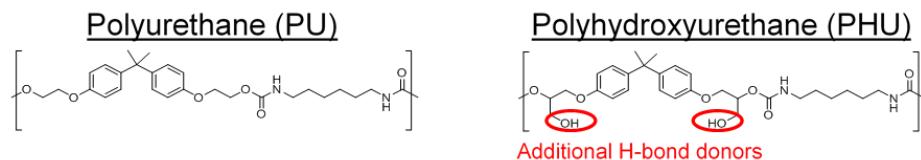


Figure 3. Monomer units for PU and PHU with an indication of the additional hydrogen bonding donors available on the PHU backbone.

For the initial studies, PDMS (Dow Corning™ SYLGARD® 184) was also used in gravimetric uptake experiments (Section 3.2) since numerous sorption and transport studies have been reported in the literature.

2.2 Penetrant and solvent selection

Penetrants and solvents were selected for varying hydrogen bonding interactions with the PU and PHU polymers. Priority was placed on selecting homomorphic penetrant compounds differing only in hydrogen bonding capability with similar molar volumes and to allow for a focus on chemical interaction effects with minimal molecular size influences. Table 1 lists the penetrants chosen for initial study in order to specifically probe hydrogen bonding interactions. The homomorphic series hexane, pentylamine, butyldiamine have increasing number of hydrogen bonding donors and acceptors, the series *p*-xylene, lutidine, dimethylpyrazine have increasing number of hydrogen bonding acceptors only, and the series methylamine, formaldehyde and methanol have a single hydrogen bond acceptor with varying functional group electronegativity.

Table 1. Penetrants chosen for initial studies that permit systematic variations in hydrogen bonding interactions through three different homomorphic series.

Chemical	Structure	Molar Volume ^a (cm ³ /mol)	No. of H-bond acceptors	No. of H-bond donors	Functional Group Electronegativity ³²
hexane		127	0	0	2.23
pentylamine		114.7	1	2	2.61
butyldiamine		101.9	2	4	2.61
<i>p</i> -xylene		122.0	0	0	N/A
lutidine		115.2	1	0	N/A
dimethylpyrazine		108.4	2	0	N/A
methylamine		48.7	1	2	2.61
formaldehyde		43.8	1	0	3.14
methanol		40.8	1	1	3.51

^aEstimated from ACD/Labs PhysChem Module.

The solvents for study were water and the series of alcohols methanol, 2-propanol, *t*-butanol, and hexane. The alcohol series was chosen since the hydroxyl groups on these molecules have a strong hydrogen bonding capability with respect to the penetrants listed in Table 1, which allows testing of the hypothesis that the relative strength of polymer-solvent and polymer-penetrant interactions can alter penetrant transport rate as solvent is introduced to the system. Hexane was carried as a nonpolar control.

2.3 Experimental characterization of transport

Gravimetric uptake experiments were performed for selected penetrants and solvents in PU, PHU, and PDMS. In these experiments, a nominal 1.13 cm diameter, variable thickness (0.5-1 mm depending on specific polymer and casting method) polymer sample was weighed, placed in a bath of the liquid penetrant (or solvent) for a specified time, patted dry with a Kimwipe®, weighed again, then returned to the bath. These steps were repeated to obtain the penetrant (or solvent) mass absorbed as a function of time. This process was carried out over the course of 1-4 hours depending on

the particular liquid-polymer combination and when appreciable changes in mass were not detectable. To obtain the equilibrium mass absorbed, the polymer samples were soaked in the liquid for up to 1 week.

In the near term, the gravimetric uptake studies will be transitioned from the liquid immersion method to a quartz crystal microbalance (QCM) based method in which polymer films will be spin cast onto quartz crystals to form 1-10 μm thick films. These films will be exposed to vapors of penetrant (or solvent) of controlled activity. By using thin films, the dynamics of the uptake process are fast and equilibrium can be achieved quickly. Furthermore, having control over the activity allows composition dependence of the transport and thermodynamic equilibrium parameters (i.e., diffusivity and Flory interaction parameter) to be assessed.

2.4 Continuum modeling: Multicomponent diffusion

At the continuum level, transport of penetrant (p) and solvent (s) species within the polymer (m) is described by the general transport equation in Equations 1 and 2:

$$\frac{1}{\bar{V}_p} \frac{\partial \phi_p}{\partial t} + \nabla \cdot \mathbf{N}_p = 0 \quad (1)$$

$$\frac{1}{\bar{V}_s} \frac{\partial \phi_s}{\partial t} + \nabla \cdot \mathbf{N}_s = 0 \quad (2)$$

where ϕ is volume fraction, \bar{V} is the molar volume of pure species, and \mathbf{N} is the molar flux in the polymer. In the generalized Maxwell-Stefan equations, the driving force for species transport is the local gradient of chemical potential, μ , of the absorbed species in the polymer. This was combined with the Flory-Huggins equation for species activity in the polymer. Since the focus in the first year of this project was on understanding single species, the transport equation for species i reduces to:

$$\frac{\partial \phi_i}{\partial t} = \frac{\partial}{\partial z} \left[D_{im} (1 - 2\chi_{im}\phi_i) \frac{\partial \phi_i}{\partial z} \right] \quad (3)$$

At equilibrium in a pure liquid (where the activity is by definition unity), the Flory-Huggins equation was solved for the penetrant-polymer interaction parameter in terms of the equilibrium absorbed volume fraction of penetrant:

$$\chi_{im} = - \frac{\ln \phi_i^{eq} + (1 - \phi_i^{eq})}{(1 - \phi_i^{eq})^2} \quad (4)$$

2.5 Atomistic modeling

Self-diffusivities of penetrants and solvents in both PU and PHU were obtained by MD simulation. Ten full length chains (each a 43-mer) were placed in a periodic simulation box with 10% by weight of the penetrant molecules. All-atom simulations were performed in LAMMPS using the PCFF (polymer consistent force field) to quantify interactions between atoms and bonds. Using a 1 fs time-step, the dynamics were run for over 1 ns, and the mean-squared displacement (MSD) of each penetrant molecule ($N \sim 150$ total penetrant molecules) was calculated and used to compute the self-diffusivity, D , according to Equation 5:

$$D = \frac{1}{N} \sum_{i=1}^N \frac{\langle [\mathbf{r}_i(t) - \mathbf{r}_i(0)]^2 \rangle}{6t} \quad (5)$$

Future experimental work will use IR spectroscopy to probe the evolution of specific chemical interactions during the penetrant uptake and extraction processes. Computational spectroscopy will be used to aid in the interpretation of the experimentally obtained spectra. As a prelude to this work, IR spectra were computed from MD simulations of a single 43-mer of each PU and PHU with 10% by weight of penetrant. To capture low frequency vibrations, simulations were run to 100 ps with the PCFF force field. The IR spectrum was computed with the autocorrelation function of the dipole moment.

3 RESULTS

3.1 Polymer characterization

The results of the SEC, DSC, and TGA experiments are summarized in Table 2. Residual solvent tetrahydrofuran (THF) was observed in many of the initial samples as shown in Figure 4. Resolution of this issue was critical to moving forward with experimental studies as the presence of additional species can significantly impact the transport of the penetrant and solvent species under study here. Several alternative solvents were tested, and cyclopentane was chosen based on its compatibility with the polymers and the ability to fully evaporate it from the sample.

Table 2. Results of characterization experiments for PU and PHU.

Polymers	M_n (kDa)	T_g ($^{\circ}\text{C}$)	T_d ($^{\circ}\text{C}$)
PU	41.3	44.7	302
PHU	22.8	48.2	221

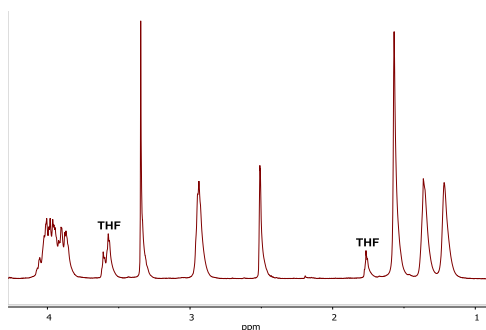


Figure 4. ^1H NMR spectra showing residual THF (casting solvent) after drying under high vacuum at a temperature of $80\text{ }^{\circ}\text{C}$.

3.2 Penetrant and solvent sorption

Uptake of the solvents into both PU and PHU was measured dynamically over a period of 60 minutes with the exception of water in PU (which was measured over 480 minutes). An example plot of the dynamic uptake data is shown for methanol in Figure 5.

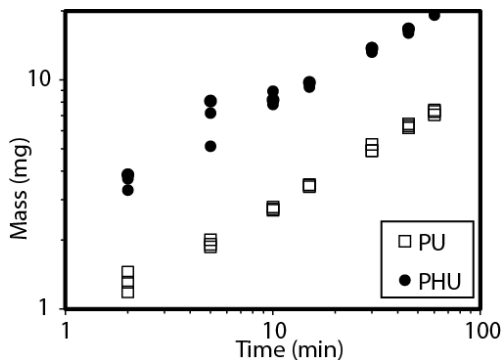


Figure 5. Gravimetric uptake of methanol in PU (empty squares) and PHU (filled circles).

The samples were left to soak in the liquid solvent for at least 6 days to obtain the equilibrium sorbed mass. The time-resolved data over the 60-minute period was used to fit values for the diffusivity according to Equation 3. The

equilibrium mass fraction of solvent was also computed using the mass of the dry polymer and this was used to find the solvent volume fraction according to:³³

$$\phi_i = \frac{\omega_i / \rho_i}{\omega_i / \rho_i + \omega_p / \rho_p} \quad (6)$$

which in turn was used to compute the solvent-polymer interaction parameter according to Equation 4. The equilibrium data and diffusivities are summarized in Table 3. Hexane is not included since the sorbed mass was negligible for both PU and PHU.

Table 3. Summary of equilibrium uptake data, Flory interaction parameter, and diffusivity for solvents in PU and PHU.

Solvent	Polymer	Equilibrium Sorbed Mass (mg)	ϕ_s^{eq}	χ_{sm}	Diffusivity (m ² /s)
Water	PU	44.3	0.43	0.84	~5x10 ⁻¹³ a
	PHU	18.11	0.15	1.44	~3x10 ⁻¹³ a
Methanol	PU	10.6	0.17	1.31	1.5x10 ⁻¹¹
	PHU	18.76	0.23	1.17	4.0x10 ⁻¹¹
Isopropanol	PU	1.28	0.027	2.78	7.0x10 ⁻¹²
	PHU	20.2	0.22	1.22	1.0x10 ⁻¹¹
<i>t</i> -butanol	PU	0.07	0.0016	5.54	N/A ^b
	PHU	10.1	0.14	1.48	4.0x10 ⁻¹³

^aSmall amount of uptake at short time led to high variance in data, so fit values of diffusivities are approximate for water.
^bVariance in data too great over 60 minutes, no clear increasing trend in mass discernable.

The lower value of χ_{sm} for the alcohol series in PHU compared to PU indicated a higher affinity for PHU, which may be due to the additional hydrogen bonding sites. Water displayed the opposite behavior. The diffusivities of the alcohol series decreased with increasing molar volume, as expected. It should also be noted that the diffusivities reported in Table 3 are the Maxwell-Stefan diffusivities, and must be distinguished from the self-diffusivities computed from the MD simulations reported in Section 3.3. The diffusivities computed for water were low compared to the alcohols despite water's lower molar volume, which may arise from stronger hydrogen bonding interactions with the polymer, slowing its motion.

The identical set of experiments was attempted for the first six penetrants listed in Table 1. However, both polymers were completely miscible with the nitrogen substituted compounds, and dissolution of the polymer occurred within 30 minutes. This problem is currently being addressed by using a QCM based gravimetric technique as described in Section 2.3 where the activity of the species at the polymer interface can be carefully controlled. In the meantime, gravimetric uptake experiments were carried out for the penetrants on PDMS to establish proper laboratory procedures for handling the penetrant liquids. Table 4 summarizes the equilibrium behavior and diffusivities of the homomorphic series of the heterocyclic arene penetrants *p*-xylene, lutidine, and dimethylpyrazine.

Table 4. Summary of equilibrium uptake data, Flory interaction parameter, and diffusivity for homomorphic series of heterocyclic arene penetrants in PDMS.

Penetrant	Polymer	Equilibrium Sorbed Mass (mg)	ϕ_s^{eq}	χ_{sm}	Diffusivity (m ² /s)
<i>p</i> -xylene	PDMS	159.0	0.65	0.65	3.0x10 ⁻¹⁰
lutidine	PDMS	40.0	0.31	1.00	1.8x10 ⁻¹⁰
dimethylpyrazine	PDMS	22.4	0.19	1.30	1.4x10 ⁻¹⁰

The results show a decreasing equilibrium volume fraction and increasing Flory interaction parameter with increasing number of hydrogen bonding acceptors on the penetrant. Considering that each monomer unit of PDMS has one hydrogen bonding acceptor and no donors, the penetrant-polymer interaction becomes increasingly repulsive as

penetrant hydrogen bonding acceptors increases across the homomorphic series, explaining the trend in uptake. This also could explain the decreasing trend in diffusivity across this series of penetrants.

3.3 Diffusivity trends by molecular dynamics simulations

Comparing the self-diffusivities computed by the MD simulations across the two homomorphic series (linear hydrocarbons substituted with amines on either end, and heterocyclic arenes with nitrogen substituted on the phenyl ring) shown in Figure 6a shows a clear trend of decreasing diffusivity in PHU with increasing number of hydrogen bonding acceptors. Figure 6b shows a similar trend across the homomorphic series, showing decreasing diffusivity with increasing electronegativity of the functional group. This highlights the importance of polymer-penetrant interactions in the mobility (diffusivity) of the penetrant in the polymer. More importantly is the work that is currently being performed to introduce solvent species to see how the two-way interactions change with composition, and in turn influence penetrant diffusivity. This work is critical to developing a fundamental understanding of experimentally observed enhancements in penetrant extraction rate and to guide formulation to optimize extraction rate.

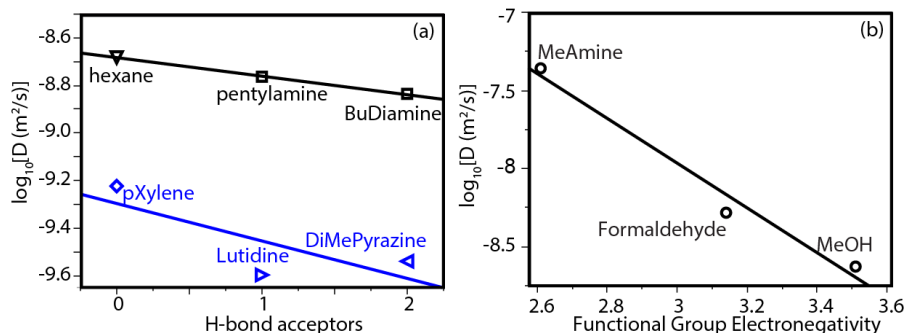


Figure 6. Increasing polymer-penetrant interaction decreases diffusivity as shown for different penetrants diffusing in PHU: (a) Both homomorphic series show decreasing diffusivity with increasing number of hydrogen bond acceptors. (b) Increasing electronegativity of functional groups with similar molar volume decreases diffusivity.

Figure 7 shows the results of successful calculation of IR spectra from MD simulations of PU and PHU with 10% by weight of *t*-butanol and butanal. The changes easiest to attribute to hydrogen bonding occur in the O-H stretching region around 3,500 cm⁻¹. For both *t*-butanol and butanal, there are differences between the PU and PHU due to the additional hydroxyl groups in PHU. Most interestingly, for butanal, calculations show additional frequencies that are shifted ~100 cm⁻¹ to the red. For the C-H stretches around 3,000 cm⁻¹, there is very little difference in frequencies between either system, indicating little interaction between methylene and hydroxyl or aldehyde groups.

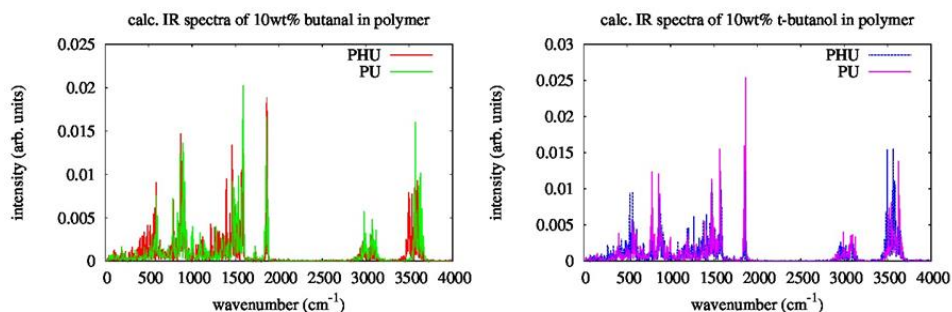


Figure 7. IR Spectra computed from MD simulations of butanal and *t*-butanol loaded at 10 wt% in both PU and PHU.

4 CONCLUSIONS

Samples of the polymers PU and PHU were prepared and characterized, enabling control over the hydrogen-bonding environment upon sorption of chemical species. The interaction of several penetrants and solvents with PU and PHU was characterized experimentally using gravimetric uptake measurements, which in turn informed phenomenological

parameters of a continuum model based on Maxwell-Stefan multicomponent diffusion and Flory-Huggins to quantify the thermodynamics of the polymer solutions. A clear connection was drawn between the penetrant-polymer interactions and the phenomenological model parameters fit to the experimental data.

MD simulations showed the same connection between the self-diffusivities of several species in both PU and PHU and the hydrogen bonding between the penetrants in polymers. In general, stronger hydrogen bonding interactions led to slower diffusivities. Of particular interest is how the introduction of solvent into the MD simulation will influence the penetrant diffusivities. This will not only help guide further experimental study, but will elucidate the molecular scale mechanisms responsible for enhancing penetrant diffusivity in a polymer in the presence of an interacting solvent. It is anticipated that the work will carve a path forward to optimize the extraction dynamics of penetrants from polymer networks.

ACKNOWLEDGMENTS

The authors acknowledge financial support from the ECBC Surface Science Initiative Program. The authors also acknowledge Nicholas Sapienza from the ECBC Decontamination Sciences Branch who carried out the gravimetric uptake experiments and is currently developing the QCM apparatus and method.

REFERENCES

- [1] Yang, Y. C.; Baker, J.A.; and Ward, J.R., "Decontamination of chemical warfare agents." *Chemical Reviews*, **1992**, 92, p1729-1743.
- [2] Love, A.H. *et al.*, "Efficacy of liquid and foam decontamination technologies for chemical warfare agents on indoor surfaces." *Journal of Hazardous Materials*, **2011**, 196, p115-122.
- [3] Varady, M.J. *et al.*, "Decontamination of chemical warfare agents from absorbing polymer substrates." (*Article in preparation*). **2015**.
- [4] Bishop, P., "Leaching of inorganic hazardous constituents from stabilized/solidified hazardous wastes." *Hazardous Waste and Hazardous Materials*, **1988**, 5(2), p129-143.
- [5] Yamamoto, T. and Yasuhara, A., "Quantities of bisphenol a leached from plastic waste samples." *Chemosphere*, **1999**, 38(11), p2569-2576.
- [6] Lee, C.K. and Rhee, K.-I., "Reductive leaching of cathodic active materials from lithium ion battery wastes." *Hydrometallurgy*, **2003**, 68(1-3), p5-10.
- [7] Bigucci, F. *et al.*, "Development and characterization of chitosan/hyaluronan film for transdermal delivery of thiocolchicoside." *Carbohydrate Polymers*, **2015**, 130, p32-40.
- [8] Ouriemchi, E.M. and Vergnaud, J.M., "Processes of drug transfer with three different polymeric systems with transdermal drug delivery." *Computational and Theoretical Polymer Science*, **2000**, 10(5), p391-401.
- [9] Rao, P.R.; Ramakrishna, S.; and Diwan, P.V., "Drug release kinetics from polymeric films containing propranolol hydrochloride for transdermal use." *Pharmaceutical Development and Technology*, **2000**, 5(4), p465-472.
- [10] Mulder, M.H.V. and Smolders, C.A., "On the mechanism of separation of ethanol water mixtures by pervaporation. 1. Calculations of concentration profiles." *Journal of Membrane Science*, **1984**, 17(3), p289-307.
- [11] Cunha, V.S. *et al.*, "Removal of aromatics from multicomponent organic mixtures by pervaporation using polyurethane membranes: Experimental and modeling." *Journal of Membrane Science*, **2002**, 206(1-2), p277-290.
- [12] Kamaruddin, H.D. and Koros, W.J., "Some observations about the application of Fick's first law for membrane separation of multicomponent mixtures." *Journal of Membrane Science*, **1997**, 135(2), p147-159.
- [13] Whitaker, S., "Derivation and application of the Stefan–Maxwell equations." *Revista Mexicana de Ingenieria Quimica*, **2009**, 8(3), p213-243.

- [14] Taylor, R. and Krishna, R., *Multicomponent Mass Transfer (1st Ed)*. John Wiley & Sons, Inc., New York. **1993**, p579.
- [15] Flory, P.J., *Principles of Polymer Chemistry*. Cornell University Press, New York. **1953**.
- [16] Young, T.H. *et al.*, "Phase behavior of eval polymers in water-2-propanol co-solvent." *Macromolecules*, **1998**, 31(4), p1229-1235.
- [17] Hovorka, S. *et al.*, "Describing the sorption characteristics of a ternary system of benzene (1) and alcohol (2) in a nonporous polymer membrane (3) by the Flory-Huggins model." *Polymer Engineering and Science*, **2015**, 55(5), p1187-1195.
- [18] Ribeiro, Jr., C.P.; Freeman, B.D.; and Paul, D.R., "Modeling of multicomponent mass transfer across polymer films using a thermodynamically consistent formulation of the Maxwell-Stefan equations in terms of volume fractions." *Polymer*, **2011**, 52(18), p3970-3983.
- [19] Krishna, R. and Wesselingh, J.A., "Review article number 50: The Maxwell-Stefan approach to mass transfer," *Chemical Engineering Science*, **1997**, 52(6), p861-911.
- [20] Paul, D.R., "Reformulation of the solution-diffusion theory of reverse osmosis." *Journal of Membrane Science*, **2004**, 241(2), p371-386.
- [21] Charati, S.G. and Stern, S.A. "Diffusion of gases in silicone polymers: Molecular dynamics simulations." *Macromolecules*, **1988**, 31(16), p5529-5535.
- [22] Li, Y. *et al.*, "Molecular dynamics simulation of diffusion behavior of cyclohexane in natural rubber during reclamation." *Journal of Applied Polymer Science*, **2014**, 131(11).
- [23] Pant, P.V.K. and Boyd, R.H. ., "Molecular-dynamics simulation of diffusion of small penetrants in polymers." *Macromolecules*, **1993**, 26(4), p679-686.
- [24] Rim, J.E.; Pinsky, P.M.; and van Osdol, W.W., "Multiscale modeling framework of transdermal drug delivery." *Annals of Biomedical Engineering*, **2009**, 37(6), p1217-1229.
- [25] Chang, K.S. *et al.*, "Free volume and alcohol transport properties of pdms membranes: Insights of nano-structure and interfacial affinity from molecular modeling." *Journal of Membrane Science*, **2012**, 417, p119-130.
- [26] Ling, C.J. *et al.*, "Diffusion behavior of the model diesel components in different polymer membranes by molecular dynamic simulation." *Chemical Engineering Science*, **2012**, 84, p292-302.
- [27] Noorjahan, A. and Choi, P., "Effect of free volume redistribution on the diffusivity of water and benzene in poly(vinyl alcohol)." *Chemical Engineering Science*, **2015**, 121, p258-267.
- [28] Yang, T.H. and Lue, S.J., "Modeling sorption behavior for ethanol/water mixtures in a cross-linked polydimethylsiloxane membrane using the flory-huggins equation." *Journal of Macromolecular Science Part B - Physics*, **2013**, 52(7), p1009-1029.
- [29] Schabel, W. *et al.*, "Sorption and diffusion measurements in ternary polymer-solvent-solvent systems by means of a magnetic suspension balance - experimental methods and correlations with a modified flory-huggins and free-volume theory." *Chemical Engineering Science*, **2007**, 62(8), p2254-2266.
- [30] Musto, P. *et al.*, "Time-resolved fourier transform infrared spectroscopy, gravimetry, and thermodynamic modeling for a molecular level description of water sorption in poly(ϵ -caprolactone)." *Journal of Physical Chemistry B*, **2014**, 118(26), p7414-7429.
- [31] Hallinan, D.T. and Elabd, Y.A., "Diffusion and sorption of methanol and water in naflon using time-resolved fourier transform infrared-attenuated total reflectance spectroscopy." *Journal of Physical Chemistry B*, **2007**, 111(46), p13221-13230.
- [32] Huheey, J.E., "Electronegativity of multiply bonded groups." *Journal of Physical Chemistry*, **1966**, 70(7), p2086-2092
- [33] Barton, A.F.M., *CRC Handbook of Polymer-Liquid Interaction Parameters and Solubility Parameters*. CRC Press, Florida. **1990**.

Understanding how exosporium hairs affect spore adhesion on surfaces

Jana S. Kesavan^{a*}, Craig K. Knox^{a,b}, Erica R. Valdes^a, Vipin K. Rastogi^a,

Pamela D. Humphreys^a, Paul J. DeLuca^a, Guzeliya Korneva^c, Robert A. Latour^c

^aU.S. Army Edgewood Chemical Biological Center, Research and Technology Directorate,
5183 Blackhawk Rd, Aberdeen Proving Ground, MD 21010

^bLeidos, Inc., P.O. Box 68, Gunpowder Branch, Aberdeen Proving Ground, MD 21010

^cDepartment of Bioengineering, Clemson University, 501-2 Rhodes Engineering Research
Center, Clemson, SC 20634

ABSTRACT

Microorganism adhesion plays important roles in numerous processes. Several pathogens of the Gram-positive endospore-forming *Bacillus* genus of bacteria have evolved a thin and highly-deformable outer layer, known as the exosporium or Hirsute hairy nap, which consists of nanometer-scale hair-like glycoprotein filaments and which is believed to play a critical role in spore hydrophobicity and adhesion, both in the environment and *in vivo*. This work used spore-probe atomic force microscopy and air flow experiments to measure the adhesive force between spores and a glass surface. *Bacillus* spores with exosporium hairs (Sterne strain of *B. anthracis* and *B. thuringiensis*) as well as similar spores without hairs (*B. globigii* and $\Delta cotE/\Delta bclA$ mutants) were studied. Protein AFM and molecular dynamics simulations were performed to probe the interactions of a single exosporium hair on a substrate. Hydrogen-bonding was observed between hydroxyl protein groups and SiO₂. These results may help provide insight into exosporium adhesion effects and spore stickiness factor prediction and guide the development of novel coatings and materials for biological agent detection, protection, and decontamination.

Keywords: Hirsute nap, filament, bacterium, mutation, aerosol, binding, AFM, molecular modeling

1 INTRODUCTION

Microorganism adhesion plays an important role in a broad range of processes. Several pathogenic members of the Gram-positive endospore-forming *Bacillus* genus of bacteria (*B. cereus/anthracis/thuringiensis*) as well as the *Clostridium* genus of bacteria (e.g., *C. botulinum*) possess a thin and highly-deformable outer layer, known as the exosporium^{1,2} or Hirsute hairy nap, which consists of a forest of ~70 nm hair-like glycoprotein filaments³ protruding from a crystalline basal layer and which is believed to play a critical role in spore hydrophobicity and adhesion, both in the environment and *in vivo*.^{4,5} Studies have suggested that the flexibility of the exosporium helps increase surface contact area,^{6,7} thus promoting adhesion, but an in-depth study to understand this behavior has not been previously undertaken.

Most of the exosporium consists of a mixture of proteins and carbohydrates, the principal component of which is believed to be the newly described glycoprotein, BclA.⁸ The crystallographic structure of this glycoprotein has recently been resolved.⁹ It forms a fibril consisting of a trimer with a collagen-like helical structure, the length of which depends on the number of GXX repeats in the amino acid sequence, which varies among spore species. The C-terminus domain (CTD) is the free end of the fibril and is rich in beta-sheets and contains several loops; the N-terminus domain (NTD) is the other end and is anchored to the crystalline basal layer. Experimental studies have not probed the molecular mechanisms of exosporium filament-surface interactions. Current knowledge about the structure and function of the exosporium hairs is mostly limited to electron microscopy studies dating back to the 1960s.^{3,10}

Our primary hypothesis is that the hairs of the exosporium respond to different chemical environments (e.g., hydrophobic versus hydrophilic, aqueous versus dry) to orient and change surface patterning at the nanoscale, affecting the contact area and thus spore adhesion. Based on the observed hydrophobicity and charge effects of BclA, we also believe that the exosporium has strong chemical interactions (perhaps electrostatic and hydrogen-bonds) with surfaces, in addition to exposing larger spore surface area, thus affecting and mediating spore adhesion.

2 METHODS

2.1 Spore preparation

Spores of *B. globigii* (*Bg*), *B. thuringiensis* (*Bt*), and Sterne strain of *B. anthracis* were prepared in-house. $\Delta cotE$ mutant (from Dr. Adam Driks, Loyola University) and $\Delta bclA$ mutant (from Dr. Alison O'Brien, Uniformed Services University Health Sciences) of the Sterne strain were procured from authentic sources. Strains were streaked for single colonies on tryptic soy agar (TSA) plate and grown overnight at 37 °C. An overnight culture of each strain was grown in tryptic soy broth (TSB) overnight at 37 °C. For each strain, an aliquot (0.5 mL/plate) was spread over Oxoid™ Lab-Lemco plates (15 cm diameter) and incubated at 37 °C for seven days or until the sporulation level reached > 95% (microscopic assessment). The spore crop over the plates was harvested by dislodging growth on plates using sterile distilled water (25 mL per four plates). The spore crop was filtered through a sterile coffee filter and washed with an additional 25-50 mL of sterile distilled water. The spores were washed by successive resuspension three times in 25 mL of sterile distilled water and heat-treated at 65 °C for 30 minutes. The extent of sporulation was confirmed microscopically and enumerated by dilution plating. Spore hardness was confirmed by heat-treatment and sensitivity to 2.5 M HCl treatment for 1 minute and 10 minutes, respectively.

To overcome potential challenges in comparing hairy versus non-hairy spores across different spore species, which may exhibit possible differences in surface properties, mutant Sterne (hairy) spores with deleted genes ($\Delta cotE$ and $\Delta bclA$) were prepared for a more direct exosporium hair versus no exosporium hair comparison within the same species. Since the $\Delta cotE$ mutant spores also lack the crystalline basal layer of the exosporium, in addition to the exosporium hairs, comparing these spores to the $\Delta bclA$ mutant spores should provide direct comparison of hair versus basal layer effects. *Bt* (hairy) and *Bg* (non-hairy) spores were also used for comparison and to provide important insights, especially given the routine use of *Bg* as a simulant for *B. anthracis*.

2.2 Protein preparation

The recombinant plasmid pBclA in *Escherichia coli* host (strain BL21) was obtained from Dr. Alison O'Brien (Uniformed Services University Health Sciences). Recombinant BclA protein purification was performed according to the protocol detailed by Brahmabhatt et al.¹¹ Briefly, the recombinant cells were grown overnight at 37 °C in a 175 rpm shaking incubator in TSB containing ampicillin (100 µg/mL). One mL broth culture was added to 1 L of TSB containing 100 µg/mL ampicillin, and the culture was grown until absorbance was 0.5-0.8 at 600 nm. IPTG inducer (Isopropyl β-D-1-thiogalactopyranoside) was added to a final concentration of 1 mM. The cultures were grown for an additional four hours, then the cells were concentrated by centrifugation. The cell pellet was frozen before use. The cell pellet was suspended in 40 mM Tris-HCl buffer at pH 8.0, containing 150 mM NaCl, 5 mM imidazole, and 0.5 mM PMSF (phenylmethanesulfonyl fluoride) at a buffer:pellet ratio of 4:1. The cells were sonicated and crude lysate was clarified by centrifugation at 20,000 rpm using an SS-34 rotor. The clear crude lysate was passed over a HisTrap™ HP affinity column. The column was first washed with 20 column-size volumes followed by washing with Tris-HCl buffer containing 1 M NaCl and 5 mM imidazole. The bound proteins were eluted using Tris-HCl buffer containing 150 mM NaCl and 500 mM imidazole. The eluted protein was run on SDS-PAGE (sodium dodecyl sulfate polyacrylamide gel electrophoresis). After Western blotting, half of the gel was hybridized with anti-His and the other half with anti-BclA IgG (Immunoglobulin G) antibodies.

2.3 Surface substrate materials

In order to compare surfaces covering a range of hydrophobicity, glass slides with a variety of surface treatments were used, as shown in Table 1. Atomic force microscopy (AFM) roughness measurements were performed to characterize the surfaces using Nanoscope Analysis software (Bruker Nano; Santa Barbara, CA) to analyze three distinct 500 nm lines and to average the results. The TruBond 200 (hydrophobic) and TruBond 380 (hydrophilic) surfaces were selected for detailed study because of their differing hydrophobicity within the same product line.

Table 1. Surface substrates. Additional source information: Chemglass Life Sciences, Inc., Vineland, NJ; Polysciences, Inc., Warrington, PA; Millennium Sciences, Inc., New York, NY; Electron Microscopy Sciences, Inc., Hatfield, PA.

Surface	Source	Description	Water Contact Angle (°)	Roughness (R _a , nm)
Fused Quartz	Chemglass	Bare quartz	< 10	
Glass	Polysciences	Bare glass		
Cell-Vu	Millennium Sciences	Gridded bare glass coverslip		
ExCell	EMS	Hydrophilic coating	46.0 ± 2.19	0.89
TruBond 380	EMS	Hydrophilic coating	33.5 ± 0.77	7.6
TruBond 200	EMS	Hydrophobic coating	62.7 ± 2.70	0.18
APTES	EMS	3-Aminopropyl triethoxysilane	56.5 ± 0.92	0.22
SuperFrost	EMS	Permanent + charge	55.2 ± 2.28	0.35
Silane	EMS	Aminoalkylsilane	66.1 ± 2.23	0.24
BrightSlide	EMS	Amino/carboxy polymer brush		2.2

2.4 Protein atomic force microscopy

The recombinant BclA protein was linked to an AFM tip via a polyethylene glycol-based tether to measure the adhesion force between the tethered protein and various functionalized surfaces. AFM tips (DNP-10, silicon nitride, Bruker, spring constant ~ 0.06 N/m) were first cleaned in piranha solution (1 part hydrogen peroxide and 3 parts concentrated sulfuric acid), rinsed with deionized water then ethanol, and dried with nitrogen. Next, the tips were functionalized with amino groups using APTES (3-aminopropyltriethoxysilane, 99%, Sigma Aldrich®) and MTES (methyltriethoxysilane, 99%, Sigma Aldrich®) solution in a 1-to-10 ratio in vapor phase overnight at room temperature. The tips were dried, baked, and rinsed with dry chloroform. Polyethylene glycol (PEG) linkers were attached to the amino groups on the tips. A PEG linker, NHS-PEG-NHS (bis-succinimidyl polyethylene glycol ester, 3400 Da, from Nanocs, Inc.) was used at 10 mg/mL concentration in anhydrous chloroform with 5 µL/mL trimethylamine as a catalyst. After two hours of PEG modifications, half of the PEG-modified tips were separated and stored in PPB (potassium phosphate buffer) solution to use as a control. The other half was used for BclA protein attachment. The BclA protein was first dialyzed in 10 mM PPB solution. The functionalized AFM tips were then immersed in 0.1 mg/mL BclA protein in PPB for three hours to link the protein to the PEG tethers. After three hours, the tips were carefully rinsed in PPB and stored in PPB solution at 4 °C until the next day for AFM measurements. AFM measurements were performed on three surfaces: (1) piranha-cleaned fused quartz slides, (2) TruBond 200 adhesive microscope slides (TB200), and (3) TruBond 380 adhesive microscope slides (TB380).

2.5 Spore atomic force microscopy

Spore-probes of *Bt* and *Bg* spores were prepared by Novascan Technologies (Ames, IA) according to a proprietary protocol. Each spore-probe contained a single spore affixed onto a silicon nitride probe (0.06 N/m nominal spring constant), an example spore-probe is shown in Figure 1. Spore-probe force spectroscopy^{7,12-18} was used to quantitatively measure the adhesive force between an individual spore, which effectively acts as the AFM tip, and the surface of a substrate from the force-displacement profile as the spore approaches, binds, and leaves a surface.

Because there is an apparent dependence on delay time, spore-probe measurements were all done with a delay time of 20 seconds. The probe speed for approaching and retracting from the surface was 100 nm/s. Each tip was used for 25 measurements, with each measurement at a different location in an evenly spaced 5 x 5 array on the surface. Results for each tip were averaged and standard error was calculated. In cases of apparent outliers, Grubb's test was used to determine if a point could be dismissed. For all measurements, the spring constants of the probes were determined experimentally by a thermal tune process.

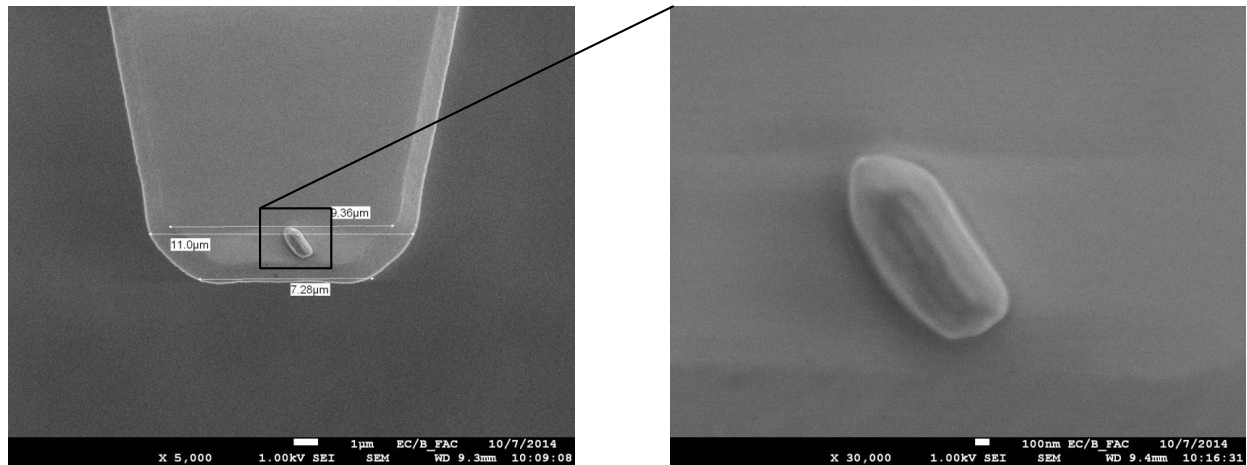


Figure 1. SEM image of representative Novascan spore-probe showing a single spore on the AFM probe. (SEM Photomicrographs, JEOL FLV 7001, 1 keV). Scale bars for left and right images are 1 μm and 100 nm, respectively.

The inverse AFM experiment was also performed, wherein a bare cantilever was scanned over a spore affixed onto a substrate and the relative adhesive force was tracked as a function of location on the spore surface. Spores were immobilized from water suspension on Poly-L-lysine coated glass microscope slides (Polysciences, Inc.; Warrington, PA). These adhesion experiments were conducted on wild *Sterne* and the ΔcotE and ΔbclA mutants as well as on *Bg* and *Bt* spores. All spore AFM work was done using a Dimension Icon® (Bruker Nano Surfaces; Santa Barbara, CA). To measure adhesion between the silicon nitride AFM tip and the surface of an immobilized spore, a DNP-10 probe, cantilever D (nominal spring constant 0.06 N/m, 20nm nominal tip radius, Bruker AFM Probes; Camarillo, CA) was used. These measurements were conducted at 53% relative humidity using the same operating modes, time delays, and sampling statistics as were used in the spore-probe measurements. For finer “adhesion imaging” of the surface of an immobilized spore, a Bruker ScanAsyst® Air silicon probe (nominally 0.4 N/m, 70 kHz, tip radius 2 nm, tip height 5 μm ; Bruker AFM Probes; Camarillo, CA) operating in Peak Force Quantitative NanoMechanical mode (PFQNM) with a scan rate of 1 Hz was used. For traditional topographical imaging of the surface of an immobilized spore, a Bruker MPP-12200 silicon probe (nominally 5 N/m, 150 kHz, tip radius 8 nm, tip height 17.5 μm ; Bruker AFM Probes; Camarillo, CA) operating in tapping mode with amplitude 154.11 mV with a scan rate of 1 Hz was used. Tips were evaluated prior to use with a TipCheck calibration standard (Aurora NanoDevices Inc.; Canada).

2.6 Electron microscopy

Field emission scanning electron microscopy (FESEM, JEOL 7001 FLV, JEOL; Tokyo, Japan) was used to morphologically characterize spores and to inspect AFM probes and spore-probes. The spores were suspended in distilled water and deposited on clean aluminum mounts and allowed to dry in air. Imaging of spores was done using the JEOL 7001 FLV in high-vacuum mode, operating at 2 keV with a nominal working distance of 7.5-10.5 mm. Spore-probes were inspected with the FE-SEM prior to force measurements. Probes were affixed to mounts using conductive carbon tape and imaged at 1 keV at a nominal working distance of 20 mm.

2.7 Air flow experiments

CELL-VU hemocytometer glass cover slides (Table 1) that contain 3 mm x 3 mm laser-etched grid were used in this experiment. The smallest square size is 0.1 mm x 0.1 mm and the largest square size is 0.5 mm x 0.5 mm. The cover slides were cleaned by washing them with soap and water followed by isopropyl alcohol to remove all particles and oils. The cover slides were air dried before particle deposition.

For wet deposition, a 6-inch diameter and 9-inch long cylinder was used to deposit the fluorescent polystyrene latex (PSL) and biological material. The PSL microspheres (1 μm , 3 μm , and 5 μm size) and spores were aerosolized, using an Aeroneb® nebulizer (Aerogen®; Galway, Ireland), into the cylinder and allowed to settle onto the gridded cover slides for use in experiments. The 1 μm , 3 μm , and 5 μm PSLs were aerosolized for 1 minute, 3.5 minutes, and 6 minutes, respectively. Biological materials were aerosolized for the following times: *Bg/Bt* spores for 5 minutes and

Sterne/mutant spores for 8 minutes. All biological material had a concentration of log 8 colony forming units (CFU)/mL.

For dry deposition, a 6-inch diameter and 24-inch long cylinder was used. The PSL microspheres and biological materials were transferred into ethanol and aerosolized separately, using a Sono-Tek aerosol generator (Sono-Tek Corporation; Milton, NY), into the cylinder and allowed to settle onto the gridded cover slides. All materials that had a particle concentration of log 8 were diluted 30 times before aerosolization to reduce clustering.

The particles in each grid were counted using a Zeiss Axioskop microscope (Carl Zeiss; New York, NY). The UV light of the microscope was employed to easily identify and count the fluorescent PSL microspheres. Visible light was used to identify and count the biological particles. Biological materials have similar size and shape; therefore, they were deposited onto separate cover slides to eliminate misidentification. Because of the ease of distinguishing PSL microspheres according to size, all sizes (1 μm , 3 μm , and 5 μm) of PSL microspheres were deposited together onto the same cover slide.

Figure 2 shows the experimental setup for removing particles using air impingement. House air supply set at 85 psi was controlled through a solenoid to deliver one puff of air through an orifice for each push of a button. A puff duration of 0.56 seconds was employed in this test to remove particles. The distance between the orifice and the surface was 1.5 cm. Markings on the surface were used to align the cover slide so that the gridded counting region was placed 1 mm off-center under the orifice to avoid the stagnant zone. This 1 mm offset was found to yield the highest re-aerosolization and was optimized by our previous aerosol experiments and with the help of computational fluid dynamics modeling. Particles on cover slides were counted using a microscope before the particle removal. A puff of air was delivered to each slide and the number of particles remaining on the cover slide was counted via microscopy. Eight replicates were performed of each experiment.

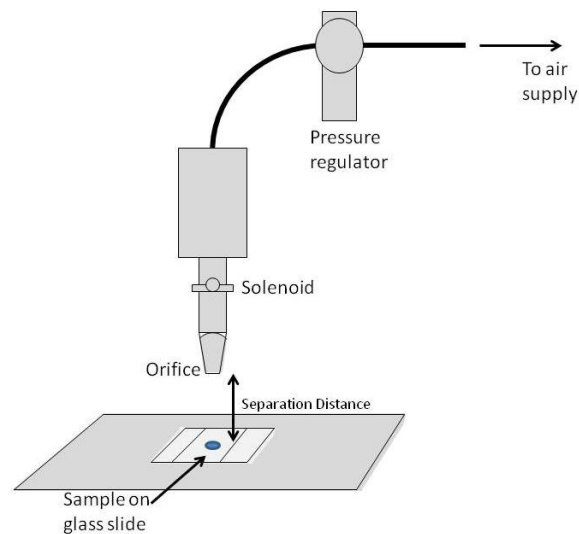


Figure 2. Experimental setup for particle removal by air impingement.

2.8 Liquid vortex experiments

A 50 μL liquid suspension of spores were placed on a surface substrate as small droplets. As a reference, similar volume was delivered to 50 mL centrifuge tubes filled with 20 mL of PBST (Phosphate Buffered Saline Tween® 20 solution). The slides were air dried and placed in 50 mL centrifuge tubes filled with 20 mL of PBST and vortexed for 10 minutes. Eight reference and eight slide samples were made for each organism. Each sample was plated to determine the amount of organisms removed from the surface.

2.9 Molecular modeling

The modeling portion focused on using steered molecular dynamics (MD) simulations with the CHARMM force field to probe the molecular-level surface interactions^{189,20} of a single exosporium filament hair (CTD of BclA trimer obtained from SWISS-MODEL²⁰⁻²³⁴ of the *Btk* strain, using 3TYJ²⁴⁵ from PDBj (Protein Data Bank Japan) as the protein threading template) with various (15 different) orientations on a bare 11.4 nm x 11.4 nm x 1.8 nm patch of an

amorphous SiO₂ glass surface (force field parameters from Cruz-Chu et al.²⁵), as shown in Figure 3. These simulations focused on probing the dominant chemical or physical interactions (e.g., electrostatic, hydrogen-bonds) and the role of hair orientation. The single-hair results may be converted to whole spore adhesive forces based on estimates of hair surface density and spore-surface contact area estimations, for comparison with experiment. Binding energies and forces, hair orientations and structures, and hydrogen-bonding have been analyzed. The total number of atoms was ~ 20,000. Materials Studio and VMD were used for building and orienting the system. Each orientation was simulated for 20 ns after placing the bottom of the hair 0.2 nm above the top of the substrate surface and pushing the hair towards the surface with a gentle (0.1 nm/ps) initial relative velocity (in addition to the random atom velocities resulting from the 300 kelvin (K) initial temperature) to accelerate initial binding and thereafter pulling the top region of the hair away from the substrate at a constant rate of 0.1 nm/ns (2 nm over 20 ns) to mimic the protein AFM experiment (top of hair was tethered to a virtual cantilever). The glass surface atoms were fixed in place (frozen), but the hair atoms were allowed to move and respond to the forces (flexible). LAMMPS was used to perform the MD simulations with a 0.8 nm switching inner cutoff, a 1.0 nm Van der Waals and long-range Coulombic outer cutoff, and a 1.0 fs time step. Long-range Coulombic interactions were calculated using the particle-particle particle-mesh Ewald method (order 6, 1.0x10⁻⁶ relative accuracy), and periodic boundary conditions extended over the entire glass surface in the *xy*-plane as well as 20 nm in the *z*-direction to prevent the hair from interacting with periodic images. Binding energies between hair and surface atoms were efficiently calculated using the LAMMPS group/group compute, and the slope of the binding energy versus tether displacement in *z*-direction away from the substrate was used to calculate the adhesive force between hair and substrate.

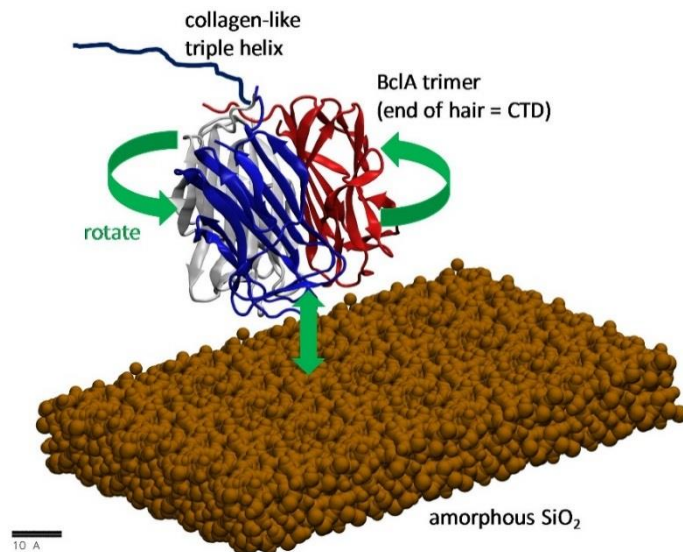


Figure 3. Model setup of single-hair on glass MD system. Glass surface atoms are shown as brown balls. The hair (BclA trimer) is represented as a cartoon, emphasizing the beta-sheet and flexible loop conformations of the CTD, and colored by protein monomer. The collagen-like triple helix of the hair is represented as a wavy blue line for simplicity. Green arrows indicate initial orientation and the hair-surface interaction. Scale bar is 1 nm.

3 RESULTS AND DISCUSSION

3.1 Spore adhesion

Results of the spore AFM (Figures 4-6), liquid vortex (Figure 7), and air flow studies (Figure 8) seem to be in agreement and may suggest the following trends:

1. Non-hairy *Bg* has stronger adhesion than hairy *Bt* on hydrophobic surfaces (confirmed by AFM, vortex, and aerosol experiments), in agreement with the EPA SPORE report.²⁶ This may refute part of our hypothesis (hairs enhance adhesion), but species differences (size, hydrophobicity, and short hair issues) may play a role.

2. Surface type (hydrophobic/hydrophilic) affects adhesion of all spore types (confirmed by AFM and vortex experiments). This may support part of our hypothesis (hairs respond to different environments and moderate adhesion).
3. *Sterne* and *AbcIA/ΔcotE* mutant adhesion comparison in aerosol data (on glass coverslips of intermediate hydrophobicity) may suggest basal layer effects on adhesion, in possible contradiction to part of our hypothesis (hair dominates adhesion).
4. Humidity (capillary forces) appears to play a minor role in adhesion of *Bg* and *Bt* and a stronger role in that of PSL beads, *Sterne* spores, and *AbcIA/ΔcotE* mutants.

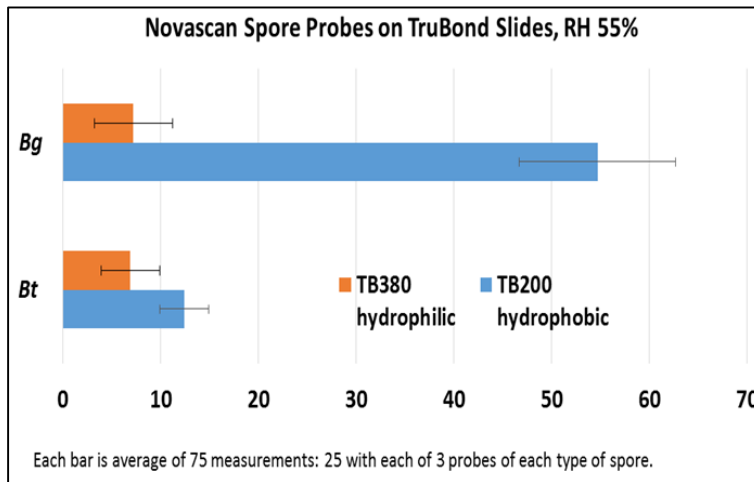


Figure 4. Adhesive force (nN) comparison of *Bg* and *Bt* AFM spore-probes on hydrophilic and hydrophobic glass surfaces at relative humidity 55%.

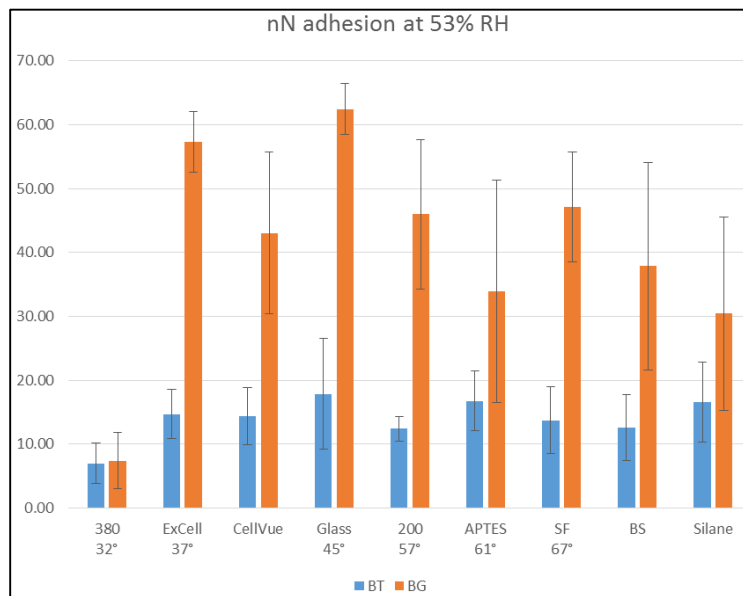


Figure 5. *Bg* and *Bt* AFM spore-probes on various surface substrates; each bar is the average of three probes (three different spores) at 25 locations on the surface (total of 75 measurements each). Surface substrates were sorted by water contact angle (degrees), listed below each material if measured.

The results of the AFM testing on nine of the surface substrates (Table 1) in Figure 6 seem to be in agreement. On all but the most hydrophilic surface, the adhesion of *Bg* was markedly higher than the adhesion of *Bt*, indicating that the exosporium hairs are not associated with higher adhesion and in fact may be associated with lower adhesion on most

surfaces. Error bars in this figure highlight variations between individual spores, as each probe is a different spore with likely variations in size, orientation, and surface structure.

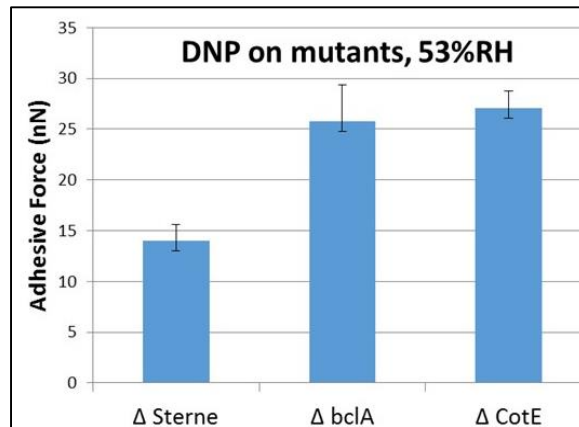


Figure 6. AFM silicon nitride DNP tip measurements on immobilized spores.

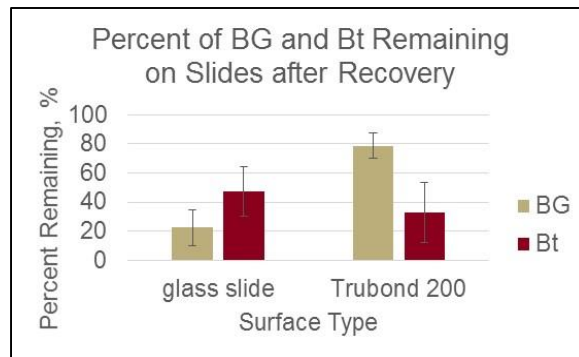


Figure 7. Percent of *Bg* and *Bt* spores remaining on glass and TB200 slides after liquid vortex experiment.

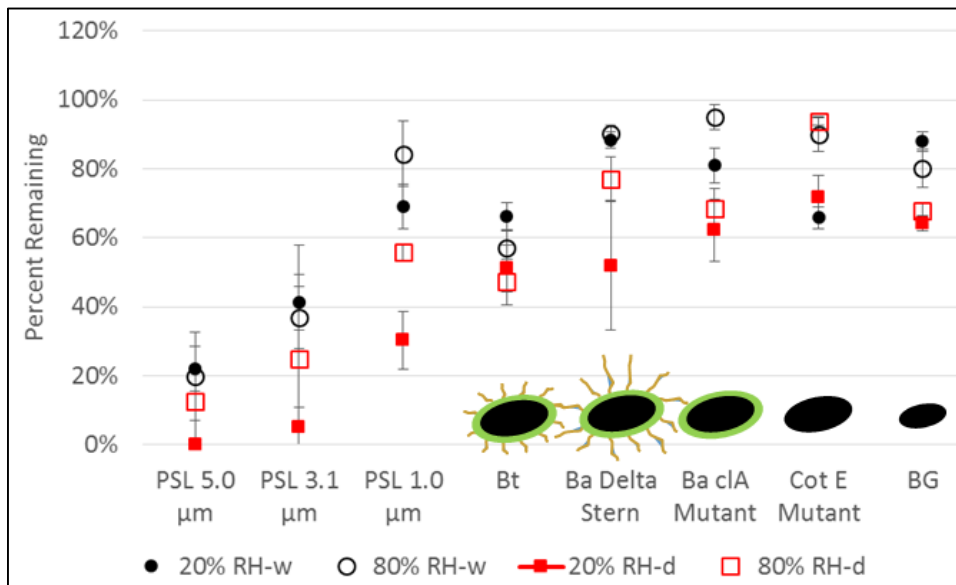


Figure 8. Percent of particles remaining on Cell-Vu gridded glass slides after air impingement experiment, including wet deposition (w), dry deposition (d), high RH (80%), and low RH (20%).

3.2 Protein adhesion

Recombinant BclA protein was prepared, purified, and characterized, and single-protein AFM experiments were performed. Circular dichroism studies are ongoing to explore the adhesion and secondary structure of this protein. BclA protein is known to assemble into multimeric forms, and this is evident from our gel analysis. The monomeric protein migrated to ~60 kDa size, and, as expected, other multimeric forms (~170-180 kDa) were also observed in the SDS-PAGE results (not shown). A total of 4 mg of protein was purified and used in the protein AFM study. Table 2 presents these results, which suggest:

1. Based on the differences in the force curves obtained for the BclA tethered to the AFM tips via the NHS-PEG-NHS linker compared with the linker-functionalized AFM tips alone without the protein (control), we conclude that we were successfully able to covalently link the BclA protein to the AFM tip via the NHS-PEG-NHS linker.
2. Based on the measurements of the debonding forces (F_1 and F_2), we conclude that the BclA protein is significantly more strongly attracted to the three surfaces tested in the following order from strongest to weakest: TB380 > TB200 > fused quartz.
3. The degree of protein unfolding of the protein as it was pulled from the surface by the AFM-tip retraction shows a slight but statistically significant increased degree of unfolding of BclA as it was pulled off of the quartz surface compared to the TB200 and TB380 surfaces, with no significant difference between TB200 and TB380. The difference for the quartz surface is likely caused by a different orientation of the protein due to this surface having negative charge density, which can be strongly orienting for protein adsorption.

Table 2. Protein AFM measurements. F_1 : Maximum debonding force. F_2 : Final debonding force. Stretching Distance: Separation of AFM tip from surface at final debonding. Statistical analyses using two-tailed Student's *t*-test shows comparisons for F_1 , F_2 , and stretching distance between fused quartz, TB200, and TB380 are all significantly different ($p < 0.05$) except for the stretching distance between TB200 and TB380.

Tip/surface		F_1 , max force, nN	(a) to (b) stretching distance, nm	F_2 , last jump force, nN
BclA on Quartz CAW < 10° n = 40	Mean	0.77	32.08	0.60
	St dev	0.12	3.26	0.10
BclA on TB200, CAW = 62.7° ± 2.70° n = 11	Mean	0.91	29.69	0.88
	St dev	0.05	2.92	0.04
BclA on TB380, CAW=33.5° ± 0.77° n = 20	Mean	1.33	30.33	1.16
	St dev	0.31	4.94	0.36

Calculated single-hair adhesive forces were ~3 nN to 5 nN, depending on orientation. MD simulation results suggest the formation of several hydroxyl H-bonds between protein and SiO₂ surface as well as deformation of protein loops to spread over the surface (see red loop in Figure 9) and increase contact area, possibly supporting the view that the exosporium hairs respond to their local environment and demonstrating one likely mechanism of response: H-bond formation.

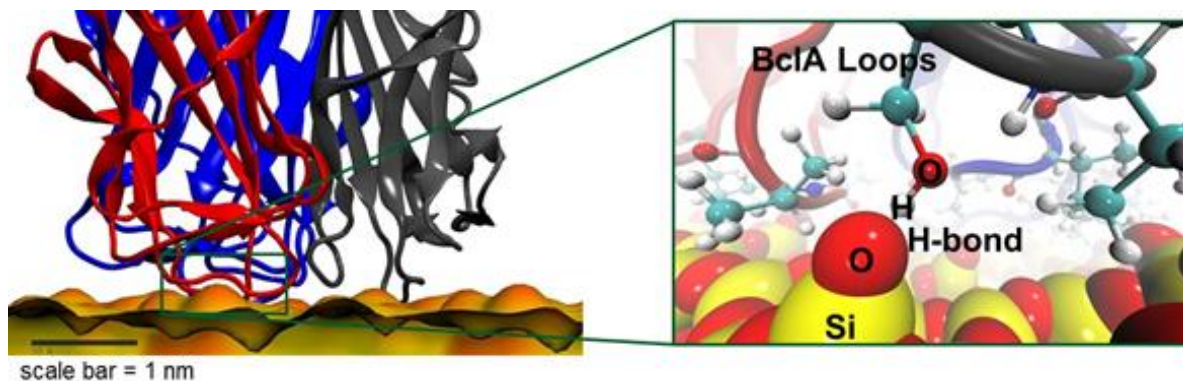


Figure 9. (Left) Side-view of loops spreading over surface contour; hair represented as cartoon and colored by protein monomer; SiO₂ surface colored yellow/orange; scale bar is 1 nm. (Right) Zoomed in view of H-bond formation between the OH group of protein (represented as ball-stick model near balls of substrate and as cartoon further away) and O of substrate; oxygen, carbon, hydrogen, and silicon atoms colored red, cyan, white, and yellow, respectively.

4 CONCLUSIONS

We have developed a methodology to measure spore and 1 μm particle removal from surfaces using air impingement. The results of the spore AFM, liquid vortex, and air impingement studies are in agreement and suggest that the exosporium hairs respond to different substrates and affect spore adhesion, in many cases lowering adhesion. These results may also suggest an important role of the exosporium basal layer, in addition to the hairs. Attachment of BclA protein to PEG tether on AFM tip was successful and protein stretching/unfolding was observed in the force-extension curves during protein detachment from surface (not shown). MD simulations have observed H-bonding between BclA protein (hair) and SiO₂ glass substrate. This may explain how hairs respond to different environments.

ACKNOWLEDGMENTS

The authors acknowledge financial support from the Edgewood Chemical Biological Center's Surface Science Initiative Program.

REFERENCES

- [1] Kailas, L. *et al.*, "Surface architecture of endospores of the *Bacillus cereus*/*anthracis*/*thuringiensis* family at the subnanometer scale." *Proceedings of the National Academy of Sciences*, **2011**, 108(38), p16014-16019.
- [2] Malkin, A.J. and Plomp, M., "High-resolution architecture and structural dynamics of microbial and cellular systems: Insights from in vitro atomic force microscopy." In: *Scanning Probe Microscopy of Functional Materials: Nanoscale Imaging and Spectroscopy*. Kalinin, S.V. and Gruverman, A. (Eds.). Springer Science Business Media, LLC, New York. **2010**.
- [3] Hachisuka, Y.; Kojima, K.; and Sato, T., "Fine filaments on the outside of the exosporium of *Bacillus anthracis* spores." *Journal of Bacteriology*, **1966**, 91 (6), p2382-2384.
- [4] *Anthrax in humans and animals, 4th Ed.* World Health Organization: Geneva, Switzerland. **2008**. p60.
- [5] Faille, C. *et al.*, "Occurrence of *Bacillus cereus* spores with a damaged exosporium: Consequences on the spore adhesion on surfaces of food processing lines." *Journal of Food Protection*, **2007**, 70(10), p2346-2353.
- [6] Lequette, Y. *et al.*, "Role played by exosporium glycoproteins in the surface properties of *Bacillus cereus* spores and in their adhesion to stainless steel." *Applied Environmental Microbiology*, **2011**, 77(14), p4905-4911.

- [7] Bowen, W.R. *et al.*, "The measurement of *Bacillus mycoides* spore adhesion using atomic force microscopy, simple counting methods, and a spinning disk technique." *Biotechnology and Bioengineering*, **2002**, 79(2), p170-179.
- [8] Sylvestre, P.; Couture-Tosi, E.; and Mock, M., "A collagen-like surface glycoprotein is a structural component of the *Bacillus anthracis* exosporium." *Molecular Microbiology*, **2002**, 45(1), p169-178.
- [9] Rety, S. *et al.*, "The crystal structure of the *Bacillus anthracis* spore surface protein BclA shows remarkable similarity to mammalian proteins." *Journal of Biological Chemistry*, **2005**, 280(52), p43073-43078.
- [10] Moberly, B.J.; Shafa, F.; and Gerhardt, P., "Structural details of anthrax spores during stages of transformation into vegetative cells." *Journal of Bacteriology*, **1966**, 92(1), p220-228.
- [11] He, L.M. and Tebo, B.M., "Surface charge properties of and Cu(II) adsorption by spores of the marine *Bacillus* sp. strain SG-1." *Applied and Environmental Microbiology*, **1998**, 64 (3), p1123-1129.
- [12] Chung, E. *et al.*, "Adhesion of spores of *Bacillus thuringiensis* on a planar surface." *Environmental Science and Technology*, **2010**, 44(1), p290-296.
- [13] Chung, E. *et al.*, "The role of the electrostatic force in spore adhesion." *Environmental Science and Technology*, **2010**, 44(16), p6209-6214.
- [14] Kweon, H.; Yiaccoumi, S.; and Tsouris, C., "Friction and adhesion forces of *Bacillus thuringiensis* spores on planar surfaces in atmospheric systems." *Langmuir*, **2011**, 27(24), p14975-14981.
- [15] Lee, I. *et al.*, "Scanning surface potential microscopy of spore adhesion on surfaces." *Colloids and Surfaces B: Biointerfaces*, **2012**, 92, p271-276.
- [16] Loskill, P. *et al.*, "Reduced adhesion of oral bacteria on hydroxyapatite by fluoride treatment." *Langmuir*, **2013**, 29(18), p5528-5533.
- [17] Whisman, N. *et al.*, "Probing microplatform for the study of biological adhesion forces." *Review of Scientific Instruments*, **2003**, 74(10), p4491-4494.
- [18] Snyder, J.A. *et al.*, "Development of a tuned interfacial force field parameter set for the simulation of protein adsorption to silica glass." *Biointerphases*, **2012**, 7(1-4), p56.
- [19] Vellore, N.A. *et al.*, "Assessment of the transferability of a protein force field for the simulation of peptide-surface interactions." *Langmuir*, **2010**, 26(10), p7396-7404.
- [20] Arnold, K. *et al.*, "The SWISS-MODEL workspace: A web-based environment for protein structure homology modelling." *Bioinformatics (Oxford, England)*, **2006**, 22(2), p195-201.
- [21] Biasini, M. *et al.*, "SWISS-MODEL: Modelling protein tertiary and quaternary structure using evolutionary information." *Nucleic Acids Research*, **2014**, 42(Web Server issue), W252-W258.
- [22] Guex, N.; Peitsch, M.C.; and Schwede, T., "Automated comparative protein structure modeling with SWISS-MODEL and Swiss-PdbViewer: A historical perspective." *Electrophoresis*, **2009**, 30(Suppl. 1), S162-S173.
- [23] Kiefer, F. *et al.*, "The SWISS-MODEL repository and associated resources." *Nucleic Acids Research*, **2009**, 37 (Database issue), D387-D392.
- [24] Kirchdoerfer, R.N. *et al.*, "Variable lymphocyte receptor recognition of the immunodominant glycoprotein of *Bacillus anthracis* spores." *Structure*, **2012**, 20(3), p479-486.
- [25] Cruz-Chu, E.R.; Aksimentiev, A.; and Schulten, K., "Water-silica force field for simulating nanodevices." *Journal of Physical Chemistry B*, **2006**, 110(43), p21497-21508.
- [26] Wiener, R.W., "Determination of the Difference in Reaerosolization of Spores off Outdoor Materials." **2014**, EPA/600/R-14/259.
- [27]



SEEDLING PROJECTS

The nature of CWA adsorption on graphene

Harold D. Banks*

U.S. Army Edgewood Chemical Biological Center, Research and Technology Directorate,
5183 Blackhawk Rd, Aberdeen Proving Ground, MD 21010

ABSTRACT

The investigation of the adsorption of chemical warfare agents on graphene, a carbon allotrope with tremendous nano-technological potential, has fundamental significance for military applications due to the possibility that it will lead to the development of detectors and sensors for toxic materials of significantly reduced size, lowering the burden of the Warfighter. For electronic devices, pristine graphene itself is not useful due to its zero bandwidth. Nitrogen-doped graphene, however, has a nonzero bandwidth and was chosen for this study. Computational chemistry is ideal for studying this phenomenon since it produces results relatively quickly, inexpensively and safely removed from work with hazardous agents. Graphene models in the past that have modeled this substance with polynuclear aromatic hydrocarbons are flawed due to the fact that they ignore the findings that graphene chemistry occurs at its edges and defects, and that these areas are reactive intermediates, not stable compounds. The free energies of activation for the Stone-Wales rearrangement of free radical intermediates using heterocyclic model compounds to model the actual structures of N-doped graphene were determined at the B3LYP/6-31G level to assess the actual surface presented for adsorption by the chosen agent, sarin.

Keywords: N-doped graphene, Stone-Wales rearrangement, free radical edges, DFT, computational models

1 INTRODUCTION

The detection and sensing of graphene (Figure 1), the most recent addition to the family of carbon allotropes, has a wealth of properties that render it attractive for theoretical and experimental investigation.¹ Due to the potential of developing devices sensitive to the adsorption of chemical (and biological) agents on graphene,² the adsorption of the chemical warfare agent (CWA), sarin, was undertaken. It should be noted that the results of configuration interaction calculations on sarin using a C₂₂H₁₂ model for graphene was recently published.³ Unfortunately, the results are flawed since the graphene model is only somewhat larger than sarin. The C₂₁₆H₃₆ model of Grimme⁴ would be an improvement except that the computational expense would become prohibitive and the edges are not realistic because they are passivated with hydrogens (*vide infra*).

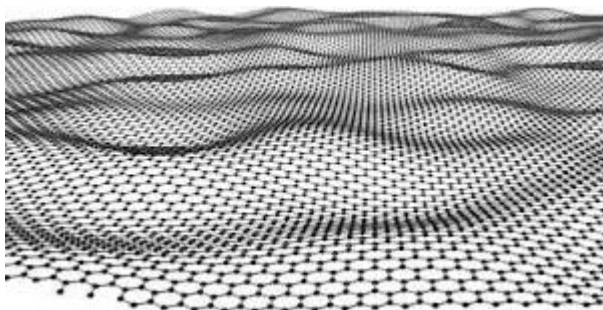


Figure 1. Partial structure of graphene. The edges are not passivated. This structure represents an initially-formed reactive species that resulted in rearranged edge structures.

It is tempting for an organic chemist to regard graphene as a huge polynuclear aromatic hydrocarbon (PAH). Several investigations have modelled graphene in this manner.⁵ This approach is unsound. The edges of graphene do not consist of C-H bonds, but rather of reactive centers. Graphene is best conceptualized as a two-dimensional lattice, whose extended honeycomb lattice may be analyzed in the form of two triangular structures. The in-plane bonds (sp^2) are not involved in conductivity; the remaining p orbital at each carbon contributes to the formation of π and π^* bands,

designated valence and conduction bands, respectively. The extensive lattice of graphene, formed from a two-atom unit cell, creates an environment quite different from the considerably smaller PAHs. Fortunately, a considerable body of research has demonstrated that the chemistry of graphene occurs not at the interior (the so-called graphitic sites) but rather at the edges and defects.⁶ The orbital energies depend on the momentum of charge carriers in the Brillouin zone, defined by the two points of coincidence of the bands.⁷

Although pristine graphene has many potential applications, those of particular military interest are those that have electronic components. Graphene has no band width, or separation between its valence and conduction bands, and therefore, the accessible on/off states essential for circuitry are absent. This deficiency can be overcome by the formation of nanoribbons of 10 nm or less (quantum confinement of electrons), or doping graphene with boron, sulfur, phosphorus, or nitrogen.⁸ Due to recent success in the preparation of nitrogen-doped graphene in which pyridine and pyrrole rings predominate⁹ and the author's extensive experience with nitrogen heterocycles (model compounds), a study of the adsorption of sarin on N-doped graphene was undertaken (Figure 2). Characterization of the structure of the edges and defects became the focus of this project.

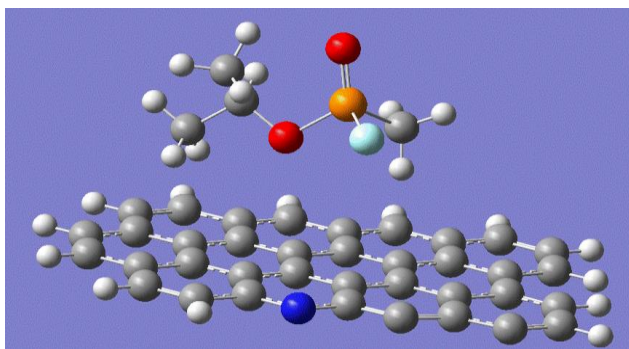


Figure 2. One configuration of sarin on a heterocyclic nitrogen model bearing a diradical edge.

When graphene is prepared by a top-down method (e.g., exfoliation) or a bottom-up method (e.g., chemical vapor deposition), reactive species are produced at the edges. Depending on the nature of the edge (zigzag, armchair, or Klein), these structures self-passivate. Koskinen and coworkers¹⁰ found that the Stone-Wales rearrangement (Figure 3) took place for zigzag and armchair edges, generating five- and seven-membered rings.¹¹

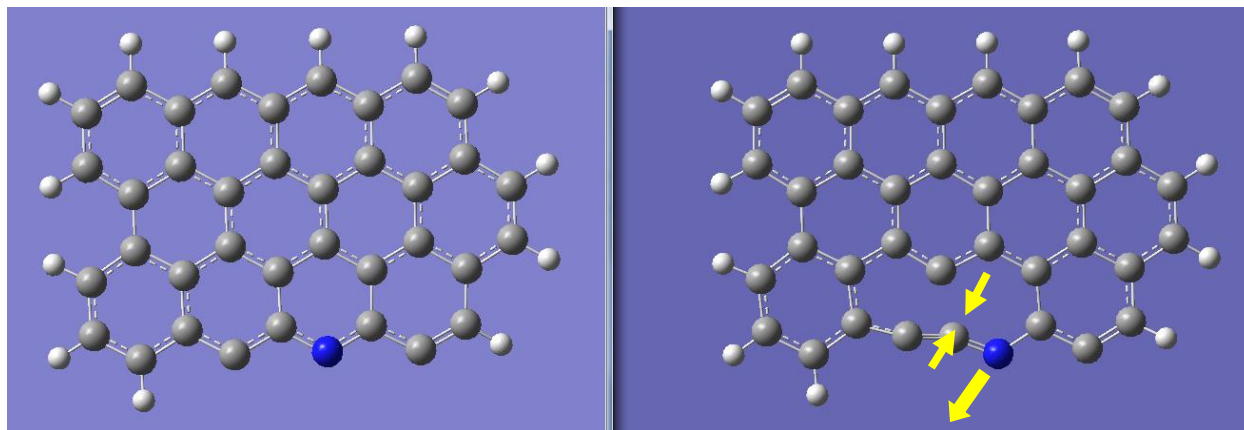


Figure 3. Stone-Wales rearrangement of a ground state diradical into a 5/7 heterocyclic structure. This is typical of the behavior of a zigzag edge. The arrows indicate the pathway to the new ring structure.

Therefore, we chose to calculate the free energies of activation for self-passivation by means of this mechanism for singlet and triplet free radicals to obtain a realistic picture of the nature of the edges and defects (Figure 4) likely to be encountered by an adsorbate. The challenge of the computational chemist is to find a suitable model for the vast graphene molecule that can yield reasonable results with affordable calculations. Accordingly, simple nitrogen heterocyclic diradicals were chosen initially to serve as models for the edges of the N-doped graphene surface; complexity was increased until the computational limit was reached.

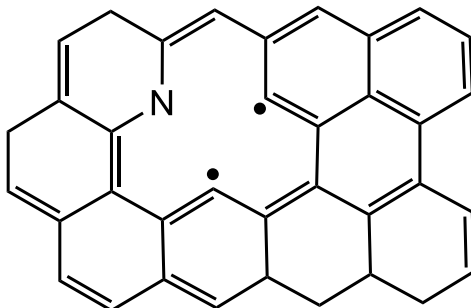


Figure 4. A diradical monovacant defect resulting from the removal of a single carbon in the vicinity of the heterocyclic nitrogen atom. This structure also features zigzag and armchair edges. The zigzag edges are horizontal, and the armchair edges are vertical.

2 METHODOLOGY

The aim of this project was to design molecules that were within our computational resources that maintained the salient structural features of N-doped graphene. The strategy was to start with relatively small heterocyclic nitrogen compounds and increase the number of fused rings, until an acceptably small difference in calculated free energies of activation for the Stone-Wales rearrangement was determined. Initial computations were performed on monoradicals; however, diradicals were deemed to be more reflective of the environment initially found at an N-doped graphene edge. The prominent cyclic features of N-doping are pyridine and pyrrole rings. Heterocycles featuring the former ring were chosen. Calculations were performed at the UB3LYP/6-31G level of theory using the Gaussian 09 suite of programs (Gaussian, Inc.; Pittsburgh, PA).¹² Due to the calculations for free radicals, an unrestricted method was employed. Thermal energies were scaled by 0.9804. This level of theory has proven a reasonable compromise between accuracy and expense. Avogadro proved useful to import the starting PAH structures. Ground states and transition states were characterized by the absence and presence of one imaginary frequency, respectively. The free energies of activation were calculated in the absence of solvent at 298.15 kelvin (K) and 1.000 atm, using the calculated enthalpy and entropy differences from the thermochemical analysis. Transition states could be further studied by animation of the imaginary frequency using GaussView 3.09 (Gaussian, Inc.; Pittsburgh, PA).¹³ Given our computational resources, the dibenz[bc,ef]ovalene (DBO) diradical was the limiting structure in this study. Calculation of half-lives was accomplished by use of the free energy of activation to obtain the first-order rate constant under standard conditions, and then dividing $\ln 2$ by the rate constant.

The characterization of the edges (zigzag, armchair, or Klein) and monovalent defects of N-doped graphene models was an introductory step to the rigorous calculation in this project. Although it has been established that the primary sites of attachment of sarin are at the edges and defects, the structures of which have been studied in this project, the adsorption interaction energies of these model structures with sarin must be determined. One can conceive of several configurations that would be assumed by sarin and its modeled adsorbant. A molecular mechanics program such as found in the Forcite program (Materials Studio) is required to provide approximate energies of the various configurations. Data of increased accuracy will then be obtained by optimization of these binary systems with density functional theory (DFT) calculations.

3 DATA

The results of the B3LYP/6-31G calculations are presented in Table 1. The thermochemical results pertain to 298.15 K and 1.000 atm in the absence of solvent. All transition states were found to have a unique imaginary frequency. Animation of this frequency demonstrated that particular six-membered rings at the edges were cleaved with formation of five- and seven-membered rings.

Table 1. Energy, thermal correction, and entropy data used to calculate the diradical free energies of activation. The entries presented in red pertain to the free energy difference between the reactant and the Stone-Wales product (not the transition state).

	DiRadical	Ground State				Transition State				TS freq (cm ⁻¹)	
		Energy	Thermal Corr	Corrt'd Energy	Entropy	Energy	Thermal Corr	Corrt'd Energy	Entropy		
		Hartrees	Hartrees	Hartrees	eu	Hartrees	Hartrees	Hartrees	eu		
<i>Anthracene</i>											
1	s	1N-8,9	-554.0059215	0.1658341	-553.8433377	95.185	-553.8753927	0.1615781	-553.71694922	98.673	-503.00
2	t	1N-8,9	-554.0473280	0.1673631	-553.8832452	95.999	-553.9146137	0.1621052	-553.75565334	100.215	-453.38
3	s	1N-8,9	-554.0059215	0.1658341	-553.8433377	95.185	-553.9779625	0.1638336	-553.81730727	95.844	-615.67
4	t	1N-8,9	-554.0473280	0.1673631	-553.8832452	95.999	-553.9548985	0.1618804	-553.79615858	100.229	-749.48
5	s	(all C)-8,9	-537.9915712	0.1782330	-537.8168316	95.506	-537.9642844	0.1762913	-537.79141315	95.930	-599.74
6	s	2N-1,9	-553.9429430	0.1658975	-553.7802971	95.993	-553.8787485	0.1611479	-553.72072687	97.101	-717.13
7	t	2N-1,9	-553.9832703	0.1675115	-553.8190420	96.659	-553.9042562	0.1615999	-553.74579134	97.415	-541.23
8	t	2N-8,9	-554.0481636	0.1674705	-553.8839755	96.148	-553.9146137	0.1621052	-553.75565334	100.215	-453.38
<i>Phenanthrene</i>											
9	s	1N-8,9	-554.0173361	0.1660220	-553.8545681	96.491	-553.9838390	0.1643360	-553.82269112	94.342	-505.69
10	t	1N-8,9	-554.0599543	0.1676743	-553.8955664	96.073	-553.9260900	0.1624196	-553.76682134	97.660	-280.94
11	s	2N-8,9	-554.0150227	0.1660981	-553.8521801	96.525	-553.9822886	0.1644431	-553.82103570	94.473	-502.20
12	t	2N-8,9	-554.0575078	0.1677427	-553.8930529	96.141	-553.9230304	0.1620085	-553.76416486	98.069	-359.38
13	s	(ΔG) 1N-8,9	-554.0059215	0.1658341	-553.8433377	95.185	-554.0749661	0.1679250	-553.91029885	94.592	XXXX
<i>Pyrene</i>											
14	s	1N-8,9	-630.2345595	0.1797033	-630.0583784	97.398	-630.1967313	0.1781338	-630.02205330	99.928	-505.69
15	t	1N-8,9	-630.2751101	0.1812665	-630.0973964	98.151	-630.1661269	0.1772301	-629.99233506	102.611	-280.94
16	s	2N-8,9	-630.2312684	0.1796689	-630.0551210	97.536	-630.1627065	0.1772725	-629.98887309	103.000	-502.20
17	t	2N-8,9	-630.2718447	0.1812460	-630.0941511	98.317	-630.1949907	0.1781522	-630.02029465	99.369	-359.79
<i>Ovalene</i>											
18	s	1Noval89	-1242.3221780	0.3342093	-1241.9945192	133.033	-1242.2908858	0.3327269	-1241.96461380	133.496	-625.66
19	t	1Noval89	-1242.3655330	0.3358389	-1242.0362765	133.727	-1242.2350244	0.3301462	-1241.91128304	137.503	-693.60
20	s	2Noval89	-1242.3270259	0.3344076	-1241.9991727	132.845	-1242.2970427	0.3329536	-1241.97054840	133.075	-608.93
21	t	2Noval89	-1242.3675533	0.3358389	-1242.0382968	133.727	-1242.2383189	0.3302594	-1241.91446653	137.257	-699.02
<i>DBO</i>											
22	s	7N-89BDO	-1472.1194341	0.3972220	-1471.7299977	149.863	-1472.0491470	0.3951099	-1471.66170223	150.722	-504.80
23	s	7N-68BDO	-1472.0960542	0.0396552	-1472.0571762	148.865	-1472.0500970	0.3983290	-1471.65949553	150.650	-253.00
24	s	6N-89BDO	-1472.1207967	0.3971643	-1471.7314168	150.932	-1472.0259891	0.3942600	-1471.63937774	151.207	-466.64
<i>Coronene</i>											
25	s	2N4,5	-936.2875321	0.2570287	-936.0355412	115.075	-936.1513519	0.2540237	-935.90225626	117.886	-662.00

In addition to calculating the free energies of activation of the diradicals in the Stone-Wales rearrangement, it was of interest to determine the enthalpy change. An example is provided (entry 13 in red) for the 8,9-diradical of azaanthracene. In this example, the data entered correspond to the product of the reaction, and not the transition state. This reaction was determined to be exothermic by 41.8 kcal/mol. The energy (equivalent to enthalpy in these rearrangements) differences were calculated in Hartrees followed by multiplication by 627.51 for conversion to kcal/mol. The entropy values are expressed in cal/mol-K. The anthracene-derived diradicals modeled a zigzag edge exclusively, while those from phenanthrene modeled an armchair edge. Pyrene-, ovalene-, DBO-, and coronene-derived model diradicals featured both armchair and zigzag edges. The transition states for the models investigated had only one imaginary (expressed as negative values) frequency. Animation of these frequencies demonstrated that the Stone-Wales rearrangement was involved.

4 RESULTS

In our preliminary studies, monoradical models were employed; however, it became apparent that diradicals were more reasonable species in approximating the edge structure of freshly prepared graphene. The data of Table 1 may be used to calculate the regiochemistry for the diradicals that were studied in this project. For the large DBO model compound, **24** is only slightly more stable than **22**. When two radical sites are found next to nitrogen as in **22**, the structure is destabilized with respect to **24** by 27.2 kcal/mol.

For the model compounds investigated, the singlet diradicals rearranged more readily than the corresponding triplets. Accordingly, for the larger models, calculations were performed only on those uncharged radicals with a multiplicity of one. In Figure 5, 1-azanaphthalene (identified by **1** – **4**) provided the intriguing results that Stone-Wales cleavage of the carbon-carbon bond (black line) proceeds significantly more readily than carbon-nitrogen cleavage (red line).

		Singlet (kcal/mol)	Triplet (kcal/mol)
	1, 2	16.1	53.4
	3, 4	78.3	78.8
	5, 6	76.0	79.3
	7, 8	37.1	45.7
	9, 10	20.6	80.3
	11, 12	20.1	80.3
	14, 15	20.2	64.6
	16, 17	39.9	46.0
	18, 19	18.6	77.3
	20, 21	17.9	76.6
	22	42.6	—
	23	249.0	—
	24	57.7	—
	25	82.8	—

Figure 5. Free energies of activation for the Stone-Wales rearrangement of diradical singlet and triplet models for N-doped graphene. (See Table 1 for identification numbers.)

Since this rearrangement is a pseudo first-order reaction, one can calculate a half-life of less than 5 seconds under standard conditions. Regioisomeric 2-azanaphthalene **5** is considerably less reactive; however, its isomeric diradical **7**, while lagging behind the reactivity of the **1**, is considerably more reactive than **5**. The azaanthracenes are primitive models for the zigzag edge of N-doped graphene. To begin modeling the armchair edge, azaphenanthrenes were employed. The position of nitrogen on diradicals **9** and **11** has little effect on reactivity. The half-lives for these

compounds is also less than 5 seconds. The significantly higher reactivity of **20**, with respect to **22**, may be related to stabilization of the diradical by a larger aromatic system. Support for this analysis is provided by the free energy of activation of **24**. It would be interesting to investigate the apparent anomalous behavior of **23**.

5 CONCLUSIONS

Singlet and triplet diradicals bearing a pyridine ring were included in this preliminary study to define the environment that would be encountered by the CWA, sarin, in the presence of N-doped graphene. The size and shape of the edge (zigzag or armchair) was varied. For example, the azaanthracenes have zigzag edges, while the azaphenanthrenes have armchair edges. It should be noted that in the case of 1-azaanthracene, cleavage of the benzene moiety is favored over that of the pyridine moiety. In general, rearrangement occurs considerably faster by means of the singlet as opposed to the triplet for all diradicals studied. The free energies of activation increase for the larger diradicals possibly reflecting a stabilization of the ground state molecules by means of extended conjugation. Since it is reasonable to expect adsorption to occur at the edges and defects of the graphene derivative and not in its vast interior (a graphitic region), it is herein hypothesized that small, computationally accessible models will produce acceptable results when the adsorption results are pursued in an extended study.

ACKNOWLEDGMENTS

Support for this research was provided by the U.S. Army Edgewood Chemical Biological Center Research and Technology Directorate's Seedling Program.

REFERENCES

- [1] (a) Georgakilas, V. *et al.*, "Broad family of carbon nanoallotropes: Classification, chemistry, and applications of fullerenes, carbon dots, nanotubes, graphene, nanodiamonds, and combined superstructures." *Chemical Reviews*, **2015**, 115(11), p4744-4822. (b) Tour, J.M., "Top-down versus bottom-up fabrication of graphene-based electronics." *Chemical Reviews*, **2014**, 26 (1), p163-171. (c) Rubio-Pereda, P. and Takeuchi, N., "Density functional theory study of the organic functionalization of hydrogenated graphene." *Journal of Physical Chemistry C*, **2013**, 117(36), p18738-18745. (d) James, D.K. and Tour, J.M., "Graphene: Powder, flakes, ribbons, and sheets." *Accounts of Chemical Research*, **2013**, 46(10), p2307-2318. (e) Navolon, S. *et al.*, "Carbocatalysis by graphene-based materials." *Chemical Reviews*, **2014**, 114(12), p6179-6212. (f) Georgakilas, V. *et al.*, "Functionalization of graphene: Covalent and non-covalent approaches, derivatives and applications." *Chemical Reviews*, **2012**, 112(11), p6156-6214. (g) Allen, M.J.; Tung, V.C.; and Kaner, R.B., "Honeycomb carbon: A review of graphene." *Chemical Reviews*, **2010**, 110(1), p132-145. (h) Rodríguez-Pérez, L.; Herranz, M.Á.; and Martín, N., "The chemistry of pristine graphene." *Chemical Communications*, **2013**, 49, p3721-3735. (i) Wan, X.; Huang, Y.; and Chen, Y., "Focusing on energy and optoelectronic applications: A journey for graphene and graphene oxide at large scale." *Accounts of Chemical Research*, **2012**, 45(4), p598-607. (j) Pavlidis, I.V. *et al.*, "Graphene-based nanobiocatalytic systems: Recent advances and future prospects." *Trends in Biotechnology*, **2014**, 32, p312-320. (k) Ojha, K.; Anjaneyula, O.; and Ganguli, A.K. "Graphene-based hybrid materials: Synthetic approaches and properties." *Current Science*, **2014**, 107(3), p397-418. (l) Zhan, D. *et al.*, "Engineering the electronic structure of graphene." *Advanced Materials*, **2012**, 24(30), p4055-4069. (m) Sun, Z.; James, D.K.; and Tour, J.M., "Graphene chemistry: Synthesis and manipulation." *Journal of Physical Chemistry Letters*, **2011**, 2(19), p2425-2432. (n) Jacob, M.V. *et al.*, "Catalyst-free plasma enhanced growth of graphene from sustainable sources." *Nano Letters*, **2015**, 15(9), p5702-5708.
- [2] Lazar, P. *et al.*, "Adsorption of small organic molecules on graphene." *Journal of the American Chemical Society*, **2013**, 135(16), p6372-6377.
- [3] Pappas, B.N. *et al.*, "CI and DFT Studies of the adsorption of the nerve agent Sarin on surfaces." *Journal of Physical Chemistry C*, **2014**, 118(40), p23042-23048.

- [4] (a) Antony, J. and Grimme, S., "Structures and interaction energies of stacked graphene–nucleobase complexes." *Physical Chemistry Chemical Physics*, **2008**, 10, p2722-2729. (b) Grimme, S.; Mück-Lichtenfeld, C.; and Antony, J., "Noncovalent interactions between graphene sheets and in multishell (hyper)fullerenes." *Journal of Physical Chemistry C*, **2007**, 111(30), p11199-11207.
- [5] (a) Cao, Y. *et al.*, "Diels-Alder reactions of graphene: Computational predictions of products and sites of reaction." *Journal of the American Chemical Society*, **2013**, 135(46), p17643-17649. (b) Denis, P.A., "Organic chemistry of graphene: The Diels-Alder reaction." *Chemistry: A European Journal*, **2013**, 19(46), p15719-15725.
- [6] (a) Geim, A.K. and MacDonald, A.H. "Graphene: Exploring carbon flatland." *Physics Today*, **2007**, 60(8), p35-41. (b) Ojha, K.; Anjaneyulu, O.; and Ganguli, A.K., "Graphene-based hybrid materials: Synthetic approaches and properties." *Current Science*, **2014**, 107(3), p397-418. (c) Avouris, P., "Graphene: Electronic and photonic properties and devices." *Nano Letters*, **2010**, 10(11), p4285-4294.
- [7] Machado, F.B.C.; Aquino, A.J.A.; and Lischka, H., "The diverse manifold of electronic states generated by a single carbon defect in a graphene sheet: Multi-reference calculations using a pyrene defect model." *Chemical Physics Physical Chemistry*, **2014**, 15(15), p3334-3341.
- [8] (a) Pumera, M.J., "Heteroatom modified graphenes: Electronic and electrochemical applications." *Journal of Materials Chemistry C*, **2014**, 2, p6454-6461. (b) Han, J. *et al.*, "Generation of B-doped graphene nanoplatelets using a solution process and their supercapacitor applications." *ACS Nano*, **2013**, 7(1), p19-26. (c) Yang, Z. *et al.*, "Sulfur-doped graphene as an efficient metal-free cathode catalyst for oxygen reduction." *ACS Nano*, **2012**, 6(1), p205-211.
- [9] (a) Yazdi, A.Z. *et al.*, "Helical and dendritic unzipping of carbon nanotubes: A route to nitrogen-doped graphene nanoribbons." *American Chemical Society Nano*, **2015**, 9(6), p5833-5845. (b) Mondal, T. *et al.*, *Chemistry of Materials*, **2015**, 27(3), p716-725. (c) Wang, H.; Maiyalagan, T.; and Wang, X., "Review on recent progress in nitrogen-doped graphene: Synthesis, characterization, and its potential applications." *ACS Catalyst*, **2012**, 2(5), p781-794. [Including other references cited therein].
- [10] Koskinen, P.; Malola, S.; and Hakkinen, H., "Self-passivating edge reconstructions of graphene." *Physical Review Letters*, **2010**, 101, e115502 (published online).
- [11] (a) Zhang, Z.; Kutana, A.; and Yakobson, B.I., "Edge reconstruction-mediated graphene fracture." *Nanoscale*, **2015**, 7, p2716-2722. (b) Robertson, A.W. *et al.*, "Stability and dynamics of the tetravacancy in graphene." *Nano Letters*, **2014**, 14(3), p1634-1642.
- [12] Gaussian 09, Revision D.01, Frisch, M.J. *et al.*, Gaussian, Inc., Wallingford, Connecticut, **2009**.
- [13] GaussView 3.09 (Carnegie Office Park, Building 6, Pittsburgh, Pennsylvania 15106). *Visualization of vibrational frequencies generated by Gaussian 09 can be enabled by removing a space in the log file for "Atom AN."*

Assessing the biological threat from suicide bombers

Jerry Cabalo^{a*}, Katelynn Stafford^b, Cristian Maldonado-Figueroa^c, Daniel McGrady^d

^aU.S. Army Edgewood Chemical Biological Center, Research and Technology Directorate,
5183 Blackhawk Rd, Aberdeen Proving Ground, MD 21010

^bExcet, Inc., 8001 Braddock Rd, Suite 303, Springfield, VA 22151

^cUniversity of Puerto Rico at Mayagüez, 259 Blvd Alfonso Valdez Cabian, Mayagüez, PR 00680

^dAASKI Technology, Inc., 2108 Emmorton Park Rd, Edgewood, MD 21040

ABSTRACT

In order to assess the biological threat posed by suicide bombers, we detonated ballistic gelatin blocks using *Bacillus atrophaeus* (BG) spores as an infectious organism simulant in increasing scaled size in three tests. For each test size, two identical gelatin blocks were poured, with BG added to the block serving as the test case. Microscope slides and glazed tiles were used as sample collection surfaces. The slides were rinsed with water, and the tiles swabbed, and the rinse plated onto agar plates for detection of viable bacteria. Aerosols were monitored with a TSI® Aerodynamic Particle Sizer® and a TACBIO fluorescent particle counter. The results of our test shows that organisms can 1) survive the blast, and 2) be widely dispersed in both aerosol and visible remains of the bomber. These results show an aerosol threat. We detected living organisms in large pieces of gel as well as on the collection tiles without any visible contamination. Significant aerosol concentrations of ballistic gelatin were detected by an ultraviolet-fluorescence based particle counter.

Keywords: Suicide bomber, aerosol, biological threat, pathogen

1 INTRODUCTION

1.1 Objective

Our major objective is to understand the biological threat posed by a suicide bomber. In addition to the kinetic energy damage from the bomb itself and shrapnel, it is possible for a suicide bomber to carry pathogenic organisms. The organisms can either be carried externally, or even within the bomber himself. The latter is especially troubling since many of the barriers that have traditionally made use of biological weapons difficult (e.g., keeping the infectious organisms alive until delivery), are no longer an impediment. To accomplish the major objective, we wish to determine what fraction of organisms survive the heat and pressure of the detonation of high explosive in a suicide bomb, especially in aerosol form, and the spatial extent of dispersal of living organisms. Both the survivability and the spread of organisms are essential to understanding the biological dimension of the suicide bomber threat.

1.2 Background

Studies performed in Israel and in London after the 2005 bombings highlighted the infectious biological dimension to suicide bombings due to implantation of bone fragments and exposure to the flesh and blood remains of the bomber. Israeli studies^{1,2} noted that bone fragments from some bombers tested positive for hepatitis B and it was believed that surviving victims had been infected by the bomber. Studies of the London 2005 bombings^{3,4} also observed extensive implantation of bone fragments. Due to the ability of the Hepatitis B virus to spread through wounds, testing and prophylaxis for hepatitis and other potential infections were recommended for people close to a suicide bombing. It is clear that bone fragments can harbor and protect infectious organisms from the heat and pressure of the initial high explosive blast; however, these studies have focused on the unintentional transmission of infectious disease. The threat of the intentional combination of infectious disease with a suicide bombing must be considered including other potential mechanisms for infection, such as inhalation of aerosols generated from the bombing.

Other pathogenic organisms must be taken into account when considering the biological threat component of suicide bombers. A somewhat recent Air Force study considered the threat of transmission of HIV from a suicide bomber, showing the plausibility of a variety of biological threats.⁵ Organisms without available medical treatments or

vaccines, such as Ebola, have also been considered as a potential bioterrorist material.⁶⁻⁸ There are technical barriers that make it difficult to manufacture the organisms in high concentrations as well as to stabilize and store the organisms in a weapon. However, if a suicide bomber deliberately contracts the organisms, and travels to a destination while still asymptomatic, the two technical barriers above are easily surmounted. As a result, there could be catastrophic consequences in addition to the traditional aftermath of a suicide bomber. We contend that it is of the utmost importance to determine what kind of fragments are produced in a suicide bomber, if some of these fragments are in the form of aerosols, if even small particles can shield living organisms from the heat and pressure of the high explosive blast, and the extent of dispersion for the fragments.

Previous testing performed by the Edgewood Chemical Biological Center's Pyrotechnics Branch with 26 g of explosive and a 100-g gel block suggest fragments travel quite far. Our test is a continuation of that study scaled to larger gel blocks and larger high-explosive charges. We contend that highly contagious diseases could be exploited in a suicide bombing, and that it is essential to understand the propagation of biological material from that event. To that end, we intend to understand the extent of the dispersion of body fragments, potential generation of aerosol that wind can transport, and whether any organisms within the bomber's remains stay viable, and obtain rough measurements of the fraction of biological material that surface the detonation of the high explosive.

2 METHODOLOGY

2.1 Overview

There were a set of specific questions we sought to answer in our assessment of the biological threat from a suicide bomber. First, do organisms survive the thermal and blast effects of the high explosive detonation? Second, how does the survivability scale with the size of the high explosive blast? Third, for aerosol particles, how does particle size affect organism survivability? Lastly, how widespread could a contaminated area be? In order to answer these questions we endeavored to perform a test with a model suicide bomber that could be seeded with an organism, and then detonated under controlled conditions. Clearly, the human body is a complex mixture of different tissues, organs, bones, and fluids that each would have a unique response to the detonation event. Ideally, either a human or animal cadaver would provide the most realistic results.

We chose to utilize a very simple suicide bomber model composed of ballistic gelatin for a number of reasons. First, with ballistic gelatin, it is possible to uniformly seed the material with a test organism. The uniformity allows us to make a comparison between samples before and after the explosion and facilitates the interpretation of the data. Second, because a test of this kind has not been performed to the authors' knowledge, this was a range finding test to determine within an order of magnitude the kind of response to expect. Simplicity of the test was essential. Third, due to budget and time constraints, it was not practical to perform a full blown, complex test.

For the test organism, we utilized *Bacillus atrophaeus* (BG) spores for two reasons. First, we wanted to maintain a consistent concentration of organisms between different blocks of gelatin. We had little control of the time between preparation of the gel block and use in a test. We feared outright use of vegetative cells might significantly change the concentration of organisms during that lag time. Second, BG spores are readily available and covered by existing standing operating procedures (SOP) at the test sites. We had considered using bacteriophage MS2 to simulate the behavior of viruses, yet modifying the SOPs to include MS2 would have prevented us from performing the program within the time allotted. As a result, these initial range finding tests utilized only BG spores.

2.2 Gel preparation

Based on guidance from the Army Research Laboratory's Survivability, Lethality, Analysis Directorate, we utilized a 20% by weight formulation of natural porcine and bovine ballistic gelatin procured from Fisher Scientific™. A food-grade fluorescent dye (WATER-GLO™ 801, Spectroline®, Inc.; Westbury, NY) was added to act as a tracer. Distilled water was used to dissolve the gelatin. Unwashed "Danish milled" BG spores manufactured at Dugway Proving Ground were used as the test organism. Table 1 shows the amounts of material used for each ballistic gelatin sample. For the small and medium scale tests, we did not possess a means of rigorously mixing the gelatin powder into the water. We found that mixing the powder into the water first followed by heating to 150 °F ensured complete dissolution of the gelatin powder and a uniform liquid. For the large scale tests, involving ~25 kg of gelatin, a large oven set to 160 °F was used to heat the water. Due to the time necessary to heat ~25 L of water at once, the water was preheated and measured to ensure the correct concentration of gelatin. An industrial scale mixer was used to introduce

the gelatin into the water and ensure the uniformity of the mixer. To avoid heat damage to the fluorescent dye tracer and the BG spores, these were not added to the liquid gelatin until the solution cooled to 120 °F. The gelatin was poured into molds before being placed into a refrigerator. The solid ballistic gelatin melts around 105 °F. For the large scale ballistic gelatin blocks, a seven-gallon waste basket lined with a plastic bag was used as a mold. This approximated the size of a torso of a small person.

Table 1. Formulation of ballistic gelatin.

Test	Mass of Gelatin (kg)	Mass of Water (kg)	Volume of Dye (µL)	Mass of BG for positive test (g)
Small (-)	0.02	0.08	2	0.0
Small (+)	0.02	0.08	2	0.024
Medium (-)	0.43	1.72	40	0.0
Medium (+)	0.43	1.72	40	0.2
Large (-)	5.27	21.6	500	0.0
Large (+)	5.27	21.6	500	2.12

The purpose of the fluorescent dye was to serve as a quantitative tracer for collected gelatin particles that were too small to measure with a mass balance. A fluorimeter with 365 nm excitation filter and 430 nm fluorescence emission filter was used to measure fluorescence from samples of gelatin and dye. It was found that the gelatin had intrinsic fluorescence, and so calibration curves were generated with a fixed amount of gelatin while varying the concentration of dye. The measurements were performed until the fluorescence emission saturated, and the concentration of dye in the gel was chosen to be before the plateau in the calibration curve. Given the known concentration of dye, it was intended to be able to scale fluorescence measurements to the mass of ballistic gelatin collected. Undiluted rinses from both the microscope slides and the swabs were measured with the fluorimeter. The amount of gelatin collected did not produce any measurable fluorescence signal. No additional fluorescence measurements were made.

To measure the amount of colony forming units (CFU) in the ballistic gel before the explosion, for each test, a small sample of the gelatin was taken. The mass of the sample was measured, dissolved in water. The resulting solution was then plated onto agar plates, and the colonies counted. Three samples from different parts of the gel blocks were taken to demonstrate a uniform mixing of the BG into the gel.

2.3 Sample collection

Samples were collected using three methods. The first method used color changing watch cards. These cards were fixed into place with double sided tape. Some vertical surfaces on reinforced concrete structures were available on the test pad, and some of the watch cards were fixed there. Watch cards were collected and bagged after each test. No further processing or handling occurred with the watch cards. The second method utilized plastic 1-inch x 2.5-inch microscope slides. Because the wind easily moved the slides, these were taped down to the same surfaces as the watch cards with double sided tape. At the end of each test, these were collected into 50 mL vials, and promptly placed in a cooler following the tests. To detect collection of viable BG, the slides were rinsed with a calibrated amount of ultrapure water, and the rinse was plated onto agar plates. An optical counter was used to count BG colonies. Lastly, glazed 8-inch x 4-inch tiles in conjunction with swabs were used to collect samples. These were sterilized with a bleach solution, rinsed with distilled water, and allowed to air dry. The swabs consisted of small wipes with a calibrated amount of ultrapure water. The rinse was plated onto agar plates in the same manner as the microscope slides. Some visible pieces of gelatin were collected (prior to melting) directly into 50 mL vials and stored in an icebox.

Testing occurred over two days. The small scale, medium scale, and BG negative large scale shots were performed on the first day. The large scale test that included BG was done on the second day of testing. Aerosol measurements were also performed using a standard TSI® Aerodynamic Particle Sizer® (APS) model 3321, and a TACBIO fluorescent particle counter. The standard APS relies on light scattering alone to detect particles, and thus detects all particles generated during the test regardless of composition. The TACBIO, on the other hand, utilizes both fluorescence and elastic scattering from a deep ultraviolet light emitting diode (UV LED) at 273 nm wavelength to detect aerosols. Because the ballistic gelatin is composed of protein and fluorescent dye, it is highly fluorescent so that the TACBIO only senses aerosols resulting from the ballistic gel. The APS was mounted on a table, approximately 1 meter above the ground. The TACBIO was mounted on a tripod approximately 1.5 meters above the ground. To

avoid damage to the instruments, they were positioned about 100 meters away from test. These devices ran continuously during the tests while automatically logging aerosol count data.

2.4 Explosives testing

Three tests scales were performed: small, medium, and large. A pentaerythritol tetranitrate (PETN) blasting cap with 2 g of high explosive was used for the small scale test. The gelatin was mounted on an inverted plastic cup. For the first shot, without BG, the blasting cap was placed next to the gel block. The result was very little fragmentation of the block, but a rather large piece got thrown ~10 meters. For the second test with BG, the blasting cap was inserted into the center of the block, resulting in much greater dispersion of the gelatin. For the medium scale tests, the gel block was placed on top of a cardboard can 1 m high and next to a 1-lb stick of military grade trinitrotoluene (TNT). For the large scale tests, the gel block was placed on top of a custom built wood platform (to minimize shrapnel for safety), so that it stood approximately man high. A model suicide vest was formed from eight 1-lb pound sticks of TNT sewn to a vest made from a bath towel. The sticks were arranged four in front and four in back. The detonation cord was arranged so that the TNT would detonate in an even sequence. Both standard and high speed video cameras recorded the explosive events. The tests were conducted on the test range in the Aberdeen Proving Ground-Edgewood Area. The test was conducted on a concrete pad consisting of individual 30-foot x 12.5-foot slabs, forming a grid pattern of 12 x 24 slabs. This resulted in a total pad dimension of approximately 300-feet x 360-feet. The grid pattern facilitated mapping of the sample collection.

3 RESULTS AND DISCUSSION

3.1 High speed video

The high speed video shows production of aerosol, as well as significant amounts of large scale chunks. Figures 1 through 3 show still frames of the different scale tests. For the small scale tests with the blasting cap, fragmentation of the gel block was poor, especially for the first test where the blasting cap was placed next to the gel. A large chunk approximately half the size of the original block was left over. For the medium scale test with 1 lb of high explosives, the gel block was completely destroyed. In the last frame in Figure 2, significant aerosol and larger scale fragments are apparent in the video. As would be expected, much more aerosol is released with the large scale test. In the second still from in Figure 3, on the leading edge of the fireball, aerosol riding the edge of the explosion can be seen. In the last frame of Figure 3, the ejection of the larger scale particles are apparent around the remaining fireball.

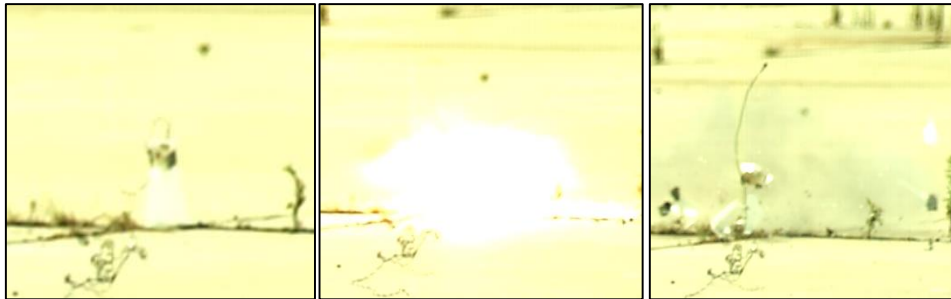


Figure 1. Still frames from first small scale test.



Figure 2. Still frames from medium scale test.



Figure 3. Still frames from large scale test.

3.2 Sample collection maps

Figures 4 through 6 show the locations of samples collected on the grid formed from individual slabs of concrete that formed the test pad area. Results from the small and medium scale runs are not shown because only the microscope slides could be collected from both gel blocks without BG (control) and blocks with BG (experiment). The microscope slides had to be anchored with double sided tape. We found that we could not easily remove the double sided tape, and as a result, dirt present on the pad also got rinsed and plated. The result was many non-BG bacterial colonies were detected, as well as significant contamination from previous tests. We found that the glazed tiles could be swabbed without any contact to the ground, thus greatly reducing the possibility of contamination from previous tests. As a result, only swab data, or directly sampled large pieces are reported.

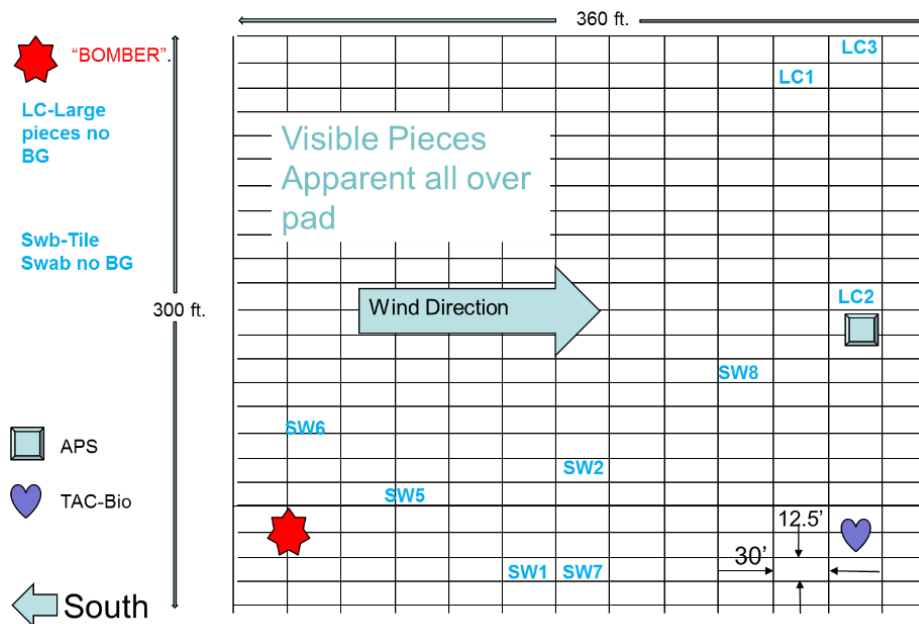


Figure 4. Sample collection map for large scale test without BG, showing the approximate locations of large sample collections ("LC" prefix), and swabbed tile locations (prefix "SW").

Figure 4 shows the results from the test control without BG. The locations of the APS and TACBIO sensors are shown on the map as well. The test explosion was positioned on the crossing of grid lines as shown in the map. The need to avoid damaging other structures on the pad dictated the location of the large scale test at the southeast corner. The direct sampled pieces of gel and glazed tiles were positioned on the grid as shown on the map, with visible pieces of gel covering the entire concrete pad. As should be expected, large pieces sampled showed no concentration of BG, and most of the tiles showed zero BG colonies. Only three tiles showed BG colonies. One of the background tiles had been dropped on the ground, resulting in contamination, and was not considered for determining the background colony counts, with an average of 21 CFUs and standard deviation of 40 CFUs. The near absence of BG colonies indicate that positive detections of BG come from the ballistic gel alone. Had the BG come from the ground, from

previous tests, or from contamination of the biological laboratory, then addition of BG to the gel block should have led to a minimal difference in bacterial colonies.

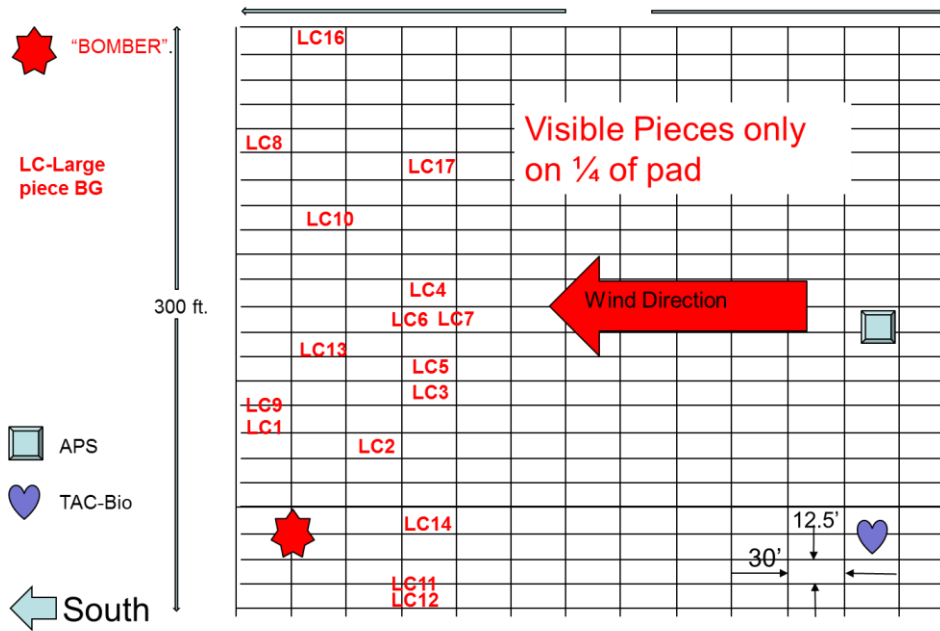


Figure 5. Sample collection map for large scale test with BG, showing the approximate locations of large sample collections ("LC" prefix) only. Due to the wind direction during the test, only the southern quarter of the pad had visible large pieces of gelatin.

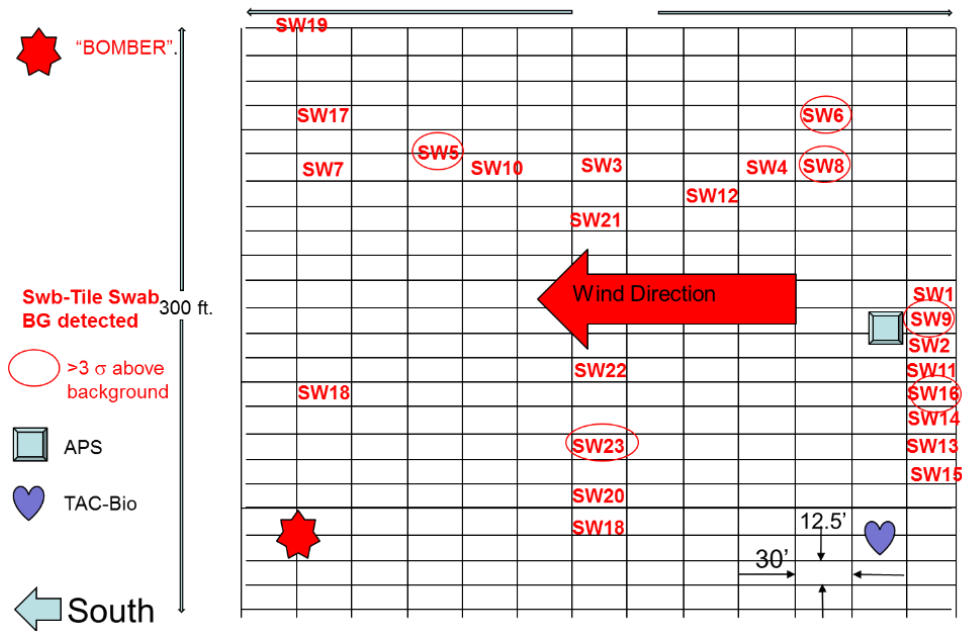


Figure 6. Sample collection map for large scale test with BG, showing the approximate locations of the swabbed tiles only. A number of tiles, even ones quite far from the explosion site, exhibited bacterial colonies of BG far above that observed for the background (tests with no BG in the gel). These locations are circled. Tiles with the highest concentration of BG colonies were placed about 350 feet away from the blast site.

Figures 5 and 6 show the mapping of samples collected for the large scale test with BG introduced into the ballistic gel block. These are divided into two maps for the sake of the clarity. Figure 5 shows the direct sampling of visible

pieces of gel. Although the outside of the pieces appeared to be singed, the visible bits of gel were solid and had not melted, despite the low melting temperature of ~105 °F. Not surprisingly, these pieces protected the BG spores within quite effectively, so that on a mass-to-mass basis, there was a negligible reduction in viable organisms. This is consistent with the Israeli and London bombing observations that bone fragments can transmit disease. Also, the wind direction had changed on the day we ran the BG positive large scale test, so that visible fragments were only visible on about a quarter of the pad. No visible pieces or flecks could be seen on the sample collection tiles. These appeared to be uncontaminated.

Although we nominally expect large visible pieces of gel to shield organisms from the heat and pressure of the high explosive blast, our results show particles too small to see with the naked eye had placed viable bacteria on our sample collection points. Figure 6 shows the locations for the collection tiles that were swabbed. We attempted to place a line of tiles somewhat close to the test site to maximize the chance of collecting viable material, while at the same time leaving some of the tiles at the edge of the testing pad to capture how far material could travel. Because of the change in wind direction and because of the absence of visible material in the vicinity of the tiles, we expected no viable organisms to be collected at all. Surprisingly, more CFUs than the background average plus three times the standard deviation of BG colonies (3 sigma) were cultured from six tiles placed up to 350 feet away, upwind. As shown in Table 2, seven additional tiles also had BG colonies, but the numbers did not exceed the 3 sigma threshold. These results show that several sampling points were contaminated with organisms although there was no visible contamination.

Table 2. Raw colony counts from large scale BG positive test.

Sample	CFU's/mL
LSBG+Sw1	0
LSBG+Sw2	0
LSBG+Sw3	0
LSBG+Sw4	66.66666667
LSBG+Sw5	200
LSBG+Sw6	1666.666667
LSBG+Sw7	0
LSBG+Sw8	533.3333333
LSBG+Sw9	6533.333333
LSBG+Sw10	0
LSBG+Sw11	66.66666667
LSBG+Sw12	0
LSBG+Sw13	0
LSBG+Sw14	133.3333333
LSBG+Sw15	133.3333333
LSBG+Sw16	266.6666667
LSBG+Sw17	66.66666667
LSBG+Sw18	66.66666667
LSBG+Sw19	0
LSBG+Sw20	0
LSBG+Sw21	66.66666667
LSBG+Sw22	0
LSBG+Sw23	2666.666667

3.3 Aerosol sampling

In order to make some measurement of the aerosol particles produced during the testing, both an APS and a TACBIO detector were employed. Because the APS detects any particle that elastically scatters light, upwards of hundreds of thousands of particles per liter are detected. Only fluorescent gelatin particles appear in the TACBIO readout, and so

fewer particles are detected. Neither the APS nor the TACBIO had been configured to detect BG spores embedded in the gelatin particles.

Figure 7 shows the output of both the APS and the TACBIO for the first day of testing. Because both sensors were not collocated, they do not necessarily observe the same events. None of the small scale tests produced a response in the TACBIO; although, the sensor was not downwind. Only one of the small scale tests appear in the APS data. Both medium scale shots appeared in the data, although weakly in the TACBIO data. These events appear as sharp spikes in the particle counts. This is not surprising given the breezy conditions; particles kicked up by the explosion were removed from the test site within a minute or so. For the APS, which detects all particles generated, upwards of 150,000 particles per L were detected for the large scale test, while approximately 1,000 particles per L were detected with TACBIO for the same test. These sensors were downwind of the test, and so many particles were detected.

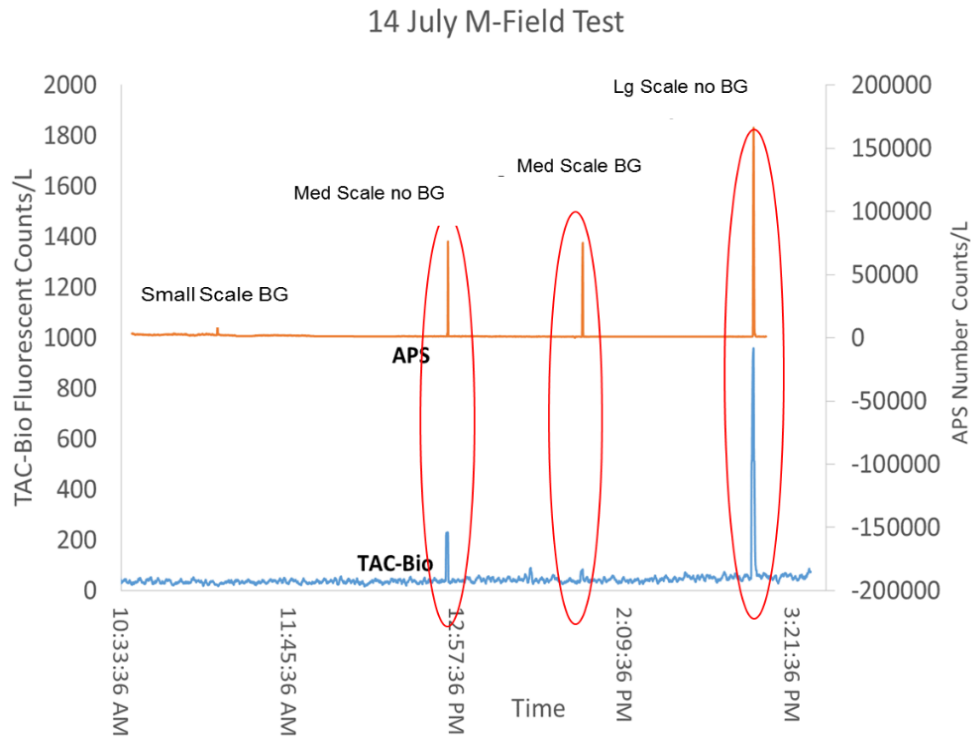


Figure 7. APS and TACBIO data for the first day of testing. The large scale BG negative test appears as the last event in the chart. TACBIO data scale appears on the left, while the APS scale appears on the right axis. TACBIO only senses the gelatin particles.

Aerosol measurements performed on the day of the large scale BG positive test show that it is most likely the viable bacteria collected on the tiles were most likely carried by aerosol particles. Figure 8 shows the results of the second day of testing when the wind direction changed and both sensors were then upwind of the test. As might be expected from the dispersion of visible gelatin chunks away from the sensors, the APS shows no increase in particulates. However, because the TACBIO is selective to the gelatin particulates, it is able to see a 200 particle-per-liter increase due to the test. We attribute the attenuation in particle counts on the TACBIO and APS to the wind direction. Although the collection tiles and the TACBIO sensor were upwind of the test by about 350 feet, it is clear some aerosol particles “surf” the shockwave from the blast and were carried a distance upwind. Had the sampling surfaces been downwind, we expect the amount of bacterial contamination would have been more extensive.

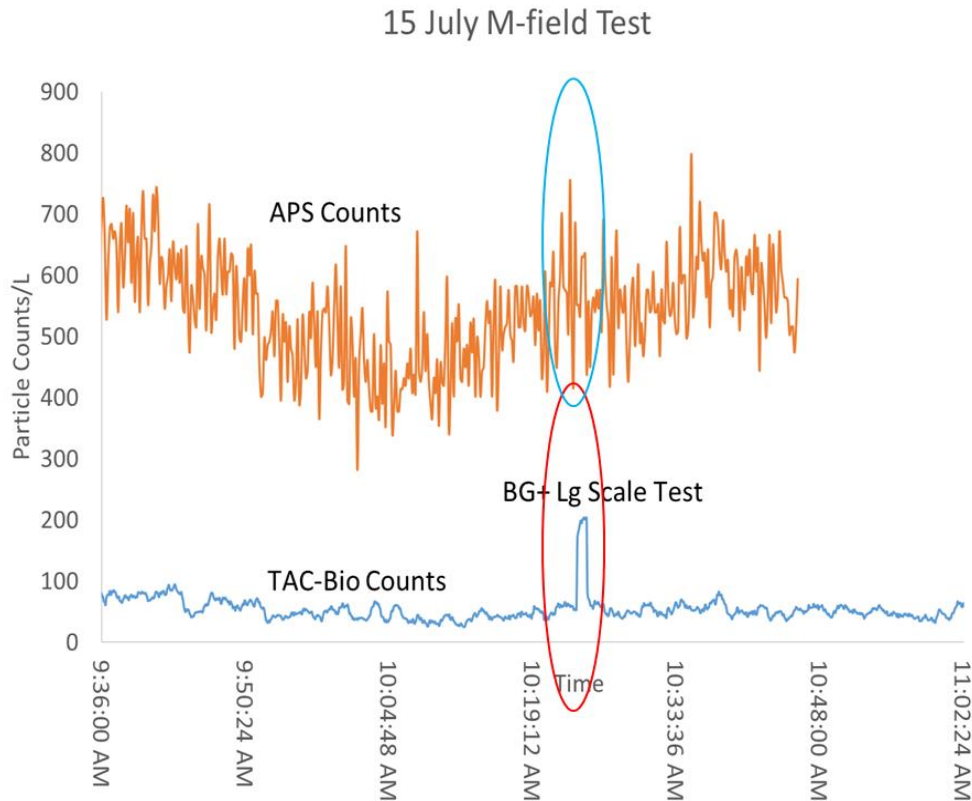


Figure 8. APS and TACBIO data for the second day of testing with the large scale, BG positive test. Because of the wind direction, no additional particles relating to the test were detected, and so both outputs appear on the same scale.

We believe these results answer at least two of the questions posed at the beginning. The detection of BG colonies on sampling tiles far upwind of the test site show that organisms can be shielded and protected by aerosol particles. Given that surfaces could be contaminated without visible chunks, it can be seen there is a significant potential threat. Aerosol measurements show that particles that can only come from the ballistic gelatin are generated, and we must attribute the delivery of viable organisms to the sample surfaces to these particles.

Although our results show that some aerosols are generated from the test suicide bomber, and that these particles can harbor viable organisms, we believe the threat could be much worse than indicated. First, the ballistic gelatin only approximates the mechanical properties of muscle tissue. The activity of blood and other precious bodily fluids must be considered, because they can aerosolize much more easily. Our expectation is that more aerosol would result from a more realistic test.

4 CONCLUSIONS

Within the limitations of using ballistic gelatin as a model of a suicide bomber, we demonstrated that aerosol-sized pieces of gel can protect organisms from the effect of a high explosives blast. We show that these small particles containing organisms can be hurled hundreds of feet by the blast. We expect aerosolization from a real human who contains blood and other bodily fluids that will aerosolize even more material. We intend to seek additional funding to continue finer grained tests that incorporate other organisms, such as bacteriophage MS2, or vegetative *Escherichia coli*, to assess how survivability changes based on the threat organism.

ACKNOWLEDGMENTS

Support for this research was provided by the U.S. Army Edgewood Chemical Biological Center Research and Technology Directorate's Seedling Program. We acknowledge the significant support from the Pyrotechnics Branch in the Engineering Directorate, as well as the assistance of Paul DeLuca in the collection of aerosol data.

REFERENCES

- [1] Eshkol Z. and Katz, K., "Injuries from biologic material of suicide bombers." *Injury*, **2005**, 36, p271-274.
- [2] Braverman, I. *et al.*, "A novel mode of infection with hepatitis B: Penetrating bone fragments due to the explosion of a suicide bomber." *Israeli Medical Association Journal*, **2002**, 4, p528-529.
- [3] Patel, H.D.L. *et al.*, "Human body projectiles implantation in victims of suicide bombings and implications for health and emergency care providers: The 7/7 experience." *Annals of the Royal College of Surgeons of England*, **2012**, 94, p313-317.
- [4] Wong, J.M.-L. *et al.*, "Biological foreign body implantation in victims of the London July 7th suicide bombings." *Journal of Trauma-Injury Infection and Critical Care*, **2006**, 60, 402-404.
- [5] Clint, B., "Force protection and infectious risk mitigation from suicide bombers." *Military Medicine*, **2009**, 174, 709-714.
- [6] Borio, L. *et al.*, "Hemorrhagic fever viruses as biological weapons." *Journal of the American Medical Association*, **2002**, 287, p2392-2405.
- [7] Teckman, A.M., "The bioterrorist threat of Ebola in East Africa and implications for global health and security." *Global Policy*, **2013**.
- [8] Ustun, C. and Ozgurler, O., "Ebola: A significant threat as an infectious disease, and as a potential bioterrorism agent." *Turkish Journal of Medical Science*, **2005**, 35, p1-4.

Tunable color filters using aluminum based nano-sandwiches

Zion Aranda^a, Mathew Zablocki^a, Mark Mirotznik^a, Zach Zander^b, Brendan G. DeLacy^{b*}

^aDepartment of Electrical and Computer Engineering, University of Delaware,
Newark, DE 19711

^bU.S. Army Edgewood Chemical Biological Center, Research and Technology Directorate,
5183 Blackhawk Rd, Aberdeen Proving Ground, MD 21010

ABSTRACT

We detail the computational design, fabrication, and optical characterization of an aluminum-based nano-sandwich optical filter. These multilayer thin-films consist of an aluminum base plane, a dielectric cavity layer with variable thickness, and a top thin film of aluminum. This architecture provided a means of filtering out certain bands of incident radiation via the constructive and destructive interference that occurs with this Fabry-Perot structure. Rigorous coupled-wave and finite difference time domain calculations were used to computationally design the structures. A simple plasma sputtering technique was used to deposit thin films of each layer onto a glass slide. Finally, visible spectroscopy and photography were used to characterize the optical properties of the fabricated structures.

Keywords: Fabry-Perot, optical filters, plasmonics

1 INTRODUCTION

The optimization and design of plasmonic nanostructures continue to highlight progress being made in the nanophotonic field of research. This progress is largely due to the ability of these structures to control light-matter interactions at the nanoscale. The optical properties of these engineered materials are highly dependent on the size, shape, and periodicity of metallic and dielectric components. Hence, a plethora of designs have been explored as a means of generating and tuning various optical properties including transmission, reflection, absorption, and emission.¹⁻³ One particularly intriguing and simple design is the use of a Fabry-Perot cavity to further tune and filter various bands of incident radiation, via the constructive and destructive interference of the incident radiation as it propagates through a three-layered system. These multilayer thin-films typically consist of a metallic base plane, a dielectric cavity layer with variable thickness, and a top layer consisting of the plasmonic array. The optical properties of a metal-insulator-metal “nano-sandwich” structure (e.g., Ag-SiO₂-Ag) were recently reported in the literature.⁴ This thin film architecture provided a means of filtering out a vast portion of the visible spectrum, while allowing the transmission of a narrow band of visible light (i.e., a specific color). The thicknesses of the metal and insulator layers played a vital role in choosing the color of transmission. Typical multilayered plasmonic structures, including the one described above, incorporate precious metals such as gold and silver. Aluminum is an abundant and cheaper alternative to the commonly used precious metals, while also providing the prerequisite plasmonic properties that generate the desired optical properties within the visible region. In this project, a metal-insulator-metal sandwich structure, composed of Al-Al₂O₃-Al, was computationally designed, fabricated, and characterized. The goal of this effort was to demonstrate the ability of this architecture to filter a white light source and subsequently generate three different colors (red, green, and blue). A schematic of the concept is provided in Figure 1.

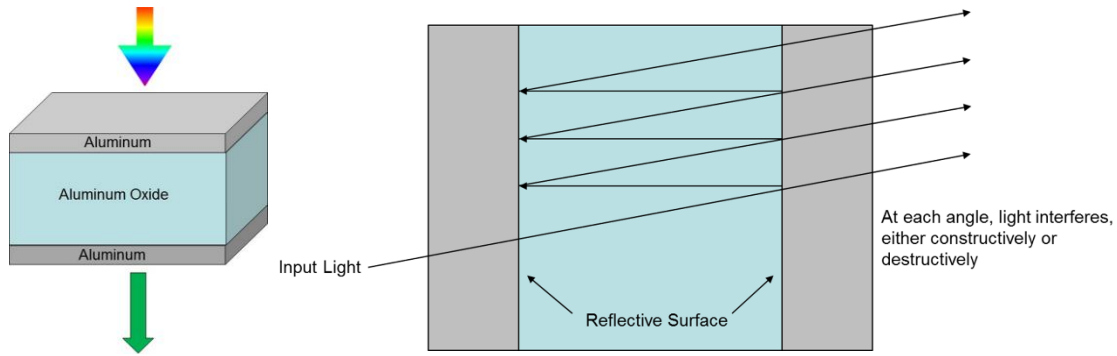


Figure 1. On the left, a schematic of the concept in which multicolored light is filtered to produce a green color. On the right, a schematic of the Fabry-Perot concept in which the three-layered architecture permits only certain wavelengths to propagate due to constructive and destructive interference.

2 METHODOLOGY

2.1 Brief description of the computational models

Electromagnetic computations using the rigorous coupled wave (RCW) method and the finite difference time domain (FDTD) technique were used to design the Al-Al₂O₃-Al thin films. These computations predicted the required thicknesses for both the aluminum and alumina layers. The aluminum layers were required to be sufficiently thin to allow for the transmission of light thru the “top” and “bottom” layers of the nano-sandwich, while the thickness of the Fabry-Perot silica cavity ultimately determine which frequencies of light are either attenuated or permitted to pass. A description of each technique is provided below.

2.2 Rigorous coupled wave method

Our specific implementation is based on the enhanced transmittance matrix approach introduced by Moharam.⁵ Using this method, we define regions within the solution domain illustrated in Figure 2. These are (1) an incident region that is assumed to be an infinite half-space filled with a lossless dielectric of index n_{inc} , (2) an exit region that is assumed to be another infinite half-space filled with a lossless dielectric of index n_{exit} , and (3) a layered grating region that contains multiple layers with periodic metallic structures. The total thickness of the layered region is

$$Z_{tot} = \sum_{n=1}^N \Delta z_n \tag{1}$$

where Δz_n denotes the thickness of each layer and N denotes the total number of layers. The first step in the RCW method is to represent the electromagnetic fields in each of the three regions.

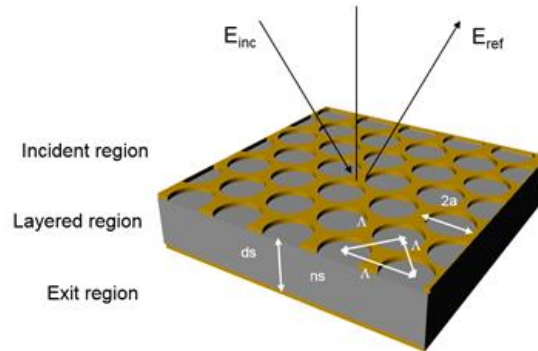


Figure 2. Illustration of geometry used for rigorous coupled wave algorithm.

2.2.1 Incident region

Within the incident region, denoted as region I, the electromagnetic fields consist of an incident plane wave plus all of the diffracted orders reflected from the structure. This is written for the electric fields as:

$$\vec{E}_I = \hat{u} \exp(-j\vec{k}_I \cdot \vec{r}) + \sum_{m=-\infty}^{\infty} \sum_{n=-\infty}^{\infty} \vec{R}_{mn} \exp(-j(\vec{k}_{I,mn} \cdot \vec{r})) \quad (2)$$

where \vec{k}_I and \hat{u} denote the wave vector and unit polarization vector of the incident plane wave, respectively. The second term in (2) accounts for all the reflected diffractive orders. Since each of the components in (2) represents a plane wave, the magnetic field equations can be easily derived from these. In Equation (2), \vec{R}_{mn} and $\vec{k}_{I,mn}$ denote the vector reflection coefficient and wave vector of the mn-th reflected order in region I, respectively. The vector components of $\vec{k}_{I,mn}$ result from the phase matching and Floquet conditions, and are given by:

$$\begin{aligned} \vec{k}_{I,mn} = & \hat{u}_x \left[k_o n_{inc} \sin(\theta_{inc}) \cos(\phi_{inc}) - \frac{2\pi m}{\Lambda_x} \right] \\ & + \hat{u}_y \left[k_o n_{inc} \sin(\theta_{inc}) \sin(\phi_{inc}) - \frac{2\pi n}{\Lambda_y} \right] - \hat{u}_z k_{z,lmn} \end{aligned} \quad (3)$$

where η_{inc} is the polar angle and θ_{inc} is the azimuth angle of the incident plane wave. The z component of the wave vector, given in (3), is written more explicitly as:

$$k_{z,lmn} = \begin{cases} \sqrt{(n_i n_{\mathcal{L}o})^2 - k_{x,m}^2 - k_{y,n}^2}, & k_{x,m}^2 + k_{y,n}^2 < (n_i n_{\mathcal{L}o})^2 \\ -j\sqrt{k_{x,m}^2 + k_{y,n}^2 - (n_i n_{\mathcal{L}o})^2}, & k_{x,m}^2 + k_{y,n}^2 > (n_i n_{\mathcal{L}o})^2 \end{cases} \quad (4)$$

where $k_{x,m}$ and $k_{y,n}$ denote the x and y component of the wave vector given in (3). It is easily deduced from (3) and (4) that, if the grating periods Λ_x and Λ_y are small compared to the incident wavelength (λ_o/n_{inc}), only the ($m = n = 0$) diffractive order will propagate in reflection and transmission (i.e., all other diffractive orders will be evanescent). This condition is written mathematically as:

$$\Lambda_x < \frac{\lambda_o}{n_{inc}(1 - \sin(\theta_{inc}) \cos(\phi_{inc}))}, \quad \Lambda_y < \frac{\lambda_o}{n_{inc}(1 - \sin(\theta_{inc}) \sin(\phi_{inc}))} \quad (5)$$

2.2.2 Exit region

Within the exit region, denoted as region III, the electromagnetic fields consist of all the diffracted orders transmitted through the structure. This is written for the electric fields as:

$$\vec{E}_{III} = \sum_{m=-\infty}^{\infty} \sum_{n=-\infty}^{\infty} \vec{T}_{mn} \exp(-j(\vec{k}_{III,mn} \cdot \vec{r})) \quad (6)$$

Here \vec{T}_{mn} and $\vec{k}_{III,mn}$ denote the vector transmission coefficient and wave vector of the mn-th transmitted order in region III, respectively. The wave vector in region III takes the same mathematical form as (3) and (4) with the one exception of replacing n_{inc} with n_{exit} . Using a similar analysis to that of region I, it can easily be shown that, to avoid any propagating diffractive orders in the transmitted region other than the $m = n = 0$ term, the grating periods must satisfy the relations:

$$\Lambda_x < \frac{\lambda_o}{n_{exit}(1 - \sin(\theta_{inc}) \cos(\phi_{inc}))}, \quad \Lambda_y < \frac{\lambda_o}{n_{exit}(1 - \sin(\theta_{inc}) \sin(\phi_{inc}))} \quad (7)$$

2.2.3 Multi-layered grating region

Between the incident and exit regions is a periodic layered medium. In the RCW method, the electric and magnetic fields within each layer of the grating region, denoted by the superscript p , are written as a Fourier expansion of spatial harmonics given by:

$$\begin{aligned}\vec{E}_{II}^p &= \sum_{m=-\infty}^{\infty} \sum_{n=-\infty}^{\infty} \vec{S}_{mn}^p(z) \exp(-j(k_{xm}x + k_{yn}y)) \\ \vec{H}_{II}^p &= -j \sqrt{\frac{\epsilon_o}{\mu_o}} \sum_{m=-\infty}^{\infty} \sum_{n=-\infty}^{\infty} \vec{U}_{mn}^p(z) \exp(-j(k_{xm}x + k_{yn}y))\end{aligned}\quad (8)$$

where $\vec{U}_{mn}^p(z)$ and $\vec{S}_{mn}^p(z)$ represent the amplitudes of the spatial harmonics in the p th layer for the magnetic and electric fields respectively. Substituting (8) into Maxwell's two curl equations and eliminating the z component results in the following coupled system of first order differential equations for the spatial harmonic amplitudes of (8):

$$\begin{aligned}\frac{\partial S_{ymn}^p(z)}{\partial z} &= U_{ymn}^p(z) + \frac{k_{ym}}{k_o^2} \sum_{q=-\infty}^{\infty} \sum_{r=-\infty}^{\infty} \xi_{m-r,n-q}^p (-k_{yq} U_{xq}^p + k_{xr} U_{yq}^p) \\ \frac{\partial S_{xmn}^p(z)}{\partial z} &= -U_{xmn}^p(z) + \frac{k_{xm}}{k_o^2} \sum_{q=-\infty}^{\infty} \sum_{r=-\infty}^{\infty} \xi_{m-r,n-q}^p (-k_{yq} U_{xq}^p + k_{xr} U_{yq}^p) \\ \frac{\partial U_{ymn}^p(z)}{\partial z} &= \sum_{q=-\infty}^{\infty} \sum_{r=-\infty}^{\infty} \epsilon_{m-r,n-q}^p S_{xq}^p + \frac{k_{ym}}{k_o^2} (k_{xm} S_{ymn}^p - k_{yn} S_{xmn}^p) \\ \frac{\partial U_{xmn}^p(z)}{\partial z} &= -\sum_{q=-\infty}^{\infty} \sum_{r=-\infty}^{\infty} \epsilon_{m-r,n-q}^p S_{yq}^p + \frac{k_{xm}}{k_o^2} (k_{xm} S_{ymn}^p - k_{yn} S_{xmn}^p)\end{aligned}\quad (9)$$

In (9), $\epsilon_{m,n}^p$ and $\xi_{m,n}^p$ denote the Fourier components for the permittivity distribution, $\epsilon^p(x,y)$, and the inverse permittivity distribution, $1/\epsilon^p(x,y)$ of the p th layer given by:

$$\begin{aligned}\epsilon_{m,n}^p &= \frac{1}{\Lambda_x \Lambda_y} \int_0^{\Lambda_x} \int_0^{\Lambda_y} \epsilon^p(x,y) \exp(-j\left(\frac{2\pi m x}{\Lambda_x} + \frac{2\pi n y}{\Lambda_y}\right)) dx dy \\ \xi_{m,n}^p &= \frac{1}{\Lambda_x \Lambda_y} \int_0^{\Lambda_x} \int_0^{\Lambda_y} \frac{1}{\epsilon^p(x,y)} \exp(-j\left(\frac{2\pi m x}{\Lambda_x} + \frac{2\pi n y}{\Lambda_y}\right)) dx dy\end{aligned}\quad (10)$$

For the geometries of interest here (10) can be solved analytically. After substituting (10) into (9) and enforcing boundary conditions across all planar interfaces, an eigenvalue problem results that can be solved numerically for the reflected and transmitted diffracted orders \vec{R}_{mn} and \vec{T}_{mn} . Our custom RCW code, developed using the MATLAB® programming environment, was used to calculate the complex transmission and reflection coefficients from the plasmonic surfaces.

2.3 Finite difference time domain method

The second modeling method we used to predict the optical response from plasmonic surfaces was the FDTD method. For this approach, we used commercial FDTD code developed by Lumerical Solutions, Inc. (Vancouver, BC, Canada) Using Lumerical FDTD Solutions, we created specific models that predict the response from plasmonic layered surfaces with complicated geometrical features. The advantage of the FDTD method over the RCW technique is its ability to analyze the optical response from non-periodic surfaces (or surfaces with a finite number of periods). However, the major disadvantage of the method is the high computational expense compared to the RCW method. For most of the test devices analyzed thus far, the RCW is at least an order of magnitude faster.

2.4 Fabrication of aluminum based nano-sandwiches

Aluminum or aluminum oxide nano-sandwich optical filters were prepared on glass microscope slides which were initially cleaned in oxygen plasma using a SAMCO PC-300 system (Kyoto, Japan). The aluminum layers were sputter deposited using an ÅMOD sputter deposition system 01604-2 (Angstrom Engineering; Kitchener, Ontario, Canada) using DC powder. The aluminum targets (99.99% aluminum, 3-inch diameter, 0.125-inch thick) were purchased from Kurt J. Lesker Company (Jefferson Hills, PA). The aluminum layers were deposited at a rate of 0.5 \AA/s in the presence of 6 sccm Argon at a pressure of 2 mTorr. The aluminum oxide cavity layer was deposited using the same system parameters as for the aluminum layers, with the exception that the aluminum was deposited at a rate of 0.15 \AA/s , in the presence of 10 sccm Argon and 2.5 sccm oxygen, and a pressure of 2 mTorr.

3 DATA AND RESULTS

A comparison of experimental and computational results (RCW) obtained in this study is provided in Figure 3. As denoted in Figure 3, the top and bottom aluminum layers were set at 10 nm thick, while the Al_2O_3 cavity thickness were varied at 234 nm, 282 nm, and 330 nm.

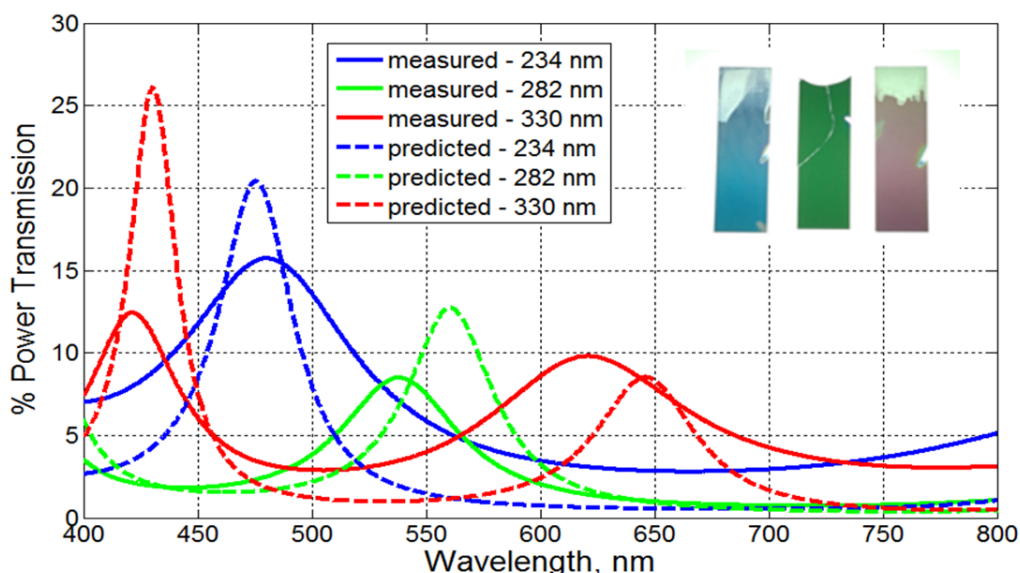


Figure 3. Computational (dashed curves) and experimental (solid curves) for the power transmission through the Al- Al_2O_3 -Al nano-sandwiches.

Inspection of Figure 3 reveals that as the cavity thickness is increased, the color of the transmitted light goes from blue, to green, to a purplish-red (see inset in Figure 3). Good correlation between the predicted (dashed curves) and experimental (solid curves) transmission data is observed. Discrepancies between the magnitude and width of the transparency bands are hypothesized to be due to: 1) slight differences in the actual thickness of the layers relative to that which was used in the computations, and 2) non-uniformity in the individual layer thicknesses, which would ultimately produce a non-parallel three-layered stack (i.e., the top aluminum layer would not be parallel to the bottom aluminum layer). The end goal of this study was to demonstrate the utility of this architecture in generating an optical filter which could generate blue, green, and red colors. Indeed, the blue and green colors were produced, as well as the red color to a lesser extent. The purplish hue that is present in the “red” slide is due to the simultaneous emission of blue light (near 420 nm) with red light. Mitigation of this harmonic production of both blue and red colors may be the subject of future work; however, we hypothesize that alternative layer thicknesses and/or an alternative cavity material will negate this effect.

4 CONCLUSIONS

Aluminum-based Fabry-Perot architectures (i.e., aluminum nano-sandwiches), are plausible structures for optical filtering. Aluminum is an abundant and cheaper alternative to the commonly used precious metals, while also providing the prerequisite plasmonic properties that generate the desired optical properties within the visible region. The ability to tune the color of light that is generated from a white light source was demonstrated both computationally and experimentally. Future efforts will focus on 1) the ability to generate more narrow and efficient optical filters, and 2) the development of architectures that are amenable to generating colors dynamically (i.e., the ability to change colors within fractions of a second).

ACKNOWLEDGMENTS

Support for this research was provided by the U.S. Army Edgewood Chemical Biological Center Research and Technology Directorate's Seedling Program.

REFERENCES

- [1] Landy, N.I. *et al.*, "Perfect metamaterial absorber." *Physical Review Letters*, **2008**, 100(20), p1-6.
- [2] Aydin, K. *et al.*, "Broadband, polarization-independent resonant light absorption using ultrathin, plasmonic super absorbers." *Nature Communications*, **2011**, 2(517), published online.
- [3] Pala, R.A. *et al.*, "Design of plasmonic thin-film solar cells with broadband absorption enhancements." *Advanced Materials*, **2009**, 21(34), p3504-3509.
- [4] Li, Z.; Butun, S.; and Aydin, K., "Large-area, lithography-free super absorbers and color filters at visible frequencies using ultrathin metallic films." *ACS Photonics*, **2015**, 2(2), p183-188.
- [5] Moharam, M.G. *et al.*, "Stable implementation of the rigorous coupled-wave analysis for surface-relief gratings: Enhanced transmittance matrix approach." *Journal of the Optical Society of America A*, **1995**, 12(5), p1077-1086.

Paper-based sequence detection with minimal sample preparation

James M. Myslinski^a, Vanessa Funk^b, Steve Blum^a, Matthew W. Lux^{b*}

^aExcet, Inc., 801 Braddock Rd, Suite 303, Springfield, VA 22151

^bU.S. Edgewood Chemical Biological Center, Research and Technology Directorate,
5183 Blackhawk Rd, Aberdeen Proving Ground, MD 21010

ABSTRACT

Recently, a novel synthetic biology approach was described by freeze-drying several engineered gene-networks with *in vitro* expression machinery onto paper and showing high performance upon rehydration. These paper-based gene-networks exhibit transformative potential for synthetic biology and its applications within the Department of Defense by shifting the power of engineered gene circuits from the fragile and challenging world of the cell onto stable, reproducible paper substrates. The authors demonstrated examples of RNA and small molecule detection, showed stability of a year, and built and tested a novel Ebola assay with strain-level identification within 12 hours. Paper-based gene-networks offer a potential future for biological detection that is cheap, disposable, stable, multiplexable over targets and modalities (RNA/small molecule/protein), rapid to design and manufacture, and embeddable into paper, clothes, or other porous materials. Yet, two major open questions remain to explore the potential of this new technology: (1) how much sensitivity can be achieved by gene-network amplification circuits, and (2) can cellular lysis be embedded into the system, allowing built-in sample preparation, while maintaining robust performance. Herein, we endeavor to explore the latter by posing the following hypothesis: paper-based gene-networks exposed to bacterial lysate will function normally when mechanical lysis is employed, but not chemical lysis.

Keywords: Synthetic biology, gene networks, paper-based assays

1 INTRODUCTION

The transformative potential of the field of synthetic biology has been highly touted for the past 15 years,¹⁻² yet progress has been restricted by several technical challenges.³ In particular, the challenges of working within the complex environment of even the simplest bacteria cells have become increasingly apparent. For example, the interaction between the engineered circuit, cell, and growth conditions can be complex. While simple proof-of-concept circuits may function well in a laboratory environment, even moving those a well-controlled industrial fermenter environment can immediately disrupt function. Moving these circuits into real-world environments, especially in the face of competition from endemic microbial communities, is a daunting challenge that remains to be faced.

An alternative to circumvent the issues arising from working in living cells is to move to cell-free systems.⁴ These systems contain all the components necessary for gene expression and can either be obtained as cellular lysate or as kits of purified components. Cellular lysates have the advantage of being extremely cheap, but suffer from inconsistency between batches and confounding issues from the abundance of other unnecessary components in the cellular milieu, especially RNAses. Purified components perform far better in terms of expression and reproducibility, but are expensive. In both cases, however, cold chain storage at -20 °C is critical for functionality, which again severely limits real world applications.

Recently, Pardee et al. described a new approach to address these issues by freeze drying cell-free systems onto paper.⁵ In this groundbreaking work, they demonstrated that a variety of gene network circuits can be implemented in this format, and that functionality can be maintained at room temperature for at least a year. This discovery opens the door for a range of real-world applications of engineered gene circuits by providing a practical format in which these circuits can be used. Coupling the application of gene networks onto a paper format with work on wax-printed paper-based microfluidics opens even more possibilities. The use of these paper-based gene networks as low-cost, multiplexed sensors is particularly attractive, and the authors demonstrated the detection of both RNA sequences and small molecules, including building and testing a strain-specific Ebola detector in under 12 hours.

While the potential of paper-based gene networks to address Department of Defense needs in far-forward fieldable detection, two significant open questions remain. First, initial demonstrations of detection had low sensitivity. Several obvious approaches to building signal amplification into the circuits are possible, but have not as yet been explored. Second, a major boon to the paper-based assays for real-world use would be the ability to bypass sample preparation and allow direct detection from environmental sample. Here, the basic science around potential interference between environmental samples and embedded cell-free expression systems remain open. In this preliminary work, we probe the performance of a simple paper-based gene network in the presence of unrelated cellular lysate.

2 METHODOLOGY

2.1 Wax printing of paper tickets

All paper tickets were prepared by wax-based printing on Whatman™ chromatography paper (Grade 1) using a Xerox® Phaser™ 8560 printer. Numerous patterns were tested (see data). After printing, tickets were baked in an oven at several temperatures (110 °C, 120 °C, 130 °C, and 140 °C) and durations (1 minute, 2 minutes, 5 minutes, and 10 minutes). After baking, individual tickets were cut out by hand, then left overnight at room temperature in aqueous bovine serum albumin (5% w/v), as in Pardee et al.⁵ After drying the tickets were ready for application of the cell-free expression system and circuit DNA.

2.2 Cell-free expression

All experiments use the PURExpress® system (New England BioLabs®, Inc.; Ipswich, MA). Concentrations of components followed instructions of the kit, with template DNA varying by experiment (see Data). For plate reader experiments, total volumes were 10 µL, while for paper-based experiments, total volumes were 2 µL. All tests were performed using a plasmid containing the super-folder green fluorescent protein (sfGFP) expressed from the T7 promoter.⁶

2.3 Interfering lysate preparation

Lysates were prepared by growing lab-strain *Escherichia coli* (DH5α) in Luria-Bertani (LB) broth (10 mL) at 37 °C in a shaking incubator (220 rpm) to an optical density (OD) of 1.4. The cultures were pelleted (4,000 rpm, 10 minutes), and re-suspended in distilled water (10 mL). The re-suspended cells were cooled to 0 °C and lysed using an ultrasonic homogenizer (10 x 10 seconds) to give the cell-lysates which were used as-is, and stored at 4 °C. To prepare a concentrated solution of the lysate, the dilute lysate (10 mL) was pelleted (4000 rpm, 10 minutes) and re-suspended in Tris-buffered saline (1 mL).

2.4 Fluorescence measurements

Liquid-phase experiments were performed on a BioTek® Synergy™ 4 microplate reader (Winooski, VT) with 485 nm excitation and 510 nm emission filters, fluorescence was read every 5 minutes at 37 °C. Paper-based fluorescent imaging was performed on a custom imaging rig consisting of a digital single-lens reflex (DSLR) camera with the same filters mounted in an incubator with a blue light transilluminator. Time-lapse images were taken every 5 minutes. The incubator was set to 37 °C for the experiments shown.

3 DATA

3.1 Paper ticket optimization

We tested numerous wax-printed patterns to create hydrophobic spots of various sizes, informed by previous work.⁷ All tested maps were based on the 24 mm x 28 mm format used in the volatile organic compound (VOC) project to enable repurposing of the VOckit reader system. Different candidate formats were printed, baked at different temperatures for different amounts of time, then dye was pipetted onto spots to look for bleed-through between neighboring spots. Several volumes of dye was tested for each candidate ticket. Ultimately spots with 5 mm spacing, 2 pt. lines, and 3.8 mm dots were selected (Figure 1, top row, second from right) for subsequent work due to adequate holding of dye in spots and ability to hold at least 2 µL of dye without bleed through.

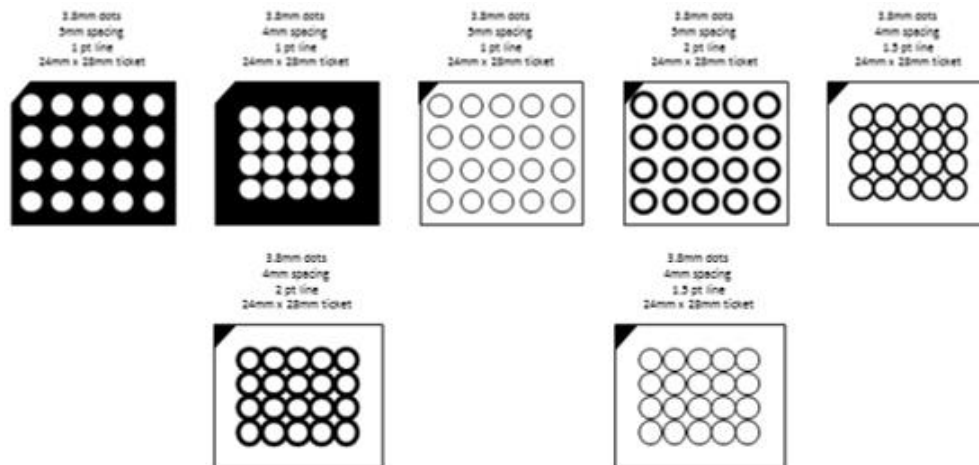


Figure 1. Sample test ticket maps. A mask was created with the specified specifications, printed, and tested for ability to hold liquid in spots.

3.2 Performance of cell-free expression system in the presence of lysate

We tested the performance of the PURExpress® system first in using a plate reader. Two variables were tested: the concentration of template DNA and the presence or absence of cellular lysate (see Methodology). Figure 1 shows time course trajectories of triplicate wells containing 0 ng, 12.4 ng, or 124 ng of template DNA with and without cellular lysate. See results for interpretation of data.

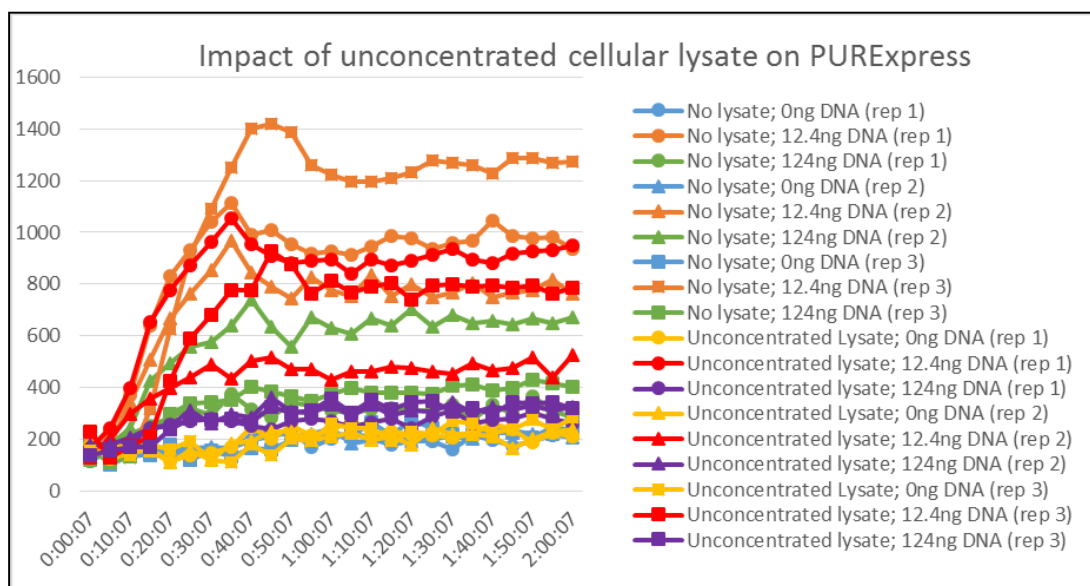


Figure 2. Impact of unconcentrated cellular lysate on PURExpress®. Timecourse fluorescent trajectories on plate reader containing no lysate and 0 ng (blue lines), 12.4 ng (orange lines), or 124 ng (green lines) of template DNA, and containing unconcentrated lysate and 0 ng (yellow lines), 12.4 ng (red lines), or 124 ng (purple lines) template DNA. Shapes (circles, triangles, squares) of the same color indicate triplicate trajectories.

Since the lysate used did not show a dramatic decrease in performance of the PURExpress® system, we repeated the tests using a higher concentration of cellular lysate (see methods). Figure 2 shows timecourse trajectories at different template concentrations (0 ng, 12.4 ng, and 124 ng) with and without concentrated lysate.

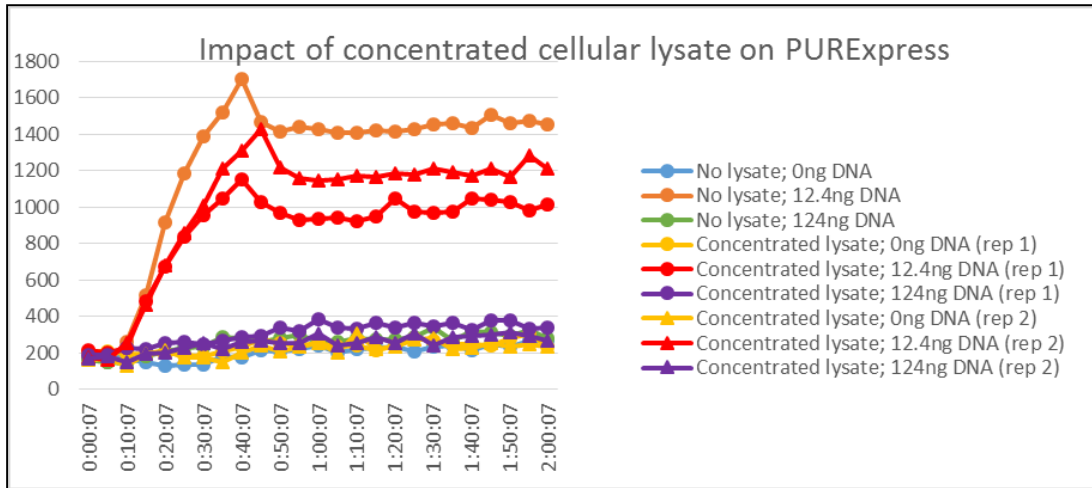


Figure 3. Impact of concentrated cellular lysate on PURExpress®. Timecourse fluorescent trajectories on plate reader containing no lysate and 0 ng (blue line), 12.4 ng (orange line), or 124 ng (green line) of template DNA, and containing concentrated lysate and 0 ng (yellow lines), 12.4 ng (red lines), or 124 ng (purple lines) template DNA. Shapes (circles/triangles) of the same color indicate duplicate trajectories.

3.3 Performance of paper-based gene network

Experiments evaluating the performance of the PURExpress® system with sfGFP plasmid on paper were similarly performed. Figure 4 shows three snap shots from a timelapse experiment showing increasing fluorescence in appropriate spots. All images were taken using the imaging rig described in the methods section. Quantitative analysis of the performance is pending completion of ongoing adaptation of image analysis software to this purpose.

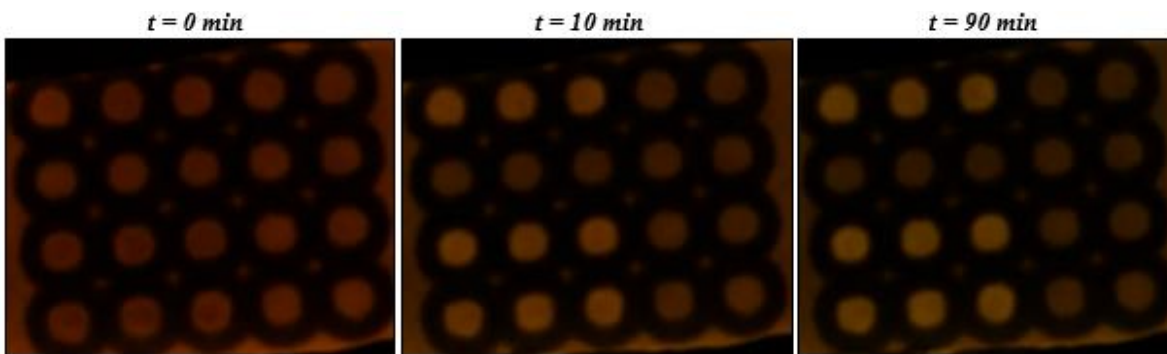


Figure 4. Snapshots of fluorescent signal from sfGFP expressed on paper tickets with PURExpress® at 0 minutes, 10 minutes, and 90 minutes after spotting on tickets. Spots in row 1 contain no lysate, while rows 3 and 4 contain concentrated lysate; row 2 and columns 4 and 5 contain nothing.

4 RESULTS

4.1 Performance of cell-free expression system in the presence of lysate

Plate reader experiments demonstrated that performance of the PURExpress® system appears to be only slightly hampered by the presence of cellular lysate (Figures 2-3). Even with concentrated lysate, the reduction in performance appears to remain limited. However, given the variability between triplicate or duplicate experiments, it is unclear the magnitude of this effect, and indeed the presence of the effect cannot be claimed with high confidence.

It is also noteworthy that the concentration of template DNA played a major role in the performance of the PURExpress® system. In fact, in all cases, the higher concentration of template DNA, which might be expected to produce a higher fluorescence signal than the lower template concentration, was only marginally distinguishable from

the no template controls. This result strongly suggests that optimization of the concentration of the template DNA will be critical to optimizing performance of these systems.

At this point, validation of the robustness of these systems on the paper substrate itself has not yet been tested. However, Figure 4 demonstrates that indeed the system is functioning on the paper tickets that have been printed here.

5 CONCLUSIONS

The preliminary results presented here suggest that paper-based gene networks may be robust to the contents of cellular lysates present in real-world samples. Here, we only tested robustness to the presence of *E. coli* lysate without any other organisms or environmental contaminants present, so significantly more testing would be necessary to further investigate how universally robust these systems might be. Additionally, we tested the simplest possible gene network in order to streamline initial tests. Impacts on performance for complex circuits may be more pronounced and limit applicability of future paper-based assays. Another important and surprising observation was that the concentration of template DNA had a huge impact on system performance, and not in a straightforward, expected way. Thus, future applications of these types of systems will need to be carefully optimized. Ultimately, the results demonstrate that the presence of bacterial lysate from crude sample preparation does not immediately inhibit functionality of cell-free expression systems freeze-dried on paper, encouraging further exploration of these systems for real-world use.

ACKNOWLEDGMENTS

Support for this research was provided by the U.S. Army Edgewood Chemical Biological Center Research and Technology Directorate's Seedling Program. We would like to acknowledge Keith Pardee, Alex Green, and James Collins for graciously facilitating the transition of their technology to our lab. In particular, we thank Keith Pardee for taking the time to teach us his methodologies in person. We also thank Alex Miklos, Randy Hoffman, and Tricia Buckley for fruitful discussion.

REFERENCES

- [1] Endy, D., "Foundation for engineering biology." *Nature*, **2005**, 438, p449-453.
- [2] Cameron, D.E.; Bashor, C.J.; and Collins, J.J., "A brief history of synthetic biology." *Nature Reviews Microbiology*, **2014**, 12(5), p381-390.
- [3] Kwok, R., "Five hard truths for synthetic biology." *Nature*, **2010**, 463, p288-290.
- [4] Forster, A.C. and Church, G.M., "Synthetic biology projects in vitro." *Genome Research*, **2007**, 17, p1-6.
- [5] Pardee, K. *et al.*, "Paper-based synthetic gene networks." *Cell*, **2014**, 159(4), p940-954.
- [6] Der, B.S. *et al.*, "Alternative computational protocols for supercharging protein surfaces for reversible unfolding and retention of stability." *PLOS ONE*, **2013**, 8(5), e64363.
- [7] Lu, Y. *et al.*, "Fabrication and characterization of paper-based microfluidics prepared in nitrocellulose membrane by wax printing." *Analytical Chemistry*, **2010**, 82, p329-335.

Estimating threat agent concentration through state-space analysis

Erin E. Shelly^{a*}, Fiona E. Narayanan^a, Michael O. Kierzewski^a, Thomas E. Ingersoll^b

^aU.S. Army Edgewood Chemical Biological Center, Research and Technology Directorate,
5183 Blackhawk Rd, Aberdeen Proving Ground, MD 21010

^bDefense Threat Reduction Agency, 2800 Bush River Rd, Aberdeen Proving Ground, MD 21010

ABSTRACT

State-space modeling was used to estimate the detection probability as well as the abundance of *Bacillus thuringiensis* spores in a field test using the TACBIO Generation II (TBG2) and the Dry Filter Unit 2000 (DFU). We found that there was a very large difference between the estimated detection probabilities of the DFU (~81%) and the TBG2 (~11%). Estimating detection probabilities enables data fusion between sensors of unequal sensitivities and between heterogeneous environments. Furthermore, fusion of data from a variety of sensors might be used to estimate false-positive probabilities. We also found that the abundance varied based on sensor location, and our estimates of relative abundance coincided with the alarm/not alarm data from the field test. This demonstrated that it is possible to use this method to produce estimates of abundance. The utility of state-space modeling demonstrates that environmental science methods can be readily adapted to military science.

Keywords: Data-fusion, state-space models, hierarchical models, abundance-dependent occupancy, detection probability

1 INTRODUCTION

Estimating concentrations of dangerous aerosols under battlefield conditions is a difficult problem. Typically, field sensors are designed to provide a warning that threat agents are present but are inadequate for measuring concentrations. Sensors are often designed for alarm-on-detection (i.e., presence/absence of threats), rather than quantification of aerosol densities. Furthermore, detection probability of aerosols is affected by the density of the detected aerosol, sensor design, and environmental conditions such as temperature, humidity, and presence of obscurants. Variations in sensor performance under non-optimal conditions can result in under-reporting (false-negatives). Even when sensors are designed to report concentrations, these values may be underestimated because of conditions that result in underreporting.

A method called state-space modeling, also called hierarchical modeling or mark-recapture modeling, explicitly estimates the probability of detection, along with density or distribution, by using repeated measures where sensors are deployed in unison.¹ The relationship between detection probability and concentration can be used to estimate concentration from binary alarm-on-detection data.² State-space modeling can be used to correct for underreporting when detection is imperfect or uneven.³ Furthermore, the probability of detection is itself a useful metric, indicating locations or conditions where surveillance may be inadequate.⁴ State-space modeling was originally designed for ecology studies to determine the abundance of animal species, and it was first used for counting birds.^{5,6} Although state-space modeling has been used extensively by the environmental monitoring community, we were not aware of any Department of Defense-specific applications at the start of this project.

We applied the method of Royle and Nichols² to ECBC's Sensors, Signals, and Aerosol Technologies (SSAT) Branch's aerosol sensor data for bar-coded *Bacillus thuringiensis* spores released under field conditions. We estimated detection probability in relation to two sensor designs, the TACBIO Generation II (TBG2) and the Dry Filter Unit 2000 (DFU), and then used the detection probability to scale alarm-on-detect data for differences in alarm sensitivity. Finally, we used the Royle-Nichols model to estimate spatial differences in concentration downwind and cross-wind from release points.

2 METHODOLOGY

2.1 Test description

Data were collected by ECBC's SSAT branch. The tests were conducted at ECBC's secure M-field. In each trial, one TBG2 sensor was paired with one DFU sensor at each of nine locations on a grid. Each sensor location was assigned an alphabetical letter (Figure 1).⁷

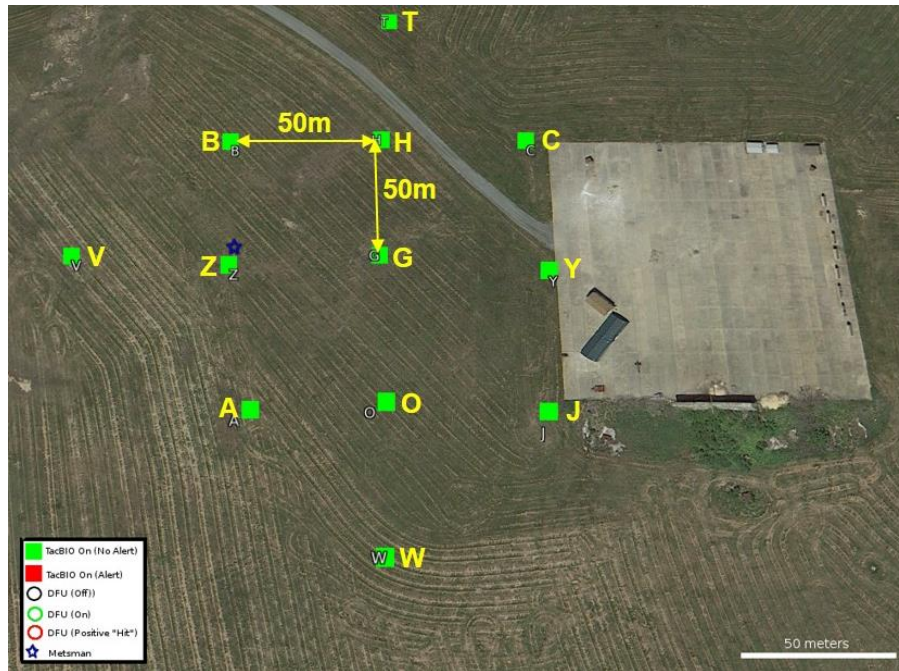


Figure 1. Test grid illustrating alphabetical sensor locations.

The TBG2 is a small sensor that was developed at ECBC using emerging semiconductor ultraviolet (UV) optical sources (SUVOS) technology.⁸ The SUVOS are small, low-cost alternatives to the UV lasers historically used in sensors.⁸ Biological threat agents produce detectable fluorescent and scattering signals when excited by UV light.⁹

The DFU 2000 collects biological particulates from the air for analysis. It consists of a DFU 1000 sampler, as well as a blower motor and casing, air inlet, and filters, all of which are housed in a protective shell. The DFU 2000 also possesses a mast, in addition to a pre-separator intended to reduce the intrusion of large particles, rain, or insects.¹⁰

The tests used for the purpose of this project were conducted in January 2014. For each test, 50 g of *B. thuringiensis* spores were released, but the release locations varied by test. Each release lasted between 1-2 minutes. Samples were collected for approximately 15-20 minutes following each release. Meteorological data was collected for each test.⁷

2.2 Model description

We applied a state-space model, the abundance-dependent occupancy method of Royle and Nichols,² to the paired aerosol sensor data. This model is a two-tiered state space model for occupancy and detection, where detection is a function of abundance. The Royle-Nichols model assumes that the probability of detecting at least one individual in a sample containing multiple individuals (p_i), follows a simple relationship with abundance (in our case the number of spores in a sample (N_i), and the individual detection probability (r_j), according to the rules of probability:

$$p_i = 1 - (1 - r_j)^{N_i}$$

The alarm-level data (y_i), where $y_i = 0$ if no spores are detected, else $y_i = 1$ if any spores are detected, was a stochastic binomial realization of the detection probability p_i , and the number of repeated measures J_i :

$$y_i \sim \text{Bin}(J_i, p_i z_i)$$

where z_i was an indicator function representing the occupancy state, $z_i = 1$ if spores were present in the sample and $z_i = 0$ if spores were not present. In our case, $J_i = 2$, where two repeated measures were taken in each sample, one from TBG2 and one from DFU.

The individual detection probability can vary according to a variety of measurable covariates that affect sensor sensitivity, such as sensor design and environmental conditions. We assumed a linear relationship between logit-transformed individual detection and sensor type:

$$\text{logit}(r_i) = \beta_0 + \beta_1 x_1 + E$$

where β_0 was an intercept value, β_1 a coefficient for scaling between sensor types, x_1 was a covariate representing sensor type, and E was an error term. Covariates were selected using Akaike's Information Criterion.¹¹ We further assumed that abundance was a stochastic Poisson realization of the expected value for abundance in the sample λ_i :

$$N_i \sim \text{Pois}(\lambda_i)$$

where log-transformed λ_i varied linearly according to location:

$$\log(\lambda_i) = \beta_2 + \beta_3 x_2 + \beta_4 x_3 + E$$

where β_2 was an intercept value, β_3 a coefficient for distance downwind, x_2 was a covariate for distance downwind, β_4 a coefficient for distance crosswind, x_3 was a covariate for distance crosswind, and E was an error term. Covariates were again selected using AIC. This allowed a likelihood function to be assembled and parameters estimated using maximum-likelihood estimation, using the functions programmed in the library unmarked¹² in the computational language R.¹³

3 DATA AND RESULTS

3.1 Detection probability

In order to determine estimates for the detection probability, we used an R computer code adaptation¹² of the Royle-Nichols model described above. The base R code was available for public use,¹ but it needed to be modified for our particular scenario. For the detection probability calculation, we chose to use the results from all seven tests conducted in order to include as much data as possible (Table 1).

Table 1. Data for model input.

TBG2	DFU	Unit	Batch	Easting	Northing	Easting R	Northing R	Down-wind	Cross-wind	Device 1	Device 2
1	1	B	B	388682.8	4356969	388569.4	4356905.3	53.5	2.8	TB	F
1	1	H	B	388733	4356965	388569.4	4356905.3	71.1	7.1	TB	F
1	1	C	B	388780.8	4356961	388569.4	4356905.3	88.6	15.2	TB	F
0	1	Z	B	388682.1	4356922	388569.4	4356905.3	47.5	13.1	TB	F
0	0	G	B	388730	4356922	388569.4	4356905.3	66.2	20.3	TB	F
0	0	Y	B	388782.5	4356912	388569.4	4356905.3	85.3	31.2	TB	F
0	1	A	B	388688.6	4356873	388569.4	4356905.3	43.6	31.1	TB	F
0	1	O	B	388729.3	4356872	388569.4	4356905.3	60.6	37.5	TB	F
0	0	J	B	388777.1	4356865	388569.4	4356905.3	79.4	47.4	TB	F
0	0	B	C	388682.8	4356969	388569.4	4356905.3	14.7	56.4	TB	F
0	0	H	C	388733	4356965	388569.4	4356905.3	28.5	73.5	TB	F
0	0	C	C	388780.8	4356961	388569.4	4356905.3	42.2	89	TB	F
0	0	Z	C	388682.1	4356922	388569.4	4356905.3	27.3	45.7	TB	F
0	0	G	C	388730	4356922	388569.4	4356905.3	40.4	63.8	TB	F
0	0	Y	C	388782.5	4356912	388569.4	4356905.3	57.9	81	TB	F
0	0	A	C	388688.6	4356873	388569.4	4356905.3	44.6	36.3	TB	F
0	0	O	C	388729.3	4356872	388569.4	4356905.3	56.3	52.5	TB	F
0	0	J	C	388777.1	4356865	388569.4	4356905.3	72.8	69	TB	F
0	0	B	D	388682.8	4356969	388616.4	4356981.1	28	10.8	TB	F
1	1	H	D	388733	4356965	388616.4	4356981.1	47.7	20.2	TB	F
1	1	C	D	388780.8	4356961	388616.4	4356981.1	66.4	29.5	TB	F
0	0	Z	D	388682.1	4356922	388616.4	4356981.1	36.4	7.8	TB	F
0	1	G	D	388730	4356922	388616.4	4356981.1	55.5	4.7	TB	F
1	1	Y	D	388782.5	4356912	388616.4	4356981.1	78.4	13.3	TB	F
0	0	A	D	388688.6	4356873	388616.4	4356981.1	49.4	24.9	TB	F
1	0	O	D	388729.3	4356872	388616.4	4356981.1	66.1	15.3	TB	F
1	1	J	D	388777.1	4356865	388616.4	4356981.1	86.5	7	TB	F
0	0	B	E	388682.8	4356969	388616.4	4356981.1	25.9	17.4	TB	F
0	0	H	E	388733	4356965	388616.4	4356981.1	43.8	32.5	TB	F
0	0	C	E	388780.8	4356961	388616.4	4356981.1	61.3	46.3	TB	F
1	1	Z	E	388682.1	4356922	388616.4	4356981.1	39.2	2.7	TB	F
1	1	G	E	388730	4356922	388616.4	4356981.1	55.5	18.2	TB	F
1	1	Y	E	388782.5	4356912	388616.4	4356981.1	77.3	32.6	TB	F
1	1	A	E	388688.6	4356873	388616.4	4356981.1	56.4	13.3	TB	F
1	1	O	E	388729.3	4356872	388616.4	4356981.1	71.4	1.8	TB	F
1	1	J	E	388777.1	4356865	388616.4	4356981.1	90.8	16.1	TB	F

Table 1 (cont.). Data for model input.

TBG2	DFU	Unit	Batch	Easting	Northing	Easting R	Northing R	Down-wind	Cross-wind	Device 1	Device 2
0	0	B	F	388682.8	4356969	388616.4	4356981.1	14.8	27.5	TB	F
0	0	H	F	388733	4356965	388616.4	4356981.1	23.5	49.2	TB	F
0	0	C	F	388780.8	4356961	388616.4	4356981.1	32	69.4	TB	F
0	0	Z	F	388682.1	4356922	388616.4	4356981.1	33.9	20	TB	F
0	0	G	F	388730	4356922	388616.4	4356981.1	40.5	41.5	TB	F
0	0	Y	F	388782.5	4356912	388616.4	4356981.1	51.9	64.2	TB	F
1	1	A	F	388688.6	4356873	388616.4	4356981.1	55.9	15.9	TB	F
1	1	O	F	388729.3	4356872	388616.4	4356981.1	62.1	34.5	TB	F
1	1	J	F	388777.1	4356865	388616.4	4356981.1	71.2	55.2	TB	F
1	1	B	G	388682.8	4356969	388682.8	4356968.5	4.9	2	TB	F
1	1	H	G	388733	4356965	388682.8	4356968.5	21.4	4.5	TB	F
1	1	C	G	388780.8	4356961	388682.8	4356968.5	36.5	8.5	TB	F
0	0	Z	G	388682.1	4356922	388682.8	4356968.5	10	15.8	TB	F
0	0	G	G	388730	4356922	388682.8	4356968.5	24.8	10	TB	F
1	1	Y	G	388782.5	4356912	388682.8	4356968.5	42.8	6.3	TB	F
0	0	A	G	388688.6	4356873	388682.8	4356968.5	17.4	30.4	TB	F
0	0	O	G	388729.3	4356872	388682.8	4356968.5	30.8	25.6	TB	F
0	0	J	G	388777.1	4356865	388682.8	4356968.5	47.2	21.4	TB	F
0	1	B	H	388682.8	4356969	388707.8	4357010.7	0	23.5	TB	F
0	1	H	H	388733	4356965	388707.8	4357010.7	0	24.7	TB	F
0	1	C	H	388780.8	4356961	388707.8	4357010.7	0	41.9	TB	F
1	1	Z	H	388682.1	4356922	388707.8	4357010.7	0	43	TB	F
0	1	G	H	388730	4356922	388707.8	4357010.7	0	42.8	TB	F
0	1	Y	H	388782.5	4356912	388707.8	4357010.7	0	58.1	TB	F
0	1	A	H	388688.6	4356873	388707.8	4357010.7	0	65.5	TB	F
0	1	O	H	388729.3	4356872	388707.8	4357010.7	0	65.6	TB	F
0	1	J	H	388777.1	4356865	388707.8	4357010.7	0	76.2	TB	F

Several models incorporating various combinations of the parameters batch, sensor type, sensor location, distance downwind from the release point, and distance crosswind from the release point were evaluated using adapted R code for the Royle-Nichols model.^{2,12} The widely-accepted Akaike Information Criterion (AIC) metric, which is an information theoretics method that calculates the trade-off between the goodness of fit and the complexity of the model, was used to compare alternative models. Rather than testing a hypothesis against an arbitrary cutoff point (as does the *p*-value), AIC compares the relative information content of the various models under consideration. Models were then ranked (Table 2) based on the AIC score.

Table 2. Model comparison and AIC score table for detection probability.

Model	nPars	AIC	delta	AICwt	cumltvWt
psi(Batch+Unit+Downwind+Crosswind)p(Device)	19	131.51	0.00	8.0E-01	0.80
psi(Batch+Unit+Downwind*Crosswind)p(Device)	20	136.33	4.81	7.2E-02	0.87
psi(Batch)p(Device)	9	136.43	4.92	6.8E-02	0.94
psi(Downwind+Crosswind)p(Device)	5	136.61	5.09	6.2E-02	1.00
psi(.)p(Device)	3	145.22	13.71	8.4E-04	1.00
psi(Batch+Unit)p(Device)	17	150.65	19.13	5.6E-05	1.00
psi(.)p(.)	2	154.20	22.68	9.5E-06	1.00
psi(Unit)p(Device)	11	159.41	27.90	7.0E-07	1.00

The *model* column describes the parameters and interactions in each possible model. The abundance estimate is represented by *psi*, and *p* denotes the detection probability. *Batch* refers to the test run, *Unit* is the particular sensor in use, *Downwind* is the distance of the sensor downwind from the release location, *Crosswind* is the distance of the sensor crosswind from the release location, and *Device* refers to the type of sensor in use. The *nPars* column lists the number of parameters in each model, *AIC* lists the AIC value calculated for each potential model, and *delta* is the difference between the AIC of the model in question and the AIC of the best model. *AICwt* lists the relative support for each model out of a total of 1, and *cumltvWt* gives the cumulative AIC weights.

Using this rank, the best model for individual detection was found to be:

$$\text{logit}(r_i) = 1.48 - 2.11x_1 + E$$

where x_1 was a covariate representing sensor type, and E was an error term.

After performing the back-transformation on the probability of detecting at least one individual, p_i , we determined the detection probability for the DFU to be approximately 81% (with a 95% confidence interval of 32% to 98%), and the detection probability of the TBG2 to be approximately 11% (with a 95% confidence interval of 2% to 45%).

3.2 Abundance

In order to calculate abundance, we found it best to select a single test case (Batch E: Figure 2), in order to reduce the effects of varying conditions on the concentrations of agent present.⁷

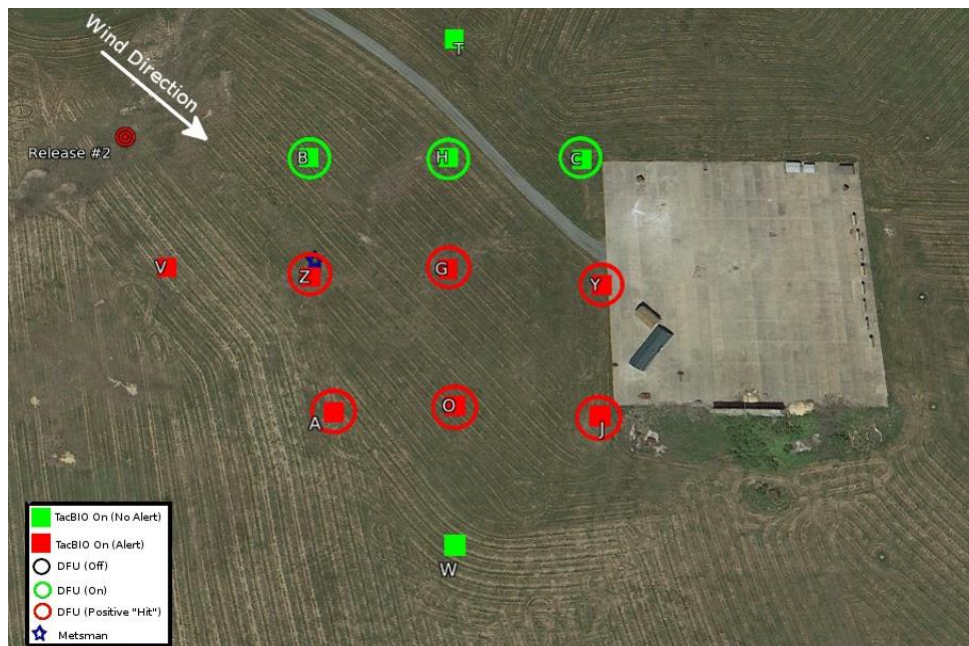


Figure 2. Test scenario used in abundance estimate.

We again used the R computer code for the Royle-Nichols model to fit several possible models, this time using only the data from Batch E. The model evaluated them using the AIC metric and produced a rank (Table 3).

Table 3. Model comparison and AIC score table for abundance.

Model	nPars	AIC	delta	AICwt	cumltvWt
psi(Downwind+Crosswind)p(Device)	5	12.74	0.00	5.3E-01	0.53
psi(Downwind+Crosswind)p(Device+Downwind+Crosswind)	7	14.00	1.27	2.8E-01	0.81
psi(.)p(.)	2	15.46	2.72	1.4E-01	0.95
psi(.)p(Device)	3	17.46	4.72	5.0E-02	0.99
psi(Downwind*Crosswind)p(Device+Downwind*Crosswind)	9	22.02	9.29	5.1E-03	1.00
psi(Downwind*Crosswind)p(Device)	6	32.70	19.96	2.4E-05	1.00
psi(Downwind*Crosswind)p(Device+Downwind+Crosswind)	8	36.70	23.96	3.3E-06	1.00

The *model* column describes the parameters and interactions in each possible model. The abundance estimate is represented by *psi*, and *p* denotes the detection probability. *Batch* refers to the test run, *Unit* is the particular sensor in use, *Downwind* is the distance of the sensor downwind from the release location, *Crosswind* is the distance of the sensor crosswind from the release location, and *Device* refers to the type of sensor in use. The *nPars* column lists the number of parameters in each model, *AIC* lists the AIC value calculated for each potential model, and *delta* is the difference between the AIC of the model in question and the AIC of the best model. *AICwt* lists the relative support for each model out of a total of 1, and *cumltvWt* gives the cumulative AIC weights.

According to this rank, the best model for abundance was found to be:

$$\log(\lambda_i) = -1.2395 + 0.0600x_2 - 0.0893x_3 + E$$

where x_2 was a covariate for distance downwind, x_3 was a covariate for distance crosswind, and E was an error term. The estimates of abundance were calculated at each location and plotted on a graph (Figure 3).

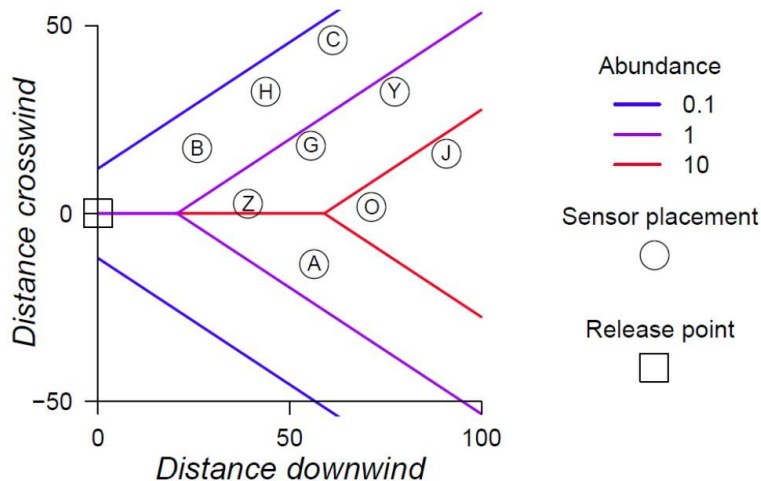


Figure 3. Abundance estimates based on crosswind and downwind parameters.

This graph displays the nine sensor locations, as well as the release point. The colored lines represent relative abundance. For example, along the red isocline, it is estimated that there are 10 times as many spores present as the area along the purple isocline. While this does not display absolute concentration, it would be possible to calculate an estimate if the volume of air sampled by the detector were known.

4 CONCLUSIONS

Inequality of detection probability between the TBG2 and the DFU demonstrated the importance of employing state-space methods. Because the TBG2 had a consistently lower detection probability than DFU, exclusive reliance on TBG2 would result in less complete surveillance coverage. However, because sensitivity spectra do not match exactly between the two sensor types, the breadth of sensitivity should be increased by using both types of detectors in unison. Furthermore, the explicit estimation of detection probability is itself useful. This can be helpful for commanders in the field, so that conditions resulting in inadequate surveillance elicit precaution, and conditions that facilitate adequate surveillance, can be optimized. State-space modeling allows real-time assessment of conditions affecting sensor performance under field conditions, rather than relying on predictions based on laboratory conditions. Estimating detection probabilities enables data fusion between sensors of unequal sensitivities and between heterogeneous environments.

Examination of the raw data provided validation for model results. Model predictions of lowest estimated concentration (Figure 3) corresponded to sensor locations that produced fewer or no alarms (i.e., locations B, H, and C). Those sensors located in the moderate and highest concentration bands produced the highest number of alarms. This demonstrated that it is possible to use this method to produce estimates of abundance.

Research into state-space modeling might be improved by expansion of efforts at the Edgewood Chemical Biological Center. First, this analysis was performed on limited data, necessitating the use of an unrealistically simple linear model. Applying these methods to a larger dataset could allow a non-linear model that shows a lowering abundance with increased range downwind. Additionally, a more explicit estimate of volume sampled by each sensor would allow an estimate of density, rather than relative abundance. An incompletely defined sensor range, that is, the area or volume surveyed by "point" detectors, is a persistent problem in state-space models for density. Data-fusion between point and standoff detectors, which include an explicit spatial component, could correct this problem. Alternatively, fusion between point-detection and linear-transects, such as with unmanned aerial vehicle mounted sensors, might be attained with a state-space method called distance-sampling. Such explicit estimates of threat density should be a goal of chemical, biological, radiological, and nuclear threat detection.

Within the Edgewood Chemical Biological Center, the JUPITR (Joint United States Forces Korea Portal and Integrated Threat Recognition) and TBG2 detector systems could benefit from the added capability to estimate agent concentrations, rather than simply identifying the presence or absence of threats. Furthermore, fusion of data from a variety of sensors might be used to estimate false-positive probabilities.¹⁴ In the broader community, the Department of Defense and the Department of Homeland Security could benefit from the development of state-space methods of analysis. State-space techniques improve reliability of threat level estimation, thus allowing for better-informed decisions about the necessity to adopt protective posture. The utility of state-space modeling demonstrates that environmental science methods can be readily adapted to military science.

ACKNOWLEDGMENTS

Support for this research was provided by the U.S. Army Edgewood Chemical Biological Center Research and Technology Directorate's Seedling Program.

REFERENCES

- [1] Royle, J.A. and Dorazio, R.M., *Hierarchical Modeling and Inference in Ecology*. Academic Press, Boston, Massachusetts. **2008**.
- [2] Royle J.A. and Nichols, J.D., "Estimating abundance from repeated presence absence data or point counts." *Ecology*, **2003**, 84(3), p777-790.
- [3] MacKenzie, D.I. *et al.*, "Estimating site occupancy rates when detection probabilities are less than one." *Ecology*, **2002**, 83(8), p2248-2255.
- [4] Ingersoll, T.E. and Hoppe, C.D., "Overview of state-space surveillance modeling for risk analysis." Poster; *Chemical Biological Defense Science and Technology Conference*, St. Louis, Missouri. **2015**.

- [5] Jolly, G.M., "Estimates of population parameters from multiple recapture data with both death and dilution – deterministic model." *Biometrika*, **1963**, 50, p113-128.
- [6] Seber, G.A.F., "A note on the multiple recapture census." *Biometrika*, **1965**, 52, p249-259.
- [7] Kilper, G.; Goad, A.; and Wong, A., "TACBIO Gen II Worldwide Test Results." *ECBC Coffee with Colleagues*. **DEC 2015**. Edgewood, MD.
- [8] "ECBC develops low-cost next generation biological detector TAC-BIO II reduces size, power usage of previous generation." *ECBC News Release*, **JUL 2013**.
- [9] "TACBIO Gen II; ECBC Pushes Convention of Biological Detection with Lightweight, Low-Cost Structure." *ECBC Featured Story*, **JAN 2015**.
- [10] "Dry filter unit." Chemical, Biological, Radiological, & Nuclear Information Resource Center, **2010**. [<http://jacks.jpeocbd.army.mil/Public/FactSheetProvider.ashx?productId=376>]
- [11] Akaike, H., "Information theory and an extension of the maximum likelihood principle." *Second International Symposium on Information Theory*, **1973**, p267-281.
- [12] Fiske, I. and Chandler, R., "Unmarked: An R package for fitting hierarchical models of wildlife occurrence and abundance." *Journal of Statistical Software*, **2011**, 43(10), p1-23.
- [13] R Core Team, "R: A language and environment for statistical computing." *R Foundation for Statistical Computing*, **2013**. [<http://www.R-project.org/>]
- [14] Royle, J.A. and Link, W.A., "Generalized site occupancy models allowing for false positive and false negative errors." *Ecology*, **2006**, 87(4), p835-841.

A novel bio-hydrogel-based sampling approach

Lisa Smith^{a*}, Laura Burton^b, Pooja Rastogi^b, Kristina Parman^b, Vipin Rastogi^a

^aU.S. Army Edgewood Chemical Biological Center, Research and Technology Directorate,
5183 Blackhawk Rd, Aberdeen Proving Ground, MD 21010

^bThe Oak Ridge Institute for Science and Education, MC-100-44 P.O. Box 117,
Oak Ridge, TN 37831

ABSTRACT

Current surface sampling approaches, including swabs, BiSKit™, and wipes, especially from porous surfaces, are generally inefficient. Bio-hydrogel is a water-based gel, which is applied as a thick viscous material, and allowed to dry into a thin film within a few hours depending on ambient conditions. The dried film is then peeled off the surface. During drying process, the gel encapsulates the biological agent and other contaminants. The concept of the bio-hydrogel presented here involves use of such a gel to sample and preserve the encapsulated biological agent off contaminated surfaces. In this study, the bio-hydrogel was used to examine the sampling efficiency and preservation of the material from contaminated surfaces. The bio-hydrogel proved to be a superior sampling tool (> 80%) from 3D objects (screws), and pinewood then current sampling devices for the recovery of spores of *Bacillus anthracis* (Δ Sterne). Hydrogel seemed to be as good as a sampling tool for painted steel, polycarbonate, pinewood, and screws, as current sampling techniques. Since the hydrogel recovered less than 1% cells of *Staphylococcus aureus* off painted steel, polycarbonate, pinewood, and screws, it seemed to be bactericidal. *B. anthracis* (Δ Sterne) spores were well-preserved at 4 °C for five weeks. Over 5-logs of *B. anthracis* (Δ Sterne) spores lost their viability within two weeks at 25 °C and 37°C, indicating poor preservation.

Keywords: Sampling, *Bacillus anthracis*, bio-preservation, *Staphylococcus aureus*, bio-hydrogel

1 INTRODUCTION

Biological sampling from environmental surfaces is a complex issue and has been an area of intensive research. Biological sampling is at the core of all pre- and post-decontamination analysis following a biological agent release event. Current surface sampling approaches, including swabs, BiSKit™, wipes, and vacuum socks, especially from porous surfaces, such as concrete are generally inefficient. One study looked at the recovery efficiency of sterile polyester-rayon blend gauze wipe on stainless steel surfaces and painted wallboard surfaces and it was less than 35%.¹ Another study investigated a BiSKit™, which is a biological sampling kit, and the percent recovery was 18.4%.² Many studies have looked at swabs as biological samplers and the percent recoveries were less than 55%.³⁻⁶ Vacuum socks can be used on large surface areas, but recovery of spores by vacuum sampling is very poor with efficiencies; Brown et al. showed percent recoveries of spores from vacuum filter socks of less than 36%.⁷ Furthermore, such sampling devices are only applicable for smooth, two-dimensional surfaces and are not suited to sample from complex 3D structures. The sample collection protocols are often unsuited to long-term preservation and for forensics and diagnostic analysis.

The bio-hydrogel is a water-based gel, which is applied as a thick viscous material, and is allowed to dry into a thin film within a few hours. The dried film is then peeled off the surface. This study investigates the use of this hydrogel as a biological sampler and as a means of preservation. The hydrogel is applied to contaminated surfaces, and then dried overnight. When the hydrogel is peeled off the contaminated surface, the spores/cells have been encapsulated in the hydrogel, therefore the hydrogel should be able to be used as a biological sampler since it collects the spores/cells. In this study, four surfaces were sampled by the bio-hydrogel (pinewood, polycarbonate, painted steel, and screws) to determine if the bio-hydrogel would be a good biological sampler for all types of surfaces including 3D surfaces.

Preservation of biological samples is a concern following a biological incident. The Centers for Disease Control and Prevention standard methods for shipping sampled biologicals state that samples must be stored between 2-8 °C and must be used within 48 hours.⁸ It has been determined that there is a loss of viability in the samples if the samples are not refrigerated right after they were taken.⁹ Studies have shown that *Bacillus subtilis* has been preserved in acacia

gum, a natural polymer, for 64 days at 5 °C, 15 °C, 25 °C, and 40 °C.¹⁰ When acacia gum was added to sampling material (i.e., cotton, wool), *Bacillus anthracis* (Δ Sterne) and methicillin-resistant *Staphylococcus aureus* (MRSA) had a higher level of protection than if it was not present.¹¹ This bio-hydrogel should be able to preserve the biological samples after they have been encapsulated in the bio-hydrogel until they are processed in the laboratory. In this study, the hydrogel was applied to two different surfaces, painted steel and polycarbonate, and the samples were stored at 5 °C, 25 °C, and 37 °C and sampled weekly for five weeks to determine if the bio-hydrogel also preserved the biological material.

2 METHODOLOGY

2.1 Test organisms and reagents

B. anthracis (Δ Sterne) was produced by Dr. Michael Kim at the Edgewood Chemical Biological Center Research and Technology Directorate's BioTechnology Branch. *S. aureus* (ATCC® 6538™; obtained from American Type Culture Collection (ATCC®); Manassas, VA) were the vegetative cells used in this study. The hydrogel used was a biodegradable polymer comprised of a chelating agent, less than 35% water, and organic solvents and was procured from METIS Scientific (info@metischem.com). Sample 3-inch x 1-inch coupons were made from pinewood, polycarbonate, painted steel, and screws (obtained from The Home Depot). The coupons were autoclaved in sterile petri plates before use. Tryptic soy agar (TSA) plates were used for culturing. 0.01% Tween 80 was used as the extraction media.

2.2 Methods

2.2.1 Sampling experiments

Painted steel coupons, polycarbonate coupons, pinewood coupons, and screws were the surfaces used for the sampling experiments. The coupons were inoculated with either 50 μ L *B. anthracis* (Δ Sterne) (1×10^7) or 50 μ L (1×10^7) *S. aureus*. The screws were dipped into the inoculum of either *B. anthracis* (Δ Sterne) or *S. aureus*. Once the inoculum dried, the hydrogel was overlaid onto the coupons. The coupons with the hydrogel were left in the biosafety hood and allowed to dry overnight. Once the hydrogel dried in a thin film, it was peeled off the coupons and placed into 20 mL of 0.01% Tween 80. The samples were incubated at 37 °C for 2 hours until the gel was rehydrated in the 0.01% Tween 80. After rehydration, serial dilutions were performed for each sample and then the dilutions were plated on TSA plates and incubated at 37 °C overnight. Control coupons, with no gel, were placed into 20 mL of 0.01% Tween 80 and then serially diluted and plated.

2.2.2 Preservation experiments

Polycarbonate and painted steel were the coupons used for the preservation experiments. The coupons were inoculated with 50 μ L *B. anthracis* (Δ Sterne) (1×10^7) and dried overnight in the biosafety hood. The hydrogel was overlaid on the coupons and then left to dry in the biosafety hood overnight. Once the gel was dried, the coupons were put in different temperatures, 4, 25, and 37 °C and coupons were sampled after 1 day, 1 week, 2 weeks, 3 weeks, 4 weeks, and 5 weeks. The coupons were taken out at the appropriate time point, and the gel was peeled off the coupons and placed into 20 mL of .01% Tween 80. The samples were incubated at 37 °C for 2 hours until the gel was rehydrated in the .01% Tween 80. After rehydration, serial dilutions were performed for each sample, and then the dilutions were plated on TSA plates and incubated at 37 °C overnight.

3 RESULTS

3.1 Sampling experiments

To determine if the bio-hydrogel was an efficient sampler, the percent recovery of *B. anthracis* (Δ Sterne) was determined by taking the average colony forming units (CFU) of the test hydrogel divided by the average CFU of the positive controls (no hydrogel) of each coupon type, times 100, see Figure 1. The bio-hydrogel proved to be a better sampling tool for 3D objects (screws) and pinewood than current sampling devices for recovery of *B. anthracis* (Δ Sterne) (> 80% recovery). The bio-hydrogel seemed to be as good as current sampling tools for painted steel and polycarbonate, such as wipes, swabs, and BiSKit™ samplers (15%-60%) for the recovery of *B. anthracis* (Δ Sterne) spores. The bio-hydrogel can be sprayed with a paint sprayer, so it would be easy and efficient to use in a large area.

The bio-hydrogel recovered 0% to 0.35% of *S. aureus* off painted steel, polycarbonate, pinewood, and screws (data not shown). This bio-hydrogel seemed to be bactericidal for vegetative cells. A ‘designer’ gel needs to be developed without bactericidal solvents to determine if a bio-hydrogel would be a good sampler for the vegetative cells.

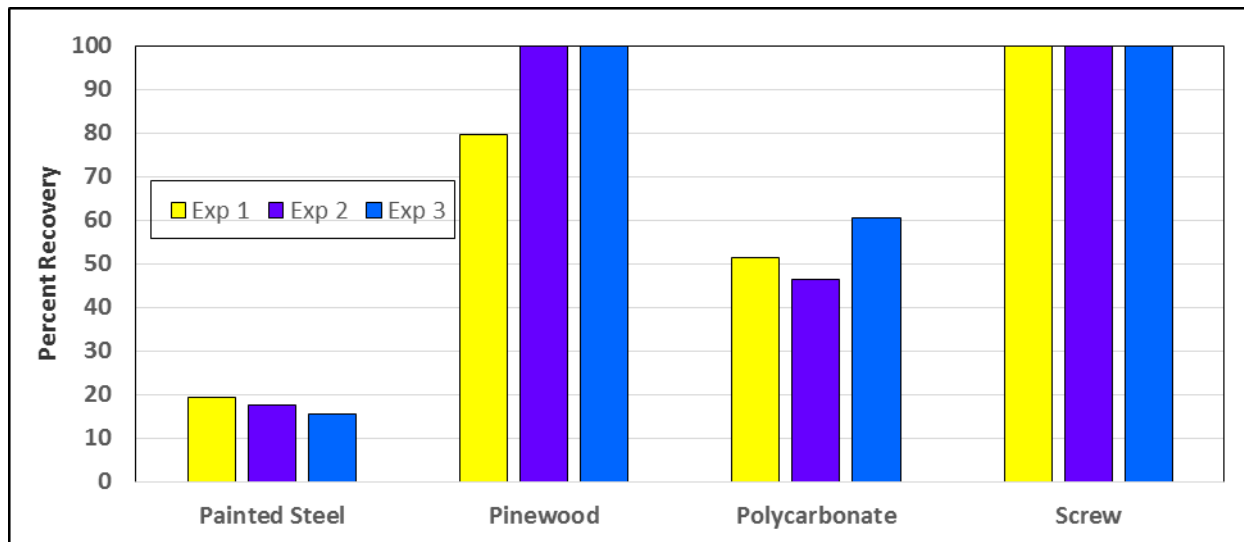


Figure 1. The recovery efficiency of hydrogel on *B. anthracis* (ΔSterne) from painted steel, pinewood, polycarbonate, and screws.

3.2 Preservation experiments

The log reduction was calculated for each sample to determine if the spores were preserved over time in each of the three different temperatures. The log reduction was calculated by taking the average log of the positive controls (no gel) minus the average log of the hydrogel at the specific time point and temperature and coupon type. The *B. anthracis* (ΔSterne) spores were preserved in the hydrogel at 4 °C for five weeks on both painted steel and polycarbonate coupons. This is longer than samples are able to be stored now before they are processed.⁸ *B. anthracis* (ΔSterne) did not survive in the hydrogel as well at 25 °C and 37 °C (see Figure 2 and Figure 3). The spores may be germinating at 25 °C and 37 °C then the cells are dying in the hydrogel. When a new designer hydrogel is developed without bactericidal agents, preservation of samples at 25 °C and 37 °C will be tested. It would be extremely beneficial if the viability of the spores remains stable in the hydrogel at 25 °C or even 37 °C for the 5 week period, so that it would not be crucial to refrigerate the samples, which is not always an option, before the samples get to the laboratory.

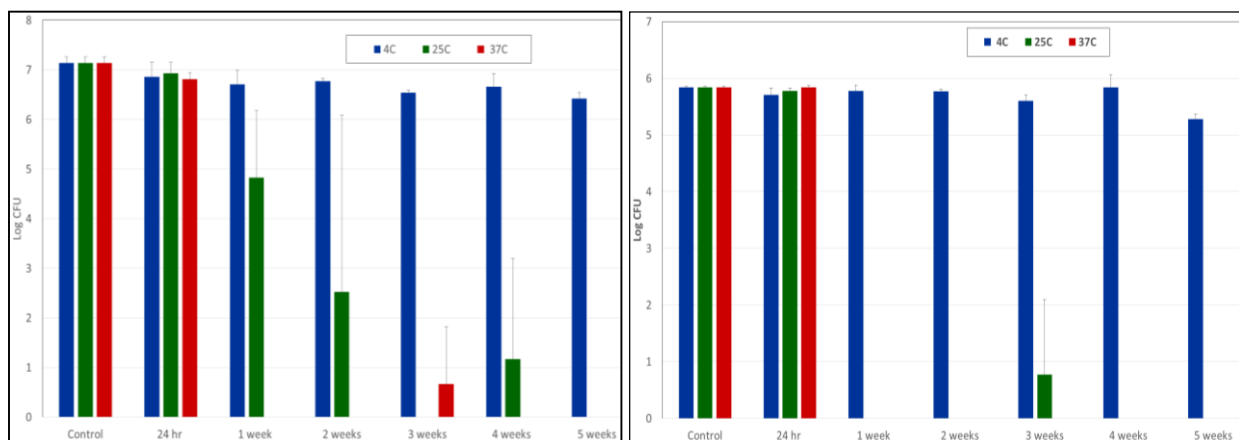


Figure 2. Preservation of *B. anthracis* (ΔSterne) in hydrogel on polycarbonate coupons over five weeks at three different temperatures for Run 1 (left) and Run 2 (right).

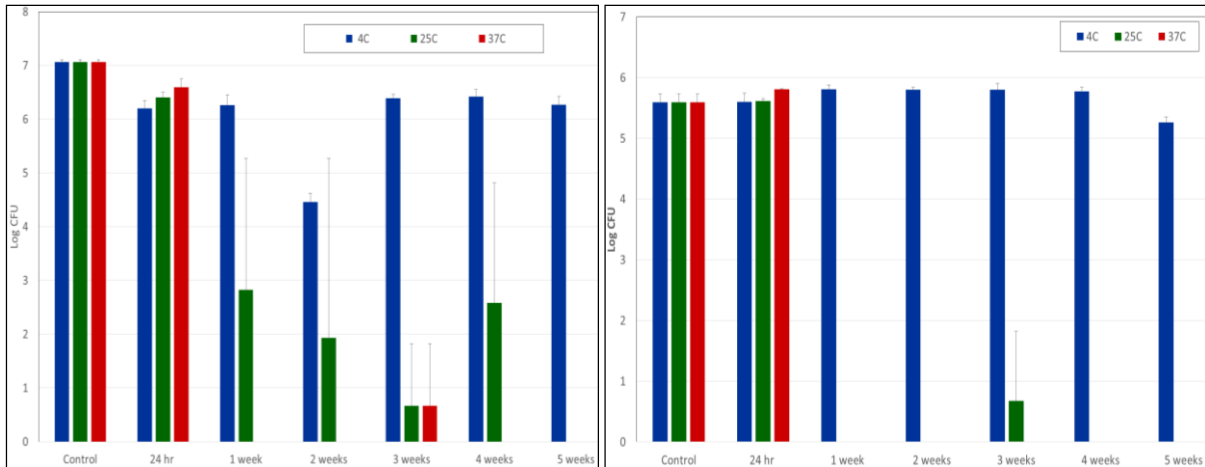


Figure 3. Preservation of *B. anthracis* (Δ Sterne) in hydrogel on painted steel coupons over five weeks at three different temperatures for Run 1 (left) and Run 2 (right).

4 CONCLUSIONS

Bio-hydrogel is an effective sampling tool for bacterial spores. It is as good as or better than the current samplers on the market and can be used in a large scale biological incident. Unfortunately the current hydrogel cannot be used to sample *S. aureus*, since it appears to be bactericidal. A ‘designer’ gel without the bactericidal agent needs to be made and the experiments with *S. aureus* (and other vegetative cells) need to be repeated. Even though it was demonstrated that bio-hydrogel was an effective sampler on the screws, more experiments need to be performed with the hydrogel and sampling on 3D objects.

The hydrogel could be used for preservation of spores for five weeks, if the samples are stored at 4 °C. Current CDC protocol states that the samples need to be used within 48 hours of the time the sample was taken and stored at 2 °C to 8 °C, but if the bio-hydrogel is used as a sampling tool, the samples may be stored longer with no spore loss. The spores did not survive at 25 °C or 37 °C for over five weeks. The spores may be germinating in the hydrogel and then the vegetative cells would die since this hydrogel has been shown to be bactericidal. Further tests of preservation should be done with a new designer gel without the bactericidal agent, to determine if spores would survive at 25 °C or 37 °C over five weeks. The designer gel without the bactericidal agent, should be tested on preservation of samples with vegetative cells.

ACKNOWLEDGMENTS

Support for this research was provided by the U.S. Army Edgewood Chemical Biological Center Research and Technology Directorate’s Seedling Program.

REFERENCES

- [1] Brown, G.S. *et al.*, "Evaluation of a wipe surface sample method for collection of Bacillus spores from nonporous surfaces." *Applied and Environmental Microbiology*, **2007**, 73(3), p706-710.
- [2] Buttner, M.P. *et al.*, "Evaluation of the biological sampling kit (BiSKit) for large-area surface sampling." *Applied and Environmental Microbiology*, **2004**, 70(12), p7040-7045.
- [3] Hodges, L.R. *et al.*, "National validation study of a swab protocol for the recovery of Bacillus anthracis spores from surfaces." *Journal of Microbiological Methods*, **2010**, 81, p141-146.

- [4] Rose, L. *et al.*, "Swab materials and *Bacillus anthracis* spore recovery from nonporous surfaces." *Emerging Infectious Diseases*, **2004**, 10(6), p1023-1029.
- [5] Hodges, L.R. *et al.*, "Evaluation of a macrofoam swab protocol for the recovery of *Bacillus anthracis* spores from a steel surface." *Applied and Environmental Microbiology*, **2006**, 72(6), p4429-4430.
- [6] Probst, A. *et al.*, "Validation of a nylon-flocked-swab protocol for efficient recovery of bacterial spores from smooth and rough surfaces." *Applied and Environmental Microbiology*, **2010**, 76(15), p5148-5158.
- [7] Brown, G.S. *et al.*, "Evaluation of vacuum filter sock surface sample collection method for *Bacillus* spores from porous and non-porous surfaces." *Journal of Environmental Monitoring*, **2007**, 9, p666-671.
- [8] Centers for Disease Control and Prevention. "Emergency Response Resources-Surface Sampling procedures for *Bacillus anthracis* spores from smooth, non-porous surfaces." [<http://www.cdc.gov/niosh/topics/emres/surface-sampling-bacillus-anthraxis.html>].
- [9] Thorne, P.S. *et al.*, "Bioaerosol sampling in-field studies - can samples be express mailed?" *American Industrial Hygiene Association Journal*, **1994**, 55, p1072-1079.
- [10] Krumnow, A.A. *et al.*, "Preservation of bacteria in natural polymers." *Journal of Microbiological Methods*, **2009**, 78, p189-194.
- [11] Sorokulova, I. *et al.*, "Natural biopolymer for preservation of microorganisms during sampling and storage." *Journal of Microbiological Methods*, **2012**, 88, p140-146.

Exploring aerosol charge characteristics due to explosive disseminations

Daniel G. Wise, Elias W. Yoon*, Daniel J. Weber
U.S. Army Edgewood Chemical Biological Center, Research and Technology Directorate,
5183 Blackhawk Rd, Aberdeen Proving Ground, MD 21010

ABSTRACT

A series of experimental trials were performed in a large explosive rated aerosol test chamber to determine the electrical charge characteristics of the aerosol particles resulting from an explosive dissemination event. These trials used small scale explosive devices to disseminate payload materials of various dielectric constants and were compared to other dissemination methods. The Dekati® Electrical Low-Pressure Impactor (ELPI®+) was used to measure the charge characteristics of the aerosols produced by the different dissemination methods. The charge distribution of explosively-disseminated submicron particles show that they are mainly positively-charged whereas other dissemination methods impart negative charge distributions or particle size dependent bipolar distributions. This unique signature suggests that thermionic emission or “flame-charging” is the predominant particle charging mechanism. However, explosive dissemination of submicron payload particles does not produce significant particle charge levels in comparison to common tribo-charging processes.

Keywords: Aerosol, dissemination, electrical charge, electrostatic, explosive, particles, pyrotechnic, thermionic

1 INTRODUCTION

Explosive, pyrotechnic, and pressure dissemination of materials are considered the most likely realistic and effective methods to create threat aerosols. Beyond the concern of threat materials, these methods are also used in the dissemination of obscurants, threat defeat aerosol scavengers, and the delivery of material defeating payloads or surface decontaminants. Most dissemination methods will result in the aerosol particles having an electrical charge.¹ The presence of an electrical charge will affect the tendency of aerosol particles to disperse or agglomerate, and subsequently adhere to surfaces. Therefore the particle size distribution characteristics and hence propagation of the aerosol cloud can depend tremendously on particle charge. Subsequently, particle charge characteristics can have order of magnitude effects on the transport of these particles through detection devices and the deposition/contamination of threat or defeat materials to surfaces or in the human respiratory tract.²

1.1 Technical background

Aerosol generation processes often result in the particles obtaining some level of electrical charge. There are several ways that an aerosol particle might acquire an electrical charge. The most common charging mechanisms that would be experienced in aerosol generation are static electrification, thermionic emission (or “flame charging”), and charging by small gas ions.³

Static electrification can occur either by contact charging, where particles (or particles and surfaces) separate without friction, or friction charging where the particles and surfaces (or two particles) rub against each other. These processes are often referred to in general as “tribo-charging.” The polarity of the charge on particles resulting from tribo-charging can sometimes be predicted if the interacting materials’ dielectric constants are known. The material with the higher dielectric constant is more likely to donate electrons to the other and therefore become positively charged.^{4,5}

Charging by gas ions generally falls into the categories of diffusion and field charging. Diffusion charging results from particle Brownian motion collision with ions, and field charging is the collision of the particles with unipolar ions that are moving rapidly due to the presence of a strong electric field. Diffusion charging is the dominant mechanism for charging particles less than 0.20 μm and field charging dominates for particles larger than 1.0 μm (both mechanisms are involved with particles between these sizes).

Flame charging can occur at high temperatures where the particle surfaces undergo thermionic emission and result in a uni-polar charge distribution. In a flame or other high temperature environment (such as an explosion) gas ions are present in high concentrations. Therefore ion and particle reactions are likely to happen and rapid charge redistribution may also occur as the particles leave the hot region.³

1.2 Study background

This study has its genesis in the interest of developing advanced obscuration technology. Developments in nanotechnology and metamaterials have resulted in materials that have great potential as obscurants. However, the performance of novel obscurant particles in actual real-world application as an aerosol cloud depends on effective dissemination. Traditional obscurant materials such as TiO₂ and brass flakes are often disseminated explosively from grenades when the goal is rapid concealment. Experimental evaluation of these of obscurant materials has shown that performance (absorption and scattering) is typically better when disseminated via pneumatic pressure driven sonic nozzles when compared to explosive grenade dissemination. Discussions to improve explosive dissemination of obscurants generated questions concerning the basic nature of explosive dissemination. We note that it is likely the pneumatic dissemination imparts large amounts of charge to the particles due to tribo-charging.⁶ Does this charge possibly help disperse the particles? If so, could something be done to pre-charge grenade payload particles or impart charge to the particles in the explosive dissemination? This leads to some basic questions: what do we know about charge on particles from an explosive dissemination? Is the resulting aerosol highly charged or does it quickly reach equilibrium? If they are charged, are they uni-charged? Searching for answers to these questions revealed that although there are many studies concerning charge on particles, there is very little if any on the topic of particle charge from explosive events

1.3 Objective

We hypothesize that, in an explosive event, charge could be imparted to the individual particles either by tribo-charging due to particle-particle interaction (or perhaps resulting from the breaking of the particle's frangible surface boundaries), free radicals present in the explosive reaction, or from the intense gas heating and pressure discontinuities of the shock wave. Our primary study objective was to measure the electrical charge characteristics of payload particles that are disseminated in an explosive event, and then possibly infer the dominant charging mechanism from these characteristics.

2 METHODOLOGY

Several experimental explosive devices were created based on an M106 obscurant grenade configuration. The outer cylindrical shell of the M106 is cardboard, 4.25 inches long and 2.25 inches inside diameter. It utilizes a full length C4 explosive central burster that has an outside diameter of 0.75 inches. The actual devices used in this study however, were custom fabricated by cutting the length of the grenade in half, so that the overall length of the device was 2.125 inches. These devices were filled with conductive and non-conductive materials (varying dielectric constant) whose native size is in the micron to sub-micron range. These devices were functioned in an explosive test chamber and the resulting aerosols were characterized to determine particle size, concentration, and particle charge. Figure 1 shows the device components and function on an outdoor range. The aerosol resulting from the explosive dissemination was then compared to various non-explosive disseminations of the same payload materials. These other disseminations present different primary particle charging mechanisms to provide perspective and comparison to the characteristics of the electrical charge resulting from the explosive device.



Figure 1. A) Explosive dissemination test item and B) explosive test item function with TiO₂ payload.

2.1 Test items

The various devices or dissemination methods used in this study were:

- Explosive Device: 1/2 of M106 body, 8 grams C4 central burster. Filled with 124 cm³ of payload material.
- Pneumatic Device: “SRI” sonic nozzle dispersing through a 6-ft piece of PVC pipe.
- Pneumatic Device: commercial powder-coating paint sprayer with corona charger.
- Pneumatic Device: Air Atomizer (airbrush).
- Shock Wave Device: Non-explosive Burst-Disc grenade (Section 219 Innovative Project product).
- Pyrotechnic Device: 8-gram mix (1.7-gram red dye payload) end-burner.
- Combustion Device: HMMWV (High Mobility Multipurpose Wheeled Vehicle) diesel.

Table 1 gives details of the various dissemination methods, the materials that were disseminated (with estimated dielectric constant), and the plausible mechanisms that could impart electrical charge to the payload particles.

Table 1. Test item configurations.

Dissemination Method	Plausible Charging Mechanism	Payload Particle Material	Dielectric Constant (Dk)
Explosive	Flame, Tribo-charging	Titanium Dioxide (TiO ₂)	80
		Polyester Powder	3
		Brass Powder	∞
Pneumatic	Tribo-charging	Titanium Dioxide (TiO ₂)	80
		Polyester Powder	3
		Brass Powder	∞
Pneumatic augmented with corona discharge	Tribo-charging, Field charging (>1-μm), Diffusion charging (<0.1-μm)	Titanium Dioxide (TiO ₂)	80
Burst Disc/shock wave	Tribo-charging	Titanium Dioxide (TiO ₂)	80
Pyrotechnic	flame	Red smoke dye	n/a
Combustion	flame	diesel	n/a

2.2 Experimental facilities

The ECBC Smoke and Obscurant Aerosol Test Chamber (Figure 2) was used to perform the explosive and pyrotechnic dissemination trials. This chamber is rated for up to 200 grams of TNT-equivalent explosive and has a 190 m³ test volume.

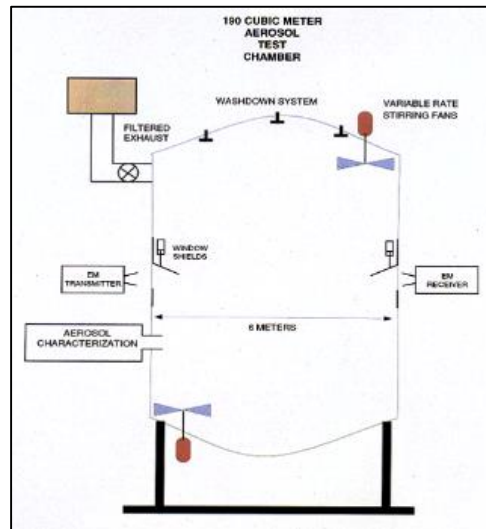


Figure 2. Diagram of ECBC's explosive test chamber.

2.3 Measurement of charge distribution

The Dekati® Electrical Low-Pressure Impactor (ELPI®+) is typically used to measure particle size distribution in real time, and due to its operating principle it is also suited for the detection of particle net charge distribution.⁷ The ELPI®+ uses cascade impactor technology, combined with particle charging and electrical detection to measure airborne particle size distribution and concentration in real-time. Cascade impactors use particle inertia to separate particles by size, collecting them on a substrate within each impactor stage. By operating at very low pressures, the Reynolds number of each stage is significantly lower than that found in classical cascade impactors, allowing inertial separation of the particles from the airstream to be effective down into the nanometer range. As configured in this test setup, it operates in the size range of 30 nm to 10 µm. Incoming particles are first charged to a known level using a corona charger. As the particles pass through the corona charger they accumulate a high charge level which is known as a function of particle size. The impactor stages are connected to sensitive electrometers which detect the accumulation of particles on each stage by the detection of the charge they impart to the stage substrate. The charge per particle is known therefore providing number count of particles on each stage providing real time measurement of the particle size distribution.⁸ The ELPI®+ operation is illustrated in Figure 3.

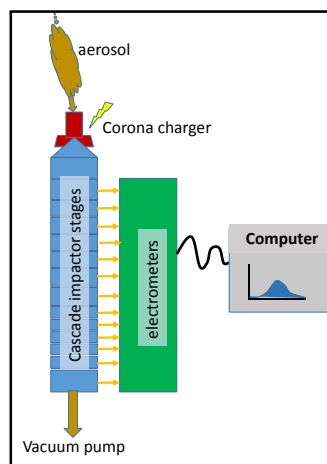


Figure 3. Diagram of the Dekati® ELPI®+ system.

The sensitive electrometers can measure currents as small as 2-fA.⁹ If the corona charger is turned off then the charge (both positive and negative levels) measured on each stage is due to the net characteristic charge of particles on that stage. By turning the charger on and off in cycles, both the number count and the overall charge distribution are measured. These charge and number measurements are then used to obtain the charge per particle (CPP) of the aerosol.

As a response to interest in particle charge measurement studies, Dekati® has incorporated a “charge measuring” feature into the latest ELPI® control software.⁹ However, we have found that electrometer instability from cycling the ELPI®+ charger at the high particle concentrations common to our trials in this study renders this feature unreliable. Data reduction and analysis is best done by manual inspection of the raw current history and selecting small blocks of sampling times from the charger off cycle where raw current is consistent and pairing it with number concentration measurements from the end of the previous charger on cycle.

3 DATA

Several trials of the various dissemination methods were performed and the overall number concentration particle size distribution of the resulting particle cloud was obtained. The explosive dissemination in particular produced a particle cloud that contained not only the payload materials which was of interest to the charge measurement study, but also produced a large amount of non-interest debris from the grenade body and components. Examining the particle size distribution from the other dissemination methods which did not result in ancillary debris and also functioning blanks (explosive configurations without payload materials) focused the charge characterization to data associated primarily with the payload particles. Figure 4A shows the overall number distribution of all the dissemination trials. This figure indicates that the charge characterization data pertaining to the payload particles should focus primarily in the 0.1-2.0 μm size range, as the blank explosive trial indicates that the high particle concentration below 0.1 μm appears to be from explosive debris, not payload. Figure 4B presents the number distribution in this window of interest with the “blank” subtracted from the explosive dissemination trials.

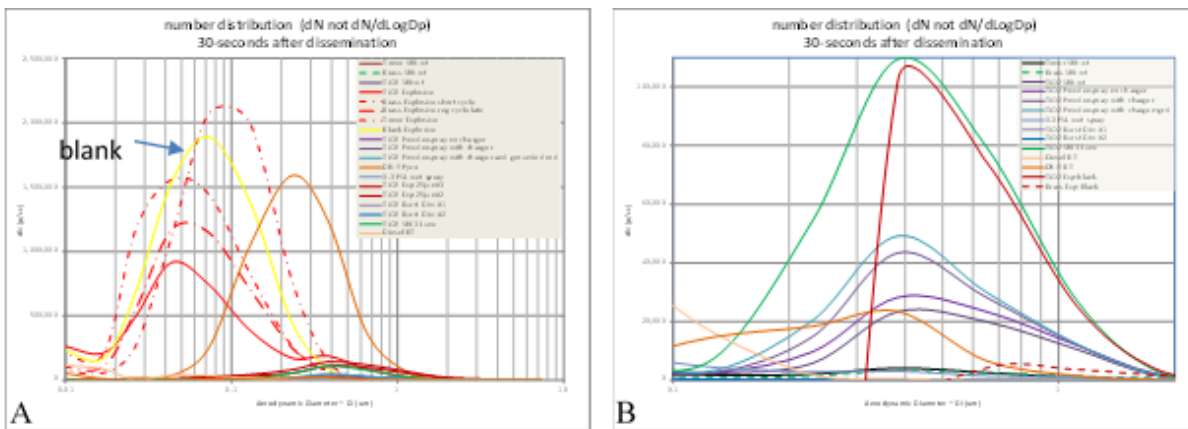


Figure 4. A) Particle number count size distribution of all dissemination configurations. B) Window of interest concerning the payload material particles (blank subtracted from explosive trial data).

Charge distribution within the size range 0.1-2.0 μm was then determined from the ensemble particle charge per stage ($Q = I t$), where I is the current detected by the electrometer and t is the sampling time for that data set (1 second). The number count per stage is determined from the ELPI®+ calculated number concentration (dN) and the ELPI®+ sampling flow rate (10 lpm) and sampling time (1 second). The ratio of the charge per stage and the number count per stage then gives the CPP for a particular size bin represented by that stage. The charge distributions and charge per particle for the various dissemination methods are shown as a function of the geometric mid-point of each size range associated with the impactor stage in Figures 5A-H.

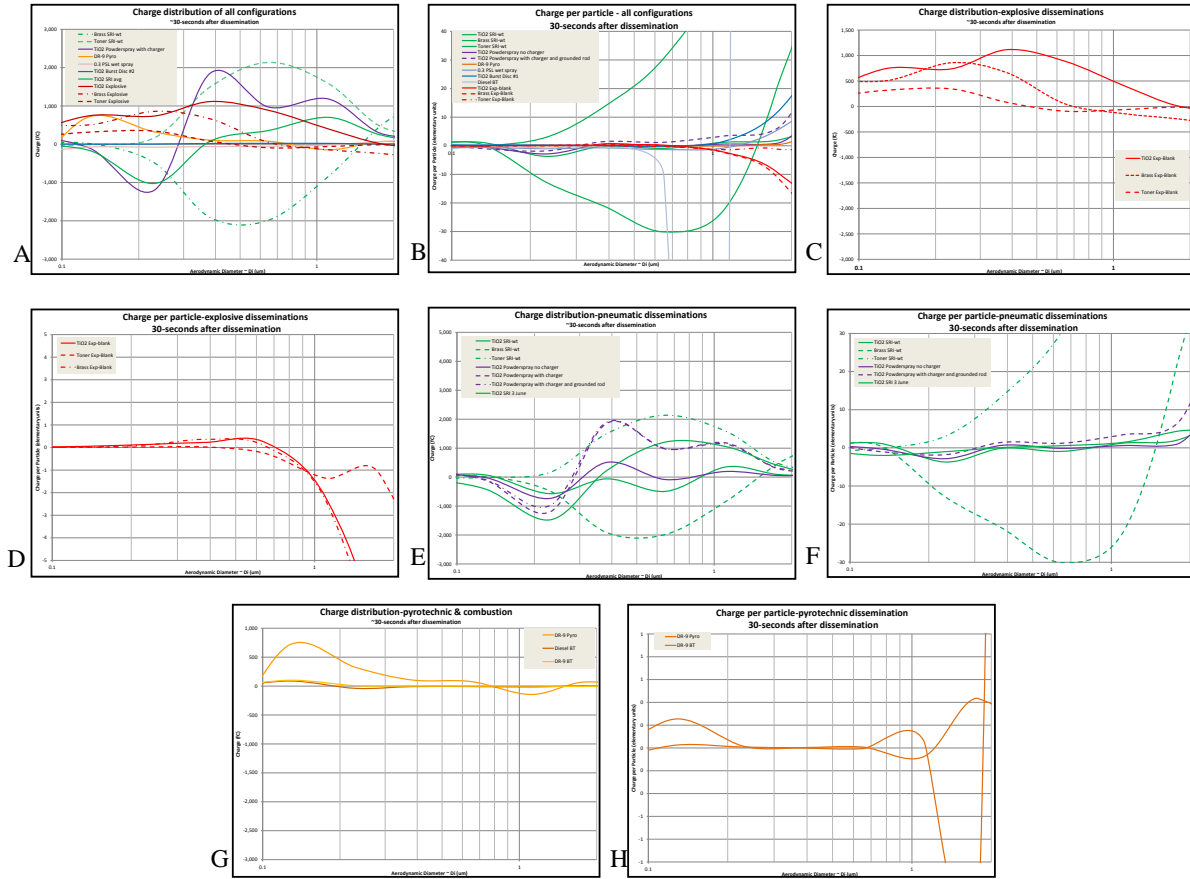


Figure 5. A-B) The first two plots depict the charge distribution and charge per particle for all disseminations. C-H) Show the same data, but are separated by dissemination method.

4 RESULTS

Pneumatic dissemination of particles will usually impart a significant charge to the particles due to various tribo-charging mechanisms. Furthermore, the polarity of the charge will be dependent on the material properties of the particle and contacting surface, (especially their dielectric constant [Dk] relative to each other).⁵ Comparing the CPP of the explosive dissemination to that of the pneumatic dissemination, indicates that the explosive dissemination does not produce a significant CPP level. This comparison is summarized in Figures 6A and Figure 6B.

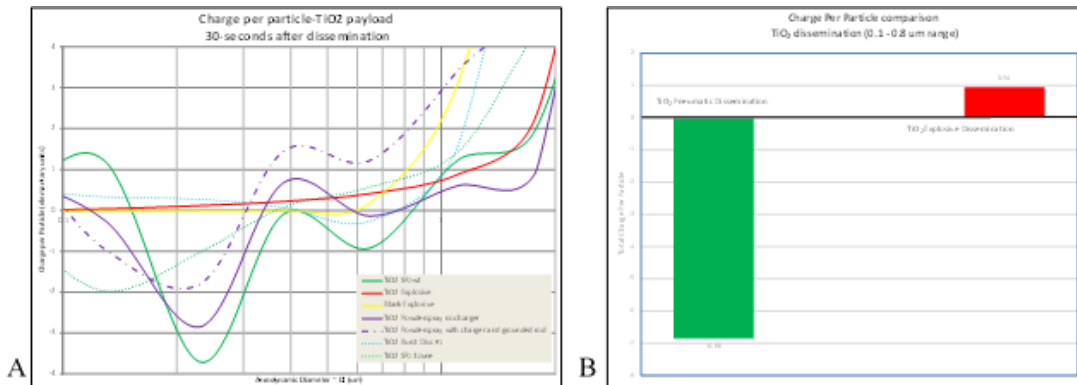


Figure 6. Explosive and pneumatic dissemination comparison. A) Charge per particle distribution and B) total charge per particle over the 0.1 to 0.8 µm range.

It is also interesting to compare the charge distribution of the various dissemination mechanisms: pneumatic dissemination, explosive dissemination, and burst disc (shock wave). This comparison is shown in Figure 7.

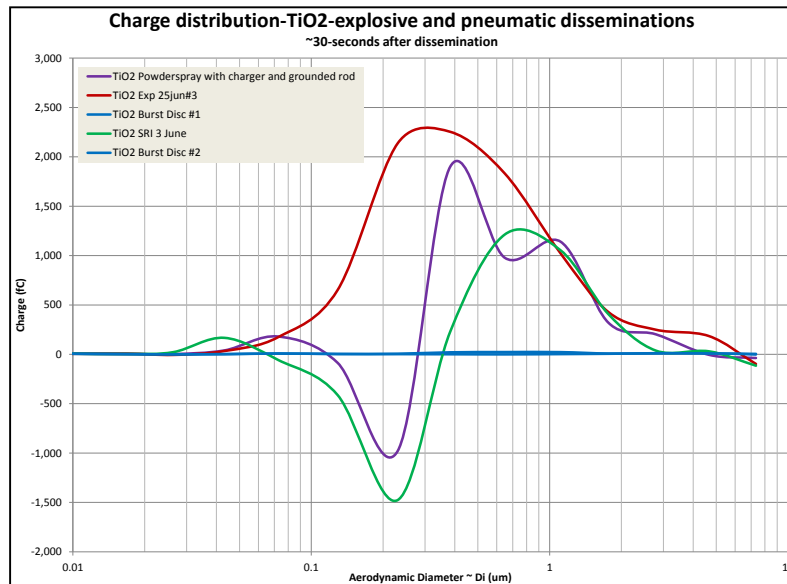


Figure 7. Charge distribution for TiO₂ payload comparing explosive, pneumatic, and burst disk disseminations.

The pneumatic disseminations usually result in a particle charge distribution that is negative in the small particle size range which then becomes positive as the size increases. There were some interesting trends observed in Figures 5E-F that may be characteristic of the tribo-charging of materials with various dielectric constants (Dk). In our setup, where a metallic body disseminator passed the particles through an electrically insulating (PVC) tube at high velocity, low Dk (~3) materials obtained a relatively high CPP that increases in positive charge as size increased. Medium Dk (~80) produced a relatively low CPP that was negatively charged for small particles and became positive charge as size increases. This result roughly correlates to studies on ultrafine particle using diffusion charging.¹⁰ Also, materials with a high Dk (∞) produced a relatively high CPP that increased in negative charge as size increased. This result correlates to previous study of charge on conducting particles used as smoke scavengers.⁶

In contrast to the pneumatic dissemination, the explosive dissemination produced a positive charged payload aerosol. Also notice that the burst disc dissemination does not impart a significant charge to the payload. This may be relevant to understanding the charge mechanism from the explosive dissemination. Similar to the explosive dissemination, the burst disc disseminator created a shock wave due to a sudden pressure discontinuity. However the burst disc did not have the heat associated with the chemical reactions front present in the explosion. Presumably the main particle charging mechanisms due to a pure shock wave would be some type of tribo-charging, either due to breaking of the particles' frangible edges or particle to particle friction. This lack of charge from the burst disc dissemination suggests that noticeable positive charging of particles in the explosive dissemination is not a result of tribo-charging but rather "flame-charging" mechanism.

4.1 Technical challenges and data validation

The explosive devices used in this study required the use of a relatively large (190 m³) explosive test chamber. This volume presents a challenge in measuring the true charge on particles immediately following the event. Electrically-charged aerosol particles will dissipate the charge due to collisions with oppositely-charged ions in the air. Typical charge relaxation times (where the charge dissipates by 37%)¹¹ can range from 2 seconds to over 100 minutes depending on ion concentration.¹ In ambient atmospheric conditions it is usually assumed that the charge neutralizes within 30 minutes.³ However, some studies on smoke particle scavengers¹² and anecdotal experience with ECBC aerosol chamber testing has shown the charge from experimental setups will dissipate within 30 seconds. Therefore it is important to note that the time for the aerosol to move from the center of the test chambers, through the sampling lines and into the ELPI@+ for measurements is on the order of 30 seconds. So it is possible that a short-lived aerosol charge may not be detected. Also, humidity plays a large part in whether charging will happen in certain processes and how quickly the charge will dissipate. We could not control humidity in our explosive chamber, but

measured it to be between 45-60% relative humidity for all trials. As a testing parameter, this is not normally considered a large variation in humidity, however the possibility that it may introduce some uncertainty in comparing charge per particle levels between dissemination methods which were performed on different days must be acknowledged.

There is very little from the literature search to guide our expectations on particle charging characteristics due to explosive dissemination. However there is some literature on charge distribution and charge per particle from the Pharmaceutical industry.¹³ These studies focused on Metered Dose Inhaler (MDI) generation of pharmaceutical aerosols. The MDI can readily tribo-charge these pharmaceutical particles, using the charge to increase deposition in the lungs. The charge distributions measured in these studies were similar to ours for tribo-charging disseminations, showing a switch from negative to positive charging as particle size increased, thereby giving confidence to our general trend conclusions. Also as a simple "sanity check" several of the pneumatic dissemination trials were performed using a corona charger to augment the tribo-charging mechanism. As expected there was a significant increase in the charge level for these trials.

5 CONCLUSIONS

A series of experimental trials were performed in a large explosive rated aerosol test chamber to determine the electrical charge characteristics of the aerosol particles resulting from an explosive dissemination event. These trials used small scale explosive devices which incorporated payload materials of various dielectric constants. The same payload materials were also disseminated by other methods for comparison to the explosive dissemination trials.

The charge distribution of explosively-disseminated submicron particles show that they are mainly positively-charged whereas other disseminations show charge distributions that can be negatively-charged or contain bipolar charges that are dependent on particle size. This unique signature may indicate that thermionic emission or "flame-charging" is the predominant particle charging mechanism, rather than tribo-charging which is common to most other dissemination methods.

However, explosive dissemination of submicron payload particles do not produce particle charge levels (charge per particle) that are significantly higher than other dissemination processes. In particular, the charge per particle level is several times less than the level created during common tribo-charging processes.

There are some interesting follow-on efforts that might be pursued. This particular study focused on the sub-micron particle fraction of the payload, however for certain payloads there is a significant mass fraction around 10 μm and above, which was not analyzed. This larger size fraction could be important, especially in scavenging applications, and might be explored further with other instrumentation.

ACKNOWLEDGMENTS

Support for this research was provided by the U.S. Army Edgewood Chemical Biological Center Research and Technology Directorate's Seedling Program. The authors thank David Redding for creating and functioning the explosive test devices, Ernest Black for use of the explosive test chamber, and Brendan DeLacy for insightful input during the project genesis.

REFERENCES

- [1] Hinds, W.C., *Aerosol Technology: Properties, Behavior, and Measurement of Airborne Particles*. John Wiley & Sons, New York. **1999**.
- [2] Xi, J.; Si, X.; and Longest, W., "Electrostatic charge effects on pharmaceutical aerosol deposition in human nasal-laryngeal airways." *Pharmaceutics*, **2014**, 6(1), p26-35.
- [3] Flagan, R.C., "Chapter 15: Electrical mobility methods for submicrometer particle characterization." In: *Aerosol Measurement: Principles, Techniques, and Applications, Third Edition*. Kulkarni, P.; Baron, P.A.; and Willeke, K. (eds.). John Wiley & Sons, New York. **2011**. p350-355.

- [4] Gallo, C.F. and Lama, W.L., "Some charge exchange phenomena explained by a classical model of the work function." *Journal of Electrostatics*, **1976**, 2, p145-150.
- [5] Mitchell, J.P. and Coppolo, D.P., "Electrostatics and inhaled medications: influence on delivery via pressurized metered-dose inhalers and add-on devices." *Respiratory Care*, **2007**, 52(3), p283-300.
- [6] Rubel, G.O. and Hogan, G., "Clearing of military smokes and aerosols." *Technical Report, CRDEC-CR-040*, **1989**.
- [7] Mikkanen, P. *et al.*, "Method for measuring variations in characteristics of inhaler single doses charge properties using ELPI." *Proceedings of Drug Delivery to the Lungs XIV (London, UK)*, **2003**.
- [8] "Dekati® ELPI®." Ecotech, [<http://ecotech.com/wp-content/uploads/2015/03/Delkati-ELPI.pdf>]. (Last accessed: 19 June 2015).
- [9] "Measuring Particle Charge with the ELPI+." Dekati Ltd. Technical Note, **2014**.
- [10] Davison, S.W. and Gentry, J.W., "Differences in diffusion charging of dielectric and conducting ultrafine aerosols." *Aerosol Science and Technology*, **1985**, 4, p157-163.
- [11] Crowl, D., *Understanding explosions*. American Institute of Chemical Engineers, New York. **2003**. p105-112.
- [12] Podzimek, J. and Martin, J., "Results of past and current investigation of the smoke particle scavenging by non-spherical collectors." *Proceedings of the Chemical Research and Development Center's 1984 Scientific Conference on Obscuration and Aerosol Research*, CRDC-SP-85007, June **1985**.
- [13] Karner, S. and Urbanetz, N., "The impact of electrostatic charge in pharmaceutical powders with specific focus on inhalation powders." *Journal of Aerosol Science*, **2011**, 42, p428-445.

